

**ELECTROCHEMICAL INVESTIGATION OF THE GROWTH OF
ANODIC FILMS ON IRON AND FERROUS ALLOYS**

by

FIONA GRAHAM

University of Natal

Submitted in partial fulfilment of
the requirements for the degree of
Doctor of Philosophy
in the
Department of Chemistry
University of Natal

PREFACE

The experimental work described in this thesis was carried out in the Department of Chemistry, University of Natal, Durban, under the supervision of Prof. H. Brookes.

These studies represent original work by the author and have not been submitted in any form to another University. Where use was made of work of others, it has been duly acknowledged in the text.

DECLARATION

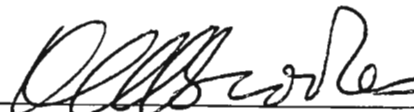
I hereby certify that this research is the result of my own investigation, which has not already been accepted in any substance for any degree, and is not being concurrently submitted in candidature for any other degree.

Signed : 

F. Graham

M.Sc (Natal)

I hereby certify that the above statement is correct.

Signed : 

Associate Professor H. Brookes

Ph.D. (Cape Town)

Professor of Inorganic Chemistry

University of Natal

Durban

ACKNOWLEDGEMENTS

My sincere appreciation is due to

Prof. H. Brookes for all his assistance throughout this project

Mr Paul Holden for his glass - blowing

Mr Garth Buhrmann for machining the components of the Teflon cell

Mr Dave Balson for his assistance with the maintenance of the electrical equipment

Mr Phil Evers and Ms Lalitha Maistry (Physics Electron Microscope Unit) for their assistance with the use of the SEM

Mr Clive Johnson (Dept. Electrical Engineering) for the use of the Milli - Q system

Mr Richard Atkinson (Dept. Physics) for interfacing the Apple II+ to the PC

Council for Scientific and Industrial Research (CSIR) for a PhD bursary

ABSTRACT

An electrochemical investigation of the corrosion of iron and Fe18Cr based stainless steel alloys was undertaken with particular emphasis on the nucleation and growth of surface films.

Chronoamperometry was shown to be a sensitive technique to investigate the initial stages of film formation and growth. In a variety of acidic ($\text{pH} < 7$), alkaline and alkaline cyanide electrolytes, providing dissolution of the substrate metal could occur rising current transients, similar to those reported in electrocrystallisation studies, were observed when the electrode was stepped to the appropriate potential. This indicated that at these potentials the surface film formed via the nucleation and growth of discrete nuclei. A significant aspect of this study was visual evidence of this nucleation and subsequent growth of the film provided by scanning electron microscopy which supported the electrochemical data and interpretation thereof.

Existing electrocrystallisation models were used to evaluate the experimental rising current transients. While these models gave an indication as to the prevailing nucleation and growth mechanism, they were found to be inadequate in describing anodic oxide formation on an oxidising substrate. A qualitative model was proposed.

In acidic electrolytes, rising chronoamperometric transients were observed for Fe, Cr and Fe18Cr at passive potentials and for Fe x Cr ($x = 16, 18, 20, 23\%$ Cr) and alloys 444, 4732, 4733, 304L and 316L at transpassive potentials. The transients were shown to be sensitive to variations of potential, temperature, electrolyte and alloy composition.

A systematic investigation of the influence of temperature ($20^\circ\text{C} - 120^\circ\text{C}$) on the chronoamperometric, cyclic voltammetric and rotating ring - disc electrode behaviour of Fe in 0.5M and 1.0M NaOH was also undertaken. In alkaline electrolytes, the formation of a duplex surface film was proposed, with x-ray photoelectron spectroscopy indicating that the protective base layer consisted of FeO while Fe₂O₃ and FeOOH constituted the upper layer. Base layer formation was favoured with increasing temperature and increasing hydroxide ion concentration of the electrolyte. Addition of 0.4M NaCN to 0.5M and 1.0M NaOH had a marked effect on the electrochemistry of the system, with CN⁻ inhibiting surface film formation, particularly of the upper layer. A mechanism for the oxidation of Fe in alkaline and alkaline cyanide electrolytes was proposed.

CONTENTS

Preface	ii
Declaration	iii
Acknowledgements	iv
Abstract	v
Contents	vi
1. INTRODUCTION	1
2. LITERATURE REVIEW	3
2.1 Fe and FeCr alloy dissolution in acidic electrolytes	3
2.1.1 Salt films	5
2.2 Fe dissolution in alkaline electrolytes	6
2.3 Electrochemistry of Fe and stainless steels in alkaline cyanide electrolytes	18
2.3.1 The CIP process	19
2.4 Surface analysis techniques used in the determination of the nature of the surface film	19
2.4.1 <i>Ex-situ</i> vs <i>in-situ</i> analysis techniques	20
2.4.2 Depth profiling	21
2.5 Nature of the surface films formed on ferrous alloys	22
2.5.1 Influence of minor alloying elements on the nature of the passive film	25
2.6 Nature of the surface film on Fe in alkaline electrolytes	26
2.6.1 Discrete layering of the duplex film	29
2.6.2 Absence of discrete layering of the duplex film	30
2.6.3 The presence or absence of Fe_3O_4 in the surface film	31
2.7 Crystalline nature of surface films on Fe and ferrous alloys	32
2.8 Film thickness	33
2.9 Electronic structure of surface films	33
2.10 Pourbaix diagrams for the Fe - H_2O and Fe - CN - H_2O systems	34
2.11 Theories of nucleation and growth of surface films	36
2.11.1 Electrocrystallisation processes	46
2.11.2 Active sites	47
2.11.3 Nucleation mechanism	48
2.11.4 Shape of nuclei	49

2.11.5	Overlap of nuclei	50
2.11.6	Nucleation exclusion zones	51
2.11.7	Electrocrystallisation models	52
2.11.7.1	Nucleation and diffusion controlled 3D growth of hemispheres	52
2.11.7.2	Nucleation and charge transfer controlled 3D growth	56
2.11.7.3	Nucleation and 3D growth leading to passivation	60
2.11.7.4	Nucleation and charge transfer controlled 2D growth	61
2.11.7.5	2D electrocrystallisation coupled to diffusion in the electrolyte with and without simultaneous metal substrate dissolution	62
2.11.7.6	Adsorption - nucleation models	63
2.11.8	Criticism of nucleation models	67
2.11.8.1	Armstrong, Fleischmann and co - workers	67
2.11.8.2	Gunawardena, Hills, Montenegro and Scharifker	68
2.11.8.3	Scharifker and co - workers	69
2.11.8.4	Bosco and Rangarajan	70
2.11.8.5	Deutscher and Fletcher	71
2.11.8.6	Pritzker	71
2.12	Prefilm	71
3.	EXPERIMENTAL	76
3.1	Samples	76
3.2	Chemicals	78
3.3	The cell	78
3.3.1	Glass cell	78
3.3.2	Teflon cell	81
3.4	Rotating electrode unit	85
3.5	Construction of the working electrodes	85
3.5.1	Disc electrodes	85
3.5.2	Ring - disc electrodes	87
3.6	Instrumentation	87
3.7	Software	90
3.8	Procedure for electrochemical measurements	90
3.8.1	Electrode pretreatment	90
3.8.2	Anodic polarisation	92
3.8.3	Cyclic voltammetric experiments	92
3.8.4	Rotating ring - disc experiments	92
3.8.5	Chronoamperometric experiments	92
3.9	Surface analysis	93

3.9.1	SEM analysis	93
3.9.2	XPS analysis	93
3.9.3	AES analysis	94
4.	RESULTS and DISCUSSION	95
	Nucleation and growth of anodic films on metals in acidic electrolytes	
4.1	Influence of electrolyte composition	98
4.1.1	H ₂ SO ₄	98
4.1.2	NaHSO ₄	100
4.1.3	HClO ₄	100
4.1.4	Na ₂ SO ₄ and NaClO ₄	100
4.2	Influence of alloy composition	104
4.2.1	Iron	104
4.2.2	Chromium	104
4.2.3	Molybdenum	108
4.2.4	FeCr	108
4.2.5	Alloys 444 and 4733	108
4.3	Influence of temperature	112
4.4	SEM analysis of the electrode surface	116
4.5	Formation of a compact white film on the surface of alloys Fe18Cr and 444	116
4.6	Analysis of transients	119
4.6.1	Fe transients	119
4.6.2	Fe18Cr transients	121
4.6.3	Nucleation model	122
4.7	Interpretation of experimental data in terms of nucleation concepts	127
4.8	Summary	129
5.	RESULTS and DISCUSSION	130
	IRON IN ALKALINE CYANIDE ELECTROLYTES :	
	Cyclic voltammetry and rotating ring - disc electrode experiments	
5.1	Fe in 1.0M NaOH	130
5.1.1	Sweep rate and temperature dependence	135
5.1.2	Growth laws	140
5.1.3	Conjugate peaks	144
5.1.4	Rotation rate dependence	146
5.1.5	Rotating ring - disc electrode experiments	147
5.2	Fe in 1.0M NaOH + 0.4M NaCN	149
5.2.1	Sweep rate and temperature dependence	153

5.2.2	Growth laws	158
5.2.3	Conjugate Peaks	158
5.2.4	Rotation rate dependence	160
5.2.5	Rotating ring - disc electrode experiments	160
5.2.6	Influence of hexacyanoferrates on the cyclic voltammetric and rotating ring - disc electrode response of a Fe electrode	164
5.3	Fe in 0.5M NaOH	168
5.3.1	Sweep rate and temperature dependence	171
5.3.2	Conjugate peaks	176
5.3.3	Rotation rate dependence	176
5.3.4	Rotating ring - disc electrode experiments	180
5.3.5	SEM analysis	182
5.3.6	XPS analysis	186
5.4	Fe in 0.5M NaOH + 0.4M NaCN	190
5.4.1	Sweep rate and temperature dependence	190
5.4.2	Rotation rate dependence	194
5.4.3	Rotating ring - disc electrode experiments	194
5.4.4	SEM analysis	194
5.4.5	XPS analysis	198
5.5	Summary	198
5.5.1	0.5M and 1.0M NaOH	198
5.5.2	Addition of 0.4M NaCN to 0.5M and 1.0M NaOH	201
5.6	Dissolution Mechanism	202
5.6.1	Dissolution Mechanism of Fe in NaOH electrolytes	203
5.6.2	Dissolution Mechanism of Fe in NaOH/NaCN electrolytes	207
6.	RESULTS and DISCUSSION	210
	IRON IN ALKALINE CYANIDE ELECTROLYTES :	
	Chronoamperometric experimemts	
6.1	Fe in 0.5M NaOH	210
6.2	Fe in 0.5M NaOH + 0.4M NaOH	221
6.3	Fe in 1.0M NaOH	224
6.4	Fe in 1.0M NaOH + 0.4M NaOH	228
6.5	Analysis of rising current transients in terms of surface film nucleation models	232
6.5.1	Nucleation model	236
6.6	Presence of an initial film on the electrode surface	238
6.7	Summary	239

7.	RESULTS and DISCUSSION	240
	XPS INVESTIGATION OF THE SURFACE FILM FORMED ON Fe IN ALKALINE ELECTROLYTES	
7.1	Standards	240
7.2	Growth of surface film on Fe in 0.5M NaOH, 20 °C	242
7.3	Influence of temperature on surface film growth	245
7.4	Influence of cyanide ions on the surface film growth at 20 °C	247
7.5	Influence of cyanide ions on the surface film growth at 80 °C	248
7.6	Influence of temperature on surface film formation on Fe in 0.5M NaOH + 0.4M NaCN	248
7.7	Summary	250
8.	SUMMARY	251
	REFERENCES	255
	APPENDIX A	268
	XPS binding energies	
	APPENDIX B	276
	Publications	

CHAPTER ONE

INTRODUCTION

The cost of corrosion to industrialised countries is reported to be in the region of 3% — 5% of the gross national product. This provides sufficient incentive for continuing research and development into understanding the causes of corrosion and methods for its minimisation and control.

The corrosion behaviour of a metal is directly related to the nature of the film of corrosion products formed on its surface. The ability of this surface film to nucleate and to continue to grow, in order to passivate or repassivate a surface, is fundamental to the corrosion resistance of metals. An understanding of the nature of this passive film is therefore essential, as any proposed mechanism must include assumptions regarding the properties of the this film.

The passivation of iron and stainless steel alloys has been extensively investigated and reported on in the literature, however there is still considerable debate with respect to the passivation mechanism and the precise physical and electrochemical characteristics of the surface films. A major cause of the discrepancies is the lack of reliable experimental data, particularly in alkaline electrolytes where the precipitation of iron oxides and hydroxides, and their subsequent stability, are a complicating factor. The diversity of results, and interpretation thereof, reported in the literature are highlighted in chapter two.

Electrocrystallisation theories are frequently used in an attempt to describe the observed rising chronoamperometric transients. Good correlation between experimental data and theoretical prediction exists for a limited number of systems, but is debatable when attempting to describe more complex systems, for example, anodic oxide formation on an oxidising substrate. The major constraint in the development of realistic models is the limitations imposed by the mathematics. A brief overview of the development and short comings of the more frequently used electrocrystallisation models is also presented in chapter two.

The use of chronoamperometry to investigate anodic oxide formation on metals has been reported in the literature, with such experiments resulting in the appearance of rising current transients similar to those obtained for the electrocrystallisation of metals. Preliminary work in this laboratory has shown chronoamperometry to be a very sensitive technique for monitoring the nucleation and growth of surface films on Fe18Cr type stainless steel alloys. The electrochemistry of such alloys in acidic electrolytes has

previously been extensively investigated in this laboratory using cyclic voltammetric, rotating ring - disc electrode, anodic polarisation, scratch chronoamperometric and ac impedance techniques. It is therefore with this background of knowledge that the formation of anodic films on Fe18Cr electrodes in various electrolytes of pH < 7 and on Fe, Cr, Mo and alloys Fe16Cr, Fe20Cr, Fe23Cr, 444, 4732, 4733, 304L and 316L in 0.1M H₂SO₄ has been investigated using single pulse chronoamperometry. Current transients were also obtained for Fe18Cr as a function of temperature. Other than papers emanating from this laboratory, such an investigation had not previously been reported in the literature.

The study was then extended to Fe and Fe18Cr stainless steels alloys in alkaline and alkaline cyanide electrolytes, over a range of temperatures from 20°C to 120°C. Despite the significant economic importance of such systems, for example, the extensive use of alkaline cyanide solutions in the gold mining industry, perusal of the literature indicates that a systematic electrochemical study of these systems has not been reported. In addition, there is considerable diversity in the published experimental results and interpretation thereof, for the Fe/OH⁻ system. Thus in chapters five and six the surface film formation on Fe in 0.5M and 1.0M NaOH, with and without the presence of 0.4M NaCN, at temperatures up to 120°C was investigated. Chapter six focuses on the initial nucleation and growth of the surface film, using chronoamperometry, while chapter five focuses on the subsequent growth of the film using cyclic voltammetric and rotating ring - disc electrode techniques. The Fe18Cr alloy data will not be presented in this thesis.

Concomitant with the electrochemical experiments, surface analytical techniques (scanning electron microscopy, x - ray photoelectron spectroscopy, Auger spectroscopy) was used to examine the electrode surfaces. A limited x - ray photoelectron spectroscopy investigation of the surface films on iron in alkaline and alkaline cyanide electrolytes was undertaken to determine the composition of the films. A significant aspect of the scanning electron microscopy was its ability to provide valuable visual evidence to support the electrochemical predictions from the initial nucleation stages through to the growth of a thick, duplex surface film.

CHAPTER TWO

LITERATURE REVIEW

Since the discovery of passivity in 1836, the nature of the passive film on metals has been controversial and as it is directly related to the passivation mechanism, an understanding of the nature of the passive film is therefore essential.

2.1 Fe AND Fe18Cr ALLOY DISSOLUTION IN ACIDIC ELECTROLYTES

The oxidation of iron and FeCr based stainless steel alloys can be succinctly described by the anodic polarisation curves of these metals, as shown in Fig. 2.1. As the various regions of such polarisation curves will be referred to throughout the thesis, a brief description of the curve will be given below.

A specimen, in contact with a corrosive environment, assumes a rest potential which is referred to as the corrosion potential, E_{corr} , relative to a reference electrode. This potential is defined as the potential at which the rate of oxidation is equal to the rate of reduction. The active region is that in which dissolution of metal occurs as the applied potential is scanned in a positive, or anodic, direction. As the measured current density increases with increasing potential, a small current peak at E_{pr} appears in dilute acidic electrolytes. With decreasing pH there is a decrease in the magnitude of this prepassive peak. The current density continues to increase to the primary passivation potential, E_{pp} , and then rapidly decreases with the onset of passivation. The beginning of this decrease is known as the active - passive transition region. As the applied potential becomes more positive the current density decreases to a minimum, known as the passive current density, where it remains over a wide range of potentials extending from the Flade potential, E_{Flade} , where the passive current density is first attained, to the transpassive potential, E_{tr} . At E_{tr} the passive film starts to break down resulting in an increase in the current density. For stainless steel alloys repassivation (secondary passivation) may occur at higher potentials. Finally, a rapid increase in the current density occurs due to the onset of oxygen evolution.

Increasing the corrosion resistance of the stainless steel by increasing the Cr content of the alloy or by the incorporation of minor alloying elements eg. Mo or V, results in a decrease in the current density at E_{pp} and in some cases a shift of E_{pp} to more negative potentials. This indicates that passivation has occurred

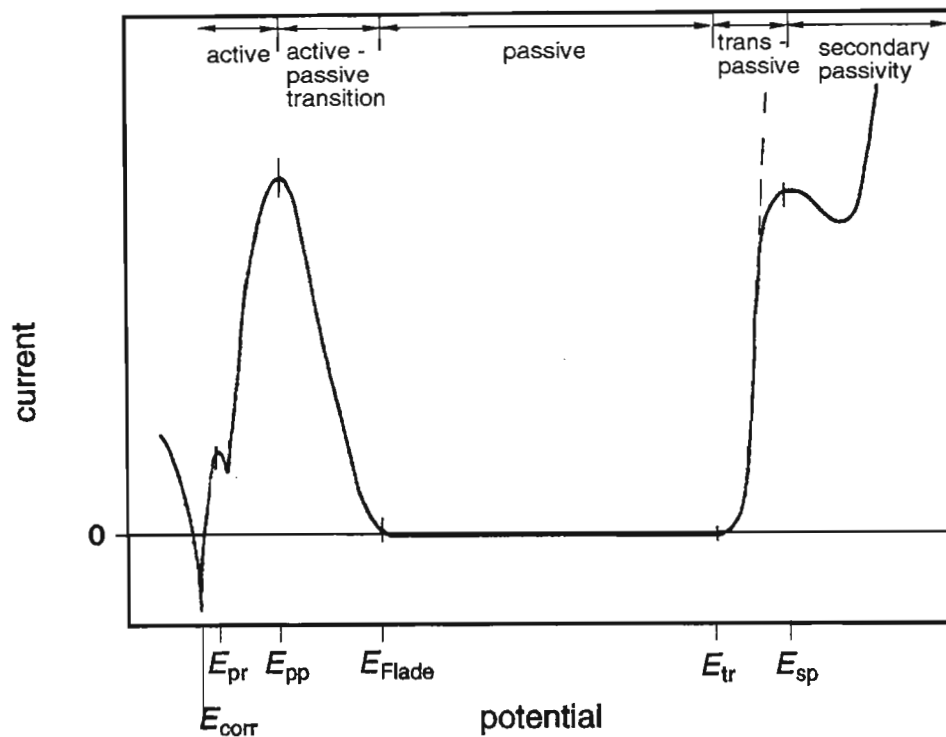


Fig. 2.1 Schematic representation of an anodic polarisation curve of iron (— — —) and stainless steel (——) in weakly acidic electrolytes.

- E_{corr} : corrosion potential
 E_{pr} : prepassive peak potential
 E_{pp} : primary passivation potential
 E_{Flade} : Flade potential
 E_{tr} : transpassive potential
 E_{sp} : secondary passivation potential

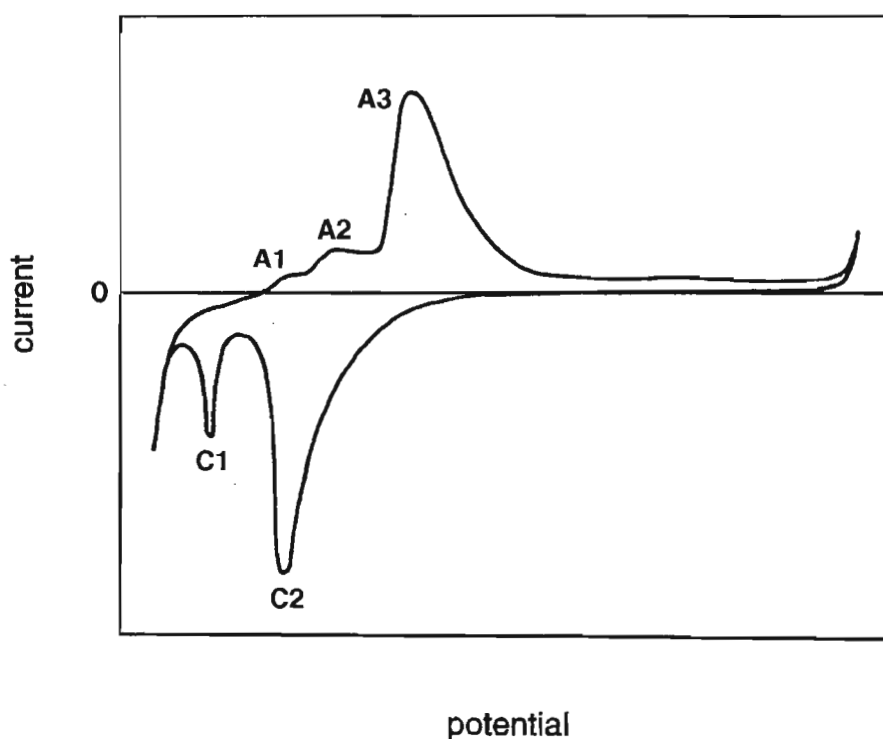
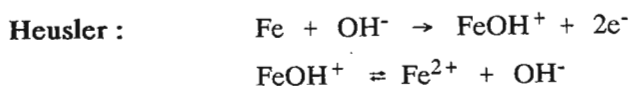


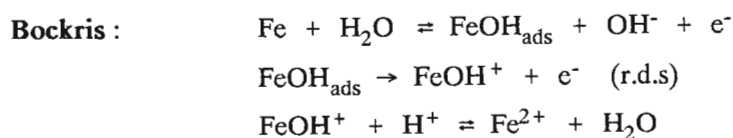
Fig. 2.2 Schematic representation of a cyclic voltammogram of Fe in alkaline electrolytes.

more readily and that less alloy dissolution has taken place. A lower passive current density is also observed with the more corrosion resistant alloys.

The kinetics of the initial dissolution of a Fe electrode in acidic electrolytes has been extensively investigated. Generally, most of the proposed mechanisms parallel either the Heusler¹ catalytic mechanism or the Bockris² non - catalytic consecutive mechanism, viz.



where transfer of ferrous ions in one step at specific sites on the surface is assumed to be rate determining



It has subsequently been shown³⁻⁶ that both mechanisms are valid with the microstructure of the substrate Fe determining which mechanism will prevail.

The formation and growth of passive films on Fe and FeCr alloys in acidic electrolytes has also been extensively investigated with numerous mechanisms having been proposed. Some of the more widely accepted mechanisms include those by the following authors and their co - workers : Macdonald,⁷ Lorenz,⁸ Bech - Nielsen,^{3,9-12} Okomoto,^{13,14} Bockris,^{15,16} Lu,¹⁷⁻²⁰ Armstrong,²¹ Schwabe²²⁻²⁴ and Burstein.^{25,26}

2.1.1 Salt Films

Since it was first reported by Müller in 1931, it has been acknowledged that the precipitation of salt films plays a major rôle in many passivation and repassivation processes of metals in acidic electrolytes. Most proposed models include an initial rapid metal dissolution stage resulting in an increase in the metal ion concentration in the electrolyte, near to the electrode surface. The precondition of supersaturation of a metal salt solution prior to passivation has been well documented, with values of 1 - 5 times the saturation concentration being cited as necessary.²⁷⁻³³ Once the required level of supersaturation is achieved precipitation of the salt film occurs which grows by continued precipitation from the supersaturated solution and by continued dissolution of the metal. Formation of a passive film is proposed to occur beneath the salt layer due to the increase in pH at the metal surface as a result of the electrolytic migration of H^+ away from the metal surface. A variety of mechanisms have been proposed for this process. At this point the electrolyte is no longer supersaturated and the salt film begins to dissolve eventually leaving only the passive oxide film on the metal surface. The time taken for the film to disappear is generally proportional to its thickness. There appears to be a lack of reliable porosity, thickness and transport data for salt films in the literature and as these parameters are fundamental to the proposed models for salt film formation, this imposes a limitation on model development and verification.

2.2 Fe DISSOLUTION IN ALKALINE ELECTROLYTES

The kinetics of Fe dissolution in alkaline electrolytes is complicated by the precipitation of iron oxides and by the changes in the nature and electrochemical properties of the surface films with time and applied potential regime. Therefore, while rapid transient techniques are required for kinetic studies, cyclic voltammetry provides a useful technique for investigating the growth of surface films.

When considering the nature and growth of passive films, distinction should be made between short term (transient) and long term (steady state) growth. These two processes should be considered independently as their kinetics and growth mechanisms may be different, as may be their response to variations of temperature, pH, electrolyte and alloy composition. Short term growth refers to the initial stages of surface film formation on a metal substrate that is essentially free from a surface film. Once a protective film has formed and rendered the metal passive, the continued growth (ie. long term growth) of the surface film is likely to be described by a different growth mechanism.

The cyclic voltammogram in Fig. 2.2 shows the most frequently reported oxidation and reduction peaks obtained with a Fe electrode in alkaline electrolytes. There is generally agreement in the literature that surface film formation occurs in 2 stages :

1st stage : formation of an initial $\text{Fe}(\text{OH})_2$ surface film, with the formation of HFeO_2^- as an intermediate species in concentrated alkali.

2nd stage : formation of Fe(III) oxides and oxyhydroxides — the exact nature of which being dependent on the applied potential regime.

There is however considerably less agreement in the literature with respect to the assignment of the various cyclic voltammetric peaks to specific reactions. Peak A1 is usually assigned to either the first stage of iron (II) oxide formation or to the oxidation of adsorbed hydrogen. Peak A2 has been variously attributed to the formation of either Fe(II) oxide / hydroxide, Fe(III) oxide or Fe_3O_4 . It is generally agreed upon that A3 corresponds to the formation of an upper layer, on the base layer, consisting of Fe(III) oxide. With continued applied potential cycling, there is a continual increase in the current density of A3 due to the increasing thickness of the surface film.

The lack of agreement regarding the corrosion mechanism is largely a result of the difficulty in obtaining reliable experimental data. Table 2.1 shows a selection of cyclic voltammograms of Fe in alkaline electrolytes, together with proposed peak assignments. As far as possible all potentials quoted in Table 2.1 are vs SCE[§] and peak identification has been standardised to facilitate comparison between the voltammograms. Notwithstanding the differences in experimental conditions it is evident that considerable variation in experimental results exists. In some cases this may be due to electrode preparation, for

[§] Unless otherwise stated, all potentials quoted in this thesis are vs SCE, 20°C.

Table 2.1

Cyclic voltammograms of Fe in alkaline electrolytes, reported in the literature

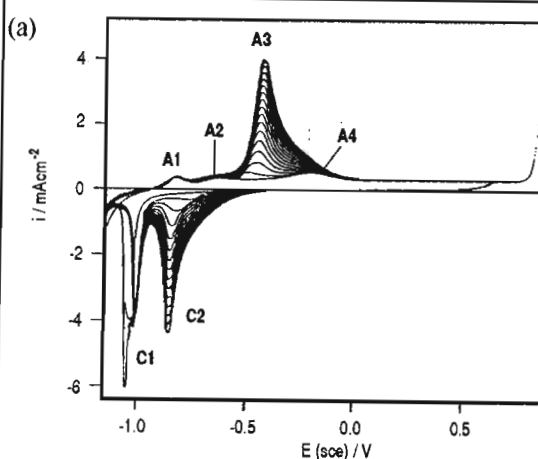
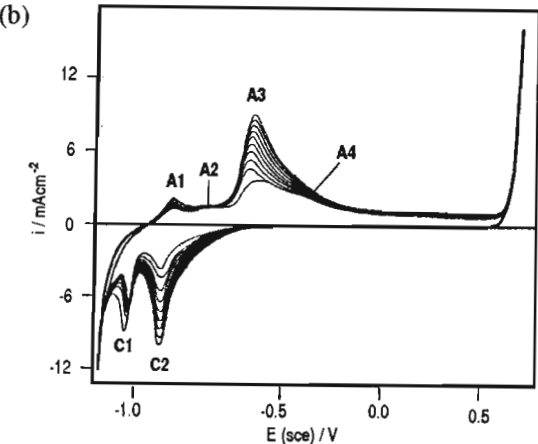
cyclic voltammogram	ref.	experimental conditions	peak assignments		
			peak	E_p /mV	species formed
<p>(a)</p> 	34 35	Fe 1M NaOH $\nu = 70 \text{ mV s}^{-1}$ $\omega = 62.5 \text{ rad s}^{-1}$	A1 A2 A3 A4 C2 C1	-1082 -879 -664 -462 -1086 -752	<p>oxidation of ≈ 1 monolayer adsorbed H_2</p> <p>$\text{Fe} \rightarrow \text{Fe}(\text{OH})_2$</p> <p>$\text{Fe}(\text{II}) \rightarrow \text{Fe}(\text{III})$ oxide or hydroxide precipitation layers</p> <p>not present during first sweep of a well prepared electrode</p> <p>inner $\text{Fe}(\text{II})$ oxide layer oxidised to $\text{Fe}(\text{III})$ oxide which has been formed up to -440 mV</p> <p>At $E > -240 \text{ mV}$ Fe_2O_3 is formed</p> <p>Reduction of $\text{Fe}(\text{III})$ oxide / hydroxide accumulated during previous cycles</p> <p>No reduction of a precipitation layer is found during the first sweep.</p> <p>$\text{Fe}(\text{III})$ oxide reduced to $\text{Fe}(\text{II})$ hydroxide and further to Fe metal</p> <p>reduction not complete with 1 - 2 monolayers of $\text{Fe}(\text{OH})_2$ remaining</p>
<p>(b)</p> 	36	Fe 1M KOH $\nu = 100 \text{ mV s}^{-1}$	A1 A2 A3 A4 C2 C1	-1021 -861 -601 -401 -1091 -1270	<p>$\text{Fe} \rightarrow [\text{Fe}(\text{OH})]_{\text{ad}} \rightarrow [\text{Fe}(\text{OH})]_{\text{ad}}^+ \rightarrow \text{Fe}(\text{OH})$</p> <p>continuation of $\text{Fe}(\text{OH})_2$ formation with simultaneous transformation of $\text{Fe}(\text{OH})_2$ into more stable structure ($\text{Fe}(\text{OH})_2$-oxide phase)</p> <p>$\text{Fe}(\text{OH})_2 \rightarrow \text{FeOOH}$</p> <p>$\text{FeOOH} \rightarrow \text{Fe}_2\text{O}_3 \cdot \text{H}_2\text{O}$</p> <p>reduction of species formed at A3</p> <p>reduction of $\text{Fe}(\text{OH})_2$</p>

Table 2.1

Cyclic voltammograms of Fe in alkaline electrolytes, reported in the literature

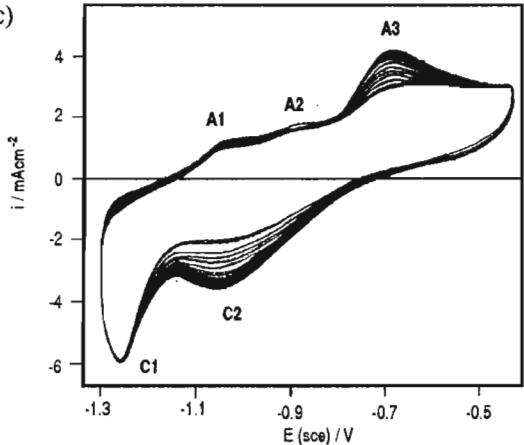
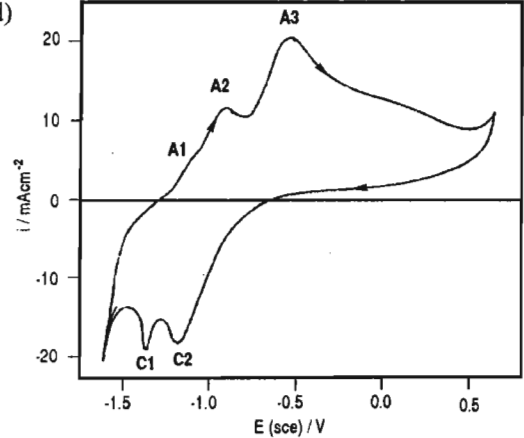
cyclic voltammogram	ref.	experimental conditions	peak assignments		
			peak	E_p /mV	species formed
<p>(c)</p> 	37	Fe 1M NaOH $T = 30^\circ\text{C}$ $\nu = 200\text{mV s}^{-1}$	A1 A2 A3 C2 C1	-1015 -890 -685 -1050 -1250	oxidation of adsorbed H_2 $\text{Fe} \rightarrow \text{Fe}(\text{OH})_2$ $\text{Fe}(\text{OH})_2 \rightarrow \text{FeOOH}$ $\text{Fe} \rightarrow \text{FeOOH}$ at $T > 60^\circ\text{C}$ $\text{FeOOH} \rightarrow \text{Fe}(\text{OH})_2$ $\text{Fe}(\text{OH})_2 \rightarrow \text{Fe}$
<p>(d)</p> 	38	Fe 1M NaOH $\nu = 90\text{mV s}^{-1}$	A1 A2 A3 C2 C1	-1090 -910 -520 -1170 -1360	$\text{Fe} \rightarrow \text{Fe}(\text{II}) \rightarrow \text{Fe}(\text{OH})_2$ formation of $\text{Fe}(\text{OH})_2$ $\text{Fe} \rightarrow \text{FeOOH}$ $\text{FeOOH} \rightarrow \text{Fe}(\text{OH})_2$ (probably only partial reduction) $\text{Fe}(\text{OH})_2 \rightarrow \text{Fe}$

Table 2.1

Cyclic voltammograms of Fe in alkaline electrolytes, reported in the literature

cyclic voltammogram	ref.	experimental conditions	peak assignments		
			peak	E_p /mV	species formed
<p>(e)</p>	39 40	Fe 1M NaOH $\nu = 40 \text{ mVs}^{-1}$ $\omega = 0 \text{ rad s}^{-1}$	A1 A2 A3	-280 -110 6	$\text{Fe} + \text{OH}^- = \text{FeOH}_{\text{ads}} + \text{e}^-$ $\text{FeH}_{\text{ads}} = \text{Fe} + \text{H}^+ + \text{e}^-$ $\text{Fe}(\text{OH})_{\text{ads}} + \text{OH}^- = \text{Fe}(\text{OH})_2 [\text{or FeO} + \text{H}_2\text{O}] + \text{e}^-$ Fe(II) / Fe(III) conversion of hydrous material at oxide - solution interface. $[\text{Fe}_2(\text{OH})_6.3\text{H}_2\text{O}]^{2-} + 3\text{OH}^- \rightarrow [\text{Fe}_2(\text{OH})_9]^{3-} + 3\text{H}_2\text{O} + 2\text{e}^-$ or $[\text{Fe}(\text{OH})_{3.5.n}\text{H}_2\text{O}]^{0.5-} \cdot (\text{Na}^+)_{0.5} + \text{e}^- \rightarrow$ $\text{Fe}(\text{OH})_{2.n}\text{H}_2\text{O} + 0.5\text{Na}^+ + 1.5\text{OH}^-$ (due to composition of hydrous material being unknown) Fe(II) / Fe(III) transition (ie. Fe_2O_3 , Fe_3O_4 , FeOOH) in the layer of compact oxide material at the inner region of the surface deposit C1 origin uncertain, but possibly reduction of inner layer of anhydrous material $\text{FeO} \cdot \text{FeOOH} + \text{H}_2\text{O} + 3\text{e}^- = \text{Fe} + \text{FeO}_2^{2-} + \text{H}_2\text{O} + \text{OH}^-$ reverse A3
<p>(f)</p>	41	Fe 1M NaOH $\nu = 10 \text{ mV s}^{-1}$ $\omega = 156 \text{ rad s}^{-1}$	A1 A2 A3 A4 A3 A4 C1 C2 C2'	-1076 -918 -759 -522 -1200 -769 -835	$\text{Fe} \rightarrow \text{Fe}(\text{OH})_2$ $\text{Fe} \rightarrow \text{Fe}_3\text{O}_4$ $\text{Fe} \rightarrow \text{Fe}(\text{OH})_2$ $\text{Fe}(\text{OH})_2 \rightarrow \text{Fe}_3\text{O}_4$ $\text{Fe}_3\text{O}_4 \rightarrow \alpha\text{-FeOOH}$ $\text{Fe}(\text{OH})_2 \rightarrow \alpha\text{-FeOOH}$ $\text{Fe}(\text{OH})_2 \rightarrow \delta\text{-FeOOH}$ $\text{Fe}(\text{OH})_2 \rightarrow \text{Fe}_3\text{O}_4$ $\text{Fe}_3\text{O}_4 \rightarrow \text{FeOOH}$ $\text{Fe}_3\text{O}_4 \rightarrow \text{Fe}(\text{OH})_2$ $\delta\text{-FeOOH} \rightarrow \text{Fe}(\text{OH})_2$ $\text{FeOOH} \rightarrow \text{Fe}_3\text{O}_4$

Table 2.1

Cyclic voltammograms of Fe in alkaline electrolytes, reported in the literature

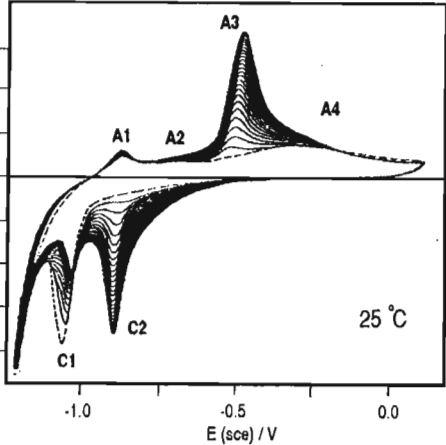
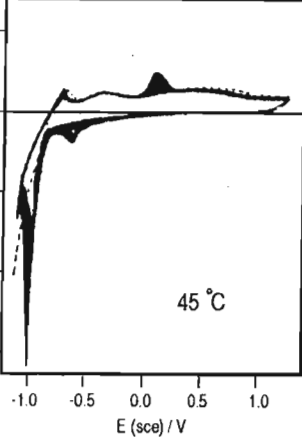
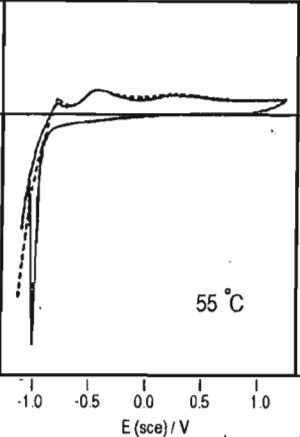
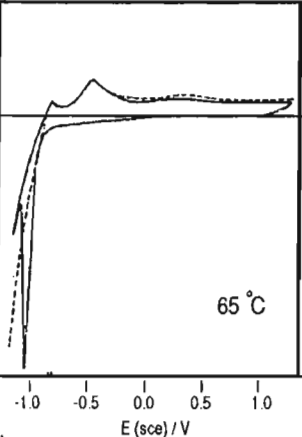
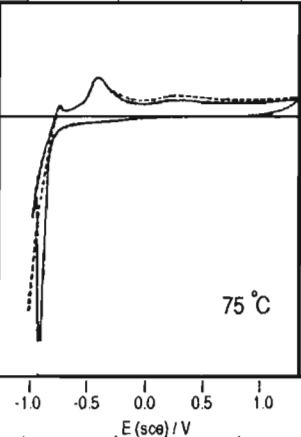
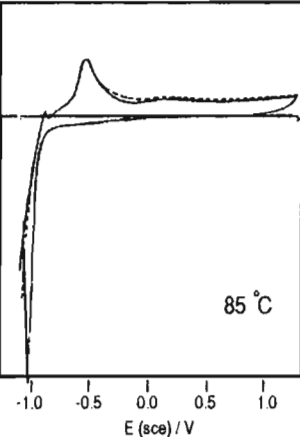
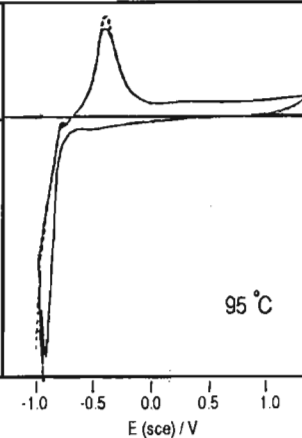
cyclic voltammogram	ref.	experimental conditions	peak assignments		
			peak	E_p /mV	species formed
(g) 	42 43	Fe 1M NaOH $T = 25^\circ\text{C}$ $\nu = 50\text{mV s}^{-1}$	A1 A2 A3 A4 C1 C2	-881 -700 -472 -296 -881 -1040	No peak assignments given, however this is one of the few studies showing the influence of a systematic increase in temperature on the voltammogram
					
					
					
					
					
					

Table 2.1

Cyclic voltammograms of Fe in alkaline electrolytes, reported in the literature

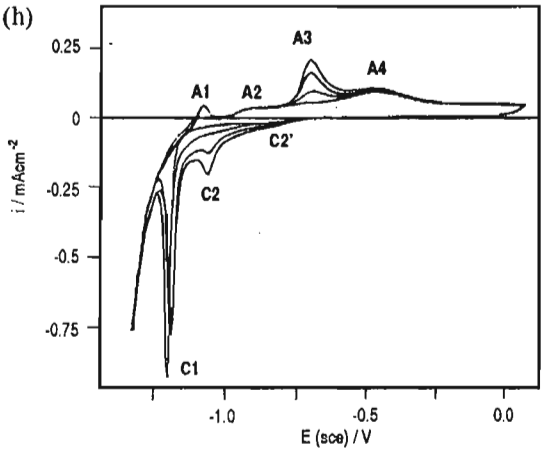
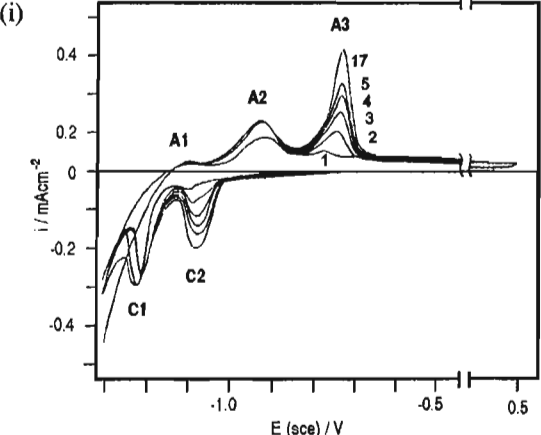
cyclic voltammogram	ref.	experimental conditions	peak assignments		
			peak	E_p /mV	species formed
<p>(h)</p> 	44	Fe 1M NaOH $T = 20^\circ\text{C}$ $\nu = 10\text{mV s}^{-1}$	A1 A1 A3 A4 C2' C2 C1	-1080 -920 -700 -490 -830 -1170 -1200	oxidation of adsorbed H_2 $\text{Fe} \rightarrow \text{Fe}(\text{OH})_2$ $\text{Fe}(\text{OH})_2 \rightarrow \text{FeOOH}$ $\text{Fe} \rightarrow \text{Fe}_3\text{O}_4, \text{Fe}_2\text{O}_3$ region C2', C2: $[\text{FeOOH}]_{\text{cryst}} \rightarrow [\text{Fe}(\text{OH})_2]_{\text{cryst}}$ region C2, C1: $\text{FeOOH} \rightarrow (\text{FeOOH})_{\text{aq}} \rightarrow [\text{Fe}(\text{OH})_2]_{\text{cryst}}$ $\text{Fe}_3\text{O}_4, \text{Fe}_2\text{O}_3 \rightarrow \text{Fe}$
<p>(i)</p> 	45	Fe 1M KOH $\nu = 1\text{mV s}^{-1}$	A1 A2 A3 C1 C2	-1100 -926 -730 -1213 -1080	$\text{Fe}(\text{OH})_2$ Fe_3O_4 passivating base layer $\text{Fe}_3\text{O}_4 \rightarrow \alpha\text{-FeOOH}$ non-adhesive upper layer

Table 2.1

Cyclic voltammograms of Fe in alkaline electrolytes, reported in the literature

cyclic voltammogram	ref.	experimental conditions	peak assignments		
			peak	E_p /mV	species formed
<p>(j)</p> <p>22°C</p> <p>200°C</p>	46	<p>Fe 1M LiOH T = 22 °C $\nu = 13.9 \text{ mV s}^{-1}$ $\omega = 43.5 \text{ rad s}^{-1}$</p> <p>T = 200 °C</p>	<p>A1 A2 A3 C2 C1</p>	<p>-1087 -941 -744 -1087 -1245</p>	<p>Fe + 2OH⁻ → Fe(OH)₂ + 2e⁻ 3Fe(OH)₂ + 2OH⁻ → Fe₃O₄ + 4H₂O + 2e⁻ Fe + 3OH⁻ → Fe(OH)₃ + 3e⁻ the Fe(OH)₃ then transforms to γ-Fe₂O₃ : 2Fe(OH)₃ → γ-Fe₂O₃ + 3H₂O reverse of A3 reverse of A1</p> <p>At 200 °C the following mechanism was proposed : Fe + 3OH⁻ → HFeO₂⁻ + H₂O + 2e⁻ 3Fe + 8OH⁻ → Fe₃O₄ + 4H₂O + OH⁻ 8e⁻ 3HFeO₂⁻ → Fe₃O₄ + H₂O + OH⁻ + 2e⁻ Li⁺ + HFeO₂⁻ → LiFeO₂ + H⁺ + e⁻</p>

Table 2.1

Cyclic voltammograms of Fe in alkaline electrolytes, reported in the literature

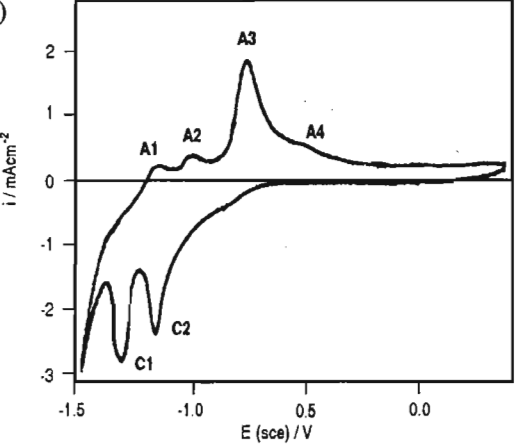
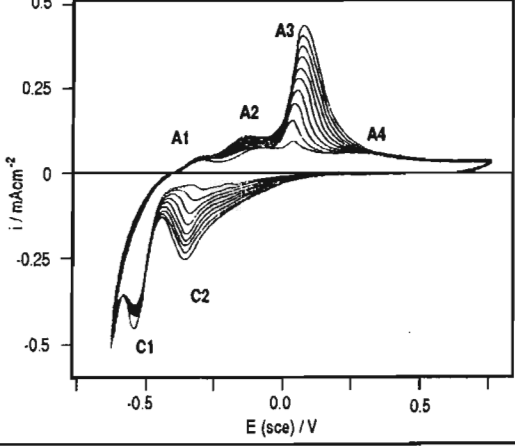
cyclic voltammogram	ref.	experimental conditions	peak assignments		
			peak	E_p /mV	species formed
<p>(k)</p> 	47	Fe 0.5M KOH (aerated) $\nu = 50 \text{ mV s}^{-1}$	A1 A2 A3 A4 C6 C1 C2	-1125 -1048 -758 -500 -800 -1322 -1171	<p>Fe_3O_4 formed via :</p> $3\text{Fe} + 8\text{OH}^- \rightarrow \text{Fe}_3\text{O}_4 + 4\text{H}_2\text{O} + 8\text{e}^-$ <p>or via chemical reaction of electrogenerated Fe^{2+} (at A1) with FeOOH according to the reaction :</p> $\text{Fe}^{2+} + 2\text{FeOOH} \rightarrow \text{Fe}_3\text{O}_4 + 2\text{H}^+$ <p>$\text{Fe}(\text{OH})_2$ $\text{Fe}(\text{OH})_2 \rightarrow \text{FeOOH}$</p> <p>$\text{FeOOH} \rightarrow \text{Fe}(\text{OH})_2$ $\text{Fe}^{\text{II}} \rightarrow \text{Fe}$ $\text{Fe}^{\text{II}} \rightarrow \text{Fe}$</p>
<p>(l)</p> 	48	Fe 0.1M NaOH $T = 20^\circ \text{C}$ $\nu = 50 \text{ mV s}^{-1}$	A1 A2 A3 A4 C2 C1	-299 -109 68 277 -344 -535	<p>$\gamma\text{-Fe}_2\text{O}_3$ and $\alpha\text{-Fe}_2\text{O}_3$ detected in base layer oxidation of $\text{Fe}(\text{II})$ oxide/hydroxide layers deposited on previous cycles</p> <p>$\text{Fe}(\text{III})$ oxide reduced, almost completely, to Fe</p>

Table 2.1

Cyclic voltammograms of Fe in alkaline electrolytes, reported in the literature

cyclic voltammogram	ref.	experimental conditions	peak assignments		
			peak	E_p /mV	species formed
<p>(m)</p>	49	Fe 0.1M NaOH $\nu = 40 \text{ mV s}^{-1}$ note; E vs HESS	A1 A2 A3 A4	-30 140 359 640	FeO Fe(III) / Fe(II) ratio increases linearly with increasing potential 0.35 → 1.0V : duplex layer of FeOOH (outer layer) and Fe(II), possibly Fe(OH) ₂ , (base layer) E > 0.5V : FeOOH → α -Fe ₂ O ₃ 1.0V → 1.5V : Fe(OH) ₂ , FeOOH, α -Fe ₂ O ₃ γ -Fe ₂ O ₃ present with α -FeOOH → α -Fe ₂ O ₃ with increasing potential : γ -FeOOH → γ -Fe ₂ O ₃ E > 1.5V : at beginning of O ₂ evolution γ -Fe ₂ O ₃ and Fe(II) present. FeOOH no longer present and α -Fe ₂ O ₃ → FeO ₄ ²⁻
<p>(n)</p>	50	Fe 0.05M NaOH $\nu = 10 \text{ mV s}^{-1}$	A1 A3 C2 C1	-1005 -779 -1130 -1321	possibly Fe(OH) ₂ Fe ₃ O ₄ , γ -Fe ₂ O ₃ by oxidation of film formed at A1 and by further oxidation of substrate metal. reduction of γ -Fe ₂ O ₃ reduction of Fe(OH) ₂

Table 2.1

Cyclic voltammograms of Fe in alkaline electrolytes, reported in the literature

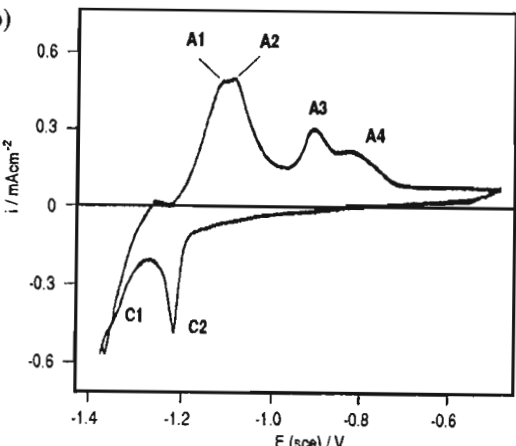
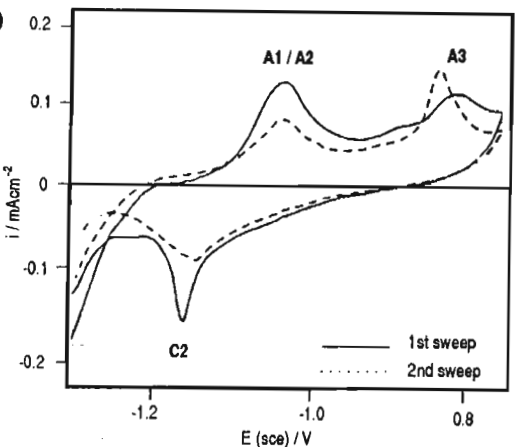
cyclic voltammogram	ref.	experimental conditions	peak assignments		
			peak	E_p /mV	species formed
<p>(o)</p> 	51	Fe 5M KOH $\nu = 4 \text{ mV s}^{-1}$ $\omega = 156 \text{ rad s}^{-1}$	A1 A2 A3 A3 C2 C1	-1100 -1075 -895 -810 -1200 -1333	$\text{Fe} \rightarrow \text{Fe}(\text{OH})_2$ oxidation of Fe proceeds via two paths : 1) a dissolution path involving HFeO_2^- soluble species and 2) a prevailing solid - state oxidation path Fe^{III} probably FeOOH oxidation of $\text{Fe}(\text{OH})_2$ and non - stoichiometric $\beta\text{-FeOOH}$ into $\beta\text{-FeOOH}$ $\text{FeOOH} \rightarrow \text{Fe}(\text{OH})_2$ (solid state mechanism) $\text{Fe}(\text{II}) \rightarrow \text{Fe}(0)$
<p>(p)</p> 	52 53	evaporated Fe layer (3.6nm thick) on Ge substrate 5M KOH $\nu = 3.3 \text{ mV s}^{-1}$	A1 / A2 A3 C2	-1110 -900 -1230	$\text{Fe} + \text{OH}^- \rightarrow \text{Fe}(\text{OH})_2 + 2\text{e}^-$ $\text{Fe}(\text{OH})_2 + \text{OH}^- \rightarrow \delta\text{-FeOOH} + \text{H}_2\text{O} + \text{e}^-$ $\delta\text{-FeOOH}$ forms initially, but after cycling (30) $\alpha\text{-FeOOH}$ forms and after 150 cycles Fe_3O_4 forms $\alpha\text{-FeOOH}$ dominates in 1M KOH while Fe_3O_4 dominates in 5M KOH. $\delta\text{-FeOOH} + \text{H}_2\text{O} + \text{e}^- \rightarrow \text{Fe}(\text{OH})_2 + \text{OH}^-$

Table 2.1

Cyclic voltammograms of Fe in alkaline electrolytes, reported in the literature

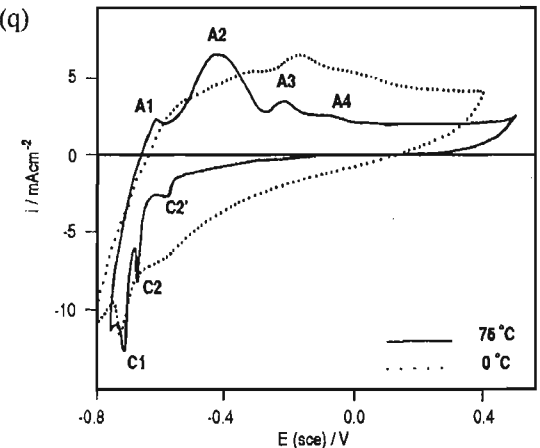
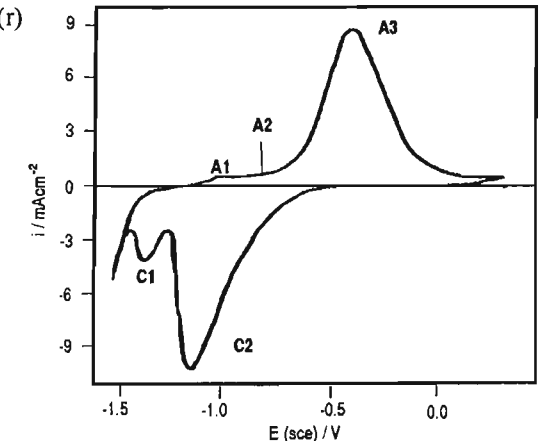
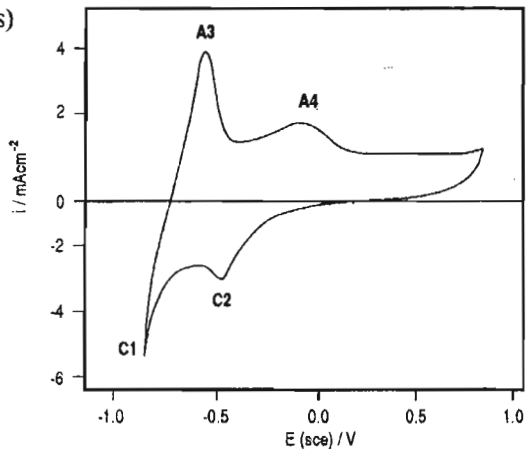
cyclic voltammogram	ref.	experimental conditions	peak assignments		
			peak	E_p /mV	species formed
(q) 	54 55	Fe 20, 26, 28% NaOH 30% KOH $-20^\circ\text{C} \leq T \leq 120^\circ\text{C}$ $\nu = 50\text{mV s}^{-1}$ $\omega = 62.5\text{rad s}^{-1}$	A1	-621	At high temperatures (75°C) : $\text{Fe} \rightarrow \text{HFeO}_2^- \rightarrow \text{Fe}(\text{OH})_2$ $\text{Fe}(\text{OH})_2 \rightarrow \text{Fe}_3\text{O}_4$ $\text{Fe} \rightarrow \text{HFeO}_2^- \rightarrow \text{Fe}(\text{OH})_2 \rightarrow \text{Fe}_3\text{O}_4$ $\text{Fe}_3\text{O}_4 \rightarrow \text{Fe}(\text{OH})_4^-$ $\text{Fe}(\text{OH})_2 \rightarrow \text{Fe}(\text{OH})_4^- \rightarrow \text{Fe}_2\text{O}_3 \rightarrow \text{FeOOH}$ $\text{Fe}_3\text{O}_4 \rightarrow \text{Fe}(\text{OH})_4^- \rightarrow \text{Fe}_2\text{O}_3 \rightarrow \text{FeOOH}$ (FeOOH produced at more anodic potentials) $\text{Fe}(\text{OH})_2 \rightarrow \text{Fe}$ $\text{FeOOH} \rightarrow \text{HFeO}_2^- \rightarrow \text{Fe}(\text{OH})_2$ $\text{Fe}_2\text{O}_3 \rightarrow \text{Fe}_3\text{O}_4 \rightarrow \text{Fe}(\text{OH})_2$ (no peak observed for last step)
			A2	-451	
			A3	-257	
			A4	-67	
			C1	-709	
			C2	-672	
			C2'	-578	
			A1		
			A2	-344	
			A3	-171	
(r) 	56	Fe saturated $\text{Ca}(\text{OH})_2$ $\nu = 200\text{mV s}^{-1}$	A1	-779	At low temperatures (0°C) $\text{Fe} \rightarrow \text{FeO}_2^{2-} \rightarrow \text{Fe}(\text{OH})_2$ $\text{Fe}(\text{OH})_2 \rightarrow \text{Fe}_3\text{O}_4$ $\text{Fe} \rightarrow \text{HFeO}_2^- \rightarrow \text{Fe}(\text{OH})_2 \rightarrow \text{Fe}_3\text{O}_4$ $\text{Fe}_3\text{O}_4 \rightarrow \text{Fe}(\text{OH})_4^-$ $\text{Fe}(\text{OH})_2 \rightarrow \text{FeOOH} \rightarrow \text{Fe}_2\text{O}_3$ $\text{Fe}_3\text{O}_4 \rightarrow \text{FeOOH} \rightarrow \text{Fe}_2\text{O}_3$ (Fe_2O_3 produced at more anodic potentials) $\text{Fe}(\text{OH})_2 \rightarrow \text{Fe}$ $\text{Fe}_2\text{O}_3 \rightarrow \text{FeO}_2^{2-} \rightarrow \text{Fe}(\text{OH})_2$ $\text{FeOOH} \rightarrow \text{Fe}_3\text{O}_4 \rightarrow \text{Fe}(\text{OH})_2$
			A2	-600	
			A3	-146	
			C2	-893	
			C1	-1107	
			A1		
			A2		
			A3		

Table 2.1

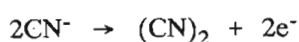
Cyclic voltammograms of Fe in alkaline electrolytes, reported in the literature

cyclic voltammogram	ref.	experimental conditions	peak assignments		
			peak	E_p /mV	species formed
(s) 	57	Fe borate buffer pH 8.4 $\nu = 40 \text{ mV s}^{-1}$	A1 A3 C2	 ≈ -680 -640 -540 -560	simultaneous dissolution of Fe(II) and formation of hydroxide layer By the potential of -640mV a monolayer of passive film has been formed and iron dissolution ceased. minimum in cyclic voltammogram corresponds to oxidation of Fe^{2+} to Fe^{3+} and is followed by a rapid increase in thickness of Fe^{3+} oxide layer associated with peak A3 reduction of the hydrated layer formed at A3. The process is controlled by the diffusion of Fe^{3+} through the film

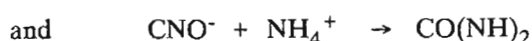
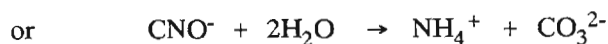
example, Haupt and Strehblow³⁴ (Table 2.1, CV(a)) report that A3 and C2 are not present on the first cycle of a clean, oxide free electrode. Similar results are shown by CV(h), (g) and by the results presented later in chapter six. However, this is clearly not the case with CV(b), (c), (i), (j), (l), (m). To further complicate the situation, frequently not all the experimental details are published regarding the number of cycles a cyclic voltammogram represents, rotation rate used and electrode pretreatment.

2.3 ELECTROCHEMISTRY OF Fe AND STAINLESS STEELS IN ALKALINE CYANIDE ELECTROLYTES

It is generally accepted that in alkaline solutions CN^- is electrochemically oxidised to cyanate or cyanogen, although further oxidation of CNO^- to CO_2 and N_2 occurs with difficulty.



While the above reaction predominates at neutral and moderately alkaline pHs, under the conditions to be used in the experimental work later, cyanate formation will predominate :



While the oxidation of cyanide to cyanate is thermodynamically favourable at ambient temperatures, the kinetics of the reaction are very slow. At high pH values, a hydrolysis reaction, particularly at high temperatures can also occur, viz.



This reaction occurs very slowly at ambient temperatures. Adams⁵⁸ has demonstrated that this reaction is more important than the oxidation to cyanate at high temperatures.

Very little electrochemical research appears to have been conducted on Fe and stainless steel alloys in alkaline cyanide electrolytes. There are contradictory reports in the literature as to the behaviour of iron in cyanide solutions. In an electrochemical series of metals in CN^- solutions it has been reported⁵⁹ that iron has a nobility comparable to that of platinum. However, cementation of gold onto steel carbon - in - pulp elution columns, with the subsequent dissolution of the steel has also been reported,^{60,61} although columns manufactured from the same steel are known to operate effectively without the gold plating occurring. The Pourbaix diagram for the Fe - CN - H_2O system⁶² indicates that the presence of CN^- should favour the dissolution of Fe due to the formation of a ferrous cyanide complex.

Two recently published papers on the corrosion of mild steel and iron in cyanide solutions have reported that CN^- inhibits⁶⁰ and accelerates^{60,63} corrosion. Kenna *et al.*⁶⁰ reported that below pH 11 the presence

of cyanide inhibited Fe oxidation due to the Fe oxidation taking place at more positive potentials in the presence of cyanide than in its absence. They found no evidence of hexacyanoferrate (II) formation. Above pH 12, the reverse effect is observed with cyanide promoting Fe oxidation. de Wet *et al.*⁶³ reported that CN⁻ additions to 0.05M NaOH and 0.5M NaOH accelerated the Fe dissolution. de Wet *et al.* explained the discrepancy between their results and those of Kenna *et al.* as being due to the presence of potassium sulphate, which Kenna used to enhance the conductivity of the electrolyte.

2.3.1 The CIP Process

One of the contributing factors in the initiation of the present research program was the corrosion of stainless steel elution columns used in the carbon - in - pulp (CIP) gold extraction process. Following is a brief description of the CIP process.

The CIP process utilises the tremendous physical affinity activated carbon has for gold. The gold is adsorbed onto the carbon from the crushed ore pulp and then in a subsequent stage of the process eluted from the carbon.

In the CIP process, two of the main routes for elution of the aurocyanide, $\text{Au}(\text{CN})_2^-$, from the activated carbon are the AARL and ZADRA processes. The AARL elution process is an 8hr batch process involving an initial hot acid wash of the loaded carbon with 3% HCl at 90°C to remove Ca, Zn, Ni, Fe, Si to minimise subsequent complications in the electrowinning and carbon regeneration stages of the process. The carbon is then washed with water prior to treatment with 0.5M NaOH + 0.4M NaCN at 110°C. The gold is then eluted from the carbon in a series of water washes. The ZADRA elution process differs from the AARL process in that the eluting solution is continuously circulated through the elution column and electrowinning cell which are in series. The ZADRA process uses 1.0M NaOH + 0.4M NaCN at 120°C. The conditions employed in both of these elution processes will be covered in this thesis.

Since the first CIP plant was commissioned in 1981, no conventional gold recovery plants have been built in South Africa. The main advantages of the CIP process over the zinc precipitation process are the lower capital and operating costs ($\approx 30\%$ lower), the ability to treat concentrates previously difficult to filter after cyanidation and the achievement of higher gold recoveries thereby making the treatment of low grade ores and residues economically feasible.

2.4 SURFACE ANALYSIS TECHNIQUES USED IN THE DETERMINATION OF THE NATURE OF THE SURFACE FILM

Surface analysis of passive films has become increasingly important in the elucidation of corrosion

mechanisms since these techniques provide information which is difficult to obtain from purely electrochemical techniques. Surface analysis techniques commonly used include x - ray photoelectron spectroscopy (XPS),^{17,18,34,35,64-69} Auger electron spectroscopy (AES),⁷⁰⁻⁷⁶ secondary ion mass spectrometry (SIMS),⁷⁶⁻⁷⁸ ellipsometry,⁷⁹⁻⁸⁸ Mössbauer spectroscopy,^{16,89-91} electron diffraction,^{79,92-94} Raman spectroscopy,^{41,45,95,96} surface analysis by ion excitation spectroscopy (SALI),^{97,98} extended x - ray absorption fine structure (EXAFS),⁹⁹⁻¹⁰² *in-situ* infrared spectroscopy (SNIFTIRS),¹⁰³ ion scattering spectroscopy (ISS),^{104,105} soft x - ray spectroscopy (SXS),⁹⁶ surface enhanced Raman spectroscopy (SERS),¹⁰⁶ potential modulated reflectance spectroscopy,^{49,107-110} scanning electron microscopy (SEM)^{44,46,111,112} and scanning tunnelling and atomic force microscopy.^{113,114}

While the corrosion and passivation of iron and iron based stainless steels has been extensively researched and reported on in the literature, the lack of agreement concerning the surface film can be attributed to both physical as well as interpretative difficulties inherent to surface analysis of electrochemically prepared surfaces. Interpretation of surface analysis data is, in certain cases, intrinsically difficult and often rather subjective, it is further complicated by the complex nature of the surface films. Physical difficulties have led to the much debated problem of *ex-situ* vs *in-situ* analysis. While the majority of analyses have been conducted *ex-situ* there are an increasing number of *in-situ* analyses being reported. *Ex-situ* techniques, while in many cases are more advanced, suffer from experimental problems of removing the electrode from the electrolyte, disconnecting the applied potential and in most cases require a high vacuum environment and the bombardment of the film with an electron or x - ray beam. Such treatment may result in oxidation, contamination, dehydration, recrystallisation — in short a change in the structure and composition of the surface film.

2.4.1 Ex-situ vs in-situ analysis techniques

Doubts have been expressed¹⁶ regarding the structure of surface films determined by *ex-situ* techniques. For example, Forty *et al.*,¹⁰⁰ using *ex-situ* and *in-situ* fluorescence EXAFS showed that the γ -FeOOH in the surface film dehydrated to γ -Fe₂O₃ after removal from the electrolyte. Lumsden and Stocker⁷³ reported oxidation and thickening of the surface film can occur as a result of transferring the electrode through air or through gasses with partial pressures of oxygen, which are high relative to ultra high vacuum (UHV) conditions. Bockris¹¹⁵ in his review on spectroscopic techniques for characterisation of surface films, stressed that with vacuum techniques care must be taken to ensure that water is not removed from the passive film by drying (vacuum) or by heating due to electron or x - ray bombardment since removal of water from the passive film destroys its passivity by destroying the amorphous nature of the film.

Other researchers^{79,92} argue that heating, as a result of electron bombardment, and dehydration by vacuum is not sufficient to create the highly orientated films observed. Haupt and Strehblow³⁵ claim that *ex-situ*

techniques, eg. XPS, as opposed to *in-situ* examination of surface films provide a more detailed insight into the film's chemical composition, thickness and formation with virtually no artifacts introduced by the technique, providing the specimen transfer from the electrochemical cell to the UHV chamber is carried out in an inert atmosphere to avoid any further oxide formation or oxidation of the components of the passive film. Thus to eliminate exposing the electrode to air during transfer, electrochemical cells have been attached to the surface analysis instrument.^{116,117} While such systems have obvious advantages, clearly they cannot prevent changes in the film which may occur on removing the electrode from the electrolyte and the disconnection of the applied potential, and dehydration of hydrous oxides in vacuo or in inert, dry atmospheres. A further disadvantage of such 'coupled' systems is that electrode handling and manipulation is usually difficult.

Using *in-situ* and *ex-situ* Mössbauer spectroscopy to study the passive film formation on Fe at controlled electrode potentials, O'Grady¹⁶ found structural changes to the film occurred on drying, with amorphous hydrated iron (III) oxide (detected *in-situ*) changing to $\gamma\text{-Fe}_2\text{O}_3$ on *ex-situ* examination. Brooks *et al.*,¹⁹ on the other hand, demonstrated that the CrO_3 detected in the surface film on 304L in 0.5M H_2SO_4 by variable angle XPS, was not a dehydration artifact caused by the spectrometer environment.

Comparison of *in-situ* and *ex-situ* Mössbauer spectra of the passive film formed on Fe in a borate buffer solution showed that films formed at 1107mV showed little change after drying (rinsed with water then dried in N_2) while those formed at 157mV changed significantly on drying.⁹¹ Similar findings were reported by Courty *et al.*⁷⁸ investigating the possible surface oxidation of an electrochemically polarised Fe25Cr alloy, in 0.1M H_2SO_4 + 0.4M Na_2SO_4 , using SIMS oxygen isotope ratio profiling. They demonstrated that anodically formed films were not further oxidised upon exposure to air during transfer while a cathodically reduced surface was highly reactive and was oxidised by air. The same conclusions were drawn by Graham *et al.*¹¹⁸ using Mössbauer, XPS and SIMS techniques to examine the surface films on Fe in borate buffer (pH 8.4). Courty also found that while mechanical abrasion under dry conditions leads to surface oxidation by reaction with oxygen, under wet conditions surface oxidation by reaction with water occurred. Evaluating the *in-situ* vs *ex-situ* debate, Gui and Devine¹¹⁹ concluded that passive films formed at low potentials will change when the electrode is removed from the electrolyte, while films formed at high potentials remain unchanged on removal from solution.

2.4.2 Depth Profiling

As surface films on Fe and alloys are unlikely to be homogeneous, depth profiling to investigate changes in composition through the film is highly desirable. To this end ion sputtering of surface films in order to obtain depth profiles is frequently performed and reported in the literature. However, there are certain limitations which have to be considered, for example, sputter mixing, sputter statistics, preferential sputtering, as sputter artifacts have been widely reported.^{35,74,77,120-130} Determination of the oxidation state of a species, particularly oxides, is meaningless unless the stability of the species has been ascertained

as, for example, preferential sputtering of oxygen can result in the reduction of iron oxides.^{120,128,130} Konno and Nagayama¹²⁸ reported that ion sputtering of $\alpha\text{-Fe}_2\text{O}_3$ and Fe_3O_4 resulted in the reduction of these two oxides to FeO and therefore ion sputtering should not be used for the analysis of oxide films on iron. Sputter depth profiling of surface films on FeCrMo alloys has been shown to result in Mo enrichment in the film since the sputter yield of Mo is lower than that of the other film constituents.^{126,129,131}

Conversely there have been publications where the authors have shown that under specific conditions, sputter artifacts are not observed; eg. Mitchell and Graham⁷⁶ showed this to be the case when heavy ions of low energy are used. The relatively new technique of surface analysis by ion excitation spectroscopy (SALI), has been reported by Macdonald *et al.*⁹⁸ who point out that an important advantage of SALI, over other surface analysis techniques (AES, XPS, SIMS, EXAFS) is that the use of low energy sputter beams minimises matrix effects. A preferred technique of depth profiling is that of variable angle XPS, where the sample under analysis is tilted with respect to the x-ray beam, which will provide the required information without the introduction of sputter artifacts.

2.5 NATURE OF THE SURFACE FILM FORMED ON FERROUS ALLOYS

The surface film on iron based stainless steels is generally characterised as a thin (50Å) amorphous film consisting mainly of oxyhydroxides of chromium and iron, with the composition of the film being strongly dependent on the composition of the substrate alloy. It is generally agreed that the surface film is enriched in chromium and has a duplex structure. However, while some investigations have shown an enrichment of chromium in the inner part of the film and iron species in the outer part,^{14,19,35,104,132-140} others have reported chromium enrichment in the outer part of the passive film.^{65,67,75,87,102,105,141,142} Alternative proposals to the duplex structure have included a four layer film,⁶⁶ and a single layer consisting of mixed FeCr hydrated oxyhydroxides.^{141,143} Some of the proposed structures for the passive film are given in Fig. 2.3 and Table 2.2.

Considering the role of chromium in the passive film, the protective nature of the passive film on FeCr alloys ($\text{Cr} \geq 12.5 \text{ wt\%}$), is attributed to the protective nature of the hydrated chromium oxyhydroxide. Olefjord^{134,139} using XPS, showed that the Cr^{3+} content of the film increased with passivation time, with the initial film formed having a high iron content. The nature of the surface film has been shown to be dependent on :

potential.^{35,128,146-148} A film formed at negative potentials is thin and has a Cr rich layer adjacent to the substrate and a very thin Fe rich outer layer, if in fact this outer layer is present at all. With increasing potential^{35,128} the thickness of the film increases and the H_2O content of the film has been shown to decrease.

pH.^{17,19,35} In acidic electrolytes the Fe oxide upper layer is very much thinner than that observed in

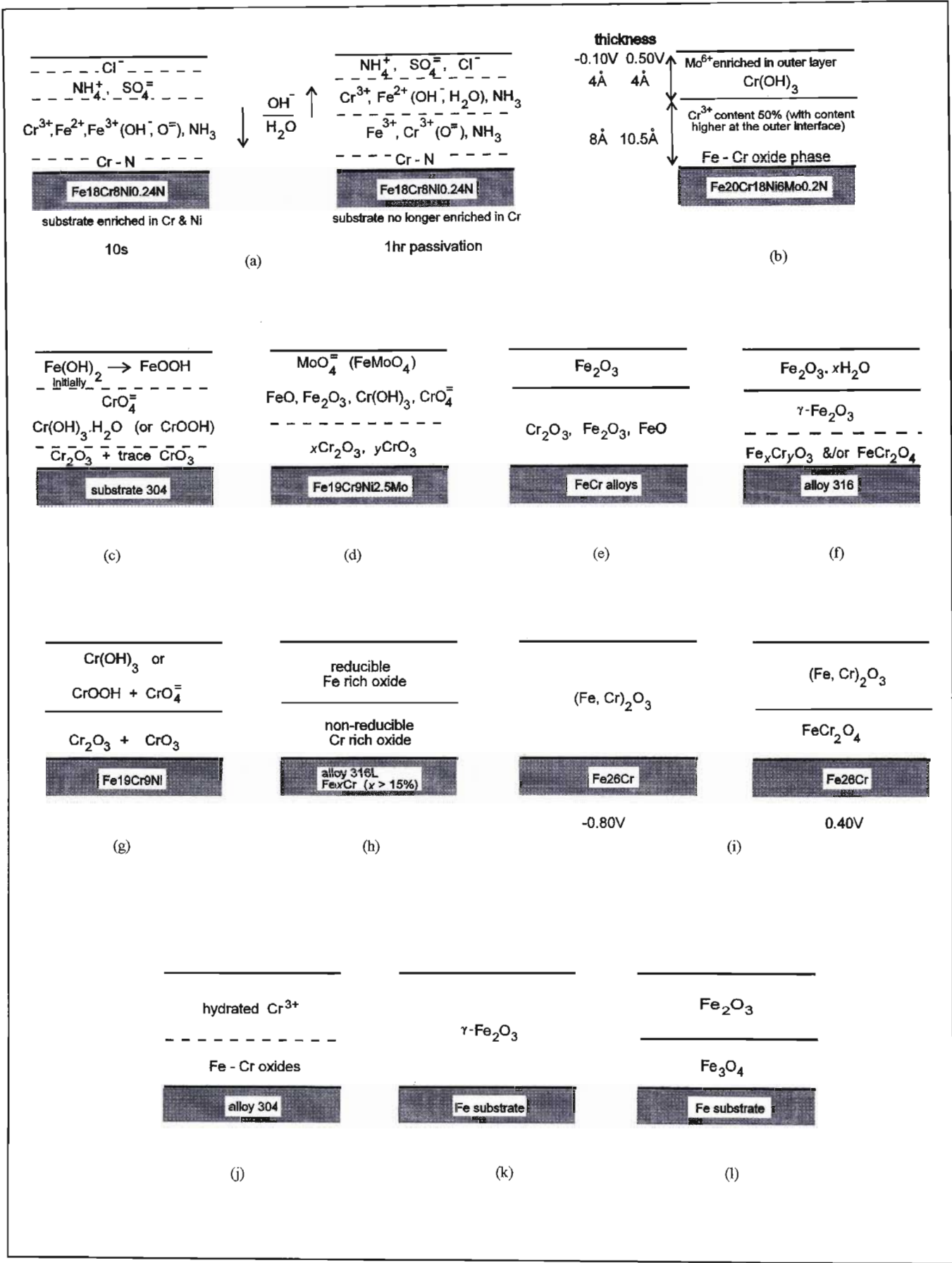


Fig. 2.3 Schematic representation of the proposed surface film formed on Fe and ferrochrome stainless steels. Details of the experimental conditions and surface analytical technique used are given in Table 2.2.

Table 2.2

Surface analytical techniques and experimental conditions used in the determination of the nature of the surface films given in Fig. 2.3

	technique		conditions	ref.
a	XPS	<i>ex-situ</i>	Fe18Cr8Ni0.24N, 0.5M H ₂ SO ₄ + 0.5M NaCl, 0V	66
b	XPS	<i>ex-</i>	Fe20Cr18Ni6Mo0.2N, 0.1M HCl + 0.4M NaCl, -0.1V, 0.5V	69
c	XPS, RHEED	<i>ex-</i>	304, 0.5M H ₂ SO ₄ , 0.5M H ₂ SO ₄ + 0.35M NaCl, 0.25V	19
d	XPS, AES	<i>ex-</i>	Fe19Cr9Ni2.5Mo, 0.1M HCl, -0.18V	18
e	ISS	<i>ex-</i>	FeCr alloys, 0.5M H ₂ SO ₄	104
f	AES	<i>ex-</i>	316, borate/boric acid buffer pH 8.6, 0.6V	74
g	XPS	<i>ex-</i>	Fe19Cr9Ni, 0.1M HCl, -0.18V	117
h	AES	<i>ex-</i>	316L, Fe _x Cr (<i>x</i> > 15%), borate buffer pH 8.4, 0 → 0.9V	133
i	AES	<i>ex-</i>	Fe26Cr, pH 2 H ₂ SO ₄ , -0.8V & 0.4V 120min	144
j	XPS	<i>ex-</i>	304, 0.5M H ₂ SO ₄ , passive potentials	145
k	ellipsometry	<i>ex-</i>	Fe, phosphoric acid pH 1.85, 0.4V → 1.4V	84
l	Raman	<i>ex-</i>	Fe, 0.5M H ₂ SO ₄ , 4CV cycles (-1.0V → 1.0V)	96

Note :

- i Unless otherwise stated, all analyses performed at 20°C.
- ii Where applied potentials are not given, indicates that the authors either didn't supply details, or that they were ambiguous.
- iii Dotted lines in Fig. 2.3 indicate a continuous transition from one layer to the next.

alkaline electrolytes and the total oxide thickness is also less. This is a consequence of the higher dissolution rate of Fe in acidic electrolytes. It has also been shown that the film is less hydrated in acidic than in neutral electrolytes. In alkaline electrolytes the average Cr enrichment of the passive film is less than that observed in acidic electrolytes.

chromium content of alloy.^{35,94,149} The chromium content of the substrate has been shown to influence the extent of chromium enrichment within the film. Film growth kinetics studies have shown that thickness and structural changes of the passive films on ferritic steels are a direct result of increasing the chromium content of an alloy, thereby promoting a more protective structure in a thinner film. The water content of the passive film was found to increase with increasing Cr content of the film, resulting in a more amorphous structure.

In a comprehensive variable angle XPS study¹⁹ on the surface film formed on 304L in 0.5M H_2SO_4 , a Cr_2O_3 layer having some CrO_3 was found at the metal - film interface, on top of which a second mixed phase of predominantly $\text{Cr}(\text{OH})_3$ or CrOOH with some $\text{CrO}_4^{=}$ was suggested. Above this amorphous mixed Cr oxide layer, an upper layer of $\text{Fe}(\text{OH})_2$ / FeOOH was proposed. Although the CrO_3 is present in low concentrations in the Cr_2O_3 layer it is the combination of the two vastly different oxidation states of Cr that provides the condition for significant bond flexibility resulting in a relatively stable noncrystalline oxide. In addition Cr_2O_3 and CrO_3 are likely to coexist under nonequilibrium conditions since it is reported that the standard free enthalpies are -136 and -141 kcal mol⁻¹, respectively.¹⁵⁰ Studies in 0.1M HCl ¹⁸ and at pH 9 showed that the same species were present, although their relative concentrations varied with pH.¹⁷

2.5.1 Influence of Minor Alloying Elements on the Nature of the Passive Film

It is widely acknowledged that the addition of low concentrations of elements such as molybdenum and vanadium significantly improve the corrosion resistance of ferrous alloys. While it is agreed upon that the addition of molybdenum results in the stabilisation of the passive film due to a complex non - linear function of both the chromium and molybdenum contents of the alloy, the location, oxidation state and interaction of molybdenum with the other species within the film is still uncertain.

Contradictory findings as to the absence^{75,135,151-157} or presence^{65,131,134,139,143,158,159} of molybdenum oxides within the film have been reported. The concentration and chemical state of molybdenum is potential dependent.^{116,131,139,156,160-162} Under open circuit conditions, at E_{corr} and at potentials in the active region, selective dissolution of iron results in an enrichment of metallic molybdenum and chromium in the outermost alloy layers.^{139,163} With increasing potential there is a decrease in the molybdenum content of the film, with Mo^{6+} predominating as MoO_4^{2-} (FeMoO_4 or H_2MoO_4) at the anodic limit of the passive region and in the transpassive region. Under conditions of advanced localised corrosion (ie. localised decrease in pH) the stable form of Mo is MoO_2 (or the hydrated oxide), which if formed within the pits will effectively suppress their propagation.

Investigating the influence of minor alloying elements on the species within the passive film on a Fe19Cr9Ni2.5Mo alloy in 0.1M HCl polarised at a passivating potential, Lu and co-workers^{18,20} reported the presence of Cr_2O_3 , CrOOH or $\text{Cr}(\text{OH})_3$, and CrO_3 and CrO_4^{2-} . The Cr_2O_3 phase is situated at the metal - film interface while the CrO_3 is incorporated in the Cr_2O_3 , and the CrO_4^{2-} is incorporated in the $\text{Cr}(\text{OH})_3$ or CrOOH phase. The addition of molybdenum to the alloy resulted in an increase in the Cr_2O_3 phase and a marked reduction of the $\text{Cr}(\text{OH})_3$ phase. The outer layers of the film were found to contain Fe^{2+} , MoO_2 and MoO_4^{2-} , possibly as FeMoO_4 , suggesting that the initial film may have been MoO_2 , which is highly stable in acidic solutions (*cf* Fig. 2.3d). Mo was also reported to cause the segregation of Cr to the inner regions of the film leaving Fe in the outer regions.

From perusal of the literature, it appears that the effect of molybdenum is not to be found in its enrichment in the passive film, but rather in changing the kinetics of anodic dissolution and passive film formation on the alloys. Olefjord¹⁴⁶ suggested that the accumulation of the alloying elements (Mo and Cr) in the outermost layers of the alloy, during the active dissolution that precedes passivation, results in a decrease in the dissolution rate, thus provoking the formation of a passive film. Castle and Qui⁶⁵ using XPS and ICP-MS concluded that Mo influences the dissolution behaviour of steel alloys by enhancing the selective dissolution of Fe during the passivation process thereby increasing the Cr enrichment in the passive layer. In addition Yaniv *et al.*⁷⁵ suggests that molybdenum improves the quality of the bonding at the metal/film interface, thus creating a barrier type oxide.

Relatively little has been published on the electrochemistry and corrosion properties of FeCrV alloys or the rôle of vanadium in the passivation process. Several researchers¹⁶⁵⁻¹⁶⁷ have however reported an increase in the resistance to pitting corrosion in chloride media. In general however, vanadium was not found to be an effective replacement for molybdenum in ferrochrome steels with partial replacement of the molybdenum with vanadium being a more viable option.

2.6 NATURE OF THE SURFACE FILM ON Fe IN ALKALINE ELECTROLYTES

The structure of the surface film on iron in alkaline electrolytes has been described by various models involving layers of different species. There is increasing consensus with regard to the formation of a duplex film,^{19,45,68,72,80,82,86,93,95,133,168-173} although some researchers^{34,35,74,83,92,174,175} propose that the film is not discretely layered but that there is a continuous change from the one layer to the next. Kruger¹⁷⁴ in his review on the nature of the passive film on Fe and ferrous alloys concluded that the film is best characterised as a chemisorbed film which is a one - layer (two dimensional) oxide or compound film. It is generally accepted that where a duplex film is present the layer adjacent to the substrate Fe is the protective barrier layer responsible for passivity while the deposited upper layer does not substantially contribute to the protectiveness of the film. Recently, however, Ord¹⁷³ proposed a duplex film model, for Fe in neutral borate, in which the upper layer gave the electrode its passive properties, while the current was said to be

limited by the field in the inner layer across which the potential appears. The thickness of the constituent layers of the duplex film has been reported by Larramona and Gutiérrez⁴⁹ to be independent of pH while Sato and co-workers^{84,171} reported a dependence on pH. A dependence on applied potential^{84,93,95,128,171,176} and on the cations present in the electrolyte^{80,86} has also been shown.

The results from *in-situ* and *ex-situ* surface analytical techniques have not provided a definitive conclusion with regard to the constituent species of the film and have shown that the passive film on iron consists of one of, or a combination of, the following: FeO (refs. 68,134), Fe(OH)₂ (refs. 36,41,51,52,56,65,80,85,103,177-179), Fe₃O₄ (refs. 41,45,53,56,72,80,82,93,95,168,171,175,180), α-FeOOH (refs. 45,53,56,95,103), β-FeOOH (refs. 51), γ-FeOOH (refs. 89,100,171,181), δ-FeOOH (refs. 41,52,95,103), α-Fe₂O₃ (ref. 48), γ-Fe₂O₃ (refs. 48,68,72,82,93,168-171,175,180,182), Fe₂O₃·xH₂O (refs. 16,71,183), cation deficient Fe₂O₃ (Fe_{2-2x}□_xO₃) (refs. 93,180,184), non-stoichiometric deficient γ-Fe₂O₃ containing varying amounts of protons γ-Fe_{2-x}H_yO₃ (ref. 185). A selection of the models of the surface films on Fe in alkaline electrolytes, reported in the literature, are shown in Fig. 2.4 and Table 2.3.

The lack of agreement concerning the surface film can be attributed to both physical as well as interpretative difficulties inherent in surface analysis of electrochemically prepared surfaces. Dünwald and Otto⁹⁵ demonstrated that the applied potential regime used can change the relative contribution of the different species participating in the oxidation and reduction reactions and consequently change the voltammetric characteristics and compositional make-up of the film.

2.6.1 Discrete Layering of the Duplex Film

Haupt *et al.*^{35,68} using XPS to investigate the passive film on Fe in 1M NaOH, concluded that the film formed under potentiostatic conditions had a duplex structure with an inner layer of FeO and Fe(OH)₂ and an outer Fe₂O₃ layer (Fig. 2.4(a)).

Based on ellipsometric data, Ord⁸² proposed a duplex film structure with a distinct change from the lower Fe₃O₄ layer to the upper γ-Fe₂O₃ layer (Fig. 2.4(b)).

Electron diffraction studies by Foley *et al.*⁹³ showed the existence of a duplex surface film, with the composition of the layers being potential dependent. With films formed at passive potentials γ-Fe₂O₃ and Fe₃O₄ were detected while Fe₃O₄ and FeOOH were present when non-passive potentials were applied (Fig. 2.4(c)).

Using ellipsometric measurements and chemical analysis, Sato *et al.*⁸⁴ showed that in alkaline and neutral electrolytes a duplex surface film was formed on Fe with an inner barrier layer (γ-Fe₂O₃) and an outer deposited layer (Fe₂O₃·1.8H₂O). The barrier layer was reported to be potential dependent, with the thickness increasing linearly with increasing applied potential, while the outer layer was dependent on the electrolyte composition. They found that the presence of ferrous ions in the electrolyte resulted in the

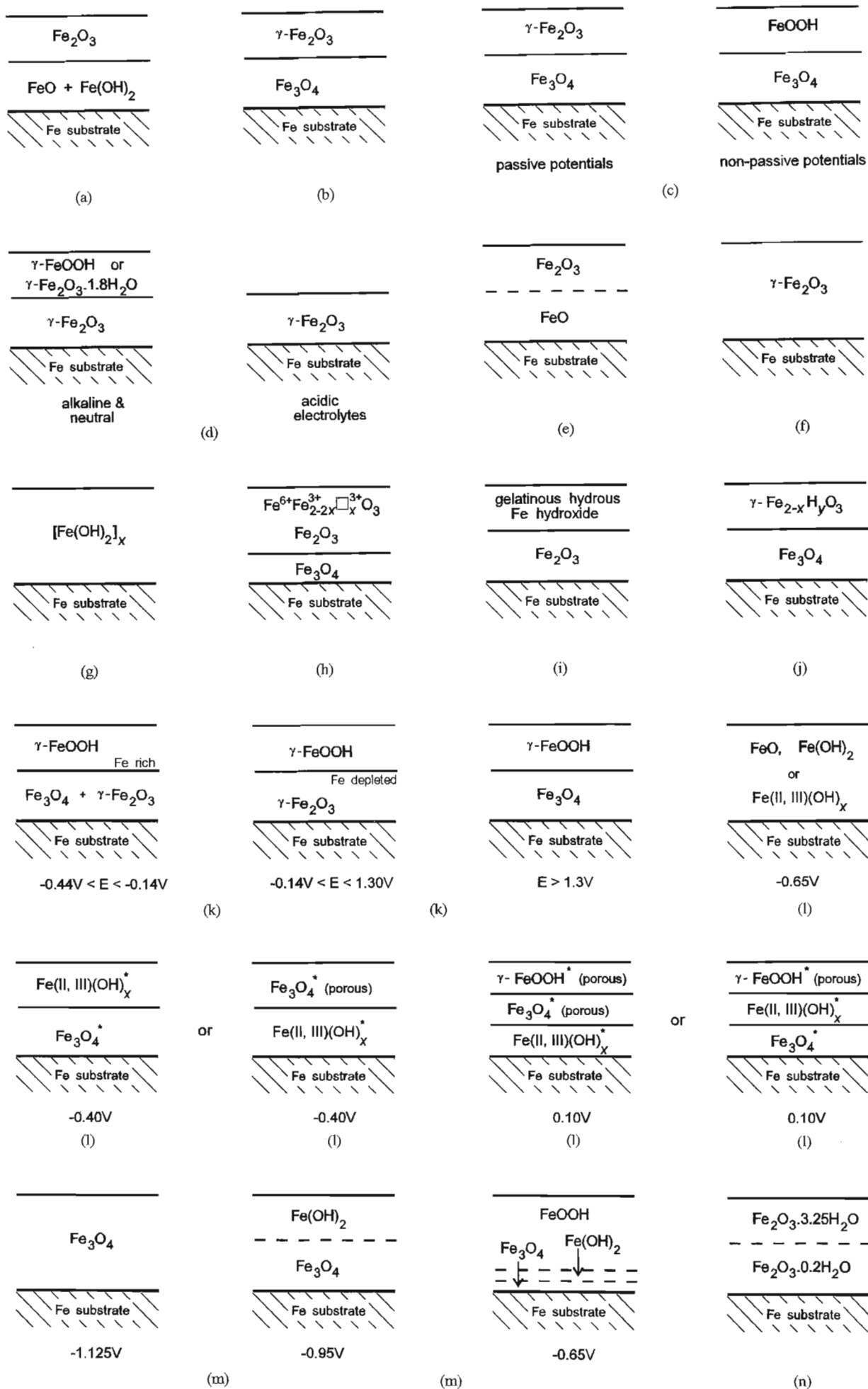


Fig. 2.4 Schematic representation of the proposed surface film formed on Fe in alkaline electrolytes. Details of experimental conditions and surface analytical technique used are given in Table 2.3.

Table 2.3

Surface analytical techniques and experimental conditions used in the determination of the nature of the surface films given in Fig. 2.4

	technique		conditions	ref.
a	XPS, ISS	<i>ex-situ</i>	1M NaOH, -1.24V \rightarrow 0.96V (SCE)	68
b	ellipsometry	<i>in-</i>	borate buffer pH 8.4	82
	ellipsometry	<i>in-</i>	borate buffer pH 8.4	168
	e ⁻ diffraction	<i>ex-</i>	HCl - borate buffer pH 7.6	184
	Auger	<i>ex-</i>	HBO ₃ - NaBO ₃ pH 8.4, -0.19V, 1hr	72
c	e ⁻ diffraction	<i>ex-</i>	0.1M NaOH, 0.5M H ₂ SO ₄ , HBO ₃ - NaBO ₃ buffer pH 8.5	93
d	ellipsometry	<i>in-</i>	borate buffer, pH 8.42, phosphoric acid, pH 1.85	84
e	XPS	<i>ex-</i>	1M NaOH, -1.4V \rightarrow 0.4V	34
f	e ⁻ diffraction	<i>ex-</i>	borate buffer, pH 8.4, 0.16V \rightarrow 1.36V	79
	ellipsometry	<i>in-</i>	borate buffer pH 8.4	88
g	Auger	<i>ex-</i>	HBO ₃ /KOH pH 8.1, 0.06V	71
h	e ⁻ diffraction	<i>ex-</i>	neutral borate buffer	92
i	ellipsometry	<i>in-</i>	0.04M NaOH, Ca(OH) ₂ (sat), pH 12.6 -1.4V \rightarrow 0.3V	80
j	ellipsometry	<i>in-</i>	borate buffer pH 8.4, range of potentials	87
k	ellipsometry	<i>in-</i>	borate buffer pH 8.4	171
l	SERS	<i>in-</i>	borate buffer pH 8.4	119
m	SERS	<i>in-</i>	5M KOH (aerated), 25°C	47

Note :

- i Unless otherwise stated, all analyses performed at 20°C.
- ii Where applied potentials are not given, indicates that the authors either didn't supply details, or that they were ambiguous.
- iii Dotted lines indicate a continuous transition from one layer to the next.
- iv In Fig. 2.4, * indicates that the species only resemble the indicated crystalline phases but are not as structurally well defined

growth of the outer layer because of anodic deposition of ferric oxide. The presence of ferrous ions had no effect on the growth of the inner layer and thus it was concluded that the outer layer can be regarded as a deposit layer and the inner layer as a barrier layer with which the overpotential of film formation is controlled. In acidic electrolytes, the outer layer was reported to dissolve away leaving only the inner layer (Fig. 2.4(d)).

Nagayama and Cohen¹⁸⁰ proposed a two layer model consisting of an inner Fe_3O_4 and an outer Fe_2O_3 layer. They suggested that the outermost part of the film has a cation defect structure such as $\text{Fe}_x^{6+} \text{Fe}_{2-2x}^{3+} \square_x^{3+} \cdot \text{O}_3$ (Fig. 2.4(h)).

Lyons and Burke^{40,186} proposed a duplex film formed on Fe in alkaline electrolytes consisting of a thin, compact inner oxide or hydroxide layer that is essentially anhydrous and a much thicker, porous outer layer that is essentially hydrated.

Seo *et al.*¹⁷⁰ reported the presence of a duplex surface film with an inner Fe_2O_3 layer forming by direct oxidation at the metal surface and the outer layer forming by solution phase transport and deposition. These results are supported by those of Mitrovic - Scepanovic *et al.*¹⁶⁹

Kanno and Nagayama¹²⁸ reported that the outer layer of the surface film was hydrated FeOOH and that the degree of hydration decreased with increasing potential. They also proposed the presence of Fe(VI) in the outer regions of the film.

2.6.2 Absence of Discrete Layering of the Duplex Film

From thermodynamic considerations Vetter¹⁷⁵ concluded that the passive film consisted of two layers, with a continuous change from the inner Fe_3O_4 layer to the upper $\gamma\text{-Fe}_2\text{O}_3$ layer.

From electron diffraction measurements and cathodic reduction curve and electrolyte analysis, Cohen⁹² proposed a duplex structure of the passive film with an indistinct boundary between the two layers and showed that the boundary is in fact a cubic lattice with the Fe concentration decreasing towards the outer regions of the film.

Haupt and Strehblow,³⁴ using variable angle XPS, suggested a duplex layer structure of an inner FeO and an outer Fe_2O_3 layer with the transition between the two layers being continuous (Fig. 2.4(e)).

Based on *in-situ* Mössbauer spectroscopy data O'Grady¹⁶ proposed that the passive film on Fe was amorphous and consisted of Fe(III) oxides with the Fe containing polymeric chains bonded by bi-nuclear iron compounds containing dioxy and dihydroxy bridging bonds between the Fe atoms. He concluded that the chains were linked together by H_2O . When the films were dried $\gamma\text{-Fe}_2\text{O}_3$ was observed.

The work of Bloom¹⁸⁵ and Yolken *et al.*¹⁸⁷ suggests that $\gamma\text{-Fe}_2\text{O}_3$ is not merely a spinel structure containing vacancies but is a modification of the Fe_3O_4 structure in which the hydrogen atoms are substituted for some of the Fe(II) ions and that HFe_5O_8 is the end result of such a substitution when all the ferrous ions have been replaced by protons.

2.6.3 The Presence or Absence of Fe_3O_4 in the Surface Film

The absence or presence of Fe_3O_4 in the passive film is frequently questioned. Unambiguous detection of Fe_3O_4 is difficult due to its structural similarity to $\gamma\text{-Fe}_2\text{O}_3$. Further, $\gamma\text{-Fe}_2\text{O}_3$ and Fe_3O_4 are totally miscible due to the relatively high mobility of the Fe ion. Heusler¹⁸⁸ and Wagner¹⁸⁹ pointed out the significance of this to passivation studies; in amorphous passive films the Fe ion mobility will be higher than in the pure spinels due to the loss of order and a considerable part of the electronic states will become localised, resulting in considerable interconvertability between $\gamma\text{-Fe}_2\text{O}_3$ and Fe_3O_4 .

Long *et al.*¹⁰² using *ex-situ* EXAFS found spinel like structures similar to those of $\gamma\text{-Fe}_2\text{O}_3$ and Fe_3O_4 in the passive film, although certain physical parameters were found to differ from those obtained for the anhydrous crystalline spinel standards.

Ferreira *et al.*¹⁰⁶ pointed out that α -, γ -, δ -FeOOH all have Raman bands at about 670cm^{-1} making it difficult to distinguish between them and from Fe_3O_4 which also has a band at 670cm^{-1} .

Using electron diffraction techniques Kuroda *et al.*⁷⁹ found no difference in the diffraction patterns of $\gamma\text{-Fe}_2\text{O}_3$ and Fe_3O_4 , however from ellipsometric and ac impedance data they concluded that only $\gamma\text{-Fe}_2\text{O}_3$ was present (*cf* Fig. 2.4(f)). However, Foley *et al.*⁹³ reported that $\gamma\text{-Fe}_2\text{O}_3$ gave additional weak reflections and had a lower lattice parameter than Fe_3O_4 and hence distinction could be made between these structurally similar spinels. In agreement with Kuroda's results ellipsometric data from Chen and Cahan⁸⁸ and Sato *et al.*⁸⁴ showed that no Fe_3O_4 was present in the film; only $\gamma\text{-Fe}_2\text{O}_3$ and hydrated $\gamma\text{-Fe}_2\text{O}_3$ were detected (Figs. 2.4(f) and 2.4(d)).

For Fe passivated in $\text{HBO}_3 - \text{NaBO}_3$ (pH 8.4) Seo,⁷² using AES, showed that the surface film consisted of two distinct layers — an inner Fe_3O_4 and an outer $\gamma\text{-Fe}_2\text{O}_3$ layer (Fig. 2.4(b)). However, Revie *et al.*,⁷¹ also using AES, questioned this conclusion since they had found that two of the peaks on Seo's spectra were due to an air-formed oxide (in transferring the electrode to the AES instrument), whereas if the transfer was made in an inert atmosphere a hydrated iron oxide was detected (Fig. 2.4(g)). These results concur with those obtained in Mössbauer studies.¹⁹⁰

Differentiating between the various iron oxides using XPS is also a non-trivial exercise. Allen *et al.*¹⁹¹ in a comparative study of iron oxides ($\alpha\text{-Fe}_2\text{O}_3$, Fe_3O_4 , FeO , $\alpha\text{-FeOOH}$) pointed out that the Fe 2p spectra

were particularly difficult to analyse due to a steeply rising background and broadened line widths, resulting from multiplet splitting and shake up phenomena. They also found that the binding energy values for Fe_3O_4 and $\alpha\text{-Fe}_2\text{O}_3$ were identical. However, McIntyre and Zetaruk¹³⁰ reported that distinction between the various iron oxides could be made if multiplet splitting effects in conjunction with binding energy shifts were considered.

Asami and Hashimoto¹⁹² are reported to have shown that the 2p spectra of $\alpha\text{-Fe}_2\text{O}_3$, $\alpha\text{-FeOOH}$, $\gamma\text{-Fe}_2\text{O}_3$ and $\gamma\text{-FeOOH}$ are virtually identical but different to that of Fe_3O_4 . They reported that the former 4 spectra have a small broad peak between the Fe 2p_{3/2} and Fe 2p_{1/2} peaks due to satellite splitting of the Fe 2p_{3/2} level. For Fe_3O_4 no such satellite peaks are observable. This observation is particularly significant due to the frequently reported similarities in the binding energies of Fe_3O_4 and Fe(III) oxides.

2.7 CRYSTALLINE NATURE OF SURFACE FILMS ON Fe AND FERROUS ALLOYS

A consensus has still not been reached with regard to the crystalline^{79,180,182,193} vs non - crystalline^{13-16,94,102,115,150,190,194} nature of passive films. However, increasing evidence for a non - crystalline film seems to be emerging, particularly for the more protective films, with the degree of crystallinity decreasing as the protective ability of the film increases; for example, electron diffraction studies⁹⁴ have shown that as the Cr content of the alloy increases so the structure of the passive film becomes increasingly non - crystalline.

The importance, and rôle, of H_2O in the formation of passive films has frequently been reported in the literature.^{16,115,171} Bockris¹¹⁵ in reviewing the results of several surface analytical techniques concluded that the amorphous nature of passive films, and hence their passivating properties, can be destroyed by heat as a result of the removal of H_2O from the film, as discussed in the previous surface analysis section, and also by the presence of aggressive anions. Increasing the temperature of an electrochemical system will improve the crystallinity of a surface film resulting in the film becoming less protective and thereby enhancing dissolution at higher temperatures.

The surface film structure is dependent on the field strength at the time of formation,¹⁹⁵ with those grown at high field strengths having only a crystalline short range order, but no long range order as possessed by films grown at low field strengths.

Those surface film models favouring a crystalline structure require the formation of well defined crystalline oxide structures which grow by field assisted oxide growth mechanisms involving primarily ionic conduction through the surface film. Inherent in non - crystalline models is the absence of long range order effects in the film and the presence of bound H_2O molecules. Typical of this type of model is the hydrated amorphous polymeric oxide model proposed by Pou *et al.*¹⁵ in which the water molecules essentially hold

the iron oxide chains together such that diffusion of Fe^{2+} ions from the metal substrate to the surface film / electrolyte interface is hindered.

2.8 FILM THICKNESS

The thickness of the passive film on iron and FeCr based stainless steel alloys has been studied by several investigators^{13,34,35,84,86,91,138,139,161,171,156,196-200} and in general has been shown to increase with increasing pH and potential although at transpassive potentials the thickness is independent of potential. For example, using Mössbauer spectroscopy to examine the surface film on Fe Eldridge⁹¹ reported an increase of $\approx 250\%$ in thickness (1.12nm to 2.8nm) when the film was formed at 1107mV as opposed to 157mV. Similar results were obtained by Szklarska - Smialowska²⁰¹ and Nagayama¹⁸⁰ with increases of 220% (2.5nm to 5.5nm) and 300% (1nm to 3nm), respectively, over the same potential range. Eldridge⁹¹ also showed that such changes only appear when the potential steps are made in an positive direction. The absence of any change when stepping in a negative direction would be expected since the iron oxide formed when passivating Fe is not very soluble and the kinetics of film growth would prevent the changes in the passive film from being reversible with potential.

For Fe in alkaline electrolytes, it has been shown^{34,86,171} that the thickness of the base layer was potential dependent while the thickness of the upper layer was dependent on the experimental conditions, eg. applied potential cycling regime, electrolyte composition. With increasing pH, there is a decrease in the thickness of the upper layer such that in acidic electrolytes the base layer constitutes the part of the surface film.

For alloys containing minor alloying elements, eg. Mo, V, disagreement exists as to whether increasing the molybdenum content of the alloy increases^{159,202} the thickness of the passive film or not.¹³⁹ The presence of Mo in an alloys was shown to improve the film formation efficiency⁶⁵ eg. at 680mV in 0.1M H_2SO_4 film formation efficiency was 64% for Fe15Cr4Mo, 36.5% for Fe17Cr and 10 - 20% for Fe (with the remainder being consumed by dissolution).

2.9 ELECTRONIC STRUCTURE OF SURFACE FILMS

The electronic properties of a passive film are a significant factor in determining the mechanism of film formation, breakdown and the rate of metal dissolution. Moreover, electron transfer reactions that occur on surfaces with passive films depend strongly on the electronic properties of such films. Much of the research in this area has involved investigating the electronic conductivity of the films, since the kinetics of passive film formation may be controlled by electronic or ionic conduction, surface reactions or a combination of all three.

The electrical conductivity of the passive film is still a subject of debate with some studies suggesting a semiconducting film²⁰³ (the outer part of the passive film, $\gamma\text{-Fe}_2\text{O}_3$, being an n - type semiconductor) while others suggest a non - conducting or low conductivity film, suggested by the field assisted ion migration growth mechanism in which a non - conducting film would be required to support the large field inherent in this mechanism. The concept of a chemiconductor has been proposed⁸³ in an attempt to reconcile the opposing views. Here the passive film is suggested to go from an insulator to a semiconductor as defects are added or removed. However, the experimental basis for this model has been questioned.

In his review on passivity, Cohen⁹² summed up the work on electronic structure of the passive film on Fe as it being a semiconductor in which both electronic and ionic transport changes with the changing composition of the film from the metal - oxide interface to the oxide - solution interface. They are also generally being thought of as an oxide having an exceptionally large defect concentration ($10^{19} - 10^{21}\text{cm}^{-3}$) and thus resembling an amorphous semiconductor with additional characteristics of its own.

Semiconductor models have often been invoked in the interpretation of capacity measurements of passive metal electrodes. The Scottky - Mott equation has usually been applied to the analysis of such data with straight lines being expected for C^{-2} vs E plots and from the linear portion the current density of charge carriers can be estimated if the dielectric constant of the passive film is known or assumed.

Using a photoelectrochemical technique Vera *et al.*²⁰⁴ showed that passive films formed on iron in borate buffer solution was an n - type semiconductor having a band gap of $\approx 2.0\text{eV}$, with the magnitude of the photoresponse a function of both passivation potential and film growth time. Simões *et al.*²⁰⁵ reported n - type semiconductor behaviour for 304 in borate buffer. They further showed that temperature had relatively little effect on the electronic structure of the passive film with the conclusion that the increased rate of dissolution with increasing temperature has a kinetic basis rather than as a result of a change in the electronic structure.

2.10 POURBAIX DIAGRAMS FOR THE Fe - H₂O and Fe - CN - H₂O SYSTEMS

While equilibrium potential - pH diagrams or Pourbaix diagrams are restricted in their applications in that the kinetics of the system are not taken into account, they provide a useful means of assessing what is thermodynamically feasible for any particular system.

The potential - pH diagrams constructed by Pourbaix and co - workers²⁰⁶ for the Fe - H₂O system (*cf* Fig. 2.5) indicate that active dissolution of Fe occurs over a narrow potential range at high pH values. Over a large potential and pH range, formation of Fe(II) and Fe(III) oxides is possible although they are likely to inhibit the kinetics of iron dissolution. These diagrams also only consider the $\text{Fe}(\text{OH})_2/\text{Fe}(\text{OH})_3$ and $\text{Fe}_3\text{O}_4/\text{Fe}_2\text{O}_3$ oxides, and as is evident from earlier sections of this literature review, FeOOH is frequently

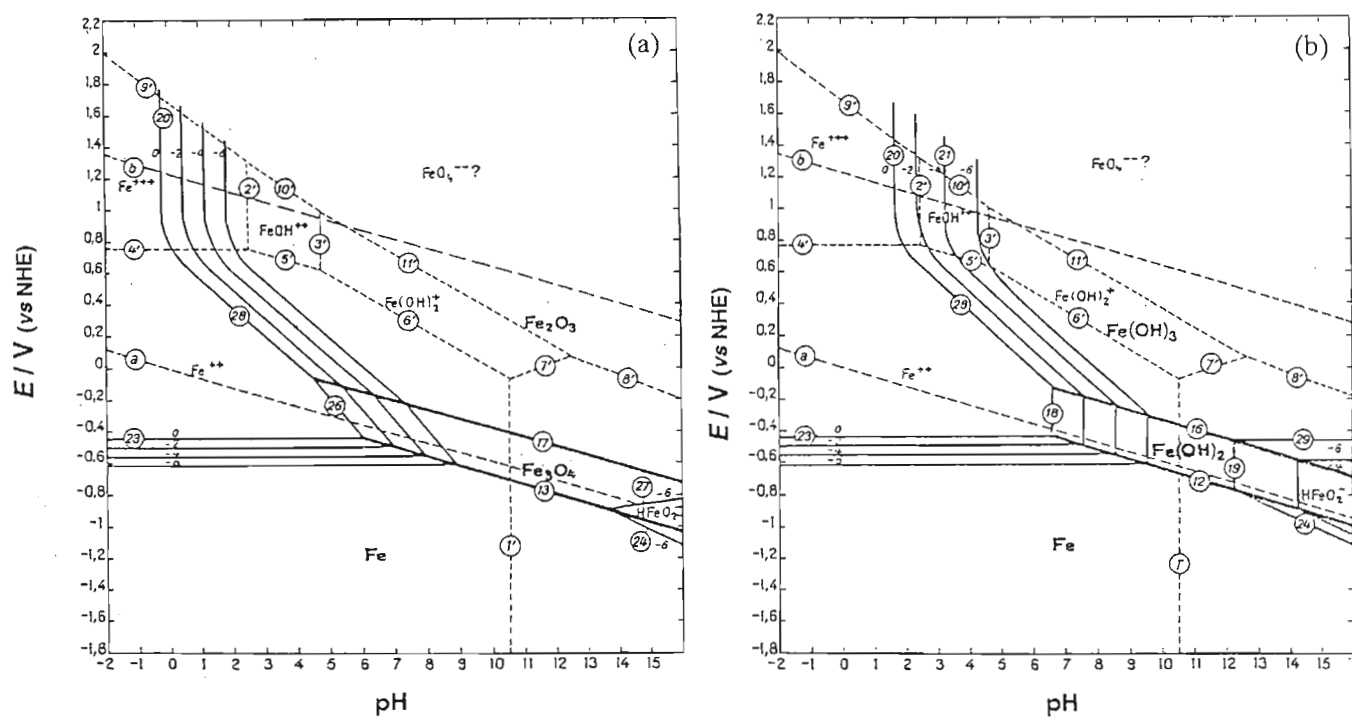


Fig. 2.5 Potential - pH diagrams²⁰⁶ for the Fe - H₂O system at 25°C.
 (a) considering Fe, Fe₃O₄ and Fe₂O₃ as solid species
 (b) considering Fe, Fe(OH)₂ and Fe(OH)₃ as solid species

reported to play a role in the corrosion mechanism of Fe dissolution in alkaline electrolytes. Potential - pH diagrams incorporating the oxyhydroxides were constructed by Misawa²⁰⁷ and are shown in Fig. 2.6.

The majority of published Pourbaix diagrams have been confined to ambient temperatures due to the dearth of thermodynamic data at other temperatures. For $T < 200^\circ\text{C}$, several potential - pH diagrams for the Fe - H_2O system have however been determined and these are shown in Figs. 2.7 - 2.10. As can be seen from these figures and from Fig. 2.11, for the Fe - Cl - H_2O system, with increasing temperature there is an increase in the stability of the HFeO_2^- ion and a concomitant decrease in that of the oxides and of Fe. Thus at elevated temperatures and in alkaline electrolytes, Fe dissolution will occur via the formation of HFeO_2^- as a soluble intermediate. This has been verified experimentally.^{46,54,55,208}

Fig. 2.12 shows the effect of the addition of cyanide to the Fe - H_2O system demonstrating that the formation of iron cyanide complexes are thermodynamically favoured with hexacyanoferrate (II) the predominant species while hexacyanoferrate (III) is confined to a narrow pH and potential range, which is outside that of the present experiments. Osseo - Asare *et al.*⁶² point out that the poor stability of iron and the iron oxides indicated in Fig. 2.12 is not observed in practice with, for example, $\alpha\text{-Fe}_2\text{O}_3$, $\alpha\text{-FeOOH}$ and Fe_3O_4 having been reported to be virtually insoluble in cyanide electrolytes. This discrepancy can be attributed to the unfavourable reduction of the Fe(III) oxides to the hexacyanoferrate (II) complex.

The Pourbaix diagram for the CN - H_2O system, without the inclusion of Fe, simplifies to that shown in Fig. 2.13. At high pH values the oxidation of cyanide to cyanate is thermodynamically favourable at ambient temperatures, however the reaction is inhibited by the exceedingly slow kinetics. In practice, it is only at elevated temperatures that this reaction becomes important.

2.11 THEORIES OF NUCLEATION AND GROWTH OF SURFACE FILMS

Significant impetus to investigate electrocrystallisation phenomena was provided by Armstrong, Fleischmann and co - workers²¹⁴⁻²²⁶ who demonstrated that nucleation can be observed experimentally, and provided theoretical interpretations to the observed data. The development of the main electrocrystallisation theories is shown in Table 2.4.

Electrocrystallisation is the electrochemical formation of a solid phase. Depending on the composition and nature of both the substrate and the deposited phase, the latter may form via discrete centres, or nuclei, having a definite geometry of growth or it may form as a uniform layer with growth controlled by ion migration across the layer. Chronoamperometry is one of the most frequently employed techniques for investigating these processes, with uniform layer formation resulting in decaying or falling current transients while the nucleation route results in the current transients having a characteristic maximum, as shown in Fig. 2.14. Experimentally this involves stepping the electrode from a potential where nucleation does not

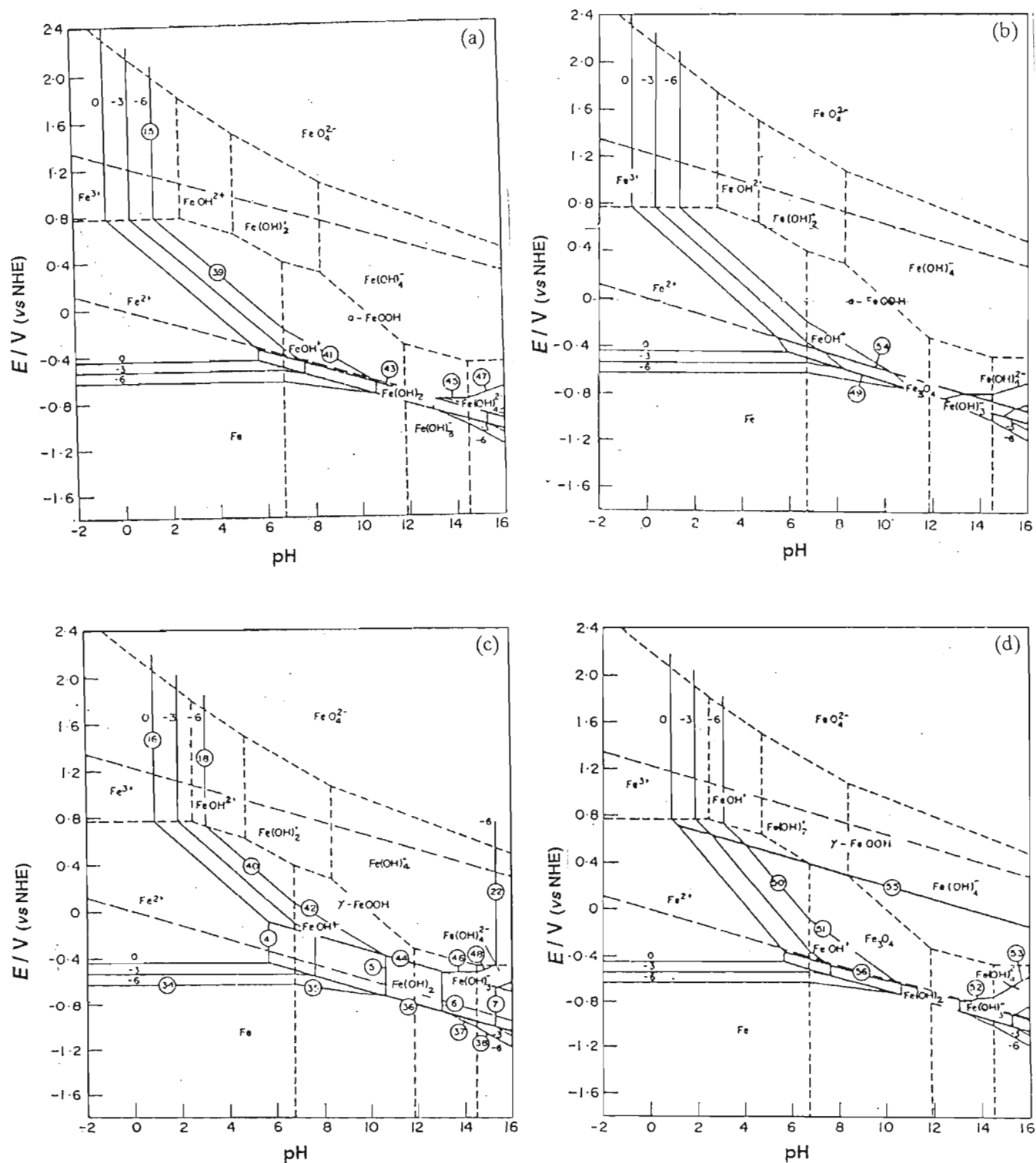


Fig. 2.6 Potential - pH diagrams²⁰⁷ for the Fe - H₂O system at 25°C.
 (a) considering Fe, Fe(OH)₂ and α-FeOOH as solid species
 (b) considering Fe, Fe₃O₄ and α-FeOOH as solid species
 (c) considering Fe, Fe(OH)₂ and γ-FeOOH as solid species
 (d) considering Fe, Fe(OH)₂, Fe₃O₄ and γ-FeOOH as solid species

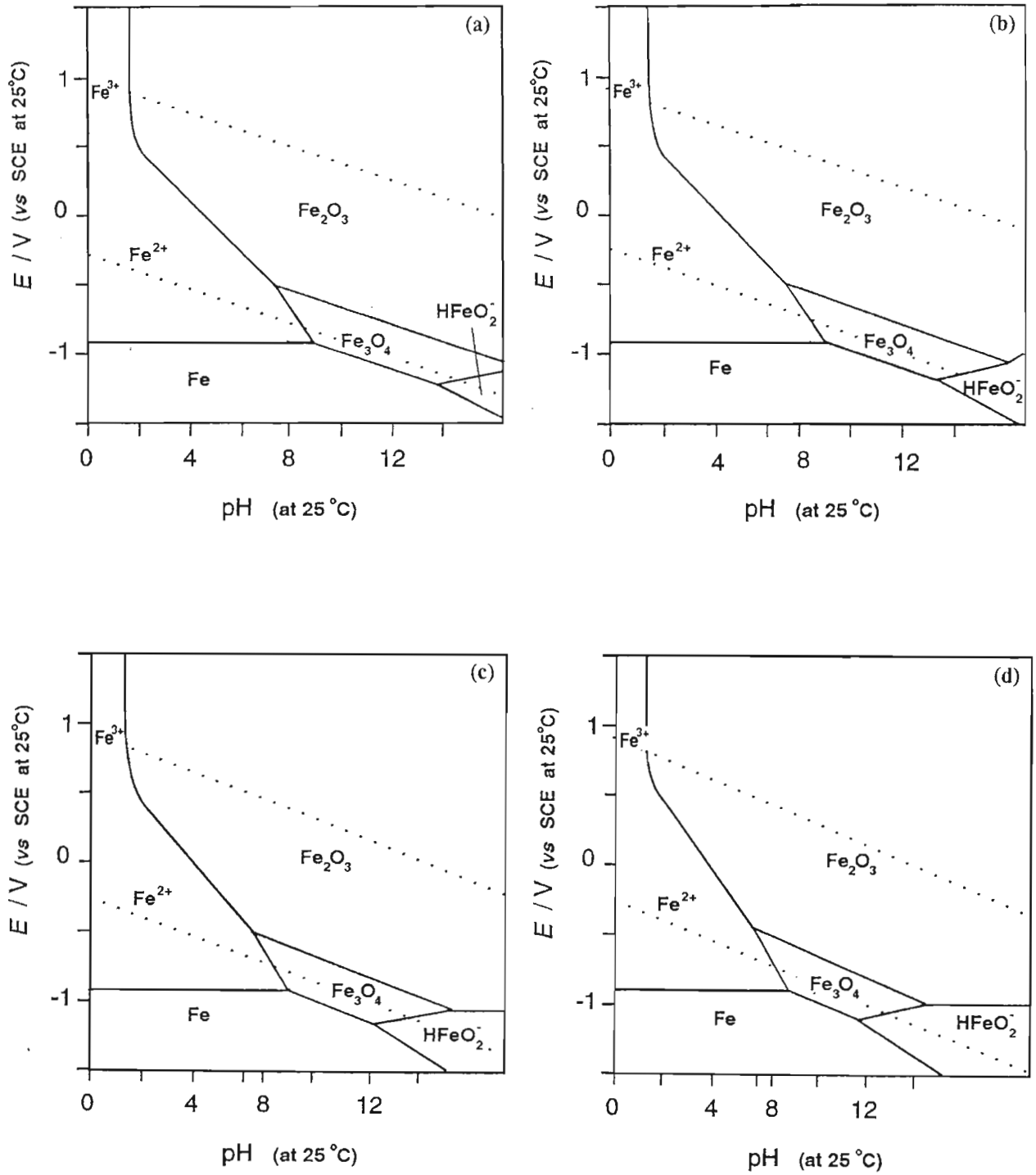


Fig. 2.7 Potential - pH diagrams²⁰⁸ for the Fe - H₂O system considering Fe, Fe₃O₄ and Fe₂O₃ as solid species at (a) 30°C (b) 50°C (c) 75°C and (d) 90°C.

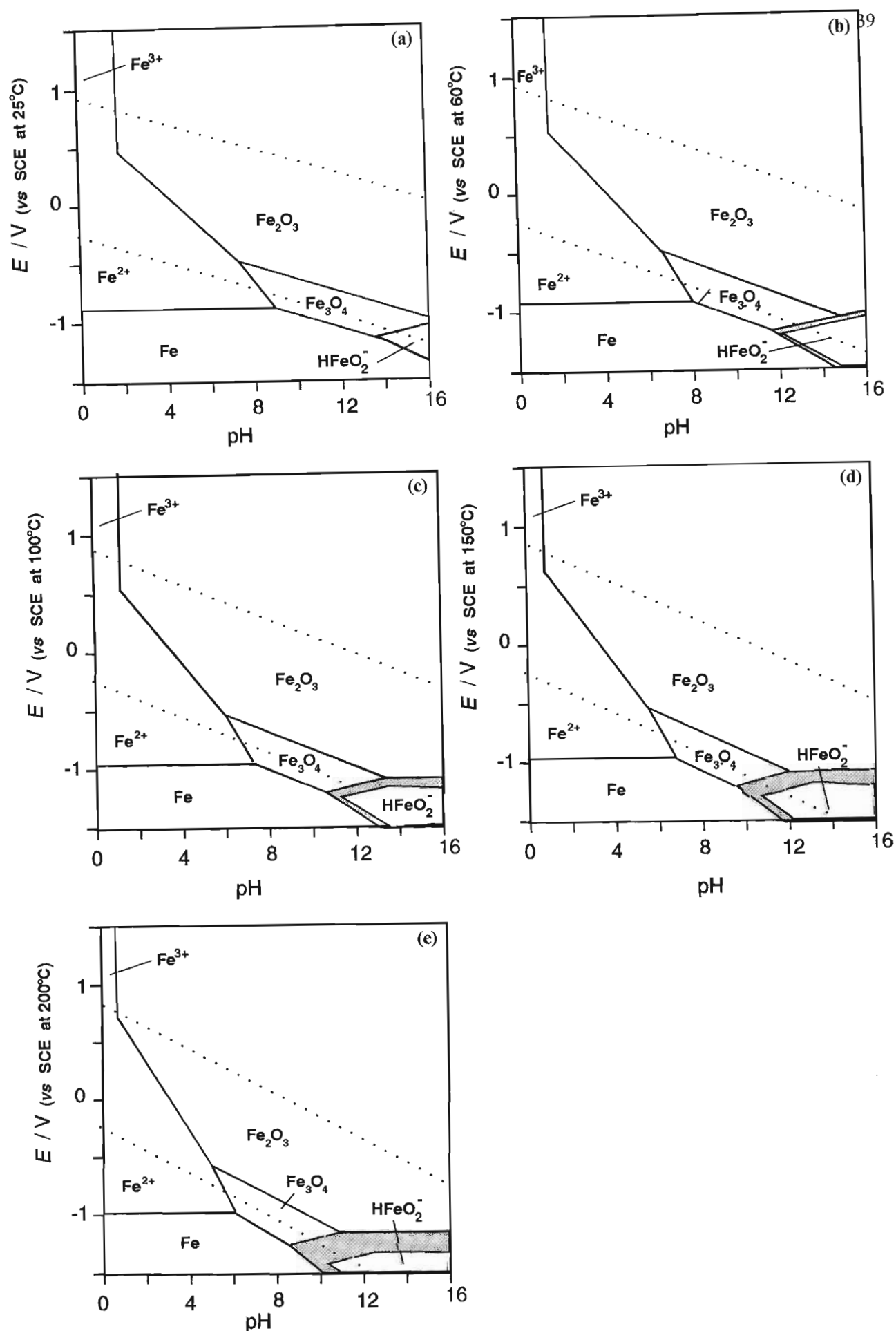


Fig. 2.8 Potential - pH diagrams²⁰⁹ for the Fe - H₂O system considering Fe, Fe₃O₄ and Fe₂O₃ as solid species at (a) 25°C (b) 60°C (c) 100°C (d) 150°C and (e) 200°C. The shaded region is due to the uncertainty in the calculation of the standard free energy of the three regions concerned

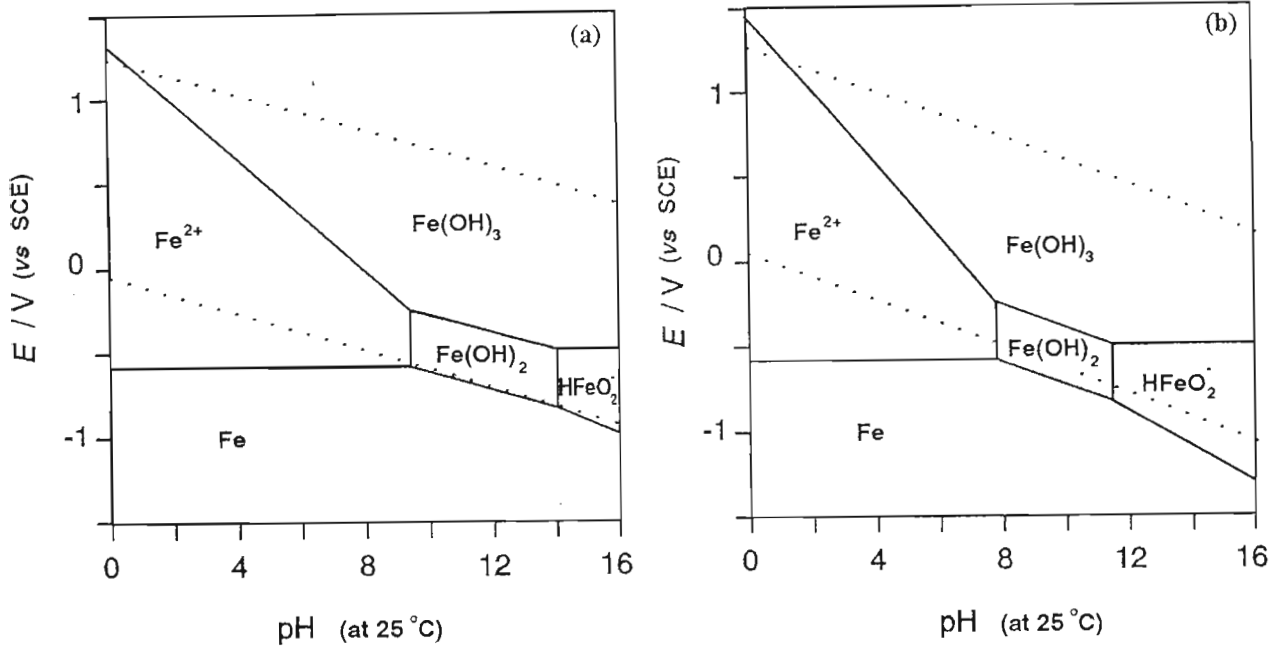


Fig. 2.9 Potential - pH diagrams²¹⁰ for the Fe - H₂O system considering Fe, Fe(OH)₂ and Fe(OH)₃ as solid species at (a) 5°C and (b) 70°C

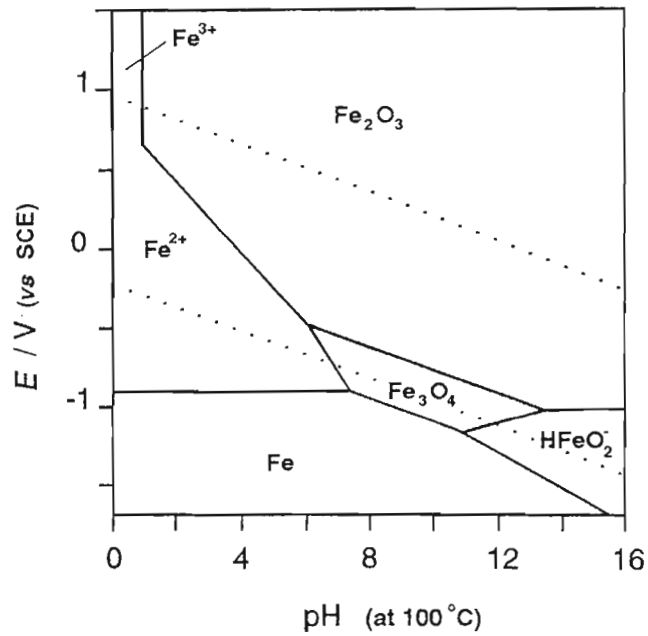


Fig. 2.10 Potential - pH diagram²¹¹ for the Fe - H₂O system at 100°C considering Fe, Fe₃O₄ and Fe₂O₃ as solid species.

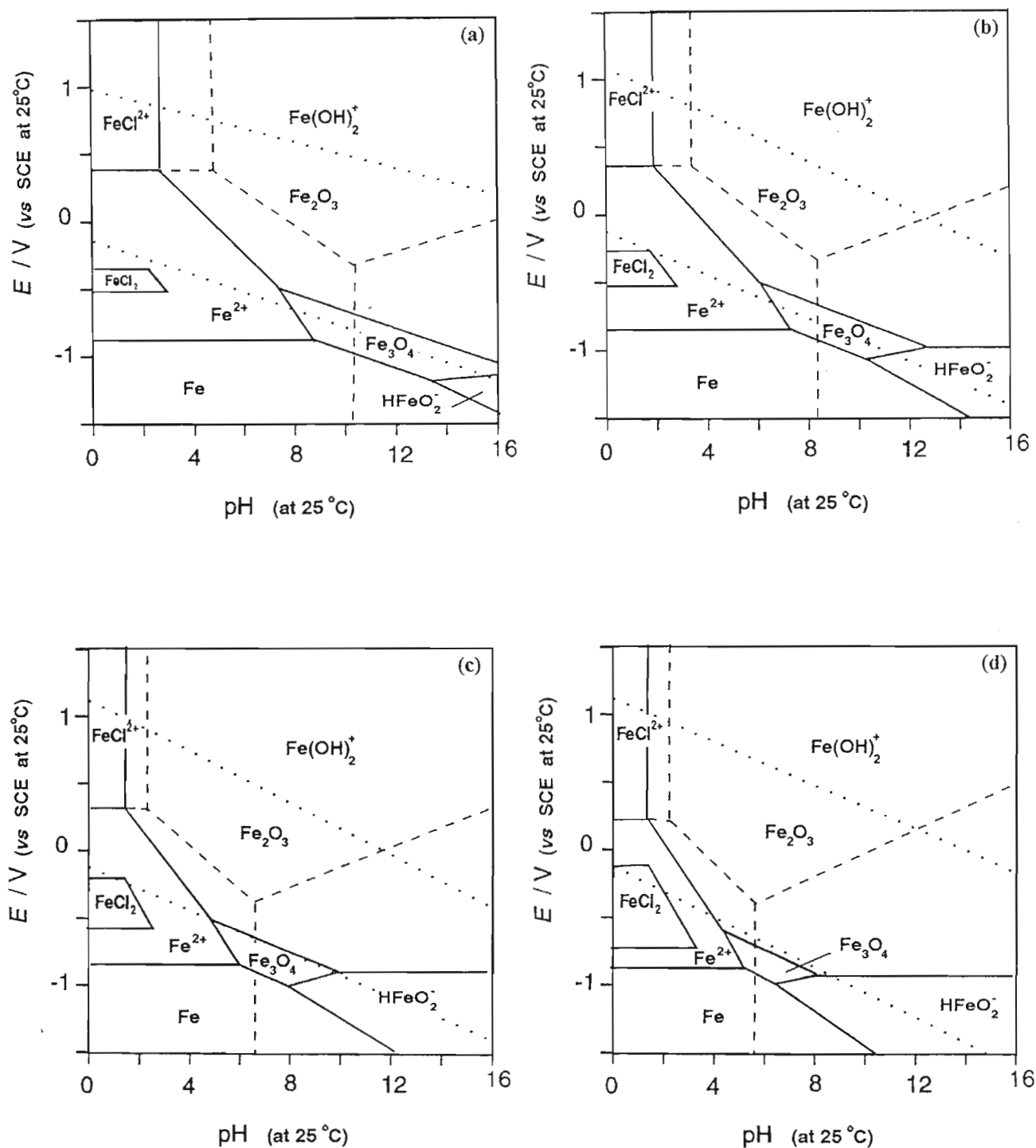


Fig. 2.11 Potential - pH diagrams²¹² for the Fe - Cl - H₂O system considering Fe, Fe₃O₄, Fe₂O₃ and FeCl₂ as solid species at (a) 25°C (b) 60°C (c) 100°C and (d) 150°C.

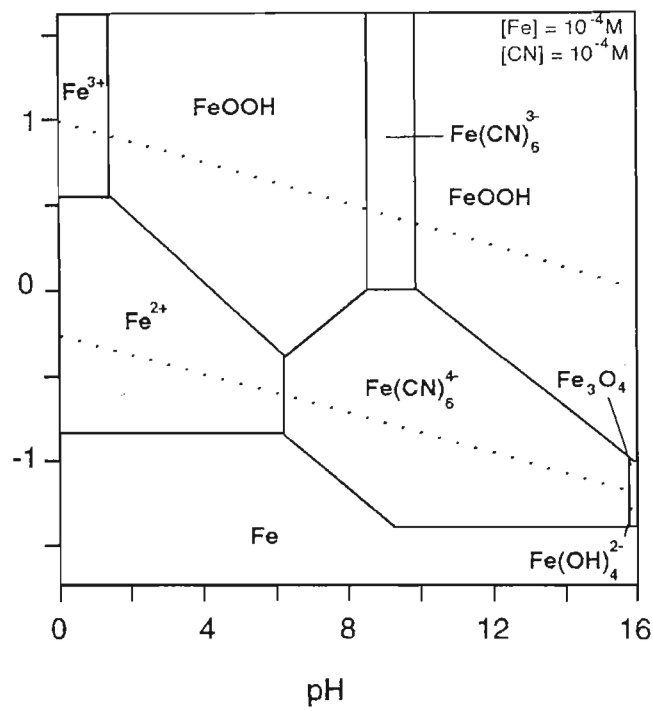


Fig. 2.12 Potential - pH diagram⁶² for the Fe - CN - H₂O system at 25° C considering Fe, Fe₃O₄ and FeOOH as solid species.

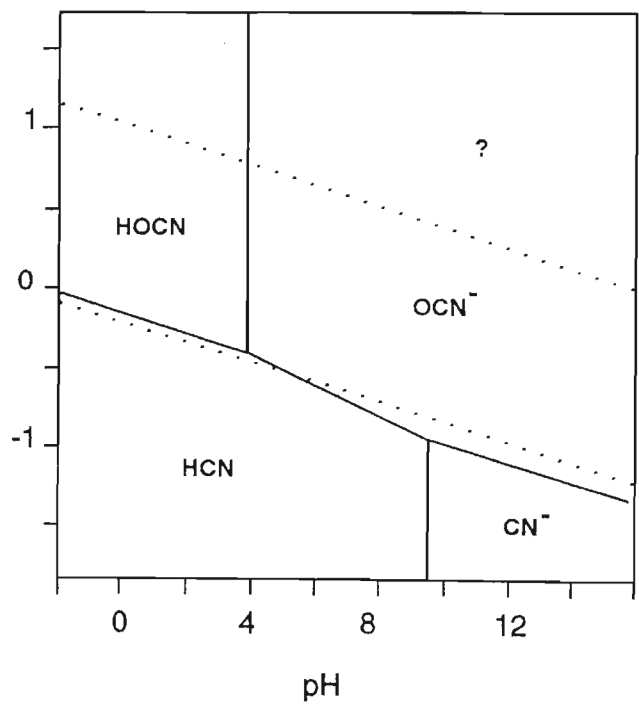


Fig. 2.13 Potential - pH diagram²¹³ for the CN - H₂O system at 25° C.

Table 2.4**Development of electrocrystallisation theory : : Major contributions****Charge transfer controlled growth models**

1959	Fleischmann and Thirsk : ²¹⁴	considered both 2D and 3D nucleation and growth
1962	Benwick, Fleischmann and Thirsk : ²¹⁷	2D nucleation and growth
1963	Fleischmann and Thirsk : ²²⁴	proposed equations to describe transients under potentiostatic conditions for the formation of a single layer
1966	Armstrong, Fleischmann and Thirsk : ²²⁵	model describing the consequences of charge transfer controlled growth for (a) 2D growth with a single, radial growth rate, (b) right circular conical and hemispherical growth with one horizontal and one vertical growth rate and (c) a 3D passivation model which assumed the vertical growth rate was proportional to the uncovered substrate area. The models defined the overall growth kinetics in terms of a time independent nucleation parameter and growth rates.
1967	Armstrong and Fleischmann : ²²⁷	re - evaluated previous model ²²⁵ to include a potential dependent nucleation rate
1969	Armstrong and Harrison : ²¹⁵	obtained a relationship by which the current contributions from successive layers could be evaluated
1975	Armstrong and Metcalf : ²¹⁶	layer by layer 2D nucleation and growth giving multi-maxima transients
1973}	Rangarajan ^{228,229}	Armstrong and Harrison's ²¹⁵ successive layer model further developed and which included the possibility that current fluctuations due to the nucleation process could occur ^{228,230} resulting in the damping oscillation previously predicted for multilayer growth not occurring.
1977	}	Abyaneh and co - workers ^{231,232} modified Fleischmann's earlier model ²²⁵ by introducing a 'time cut - off' at which vertical growth pauses only to restart with a time delay
1981		
1982	Bosco and Rangarajan : ^{233,234}	generalised Armstrong's model ²²⁵ to (a) any nucleation rate law (b) either charge transfer or diffusion control and also provided a correction to Armstrong's equation for 3D nucleation and growth leading to passivation
1982	Abyaneh : ²³⁵	re - analysed overlap for nucleation and 3D growth of hemispheres under charge transfer control, and showed previously ²³² necessary assumptions regarding the 'death' and 'rebirth' of nuclei to be unnecessary.
1982	Abyaneh and co - workers : ^{236,237}	considered 3D nucleation and growth of right circular cones

under charge transfer control

- 1986 Abyaneh : ²³⁸ considered 3D nucleation and growth of spherical cap nuclei, under charge transfer control
- 1991 Abyaneh : ²³⁹ considered 3D nucleation and growth of hemispheroids with growth controlled by charge transfer at the electrode - electrolyte interface.

Diffusion controlled growth models

- 1968 Astley : ²⁴⁰ linear diffusion controlled 3D nucleation and growth
- 1974 Hills, Schiffrin, Thompson : ²⁴¹ proposed mass transport more likely to be hemispherical
- 1978 Gunawardena, Hills and Montenegro : ²⁴² considered nucleation and growth of hemispherical nuclei, with the hemispherical geometry of both the nuclei and corresponding diffusion zones being retained during growth
- 1982 Gunawardena, Hills, Montenegro, Scharifker : ²⁴³ model further developed to incorporate overlap confirmed experimentally with Ag²⁴⁴ and Hg²⁴⁵ nucleation onto vitreous C.
- 1983 Scharifker and Hills²⁴⁶
confirmed experimentally by Tsakov and Milchev²⁴⁷
criticized and further developed by :
- 1983 Deutscher and Fletcher^{248,249}
- 1984 Scharifker and co - workers^{250,251}
experimentally verified by : Tsakova and Milchev²⁵² (1991) and Alonso *et al.*²⁵³ (1990)
- 1985 Fletcher²⁵⁴
- 1986 Barradas and Bosco²⁵⁵ incorporated simultaneous metal dissolution into model
- 1987 Sluyters - Rehbach *et al.*²⁵⁶
Bobbert *et al.*^{257,258}
- 1988 Deutscher and Fletcher²⁵⁹
Jacobs²⁶⁰
- 1989 Mulder²⁶¹
- 1990 Greef *et al.*²⁶²
Mirkin and Nilov²⁶³

Adsorption - nucleation models :

- 1981 Bosco and Ranjarajan : ²⁶⁴ proposed an adsorption - nucleation model
- 1988 Arulraj and Noel : ²⁶⁵ considered monolayer formation by simultaneous adsorption and nucleation - growth - collision processes.
- 1991 Bhattacharjee and Rangarajan : ²⁶⁶ refined previous two models^{264,265} and presented a generalised model

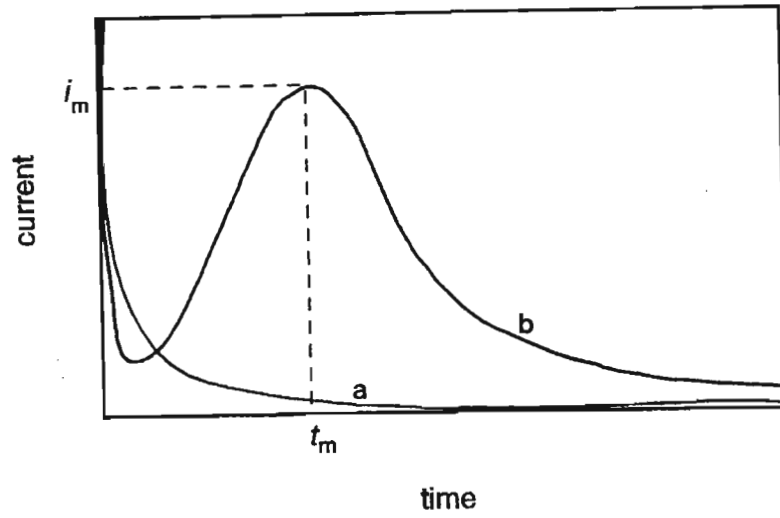


Fig. 2.14 Schematic representation of the current transient obtained for (a) uniform layer formation with growth controlled by ion migration across the layer and (b) layer formation via nucleation.

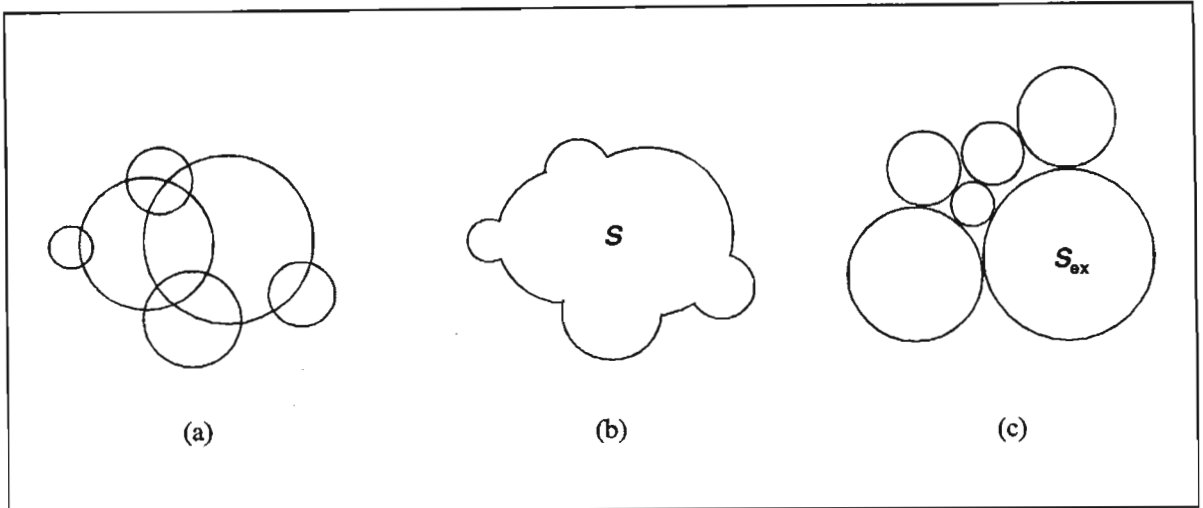


Fig. 2.15 Schematic representation of the Avrami theorem used to take into account the overlap of neighbouring nuclei (a), which relates the actual surface area (b) to the extended surface area that would have been covered in the absence of overlap (c).

occur to a potential where nucleation does occur. Depending on the experimental system, current transients reported in nucleation studies show either an initial rapid decay followed by an increase in the current to a maximum i_m at t_m , or start from zero and increase to a maximum, subsequent to which the current decays usually to a steady state. The characteristic maximum of these transients is generally considered to be due to either overlap of growth centres or abrupt cessation of growth, or both.

Current transients can also exhibit several maxima, which is indicative of the formation of successive layers of deposits. In addition to chronoamperometry, complex perturbations, eg. ac impedance and linear potential scans, have also been incorporated into the theoretical considerations, however these frequently involve complex mathematics and a large number of assumptions.

Analyses of these rising chronoamperometric transients and mathematical descriptions of the nucleation and growth process have been extensively reported in the literature,^{224,267-271} and while many of the models are quite adequate in describing simple electrocrystallisation systems (particularly deposition of metal ions, from solution, onto an inert substrate) they are inadequate in describing more complex systems, for example, anodic oxide formation on a corroding substrate. The inadequacy of most proposed models is caused by the mathematical complexity of the problem. In an attempt to simplify the mathematics assumptions and approximations have had to be introduced. As these are generally different for each author, considerable debate has ensued in the literature. A further complication arises when an in depth investigation of a particular aspect of the process is undertaken with only a cursory integration of the final conclusions into the overall model, at which stage the new results may not necessarily fit. As has been pointed out by a number of authors,^{255,256,260,263,272} for a model to be truly realistic the mathematics becomes exceedingly complicated, and at present the comment of Mirkin and Nilov²⁶³ would seem to sum up the situation: "A very strict theoretical description of the complex and multistage process of nucleation and growth is not quite possible".

Therefore the purpose of this section is to briefly describe the main concepts pertaining to electrocrystallisation, the models and equations most frequently applied to experimental data and criticism thereof.

2.11.1 Electrocrystallisation Processes

Nucleation and growth are complex phenomena made up of several processes that proceed, to varying degrees, simultaneously. The nucleation process must be preceded by deviation from equilibrium conditions, either in the form of the attainment of a particular degree of supersaturation, as required in homogeneous phase formation, or in the case of electrocrystallisation, by the application of a potential conducive to nucleation. Following the application of a potential step there is an induction period prior to nucleation. Once conditions at the surface are such that the critical energy for the formation of stable nuclei is achieved, nucleation at randomly distributed sites on the electrode surface, referred to as active

sites, can occur. Further nucleation and growth at these active sites will proceed until limited by the available surface area or the available number of active sites. The nuclei growth rate is determined by the rate of incorporation of new atoms or by the rate of diffusion of metal ions to the growing nuclei. The growth may be either two dimensional, 2D, when only a monolayer is formed without further nucleation, or three dimensional, 3D, allowing the growth of thick layers. With continued growth, coalescing of the growing nuclei, or growth centres, will occur and also, in the case of a diffusion controlled reaction, overlap of the diffusion zones surrounding each growth centre. Continuation of the process will result in complete coverage of the electrode by the deposited phase. Most of the theoretical models limit growth to either diffusion or charge transfer control. Such restrictions, imposed in order to obtain an analytical solution to the problem, have frequently come under criticism for being unrealistic, particularly those of Armstrong *et al.*,^{224,225} Gunawardena *et al.*,^{243,245} Scharifker and co-workers,^{246,250,251} Bosco and Rangarajan,^{233,234} Sluyters - Rehbach *et al.*²⁵⁶ and Abyaneh.²³⁵ Work has however been reported on more complex systems eg. Bhattacharjee and Rangarajan²⁶⁶ and Arulraj and Noel²⁶⁵ proposed an adsorption - nucleation model (although the latter limited theirs to monolayer formation) and Barradas and Bosco²⁵⁵ proposed several models incorporating transient growth, dissolution and mixed kinetic - diffusion control (again with the restrictions of 2D nucleation and growth and single monolayer coverage).

2.11.2 Active Sites

One of the initial concepts that must be defined in any model, is what constitutes and influences the number of sites available for nucleation. There is debate as to the existence and nature of the active sites^{247,259,272-276} with agreement on the definition of an active site still not having been reached, other than that it is a preferred site for nucleation. As most real surfaces are not perfect but contain a number of defect sites it is at these sites where nucleation is most frequently suggested to occur. The determination of the total number of sites, N_0 , and of the number eventually converted to nuclei, N , has generally been found to be finite and dependent on several factors, eg. electrode pretreatment, electrode potential, presence of adsorbed species or of pre-existing films, and concentration of electroactive species at the site. Further, one of the historic goals of electrochemical nucleation studies, which has still not been achieved, is the determination of the number of atoms in the critical nucleus under typical experimental conditions in order to determine if the approximations used in deriving the various nucleation theories are valid.

Fletcher and Lwin^{277,278} proposed that the activities of preferred sites are distributed in a spectrum, which they refer to as the activity density function, and which is characteristic of the surface. Deutscher and Fletcher²⁷³ later re-evaluated this proposal and defined an active site as a region having a local value of what they termed the nucleation potency, greater than that of neighbouring regions. This could be due to structural imperfections, adsorbed species, surface films, cracks etc., which would lead to a range of nucleation rates, or a nucleation rate dispersion at different locations on the electrode surface. The basis for this concept was that the specific surface energy is not uniform over an area larger than the diameter of the base of a critical nucleus, resulting in certain areas having a higher probability for nucleation. In

contrast to these ideas of Fletcher and co-workers, Markov and Kashchiev²⁷⁹ proposed that the number of active sites was dependent on the applied potential indicating that the activity of all preferred sites was uniform for a given potential.

Countering the concept of active sites, Wijenberg *et al.*²⁷² proposed the existence of a probability for the formation of a nucleus which increases with increasing concentration of electroactive species. They also proposed that as a real electrode surface has so many imperfections, the surface can be treated as homogeneous with respect to nucleation, and that the decrease in concentration of the electroactive species and ohmic drop necessarily lead to a finite value of the number of nuclei. The consequence of their proposals is that assumptions regarding the existence of active sites are unnecessary.

One of the experimental difficulties impeding the evaluation of heterogeneous nucleation theories has been the determination of the number of nuclei as a function of time and potential. Physically counting the nuclei with the aid of transmission or electron microscopes^{260,280,281} or particularly an optical microscope can be tedious and relatively inaccurate depending on the electrochemical system under consideration — especially if sufficient data is to be collected for it to be statistically representative. This problem has largely been overcome with the development of programmable microscope stages and the use of image analysis systems which, with the availability of public domain software such as IMAGE (an excellent image analysis package developed by National Institute of Health (USA)), are within the budgets of most research groups!

However, the problem still remains when comparing such nuclei counts with classical theory predictions that the nucleation sites may be occluded by the diffusion zones surrounding the growing nuclei, thereby precluding the determination of the correct functional form of the experimental time dependence of the number of nuclei. One solution to this problem was presented by Deutscher and Fletcher^{259,282,283} who developed a microelectrode assembly which allowed only one nucleation site per microelectrode. Experimental chronoamperometric transients obtained using this electrode system could then be deconvoluted allowing the determination of, for example, nucleation rate as a function of time.

2.11.3 Nucleation Mechanism

Under given experimental conditions, the rate of appearance of stable nuclei or growth centres is expected to follow first order kinetics, with the number density of the nuclei is given by

$$N = N_0 [1 - \exp(-A t)] \quad (2.1)$$

where N_0 = total number of active sites

A is the nucleation rate constant and given by

$$A = k_1 k_0 \exp(-\varphi \sigma^2 / E) \quad (2.2)$$

for 2D nuclei, and for 3D nuclei by

$$A = k_1 k_o \exp (-\varphi \sigma^3 / E^2) \quad (2.3)$$

with k_1 = frequency factor
 k_o = growth constant at reversible potential
 σ = surface free energy
 φ = factor dependent on geometry of growth centre
 E = applied potential

Eqn. 2.1 can be shown to have two limiting forms. When $A t \gg 1$, then all the nuclei form immediately conditions are conducive to nucleation, with no new nuclei forming subsequently. This is referred to as instantaneous nucleation, and is characterised by nuclei of uniform size during the subsequent growth of the nuclei. For instantaneous nucleation, eqn. 2.1 reduces to

$$N = N_o \quad (2.4)$$

The second limiting form occurs when $A t \ll 1$, resulting in eqn. 2.1 reducing to

$$N = N_o A t \quad (2.5)$$

In this case nuclei form as a function of time resulting in nuclei of varying size and in the simultaneous occurrence of nucleation and growth processes. This form of nucleation is referred to as progressive nucleation, and is generally considered to be more realistic.

While the concepts of instantaneous and progressive nucleation are scorned by some authors, they do however provide a means of simplifying the mathematics by reducing the analysis to two limiting cases of nucleation.

2.11.4 Shape of Nuclei

Once stable nuclei have formed, the individual nuclei will continue to grow, for as long as conditions are conducive to growth. The theoretical treatment of electrocrystallisation systems has been dominated by geometrical considerations regarding the shape of the growing nuclei with a wide variety of shapes having been reported, including right circular cones,^{225,236,237} hemispheres,^{225,233-235,248,257,258,284} hemispheroids,²³⁹ spherical cap nuclei,²³⁸ truncated spheres²⁵⁸ and variable geometry nuclei²³⁴ (which are dependent on the form of the growth rate).

The nuclei shape will obviously influence the form of the current transient with, for example, transients derived for nucleation and growth of right circular cones exhibiting an initial rising current followed by a current plateau after long times while current transients derived for hemispheres are characterised by a single maximum, as shown schematically by curve (b) in Fig. 2.14.

While the use of certain shapes for nuclei is on occasion criticized for being oversimplifications, eg. hemispheres and right circular cones, visual examination of the nuclei has in fact shown these shapes to be valid. For example, hemispherical Ni nuclei have been reported^{235,285} to form on glassy carbon, while Ni formation onto a (III) Cu single crystal initially exhibited a right circular cone growth form.

While the hemispherical growth model is frequently invoked in electrocrystallisation modelling, a constraint of this model is that it requires a contact angle of 90° for nucleation (which in turn requires equality of the substrate - solution and substrate - deposit interfacial free energies) and equal growth rates parallel and perpendicular to the electrode surface. The right circular cone growth model, although allowing flexibility both in the choice of contact angle, as well as the option of assigning different values to lateral and perpendicular growth rates, does not allow variation of the effect of time - dependent changes in deposit geometry on the transients. Abyaneh²³⁸ showed that the restrictions imposed by both the hemispherical and right circular cone growth models are removed with the spherical cap nuclei model. A disadvantage of this model, however, is that it does not allow the possibility of investigating the effect of different ratios of perpendicular to lateral growth rates on the transient's characteristics independently of corresponding changes in the contact angle of the nuclei. These problems were overcome by the introduction of a model²³⁹ based on hemispheroidal nucleation and growth. This hemispheroidal model is particularly useful in that by varying the eccentricity of the hemispheroid the model can be applied to the nucleation and growth of needle - like deposits through to the 2D lateral growth of discs.

2.11.5 Overlap of Nuclei

With continued growth, the isolated nuclei and diffusion zone around each nucleus, in the case of diffusion controlled growth, will eventually coalesce. This results in a reduction of the edge area available for incorporation of material into the lattice. At this point the equations describing the growth of the individual nuclei have to be modified to take into consideration this coalescing or overlap of adjacent nuclei. Although the term 'overlap' has been perpetuated over the years to describe the coalescence phenomenon, it should be pointed out that the growth centres do not physically overlap, but rather cease to grow at the points of contact.

Incorporation of overlap into the theoretical models is difficult, in that if a physically realistic treatment is considered then the complexity of the mathematics makes the problem unsolvable, necessitating simplifying assumptions which, in most cases, are physically unrealistic. This is borne out by the attempted solutions to the overlap problem reported in the literature,^{235,237,243,250,256,263} most of which however have been subsequently criticized.

Several methods have been used to describe the overlap phenomenon, the most common of which will be briefly described :

1. One of the most frequently employed methods is that of Avrami,²⁸⁶⁻²⁸⁸ who derived a relationship, referred to as the Avrami theorem, which relates the actual fractional volume, V , transformed via 3D nucleation and growth to its fractional 'extended' volume, V_{ex} , (summation of volume of individual growth centres in the absence of overlap) by

$$V = 1 - \exp(-V_{ex}) \quad (2.4)$$

In the case of 2D nucleation and growth, the above equation can be written as

$$S = 1 - \exp(-S_{ex}) \quad (2.5)$$

where S is the actual area covered by the growth centres and S_{ex} the extended area that would be covered in the absence of overlap, as illustrated in Fig. 2.15. In the derivation of the Avrami theorem, it is assumed that a) distribution of the nuclei is random, b) boundary effects are neglected and c) growth is uniform. No assumptions are made about the shape of the nuclei or about the nucleation law. The Avrami theorem does however take into account the imaginary growth of phantom nuclei within the boundaries of existing growth centres. Phantom nuclei are imaginary growth centres associated with nuclei that would have been activated into growth had they not been absorbed by existing growth centres. As the growth rate of diffusion zones surrounding the nuclei is always larger than the growth rate of the nuclei that originate them, ingestion of active sites by diffusion zones will necessarily precede ingestion by growing nuclei.

2. A second method, proposed by Evans,²⁸⁹ considers the case of 2D nucleation and growth using the following equation

$$S = 1 - \exp(-E_x) \quad (2.6)$$

where E_x is the total number of 2D growth centres expected to pass over a representative point in a 2D plane provided the centres are allowed to grow independently and S is the actual area of the growth centres.

3. A third method for the analysis of nucleation, growth and overlap of 3D growth centres, is based on the Poisson equation. Abyaneh^{235,237,239} reported that this method was particularly suited to nuclei having complex geometries, in that it was more straight forward to calculate the probability p_o that a given point P , lying in a plane a distance y from the substrate is not covered by the growth of individual growth centres in a time t , as given by the Poisson equation

$$p_o = [\exp(-E) E^n] / n! \quad \text{for } n = 0 \quad (2.7)$$

where E is the total number of growth centres expected to pass the point P in time t provided that the centres are allowed to form and grow without interference from other growth centres. Nucleation and growth processes can be described using this equation, provided the following conditions are fulfilled :

1. nucleation and growth must occur randomly by isolated events in a continuum of time.
2. the number of times the event occurs must be known
3. the number of times the event does not occur is inaccessible.

2.11.6 Nucleation Exclusion Zones

A frequently discussed phenomenon in nucleation studies is that the region adjacent to an established growth centre is devoid of new nuclei. Such regions are referred to as nucleation exclusion zones and have been attributed to :

1. ingestion of active sites by existing nuclei or by their diffusion zones.

2. the local deformation of the electric fields around a growing nucleus.^{290,291}
3. zones of reduced concentration of electrodepositing species arise around the growing stable clusters.^{250,259,292,293} The dependence of the fractional surface area covered by nucleation exclusion zones as a function of time accounting for the spread and overlap of such zones has been examined by several authors.^{233,246,256,294}
4. in concentrated electrolytes, the nucleation exclusion zones are zones of reduced overpotential appearing around the growing nuclei as a result of local ohmic drop in the electrolyte.^{290,292,293,295,296}

It is interesting to note that while nucleation exclusion zones are frequently predicted and discussed in the literature, relatively few authors have actually presented visual evidence of their existence. Scanning electron micrographs of nucleation exclusion zone on Fe in alkaline electrolytes will be presented in chapter six.

2.11.7 Electrocrystallisation Models

In this section, the key equations pertaining to main electrocrystallisation models will be presented. The purpose of this section is to show the development of the models and the influence of the various parameters on these models. This summary is significant in that no other published summary of equations is complete in its coverage of both 2D and 3D, diffusion and charge transfer controlled nucleation and growth models. Further, with the exception of some of the work by Bosco and co-workers, all symbols and notations used have been standardised to facilitate comparison of equations.

2.11.7.1 Nucleation and diffusion controlled 3D growth of hemispheres

Astley *et al.*²⁴⁰ derived the potentiostatic current - time transient for a diffusion controlled 3D nucleation and growth process of a single hemispherical nucleus. In terms of linear diffusion, the current density is given by

$$i = \frac{8 n F M^2 c^3 D^{3/2} t^{1/2}}{\rho^2 \pi^{1/2}} \quad (2.9)$$

where M , ρ , c and D are the molar mass, density, concentration and diffusion coefficient of the depositing phase, respectively. The current associated with the growth of an isolated hemispherical nucleus is therefore expected to increase as a function of $t^{1/2}$.

However, for most systems it is highly likely that more than one nucleus will form. Initially it is assumed that the nuclei grow independently of each other, such that at short times the total current is the sum of the individual currents from N nuclei. If nucleation is instantaneous, the current transient can be described by

$$i = \frac{8 N_0 n F M^2 c^3 D^{3/2} t^{1/2}}{\rho^2 \pi^{1/2}} \quad (2.10)$$

and if progressive nucleation prevails, by

$$i = \frac{16 A N_o n F M^2 c^3 D^{3/2} t^{3/2}}{3\rho^2 \pi^{1/2}} \quad (2.11)$$

where A = rate constant for nuclei formation

N_o = total number of active sites

Using eqns. 2.10 and 2.11 a discrepancy between the observed and calculated number of nuclei N_o was found and resulted in Hills *et al.*²⁴¹ proposing that the growth of the nuclei could be more realistically described by hemispherical diffusion to the growing nuclei and the above equations were modified accordingly. For the nucleation and growth of a single nucleus under hemispherical diffusion control, the current is given by

$$i = \frac{n F \pi (2 D c)^{3/2} M^{1/2} t^{1/2}}{\rho^{1/2}} \quad (2.12)$$

In the initial stages of a multiple nucleation event, where the nuclei are growing independently, instantaneous nucleation followed by 3D growth controlled by hemispherical diffusion can be described by

$$i = \frac{n F \pi (2 D c)^{3/2} M^{1/2} N_o t^{1/2}}{\rho^{1/2}} \quad (2.13)$$

and for progressive nucleation by

$$i = \frac{4 n F A \pi (D c)^{3/2} M^{1/2} N_o t^{3/2}}{3\rho^{1/2}} \quad (2.14)$$

However, the above equations were for a nucleus of fixed radius r , resulting in a difference between N_o observed and calculated that was unacceptable, with the rate of growth of N_o nuclei being significantly lower than predicted by eqn. 2.13.^{297,298} Gunawardena *et al.*²⁴² modified eqn. 2.13 to take into account the increase in the radius of the nucleus with time (the 'moving boundary' phenomenon), and for instantaneous nucleation proposed

$$i = \frac{1.04 n F \pi (2 D c)^{3/2} M^{1/2} N_o t^{1/2}}{\rho^{1/2}} \quad (2.15)$$

Although this equation provided a more realistic value for N_o than that of Hills, a discrepancy still existed between the observed and calculated values.

Incorporation of overlap

All previous nucleation theories resulted in the observed number of growth centres being lower than the calculated value. Gunawardena *et al.*²⁴³ proposed that the maximum of the transients was due to the termination of nucleation as a result of the overlap of neighbouring diffusion zones which surround each of

the individual nuclei. Although nucleation occurs on the plane of the electrode, the diffusion of the depositing species extends into the bulk of the electrolyte, resulting in a '2½D' problem. The consequence of this is that the Avrami theorem cannot be applied. Gunawardena *et al.*²⁴³ and Scharifker and Hills²⁴⁶ introduced the simplifying assumption whereby the hemispherical diffusion zones of the individual nuclei are projected onto the plane of the electrode, thereby reducing the problem to two dimensions, to which the Avrami theorem can then be applied. The models also required that new nuclei only form on those parts of the surface that are not covered by diffusion zones. Thus taking into account the overlap of neighbouring nuclei, the current for instantaneous nucleation and 3D growth can be described by

$$i = \frac{n F D^{1/2} c}{\pi^{1/2} t^{1/2}} [1 - \exp(-N_0 \pi k D t)] \quad (2.16)$$

where $k = (8 \pi c M / \rho)^{1/2}$

and for progressive nucleation

$$i = \frac{n F D^{1/2} c}{\pi^{1/2} t^{1/2}} \left[1 - \exp\left(-\frac{A N_0 \pi k' D t^2}{2}\right) \right] \quad (2.17)$$

where $k' = \frac{4}{3} (8 \pi c M / \rho)^{1/2}$

= dimensionless constant affecting the growth rate of diffusion zones

The effect of the exponential term introduced by the Avrami theorem introduces a maximum into the current transient. These equations resulted in an improvement in the correlation between the observed and calculated number of nuclei.

Eqns. 2.16 and 2.17 can be reduced to a more convenient form by using the maxima i_m and t_m to obtain expressions in terms of reduced variables. The dimensionless forms of these equations are given by

$$\frac{i^2}{i_m^2} = \frac{1.2254}{t/t_m} \left\{ 1 - \exp[-2.3367 (t/t_m)^2] \right\}^2 \quad (2.18)$$

for progressive nucleation and growth, and for instantaneous nucleation and growth by

$$\frac{i^2}{i_m^2} = \frac{1.9542}{t/t_m} \left\{ 1 - \exp[-1.2564 (t/t_m)] \right\}^2 \quad (2.19)$$

and are plotted in Fig. 2.16. These dimensionless plots provide a convenient means of evaluating experimental data, particularly when the exact nature of the depositing species is not known eg. for film formation on a corroding substrate.

Scharifker and Mostany²⁵⁰ developed this model further and showed that the current maximum provided

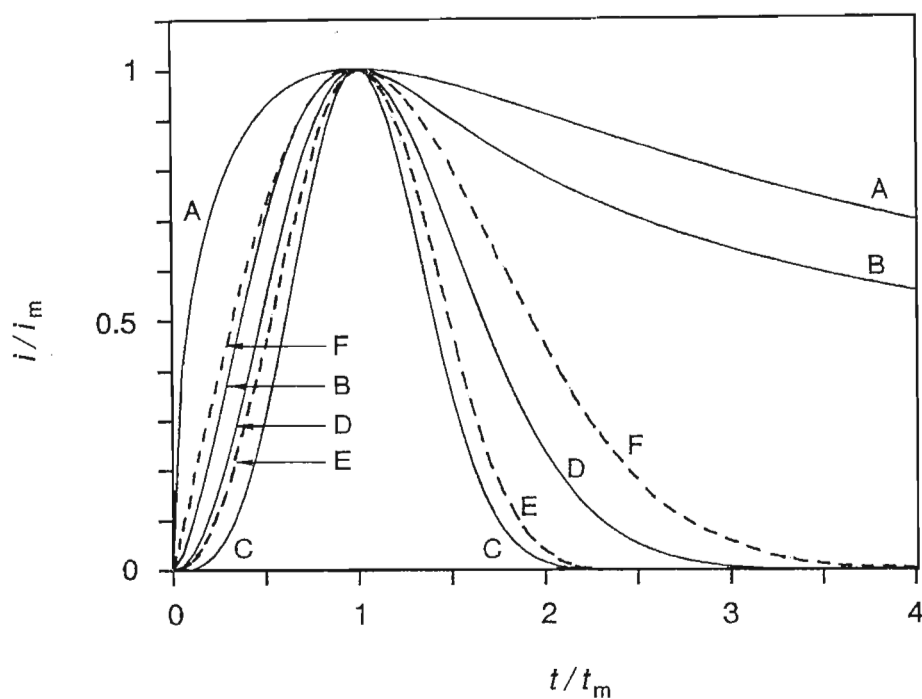


Fig. 2.16 Theoretical dimensionless plots for

- (A) instantaneous nucleation with diffusion controlled 3D growth (*cf* eqn. 2.19)
- (B) progressive nucleation with diffusion controlled 3D growth (*cf* eqn. 2.18)
- (C) progressive nucleation and charge transfer controlled 3D growth leading to passivation (*cf* eqn. 2.40)
- (D) instantaneous nucleation and charge transfer controlled 3D growth leading to passivation (*cf* eqn. 2.41)
- (E) progressive nucleation with charge transfer controlled 2D growth (*cf* eqn. 2.48)
- (F) instantaneous nucleation with charge transfer controlled 2D growth (*cf* eqn. 2.47)

the necessary information for the simultaneous evaluation of the number of active sites on the surface and of the rate of nucleation per active site. The assumptions made were (a) for a given potential, all preferred sites have the same activity towards nucleation and (b) nucleation occurs randomly on a limited number of active sites on the surface, initially available for nucleation. They proposed that the current density to the whole surface is given by

$$i = \frac{n F D^{1/2} c}{\pi^{1/2} t^{1/2}} \left[1 - \exp \{ - N_0 \pi k D [t - (1 - e^{-A t}) / A] \} \right] \quad (2.20)$$

$$\text{where } k = \frac{4}{3} (8 \pi c M / \rho)^{1/2}$$

Eqs. 2.16 and 2.17 are the two limiting cases of this equation. The current described by eqn. 2.20 passes through a maximum enabling the determination of i_m and t_m . N_0 and A can then be calculated by solving the following system of transcendental equations

$$\ln (1 - i_m t_m^{1/2} / a) + x - \alpha (1 - \exp(-x / \alpha)) = 0 \quad (2.21)$$

$$\ln (1 + 2x (1 - (1 - \exp(-x / \alpha)) - x + \alpha (1 - \exp(-x / \alpha))) = 0 \quad (2.22)$$

$$\text{where } x = N_0 \pi k D t_m$$

$$a = \frac{n F D^{1/2} c}{\pi^{1/2}}$$

$$\alpha = \frac{N_0 \pi k D}{A}$$

Further, substituting α into eqn. 2.20, this equation can be rewritten as

$$i = \frac{n F D^{1/2} c}{\pi^{1/2} t^{1/2}} \left[1 - \exp \{ - \alpha [t - (1 - e^{-A t})] \} \right]$$

and by varying the dimensionless parameter α , a range of curves between the limiting cases of instantaneous ($\alpha \rightarrow 0$) and progressive ($\alpha \rightarrow \infty$) nucleation can be obtained, as shown in Fig. 2.17. This result is particularly useful in explaining the discrepancy between the theoretical curves and much of the experimental data published in the literature.

2.11.7.2 Nucleation and charge transfer controlled 3D growth

Fleischmann *et al.*²¹⁴ considered the case where the growth of a 3D nucleus is controlled by the rate of charge transfer. They showed that the chronoamperometric transient for the nucleation and growth of a single hemispherical nucleus could be described

$$i = \frac{2 n F \pi M^2 k^3 t^2}{\rho^2} \quad (2.23)$$

where k = rate constant for nuclei growth

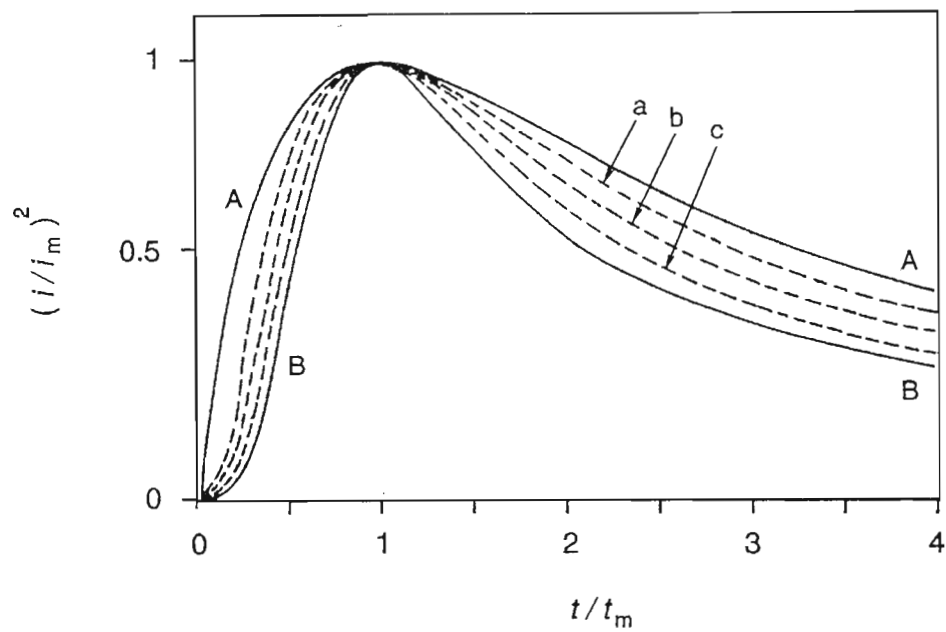


Fig. 2.17 Non - dimensional plots derived from eqn. 2.20 for (A) instantaneous and (B) progressive nucleation and the intermediate curves obtained by varying α , with (a) $\alpha = 0.16$, (b) $\alpha = 0.50$ and (c) $\alpha = 2.0$ (from ref. 250)

For multiple nucleations of independently growing nuclei, the transient for instantaneous nucleation is given by

$$i = \frac{2 n F \pi M^2 k^3 N_o t^2}{\rho^2} \quad (2.24)$$

and for progressive nucleation by

$$i = \frac{2 n F \pi M^2 k^3 A N_o t^3}{3 \rho^2} \quad (2.25)$$

These theoretical equations were shown²³² to correlate well with the experimental current transients for the electrocrystallisation of Ni.

Abyaneh and Fleischmann²³⁷ extended the model to include the nucleation and growth of right circular cones, thereby lifting the 90° contact angle constraint of the hemispherical nuclei. In addition they proposed that growth parallel to the surface takes place with a rate constant k and perpendicular to the surface with a rate constant k' . This model assumes that the rate determining step in the growth of a 3D lattice deposit is the incorporation of material into the lattice. Initially, when the nuclei are growing independently, the current for instantaneous nucleation is given by

$$i = \frac{n F k' \pi M^2 k^2 N_o t^2}{\rho^2} \quad (2.26)$$

and for the progressive case by

$$i = \frac{n F k' \pi M^2 k^2 A t^3}{3 \rho^2} \quad (2.27)$$

where k = rate constant for nuclei growth in the direction parallel to the substrate or rate constant for hydrogen evolution at the edges

k' = rate constant for nuclei growth in the direction perpendicular to the substrate or rate constant for hydrogen evolution on the top surfaces of growth centres

Taking the overlap of neighbouring nuclei into account, eqn. 2.26 becomes

$$i = n F k' \left[1 - \exp \left(\frac{-\pi M^2 k^2 N_o t^2}{\rho^2} \right) \right] \quad (2.28)$$

and eqn. 2.27 becomes

$$i = n F k' \left[1 - \exp \left(\frac{-\pi M^2 k^2 A t^3}{3 \rho^2} \right) \right] \quad (2.29)$$

Abyaneh *et al.*²³⁶ further developed the instantaneous 3D case to include the formation of a second layer of

nuclei ontop of the primary layer. In this model they considered the nucleation and growth of a thin layer of primary centres, followed by the growth of a second layer which nucleated at sites where the primary centres coalesce. The current due to instantaneous nucleation and 3D growth of the primary centres (denoted by a subscript p) is given by :

$$i_p = n F k'_p \left[1 - \exp \left(\frac{-\pi M^2 k_p^2 N_o t^2}{\rho^2} \right) \right] \quad (2.30)$$

After an induction time t_1 , growth of the secondary centres commences. The growth the secondary centres affects the total current by decreasing the current, due to the decrease in the actual area of the primary centres, by an amount

$$i_p = n F k'_p \left[1 - \exp \left(\frac{-\pi M^2 k_s^2 N_o (t - t_1)^2}{\rho^2} \right) \right] \quad (2.31)$$

and by increasing the current due to the growth of the secondary centres (denoted by a subscript s)

$$i_s = n F k'_s \left[1 - \exp \left(\frac{-\pi M^2 k_s^2 N_o (t - t_1)^2}{\rho^2} \right) \right] \quad (2.32)$$

Initially, the total current must also include a term accounting for the initial diminishing background current. Assuming that the fall in the background current is related to the coverage of the primary growth centres, then

$$i_b = i'_b \exp \left[1 - \exp \left(\frac{-\pi M^2 k_1^2 A t^3}{\rho^2} \right) \right] \quad (2.33)$$

where i'_b is the value of the current observed at $t = 0$.

The total current is then given by

$$\begin{aligned} i &= i_b + i_p \quad \text{for } t \leq t_1 \\ i &= i_b + i_p - i_p + i_s \quad \text{for } t \geq t_1 \end{aligned}$$

This model was shown²³⁶ to account for the electrocrystallisation of Zn onto polycrystalline Ag in alkaline electrolytes.

Changing the geometry of the nuclei to spherical cap growth centres, to allow for variation of the effect of changes in growth geometry as a function of time, Abyaneh²³⁸ proposed that for instantaneous conversion of N_o sites to nuclei, the current is given by

$$i = \frac{2 n F \pi M^2 k^3 N_o}{\rho} t \exp \left[\frac{-\pi M^2 k^2 N_o t^2}{\rho^2} \right] \int_0^t \exp \left[\frac{\pi M^2 k^2 N_o u^2}{\rho^2} \right] du \quad (2.34)$$

and for progressive nucleation

$$i = \frac{n F M^2 k^3 A}{\rho} \exp \left[-\frac{\pi M^2 k^2 A t^3}{3\rho^2} \right] \int_0^t (t^2 - u^2) \exp \left[\frac{\pi M^2 k^2 N_o u^2}{3\rho^2} \right] (2u^3 - 3t u^2) du \quad (2.35)$$

where u = time

A disadvantage of this model is that it is not possible to investigate the effect of different ratios of perpendicular to lateral growth rates on the transients independently of corresponding changes in the contact angle. These limitations were overcome by the further development of the model to account for the nucleation and growth of hemispheroid shaped growth centres,²³⁹ which resulted in the current transient for instantaneous nucleation being described by

$$i = 2 n F k \epsilon P_1 t \exp(-P_1 t^2) \int_0^t \exp(P_1 u^2) du \quad (2.36)$$

and for progressive nucleation by

$$i = 3 n F k \epsilon P_2 \exp(-P_2 t^3) \int_0^1 (t^2 - u^2) \exp[-P_2 (2u^2 - 3tu^2)] du \quad (2.37)$$

where ϵ = eccentricity of the hemispheroid

$$P_1 = \frac{\pi M^2 k^2 N_o}{\rho^2}$$

$$P_2 = \frac{\pi M^2 k^2 A}{3\rho^2}$$

During the initial stages of nucleation an $i - t^2$ relationship is predicted for instantaneous nucleation while a $i - t^3$ relationship is predicted for progressive nucleation. The ratio of the peak current to the steady state current is 1.285 and 1.332 for instantaneous and progressive nucleation of hemispheroidal centres, respectively.

2.11.7.3 Nucleation and 3D growth leading to passivation

If the growth of 3D growth centres, under charge transfer control, leads to passivation of the electrode surface the mathematical difficulties in describing the current response become formidable. Armstrong *et al.*²²⁵ provided an approximate solution by imposing the restriction that the species diffusing from the electrode to the surface film growth centres, which is essential for the expansion of these centres, are able to pass only through the uncovered area of the electrode. Thus at $t \rightarrow \infty$, $i \rightarrow 0$ indicating complete passivation of the electrode. For this model, the current for progressive 3D growth leading to passivation is given by

$$i = n F k' \left[1 - \exp \left(\frac{-\pi M^2 k^2 A t^3}{3\rho^2} \right) \right] \exp \left(\frac{-\pi M^2 k^2 A t^3}{3\rho^2} \right) \quad (2.38)$$

and for the instantaneous case by

$$i = n F k' \left[1 - \exp \left(\frac{-\pi M^2 k^2 N_o t^2}{\rho^2} \right) \right] \exp \left(\frac{-\pi M^2 k^2 N_o t^2}{\rho^2} \right) \quad (2.39)$$

The dimensionless form of eqn. 2.38 is

$$\frac{i}{i_m} = 4 * \left[1 - \exp \left(-0.693 \frac{t^3}{t_m^3} \right) \right] \exp \left(-0.693 \frac{t^3}{t_m^3} \right) \quad (2.40)$$

and of eqn. 2.39 is :

$$\frac{i}{i_m} = 4 * \left[1 - \exp \left(-0.693 \frac{t^2}{t_m^2} \right) \right] \exp \left(-0.693 \frac{t^2}{t_m^2} \right) \quad (2.41)$$

These last two equations are plotted as curves (C) and (D), respectively, in Fig. 2.16.

2.11.7.4 Nucleation and charge transfer controlled 2D growth^{224,226,237,268}

The formation of monolayer deposits can be considered as the nucleation, growth and eventual overlap of individual growth centres or nuclei. These may be regarded as discs one atom or one molecule thick. If it is assumed that the rate determining step in the electrocrystallisation process is the incorporation of atoms or molecules at the expanding periphery of the growth centre, then the current to an isolated growth centre is given by

$$i = \frac{2 n F \pi h M k^2 t^2}{\rho} \quad (2.42)$$

where h = height of the nucleus

As it is unlikely that only one nucleus will form, the above equation can be rewritten taking into account the nucleation and growth of N_o isolated growth centres. If the nucleation is instantaneous, the current density is given by

$$i = \frac{2 n F \pi M h k^2 N_o t}{\rho} \quad (2.43)$$

while if the nucleation is progressive by

$$i = \frac{n F \pi M h k^2 A N_o t^2}{\rho} \quad (2.44)$$

In this model it is assumed that while the nuclei may interact with each other, they don't react with the boundary. Therefore with continued growth, overlap of neighbouring nuclei will start to occur. This overlap can be taken into account by invoking the Avrami theorem, with the result that eqn. 2.43 becomes

$$i = \frac{2 n F \pi M h k^2 N_o t}{\rho} \exp \left[-\frac{\pi M^2 N_o k^2 t^2}{\rho^2} \right] \quad (2.45)$$

for instantaneous nucleation, and for progressive nucleation eqn. 2.44 becomes

$$i = \frac{n F \pi h M k^2 A N_o t^2}{\rho} \exp \left[-\frac{\pi M^2 A N_o k^2 t^3}{3 \rho^2} \right] \quad (2.46)$$

which reduced to the dimensionless form become

$$\frac{i}{i_m} = \frac{t}{t_m} \exp \left[-0.5 \left(\frac{t^2 - t_m^2}{t_m^2} \right) \right] \quad (2.47)$$

for the instantaneous mechanism and

$$\frac{i}{i_m} = \frac{t^2}{t_m^2} \exp \left[-0.66 \left(\frac{t^3 - t_m^3}{t_m^3} \right) \right] \quad (2.48)$$

for the progressive mechanism, and which are plotted in Fig. 2.16 as curves (F) and (E) respectively.

2.11.7.5 2D electrocrystallisation coupled to diffusion in the electrolyte with and without simultaneous metal substrate dissolution

Barradas and Bosco²⁵⁵ considered 2D electrocrystallisation coupled to diffusion in the electrolyte with and without simultaneous metal dissolution from the electrode. They considered three possible couplings, viz.

1. Diffusion in solution coupled to instantaneous nucleation and 2D growth.

This is the classical electrocrystallisation experiment where dissolution is not involved, and focuses on the diffusion of cations and anions in solution with their instantaneous concentration near the surface coupled to the rate of electrocrystallisation. The transients described by this model start at the origin and exhibit a single maximum.

An assumption Barradas and Bosco make in all three models is the use of a single average or effective concentration for the dissolving / diffusing species in solution near the electrode surface.

2. Nucleation and 2D growth coupled to dissolution and diffusion of metal ions.

Metal substrate dissolution is assumed to occur only through the film free surface and diffusion of these metal ions into solution with the rate of nucleation being determined by the instantaneous concentration of

metal ions at the electrode surface.

In this model the current is solely attributable to the dissolution step, with the nucleation and growth processes making no contribution. For both models 2 and 3 the total charge passed is not equal to the charge of a monolayer but is a function of experimental variables such as potential.

3. Nucleation and 2D growth, and dissolution of metal ions through the free electrode surface and their diffusion into solution.

In this model there is no active coupling between phase formation and dissolution - diffusion. The overall current in this model is a linear combination of the simple nucleation and growth current and that due to the dissolution - diffusion process.

2.11.7.6 Adsorption - nucleation models^{264-266,297}

Bosco and Rangarajan²⁶⁴ were the first to propose an adsorption - nucleation model. This was further developed by Arulraj and Noel²⁶⁵ and later Bhattacharjee and Rangarajan²⁶⁶ refined these previous models^{264,265} and presented a generalised model.

There are two possibilities of a combined adsorption - nucleation model :

1. Surface sites uniformly accessible to both processes

In this model it is assumed that (a) the surface already covered by a nucleative process would not be available for adsorptive processes and (b) the surface covered by adsorptive processes would not be available for nucleative processes. While both Bosco and Rangarajan²⁶⁴ and Arulraj and Noel²⁶⁵ incorporated the first assumption into their models, only Arulraj's model contained the second assumption. This was in fact a criticism of theirs of Bosco's model.

2. Non - competitive approach

In this model the adsorptive process takes place on a fraction of the total surface area with the remaining surface being covered by the nucleation process at a different rate.

Bosco and Rangarajan²⁶⁴ proposed a model incorporating adsorption, nucleation and growth, and which involved nucleative phase growth via direct incorporation and adsorptive discharge of metal ions on the free surface. The model consisted of firstly, activation of the nuclei and their growth by direct incorporation via the discharge of the metal ion at the lattice sites at the periphery of the growing nuclei. This was followed by an adsorption - desorption step depending on the availability of sites not occupied by the growing nuclei, with the possible involvement of partial electron transfer. A parallel process of nuclei growth assisted by adatom incorporation was ignored. The current for the instantaneous case of the general model is given by

$$i(t) = 2 q_{mL} \beta_1 t \exp(-\beta_1 t^2) + q_{mA} K_f' \left[\exp(-\beta_1 t^2) - \mu \exp(-\mu t) \int_0^t \exp(-\beta_1 \tau^2 + \mu \tau) d\tau \right] \quad (2.49)$$

and for the progressive case by

$$i(t) = 3 q_{mL} \beta_2 t^2 \exp(-\beta_2 t^3) + q_{mA} K_f' \left[\exp(-\beta_2 t^3) - \mu \exp(-\mu t) \int_0^t \exp(-\beta_2 \tau^3 + \mu \tau) d\tau \right] \quad (2.50)$$

where

$$\begin{aligned} \beta_1 &= g N_o (\gamma / n F)^2 K \\ \beta_2 &= g N_o A (\gamma / n F)^2 K^2 \\ N_o &= \text{number of active sites per unit area} \\ \gamma &= \text{molar volume} \\ g &= \text{interaction parameter} \\ A &= \text{potential dependent rate parameter} \\ \mu &= K_f' + K_r' \\ q_{mL}, q_{mA} &= \text{charge transferred for adsorption and for incorporation into the lattice} \\ K_f', K_r', K_L &= \text{rate constants for adsorption, desorption and lattice growth} \end{aligned}$$

For chronoamperometric transients Bosco and Rangarajan presented the following expression, in terms of dimensionless parameters, for instantaneous nucleation

$$I = \exp(-D_1 T^2) (2 D_1 T + G) - G \exp(-T) \int_0^T \exp(z - D_1 z^2) dz \quad (2.51)$$

and for progressive nucleation

$$I = \exp(-D_2 T^3) (3 D_2 T^2 + G) - G \exp(-T) \int_0^T \exp(z - D_2 z^3) dz \quad (2.52)$$

where

$$\begin{aligned} I &= i / (q_{mL} \mu) \\ Q &= q / q_{mL} \\ T &= \mu t \\ D_1 &= \beta_1 \mu^2 \\ D_2 &= \beta_2 \mu^3 \\ G &= (q_{mA} / q_{mL}) [K_f' / (K_f' + K_r')] \end{aligned}$$

The transients described by these equations exhibit an initial falling current which reaches a minimum then increases to a maximum before subsequently decreasing again. In the above expressions, when $D_1, D_2 \rightarrow 0$ falling transients reflecting complete adsorption - desorption control are obtained, while if $D_1, D_2 \rightarrow \infty$ nucleation and growth is the dominant process resulting in the absence of the minimum in the transients.

The shape of the current transients generated by eqns. 2.51 and 2.52 was shown²⁶⁴ to vary widely, however of particular interest in the present work, was that certain of the current transients showed a similar form to those obtained experimentally for Fe (cf chapter six) and Fe18Cr alloy⁵⁰ in alkaline electrolytes. However, as the above expressions contain a number of variable parameters which are difficult to link to

experimentally determinable values, 'analysis' of the experimental current transients, in terms of the above expressions, would be no more than a curve fitting exercise. Further, in simulating an experimental current transient it is highly likely that several different adsorption - nucleation couplings would give rise to the same transient form (a fact also commented on by Bosco and Rangarajan). Thus the use of these expressions as diagnostic criteria for the evaluation of transients is questionable.

The above model by Bosco and Rangarajan²⁶⁴ has been modified by Bhattacharjee and Rangarajan²⁶⁶ who considered the coupling of an adsorption - desorption process with one phase growing irreversibly. The model can be described as

- (a) firstly the activation of the nuclei and their growth by direct incorporation via discharge of the metal ion at the available free sites ie. along the kinks and the edges of the growing nuclei.
- (b) an adsorption - desorption step coupled with the irreversibly growing phase. This process interferes with the growth process by blocking some sites and thus reducing the number of free sites available for growth. The possible parallel path of nuclei growth aided by adatom incorporation was ignored, and only direct incorporation considered.
- (c) the amount of charge transfer associated with the contribution of the above two processes (a) and (b) to the total current at a particular instant may be different depending on the rate constants and on parameters such as concentration and potential.

Bhattacharjee and Rangarajan²⁶⁶ derived the following expression, expressed in terms of non - dimensional parameters, to describe the current transients for instantaneous nucleation

$$I = (1 - S - X) 2D_1 T + fQ (1 - S) - fX \quad (2.53)$$

and for progressive nucleation

$$I + (1 - S - X) 3D_2 T^2 + fQ(1 - S) - fX \quad (2.54)$$

where $f = q_{mA} / q_{mL}$

$$Q = K / \mu$$

$$T = \mu t \quad (T \text{ is not defined in ref. 266, therefore it is assumed to be the same as } T \text{ defined in ref. 264})$$

$$\beta_1 = \lambda_o N_o K_L^2$$

$$\beta_2 = (\lambda_o N_o A K_L^2) / 3$$

$$\lambda_o = \text{proportionality constant related to the packing density and geometrical factors}$$

$$K_L = \text{rate of radial growth of the ordered phase}$$

$$A = \text{potential dependent parameter which remains constant for the potentiostatic case}$$

$$S \text{ and } X = \text{fractions of areas covered by adsorption and growth phases, respectively}$$

$$q_{mA} \text{ and } q_{mL} = \text{related to the charge transfer associated with each component contributing to the growth and adsorption - desorption process}$$

$$K_f' \text{ and } K_r' = \text{adsorption and desorption rate constants which are independent of } X \text{ but}$$

dependent on the interfacial potential.

with other symbols as per those defined for eqn. 2.52.

Bhattacharjee and Rangarajan²⁶⁶ demonstrated the effect of varying D_1 and D_2 (parameters involved in the growth rates), Q (adsorption - desorption rate) and of f (the amount of charge transfer associated with the two processes). The influence of these variations results in the transients generally showing a minimum and a maximum, similar to the experimental transients that will be presented in chapter six. However, the use of their model is difficult to assess due to the lack of data for the above equations. Therefore comparison of the experimental data with the equations of Bhattacharjee and Rangarajan will, at best, again be merely an exercise in curve fitting.

Bhattacharjee and Rangarajan²⁶⁶ also derived equations to describe the coupling of an adsorption - desorption process with two or more irreversibly growing components. This situation would be applicable to the formation of oxides on Fe and stainless steel alloys where deposition of two or more metal oxide species is likely to occur. This model would also be applicable to metal dissolution and passivation through inert layer formation. Three cases of this model were considered :

1. Both processes are instantaneous, as described by

$$I = (fQ_1 + 1)(1 - S_1 - S_2) 2T \quad (2.55)$$

where S_1 and S_2 are the fraction of area covered by process 1 and process 2 respectively.

$$f = q_{m1}/q_{m2}$$

$$Q_1 = \beta_1/\beta_2$$

$$I = i / (q_{m2} \beta_2^{1/2})$$

$$T = \beta_2^{1/2} t$$

β_1 and β_2 are defined as $(dS_{ix}/dt) = 2\beta_i t$; $i = 1, 2$.

2. Both processes progressive, as described by

$$I = (fQ_3 + 1)(1 - S_1 - S_2) 3T^2 \quad (2.56)$$

where $f = q_{m1}/q_{m2}$

$$Q_3 = \beta_1/\beta_2$$

$$I = i / (q_{m2} \beta_2^{1/3})$$

$$T = \beta_2^{1/3} t$$

β_1 and β_2 are defined as $(dS_{ix}/dt) = 3\beta_i t^2$; $i = 1, 2$.

3. Process 1 instantaneous and process 2 progressive, as described by

$$I = (2fQ_2 + 3T)(1 - S_1 - S_2) T \quad (2.57)$$

where $f = q_{m1}/q_{m2}$

$Q_2 = \beta_1/\beta_2^{2/3}$

$I = i / (q_{m2} \beta_2^{2/3})$

$T = \beta_2^{1/3} t$

β_1 and β_2 are defined as $(dS_{1x}/dt) = 2\beta_1 t$ and $(dS_{2x}/dt) = 3\beta_2 t^2$

The transients described by these equations start at zero current then increase to the single maximum, subsequent to which the current decreases. This is contrary to the experimental transients (cf chapter six) which showed an initial decrease in the current density followed by an increase to a single maximum.

2.11.8 Criticism of Nucleation Models

From the point of view of the present study, the main criticism of the existing electrocrystallisation theories is their inability to completely describe surface film formation on an oxidising substrate. While existing theories involve metal ions, anodic oxide formation involves metal, oxide and hydroxide species. In addition the solid state properties of the oxide film which will influence the growth of the film also have to be taken into account. However, incorporation of these aspects and the development of a realistic model will only result, at present, in intractable mathematics. In this section, some of the shortcomings of the more frequently used electrocrystallisation models will be presented.

2.11.8.1 Armstrong, Fleischmann and co-workers

Armstrong, Fleischmann and Thirsk proposed models for 3D²²⁵ and 2D²²⁴ nucleation with charge transfer controlled growth.

Armstrong and Harrison²¹⁵ criticized the 3D nucleation model²²⁵ when overlap effects were included, as unrealistic since it differed from the 2D model only in that it did not limit the final size of the nuclei. This resulted in the model failing to predict transients with multiple maxima due to the formation of individual atom layers.

The model of Armstrong *et al.*²²⁵ was also criticized by Deutscher and Fletcher²⁵⁹ for "naive assumptions about the time varying number of nuclei" in the light of their proposed model^{259,273} which incorporated the more realistic concept of nucleation rate dispersion which is based on the premise that nucleation occurs at different rates at different active sites on the electrode surface, due to the variation of the specific surface energy over the electrode surface.

Bosco and Rangarajan²³³ criticized the equation of Armstrong *et al.*²²⁵ for nucleation and 3D growth leading to passivation (cf eqn. 2.38) for overestimating the number of 'ghost centres' (centres with imaginary radii) which were included in the evaluation of the true area of nucleated sites. They²³⁴ also pointed out

that the Armstrong model started with a differential form of the current which is only valid for constant growth rates. As Armstrong's passivation model was formulated as having a constant horizontal growth rate while the vertical rate was assumed to decay with time, the time - dependence that was crucial to the model had therefore not been correctly accounted for. This resulted in Armstrong's equation being incomplete. As corrected by Bosco and Rangarajan²³⁴ Armstrong's equation becomes

$$i = \frac{3 n k' F \pi M^2 k A t^3}{\rho^2} \exp \left[\frac{-4 \pi M^2 k^2 A t^3}{3 \rho^2} \right] + n F k' \left[1 - \exp \left(\frac{-\pi M^2 k^2 A t^3}{3 \rho^2} \right) \right] \exp \left(\frac{-\pi M^2 k^2 A t^3}{3 \rho^2} \right) \quad (2.58)$$

Armstrong's equation (eqn. 2.38) only contained the second term of the above equation. In the dimensionless form, the above equation can be rewritten as (cf eqn. 2.40)

$$\frac{i}{i_m} = 5.359 \left[1 - \exp \left(-1.592 \frac{t^3}{t_m^3} \right) \right] \exp \left(-1.592 \frac{t^3}{t_m^3} \right) + 14.332 \frac{t^3}{t_m^3} \left[\exp \left(-6.367 \frac{t^3}{t_m^3} \right) \right] \quad (2.59)$$

However, the present author found that Bosco and Rangarajan's correction did not yield a reasonable dimensionless plot. Correspondence with Rangarajan regarding this matter proved futile.

2.11.8.2 Gunawardena, Hills, Montenegro and Scharifker

Gunawardena *et al.*²⁴³ proposed a model for nucleation and 3D growth under hemispherical diffusion control, incorporating the overlap of neighbouring nuclei and their associated diffusion zones resulting in semi - infinite linear diffusion over the entire electrode.

Deutscher and Fletcher²⁵⁹ criticized Gunawardena's model²⁴³ by showing that it contained internal inconsistencies, for example, diffusion layer thickness determined at long times, should be the same for both instantaneous and progressive models; this result was not obtained using Gunawardena's equations. Sluyters - Rehbach *et al.*²⁵⁶ have also criticized these inconsistencies. Further, Deutscher and Fletcher pointed out that the Gunawardena model doesn't take into account the occlusion of active sites by diffusion zones of the growing nuclei. This criticism however is unfounded since Gunawardena invoked the Avrami theorem to account for the overlap of nuclei, which takes the occlusion of active sites into account.

2.11.8.3 Scharifker and co - workers

One of the main criticisms of Scharifker's model²⁴⁶ was the approximation of the diffusion fields surrounding the nuclei. Scharifker considered the equivalent area of plane surface towards which diffuses, by linear diffusion, the same amount of material that would be transferred through spherical diffusion to a hemispherical growth centre. This reduced the mass transport from spherical co - ordinates around each growth centre to linear co - ordinates. As the randomly distributed nuclei grew, the projected diffusion fields overlapped, and since the projections resulted in a 2D problem, the Avrami theorem could be invoked to calculate the actual surface area covered by diffusion zones.

The assumption that the initial total current could be equated with the amount of linear diffusion to an electrode has been questioned by several researchers leading to models using Scharifker assumptions to be found to be in error by Sluyters - Rehbach *et al.*,²⁵⁶ Deutscher and Fletcher,²⁵⁹ Jacobs,²⁶⁰ Mulder *et al.*²⁶¹ and Bobbert *et al.*²⁵⁷

Bobbert *et al.*²⁵⁸ published their solution to the problem of spherical diffusive flow to a growing sphere shielded by a plane, which did not require the unsatisfactory assumptions included in the Scharifker model. They further showed²⁵⁷ that the concept of diffusion zones surrounding a growing nucleus is mathematically inconsistent and proposed alternative theories to describe the observed behaviour. The current transient behaviour of their model was however found to be relatively similar to that of Scharifker's. Greef, Bobbert and Vlieger²⁶² further showed that while experimental transients could often not be accounted for theoretically, excellent agreement was obtained between their ellipsometrical data and electrochemical transients, with the ellipsometry allowing the determination of the nuclei density and the size distribution of the nuclei.

Scharifker proposed that the number of nuclei could be determined directly from the current transient, however, it has been reported^{260,280,281} that the calculated values are orders of magnitude smaller than that observed directly using the SEM. This is due to the projection of the hemispherical diffusion zones of individual nuclei onto the plane of the electrode, which lead to unrealistically large circular diffusion fields and therefore to an erroneously low value for the calculated number of nuclei. This fact has been pointed out by several researchers.^{260,261}

Scharifker's model also assumed that any other nucleus appearing in a projected diffusion field did not contribute to the current transient. However, the validity of this assumption is questioned on the basis of another assumption that nuclei growth takes place under diffusion control at nuclei of all sizes. Therefore if a nucleus develops in the projected diffusion zone of an established nucleus, it will establish its own diffusion zone which will be influenced by the diffusion zones of neighbouring nuclei. Wijenberg *et al.*²⁷² also make this assumption. Thus evaluation of the contribution of each nucleus to the current complicates the mathematics considerably.

Despite all the criticism of Scharifkers model, it should be noted that for certain experimental systems, good correlation between the experimental data and theoretical transients has been demonstrated^{242,247,299,301} eg. nucleation and growth of Cu on polycrystalline palladium.³⁰¹

2.11.8.4 Bosco and Rangarajan

Bosco and Rangarajan²³³ generalised the model of Armstrong *et al.*²²⁵ to include time dependent nucleation and growth rates, which they further generalised to include any nucleation rate law with either charge transfer or diffusion control.²³⁴

In order to invoke the Avrami overlap theorem, Bosco and Rangarajan used a similar approach to that of Armstrong *et al.*²²⁵ by considering the overlap of nuclei at a particular height h from the substrate as a horizontal section through the nuclei of width dh . This reduced the problem to two dimensions, with discs of height dh and radius r_x . Bosco and Rangarajan presented the following general equation to describe the nucleation and growth

$$i = (n F \rho / M) (dS / dt)$$

where S is the true area of coverage.

They expanded this equation into four special cases, viz. instantaneous and progressively nucleated with constant rate of growth and with diffusion controlled growth. These models had a fixed hemispherical geometry due to their being based on a single growth rate. This was then developed to "two - growth rate" models which allowed different geometries for different choices of the rates.²³⁴

Sluyters - Rehbach *et al.*²⁵⁶ showed that Bosco and Rangarajan's equation for diffusion controlled growth did not describe the transients at longer times. Abyaneh and Holvorsen²⁸⁴ showed that Bosco and Rangarajan's prediction²³³ that the $i - t$ transients for progressive nucleation and constant rate of growth will have two maxima and one minimum was incorrect, as there is in fact only one maximum.

It is also interesting to note that while most other workers in this field of research present their relationship describing the transients in the "conventional - time - honoured - form" of Armstrong, Fleischmann and Thirsk²²⁵ thereby readily allowing comparisons and enabling evaluation, Bosco and Rangarajan present their relationships in an obtuse form that usually requires a fair amount of mathematics and necessary assumptions, which may well differ from those made by Bosco and Rangarajan, before the relationships are obtained in a useful form.

*Adsorption - nucleation model*²⁶⁴

Arulraj and Noel²⁶⁵ criticized the adsorption - nucleation model of Bosco and Rangarajan;²⁶⁴ although the latter model incorporated the assumption that if the surface is already covered by a nucleative process it would not be available for adsorptive process, the reverse situation was not considered. Also, using Bosco

and Rangarajan's model²⁶⁴ they encountered difficulties while attempting to simulate the linear sweep voltammetric response of the model, and eventually attributed these difficulties to an incorrect mathematical approximation used by Bosco and Rangarajan.

2.11.8.5 Deutscher and Fletcher

Deutscher and Fletcher's model²⁵⁹ introduced the concept of nucleation rate dispersion which proposed that nucleation occurs at different rates at different active sites on the electrode surface, due to the variation of the specific surface energy over the electrode surface. While this model provides a more realistic approach to nucleation, it was developed using a microelectrode assembly to eliminate the problem of overlap of adjacent nuclei. The applicability of the model to conventional electrodes and electrochemical systems where overlap of nuclei and their diffusion zones occurs, must still be tested. Also their theory is for the deposition of metals from solution onto a foreign inert substrate. For oxide film formation, this model needs to be developed such that the substrate supplies the metal ions due to substrate dissolution.

Mirkin and Nilov²⁶³ question the equivalence of the microelectrodes used by Deutscher and Fletcher, to a planar macro electrode with respect to the nucleation process, since they propose that the diffusion flux towards microelectrodes will be larger than the flux towards an analogous part of a plane electrode. The larger the current density, the greater the adatom concentration which will in turn influence the nucleation rate. They also question the extent of the boundary effect influence on the nucleation and growth, and the inversion procedure used and conclude that it is doubtful whether Deutscher and Fletcher have eliminated the overlap problem.

Milchev²⁹⁶ criticized Deutscher and Fletcher's model²⁵⁹ suggesting that the current densities used by Deutscher and Fletcher to estimate the ion transfer resistance are too low.

2.11.8.6 Pritzker³⁰²

Mirkin and Nilov²⁶³ criticize Pritzker's model³⁰² (for growth of a single nucleus in the potentiodynamic regime) in that the anodic and cathodic currents are a thousand times greater than those calculated by their equation. They point out that as Pritzker doesn't state the bulk concentration (or units of concentration) that unacceptably high values for the radius of the nucleus and the total faradaic current may result. In addition, Mirkin and Nilov²⁶³ criticize his generalising conclusion that the influence of the radius of the nuclei on the form of the calculated voltammogram is negligibly small, based on the parameters used by Pritzker.

2.12 PREFILM

The presence or absence of an initial, and unintentional, surface film on the electrode prior to any

electrochemical treatment is a phenomenon that, although discussed in the literature, is frequently glossed over. An initial film of this nature will be referred to as a prefilm, in this work.

The lack of consensus regarding the presence or absence of a prefilm is complicated by the varied experimental conditions and electrode pretreatments used, as is evident from the results reported below. The significance of a prefilm in electrocrystallisation studies will be its influence on the nucleation process, eg. incomplete coverage of the electrode by the prefilm, inhomogeneities, defects, discontinuities, and stability of the prefilm will influence the number and activity of the active sites available for nucleation. In addition, depending on the thickness of the prefilm, the potential at the growth centre will be less than the applied potential due to a potential drop across the film.

Hottenhuis *et al.*,²⁷⁵ investigating silver nucleation on a single silver crystal reported the presence of an 'impurity blanket', ie. the prefilm. They proposed that if the electrode is partly covered by the prefilm, nucleation will occur on the uncovered surface, however if the electrode is completely covered by the prefilm, then it is the places at which the prefilm is thinner that will be 'punctured' when a high enough potential is applied, and nucleation will occur at these points.

Investigating the electrodeposition of Hg onto Pt, Milchev *et al.*³⁰³ concluded that whatever reactions take place on the Pt substrate the induced changes in the surface energetic state have to be related mainly to the **number** of active sites and not to their activity with respect to the process of nucleus formation. The explanation given for this was that the active sites for nucleation are holes or some other structural defect of the coverage where the nuclei of the new phase are in direct contact with the original metal surface. The activity of the active sites will be relatively similar and will be completely independent of the prefilm layer.

Deutscher and Fletcher²⁷³ reported that nucleation of the species of interest on top of impurities (ie. a prefilm) results in a significant increase in the number of nuclei, and that the nuclei are smaller than those formed in the absence of impurities. They also predicted the effect of adsorption on the specific surface energy and nucleation rate; these predictions will be discussed later, as they are validated by the experimental data presented in this thesis.

Graham and co-workers^{144,304} reported that the presence of a prefilm, formed due to an electropolishing pretreatment, influences the structure and composition of oxides subsequently formed. Not unexpectedly they reported that different electrode pretreatments influenced the nature of the prefilm which in turn influenced the subsequent oxidation rate of the substrate electrode, with the rate increasing for the following series :

mechanical polishing < electropolishing + vacuum annealing < electropolishing < H₂ reduction of prior film

Kruger³⁰⁵ performed a precise series of ellipsometry experiments on Fe in 0.1M NaNO₂ to distinguish

between the adsorption and solid film theories of passivation, i.e. whether passivation processes involved the adsorption of an oxygen film, the growth of a three dimensional oxide or a combination of both, or a transformation of an adsorbed film into an oxide. He found that if the electrolyte was saturated with air, a film (20\AA) formed instantaneously on introduction of the electrode to the electrolyte. This film then subsequently dissolved and a new film started to form on passivation of the electrode. If the electrolyte was saturated with oxygen, a film again formed instantaneously which did not dissolve but continued to grow to approximately 40\AA , at which point the electrode was completely passivated. Using an argon deaerated electrolyte an extremely thin film ($<5\text{\AA}$) formed which, unlike the prefilms formed in air and oxygen saturated electrolytes, was not passivating and rapidly dissolved. Melendres,⁴⁷ using SERS, however found that the surface of Fe in aerated 5M KOH and 0.15M NaCl was always covered by a film, possibly $\alpha\text{-FeOOH}$, even after cathodic polarisation at -1.3V .

Bockris *et al.*,³⁰⁶ Gojkovic *et al.*,³⁰⁷ Goetz *et al.*,³⁰⁸ Tsuru *et al.*³⁰⁹ and Jovancicevic *et al.*⁵⁷ using Fe in pH 8.4 deoxygenated borate buffer reported that the electrode was free from oxide if prepared under specific conditions. The same result were also reported for Fe in 0.04M NaOH and saturated Ca(OH)_2 (ref. 86) and for mild steel (99% Fe) in 1 - 19M NaOH (ref. 310). It is interesting to note that different preparation procedures were employed by each of these groups. Bhardwaj *et al.*¹¹⁴ using scanning tunneling microscopy to study film formation on Fe in borate buffer pH 8.4 (not deaerated) showed that oxides formed at potentials anodic to -0.991V could be reduced at -0.991V producing a completely oxide free surface. Haupt and Strehblow³⁴ studying the formation and reduction of passive films on Fe in 1M NaOH also reported an oxide /hydroxide free surface, which could be demonstrated by the absence of certain peaks from the first sweep of a cyclic voltammogram, as shown in Table 2.1, CV(a). The same findings were reported by Larramona and Gutiérrez⁴⁹ for Fe in 0.1M NaOH (*cf* in Table 2.1, CV(m)) and by Wieckowski and co - workers^{42,43} (*cf* CV(g), Table 2.1) for Fe in 1M NaOH.

For stainless steels, Frankenthal¹⁴⁶ reported the absence of any prefilm on a Fe24Cr alloy in 1M H_2SO_4 , during the time the electrode was held at the corrosion potential. The electrode had been cleaned by a cathodic reduction and anodic dissolution regime. In agreement with this result, Mitrovic - Scepanovic *et al.*¹⁴⁴ investigating Fe26Cr in H_2SO_4 , pH 2, reported the formation of a $\approx 20\text{\AA}$ oxide film on the electrode after electropolishing, which could be completely removed by an initial cathodic reduction procedure.

Contrary to these results, Harrington and co - workers^{311,312} proposed that a surface film was present on an iron or stainless steel electrodes brought into contact with oxygen and/or water. Ferreira *et al.*¹⁰⁶ using SERS to investigate stainless steel 316 in deaerated 0.15M NaCl proposed that a film is initially present on the electrode surface due to atmospheric corrosion (although it should be noted that the electrodes were only polished the electrode down to a 600 grit finish). They reported that this film consisted of FeOOH , Cr_2O_3 and Cr(OH)_3 , and was very difficult to reduce electrochemically and was still present after holding the electrode at -1.35V for 1hr. Ferreira and Dawson³¹³ showed that the equilibrium potential for this

initial oxide formation was -1.4V , which is comparable to the equilibrium potential of chromium oxide. These results are supported by Haupt and Strehblow³⁵ who, investigating the oxide film on FeCr alloys, concluded that Cr_2O_3 and $\text{Cr}_2\text{O}_3 / \text{Fe}_2\text{O}_3$ oxide cannot be reduced electrochemically in alkaline electrolytes, with complete reduction of the Fe content only not even being possible.

The presence or absence of a surface film can be determined by performing a scratch chronoamperometric experiment. In this thesis a scratch experiment, using a rotating electrode, is proposed. The rationale behind the scratch experiment is that scratching is not instantaneous, and therefore if film formation is spontaneous (ie. a prefilm) or if the electrode is held at a potential at which a surface film formation occurs, then as the scratch is generated the start of the scratch will have begun to repassivate before the end of the scratch has been generated. However, if the electrode is rotated at progressively faster rotation rates a point should eventually be reached at which scratching is effectively instantaneous. As shown schematically by curve (a) in Fig. 2.18, with increasing rotation rate, the bare surface area will increase (for as long as the diamond is in contact with the electrode) and hence the current will increase. This has been verified experimentally.³¹⁴ However, in the absence of a surface film the current will be independent of rotation rate, as given by curve (b) in Fig. 2.18.

The merits of scratch experiments have recently been debated³¹⁵⁻³¹⁹ with regard to the contribution to the current transient of the surrounding unscratched electrode area. In addition, depending on the potential of interest the background current from the unscratched surface may be such as to mask the scratch transient. To eliminate these two problems it is recommended that the electrode surface is masked, eg. by applying a thin coat of electrically insulating, self etch paint thereby ensuring that the current response is exclusively from the scratch scar.

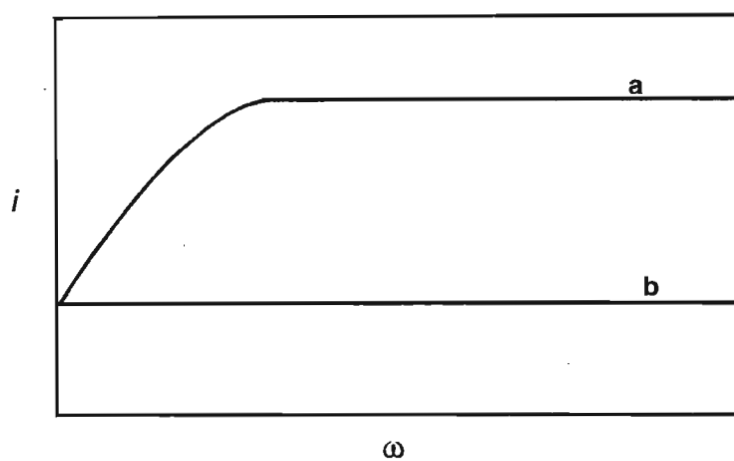


Fig. 2.18 Schematic representation of the effect of mechanically scratching an electrode (a) covered by an oxide film and (b) which is oxide free.

CHAPTER THREE

EXPERIMENTAL

3.1 SAMPLES

The working electrodes used in this investigation were made from Johnson Matthey spectroscopic grade iron (99.9% purity), pure chromium (99.5%), pure molybdenum (99.9%) and from various stainless steels, whose composition is given in Table 3.1.

The Fe18Cr, Fe20Cr and Fe23Cr alloys were prepared at ISCOR (South African Iron and Steel Corporation) by induction melting (at 1600°C) of the raw materials in an argon atmosphere and then centrifugally casting the alloy in a copper mould. The alloys were then heat treated by placing each in an Al₂O₃ crucible and holding it at 800°C for two hours, after which they were air cooled. After removal of the oxide the alloys were cold rolled (deformation approximately 10%).

The Fe16Cr alloy was prepared at ISCOR. After casting the alloy was preheated to 1200°C and held at this temperature for one hour per 25mm of thickness. The steels were then air cooled and rolled to a final gauge of approximately 5mm.

The 444, 4732 and 4733 stainless steels were supplied by the Department of Metallurgy, University of the Witwatersrand, who had obtained the 444 from Van Leer & Co. Ltd., (manufactured by the Nippon Steel Company, Japan) in the form of a rolled sheet 0.45mm thick. Since it was a commercial alloy no preparation details were available. A sample of the 444 was cast into a button at ISCOR. The V - bearing 4742 and 4733 were research samples prepared at the University of Sheffield (United Kingdom) by vacuum induction melting. After casting, the alloys were hot rolled at 1050°C to a thickness of 12mm and then annealed at between 825°C and 850°C for 30 minutes, followed by water quenching.

The commercial grade 304L and 316L were supplied by Krugersdorp Engineering (Pty) Ltd. as annealed 4.5mm plates. Annealing was performed at 1070°C followed by water quenching.

For the ring - disc electrodes, platinum rings were cut from a pure platinum tube (Johnson Matthey), i.d. 5.5mm, o.d. 7.5mm.

Table 3.1**Composition of alloys (wt%).**

alloy	Cr	Mo	Ni	V	C	Si	Mn
Fe16Cr	16.58	—	0.54	—	0.061	0.30	0.65
Fe18Cr	18.29	0.011	0.02	0.009	0.03	0.061	0.023
Fe20Cr	20.24	0.011	0.01	0.008	0.034	0.092	0.023
Fe23Cr	23.10	0.012	0.01	0.007	0.039	0.65	0.03
444	17.39	1.78	0.27	0.081	0.003	0.17	0.23
4732	18.40	0.02	0.09	2.77	0.017	0.06	—
4733	18.20	0.02	—	4.08	0.019	0.03	0.05
304L	18.23	—	9.25	—	0.037	0.46	1.35
316L	16.54	2.00	10.19	—	0.027	0.55	1.19

The balance of alloy is Fe.

— not measured

3.2 CHEMICALS

All chemicals used were of analytical reagent quality as follows :- NaOH 98% (AnalaR, B.D.H. Chemicals), NaCN 97% (AnalaR), H₂SO₄ 98% (AnalaR), NaHSO₄ 99% (Merk *pro analysi*), Na₂SO₄ 99.5% (AnalaR), NaClO₄ 99% (AnalaR), HClO₄ 60% (SAARCHM), K₄Fe(CN)₆ 99% (AnalaR), K₃Fe(CN)₆ 99% (AnalaR).

Reagent grade water (resistivity 18MΩ cm) was used to make up the solutions. This was obtained from a Milli - Q system, where tap water is passed through a reverse osmosis membrane, an activated carbon cartridge to remove organic impurities, through two ion exchange cartridges to remove dissolved inorganic impurities and finally through a polymeric membrane filter which removed all particles larger than 0.2μm. All electrolytes were freshly prepared since, for example, decomposition of cyanide has been reported.³²⁰⁻³²²

The standards used for XPS analysis were FeO (ref. 323), Fe₂O₃ 99.98% (AnalaR), FeOOH (ref. 324), Fe₃O₄ 98% (B.D.H. Chemicals).

3.3 THE CELL

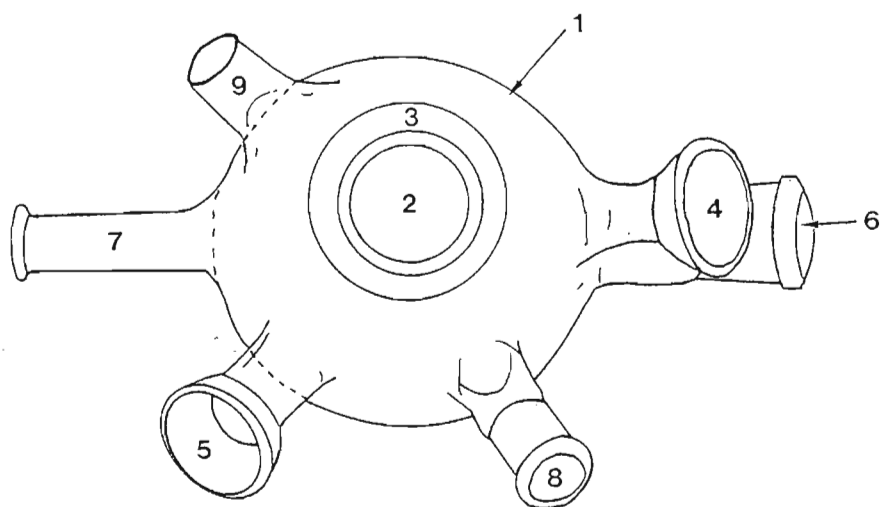
Either a three or six electrode cell was used depending on whether an experiment required one or two working electrodes. For temperatures up to 80°C a glass cell was used and for higher temperatures a Teflon cell was used.

3.3.1 Glass Cell

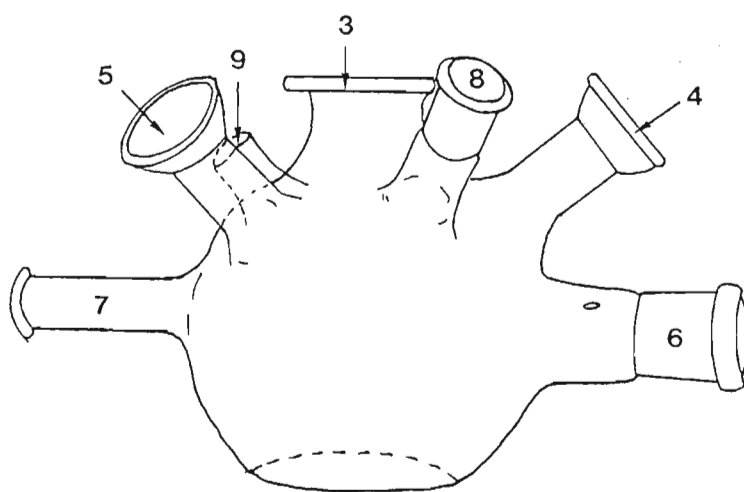
The cell consisted of a 500ml flat bottomed flask to which a flange and six ports had been fitted (Fig. 3.1).

The working electrode, inserted through the central port, consisted of either an alloy or pure metal disc or a platinum ring concentric to the disc.

The reference electrode used was a saturated calomel electrode (SCE) having a potential of +241mV against the normal hydrogen electrode. The reference electrode was placed in the reservoir above the Luggin capillary and separated from the solution via an ungreaed wetted stopcock (Fig. 3.2). The electrolyte was drawn up into the reservoir by applying a water pump vacuum to the side arm. This prevented the formation of air bubbles in the capillary. The reference electrode assembly was connected to the cell by a ball and socket joint held in position with retaining clamps. This facilitated positioning of the Luggin. The tip of the Luggin capillary was placed directly under the working electrode at a distance equivalent to twice the diameter of the Luggin capillary.



(a)



(b)

Fig. 3.1 The glass cell (a) plan
(b) side elevation

1. Flat bottomed flask
2. Central port for working electrode
3. Flange
4. Port for reference electrode 1
5. Port for reference electrode 2 or
contact thermometer
6. Port for counter electrode
7. Port for diamond scribe
8. Port for nitrogen bubbler
9. Port for microburette

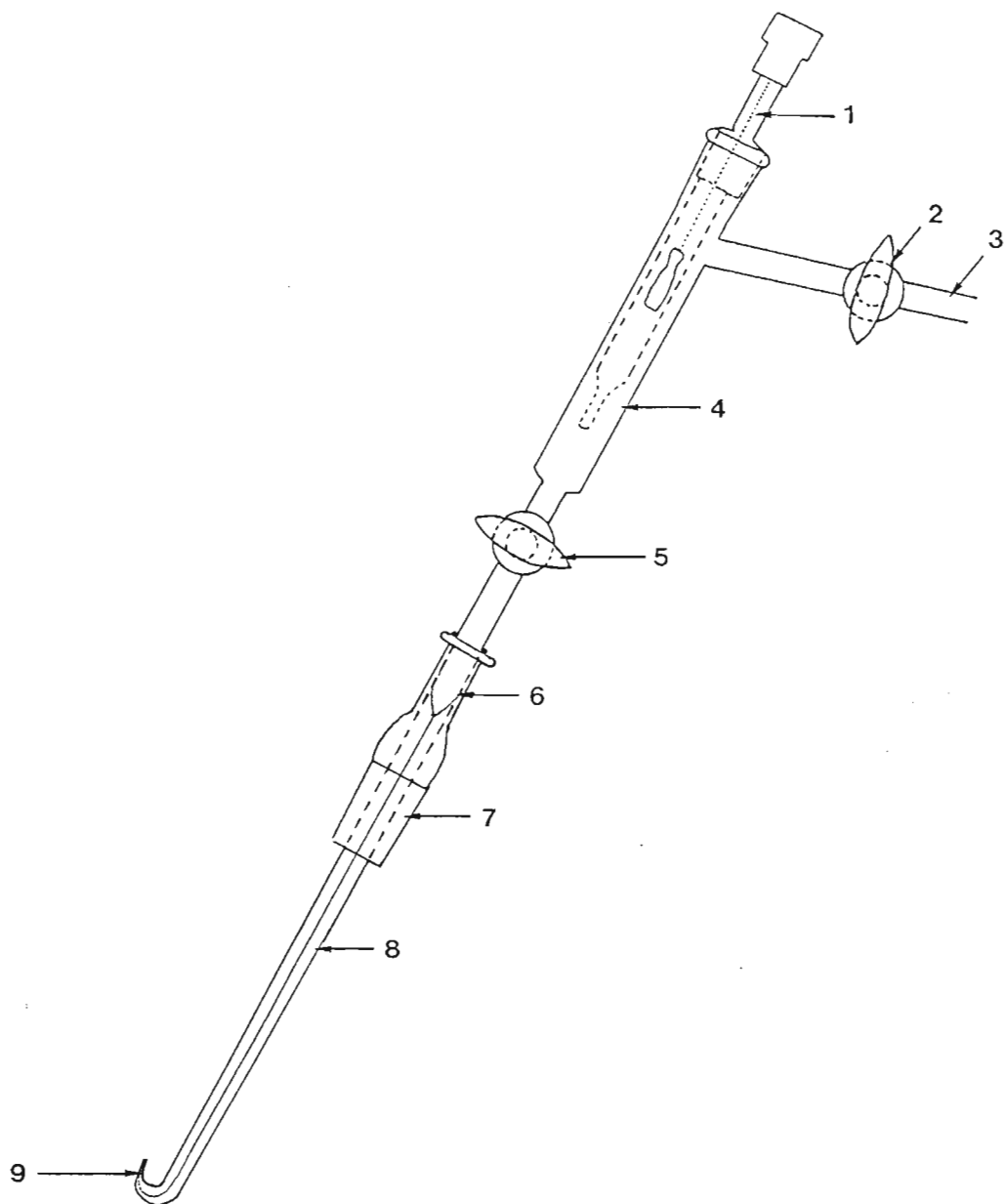


Fig. 3.2 Reference electrode assembly

1. Reference electrode
2. Stopcock
3. Arm for drawing solution into reservoir
4. Electrolyte reservoir
5. Stopcock
6. Syringe barrel
7. Ground glass cone
8. Capillary
9. Luggin capillary

The counter electrode consisted of a platinum disc which was attached to the end of a glass tube using a silicon adhesive sealant (LOCTITE Superflex) (Fig. 3.3a). When required, a second counter electrode, consisting of a coiled length of platinum wire, was fitted onto the counter electrode assembly (Fig. 3.3b). There was no physical or electrical contact between these two electrodes. Both of the counter electrodes had surface areas significantly larger than that of the working electrodes, and were placed parallel to the latter to ensure correct cell geometry.

A nitrogen bubbler, attached to an oil trap, was also inserted into the cell enabling deaeration of the electrolyte with high purity nitrogen (99.998%, < 3ppm O₂).

When required a microburette (± 0.0125 ml) could be inserted into the cell, via a rubber bung, to facilitate the addition of anions.

The sixth port (7 in Fig. 3.1) was the barrel of a borosilicate syringe, for the incorporation of a diamond scribe into the cell for scratch chronoamperometric experiments.³²⁵⁻³²⁷ In the present work the scratch technique was used for investigating the presence of a pre-existing film on the electrode surface. The diamond scribe consisted of a diamond set in an annealed brass rod. The end nearest the diamond was bent such that the culet of the diamond was perpendicular to the electrode surface. The rod was glued (PATTEX Super Glue) into a borosilicate glass syringe plunger, and all of the remaining exposed rod was covered in epoxy resin (Fig. 3.4). The use of a good quality syringe ensured no leakage of solution occurred and enabled a smooth scratch to be rapidly produced.

Temperature control ($\pm 0.5^\circ\text{C}$) was achieved by placing a contact thermometer, connected to a Heidolph hot plate / magnetic stirrer (system M2002) onto which the electrochemical cell was placed, in the electrolyte. For $T \geq 30^\circ\text{C}$ a customised, insulating asbestos jacket was placed around the cell.

3.3.2 Teflon Cell

Due to the solubility of glass in hot alkali electrolytes a Teflon cell, based on the design of the glass cell, was used for experiments performed at $80^\circ\text{C} < T < 130^\circ\text{C}$. As a precautionary measure against the possible out-gassing of the Teflon, it was preheated to 370°C prior to machining. Such a procedure has been reported to be successful,^{328,329} and so eliminating the introduction of any unknown species into the system.

One of the main criteria in the design of the Teflon cell was that results obtained using the glass cell at $T \leq 80^\circ\text{C}$ could be reproduced using the Teflon cell. This ensured that the influence of temperature on the electrochemistry of the metal, at the higher temperatures, was being studied and not spurious artifacts generated by the cell. The cell described below was thoroughly tested in a series of preliminary experiments and was found to give reproducible results from experiment to experiment and with those obtained using the

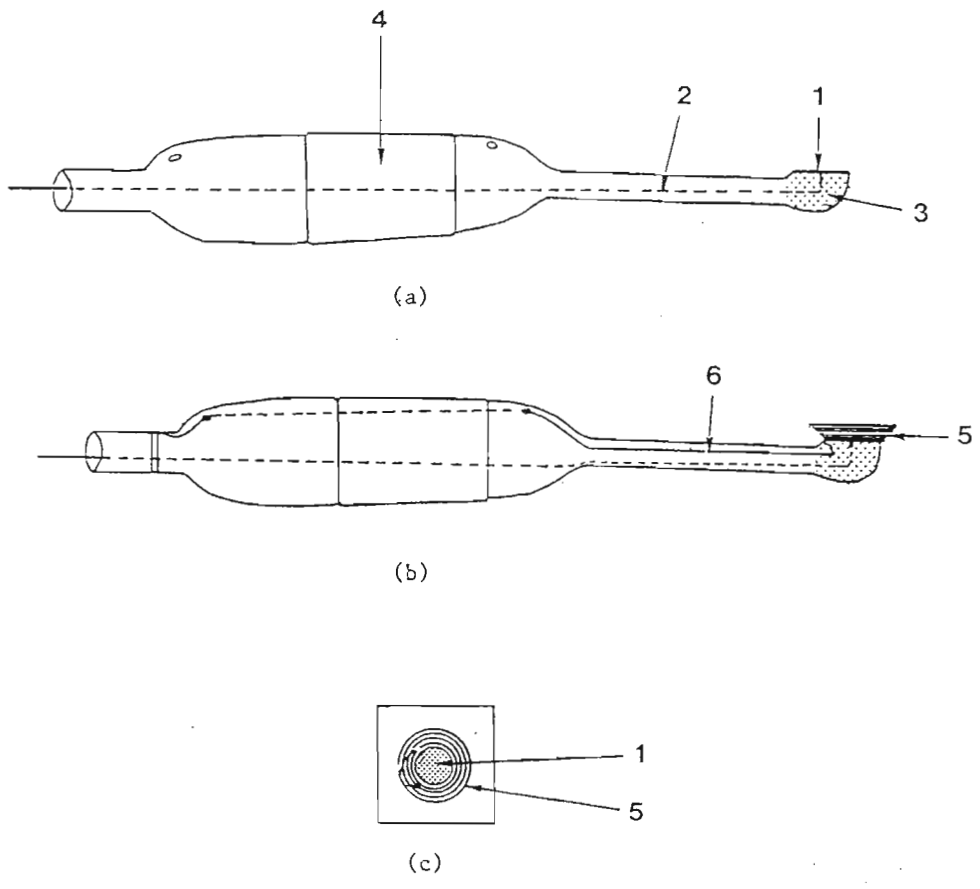


Fig. 3.3 Counter electrode assembly

- | | | | |
|-----|------------------------------------------------------------------------------------------|----|---------------------------|
| (a) | One counter electrode | 1. | Pt disc |
| | | 2. | Insulated contact wire |
| | | 3. | Silicon adhesive sealant |
| | | 4. | Ground glass joint |
| (b) | Two counter electrodes | 5. | Coiled Pt wire |
| | | 6. | Epoxy coated contact wire |
| (c) | Position of second counter electrode (5) with respect to the first counter electrode (1) | | |

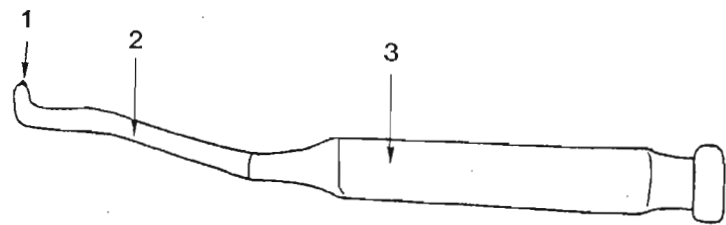


Fig. 3.4 Scratcher

- | | |
|----|------------------------|
| 1. | Diamond |
| 2. | Epoxy coated brass rod |
| 3. | Syringe plunger |

glass cell.

A cross - section of the assembled Teflon cell is shown in Fig. 3.5. The cell was placed in the Heidolph hot plate which was in turn placed on a laboratory jack. Once the cell had been assembled, and the working electrode secured to the stand, the whole assembly was raised to a predetermined height.

The cell has a cylindrical profile and a capacity of 600ml. As sealing of the cell is achieved using compression seals, the outside wall of the cell was machined to form an octagon, thus providing flat surfaces against which the external sections of the counter and reference electrodes could be screwed. Such a design provided pressure, and water tight sealing of the cell.

The counter electrode consisted of a 3.5mm thick platinum disc. Silver epoxy cement (Emerson and Cuming, Belgium) was used to secure an insulated lead onto the back of the disc. Once cured, the epoxy, back of the Pt disc and any exposed wire was covered with Araldite M resin. The machined Teflon holder was then heat shrunk onto the Pt disc. The counter electrode assembly was then be screwed into the side wall of the cell and secured using a Teflon nut fitted with a Viton o - ring.

An external reference electrode was used for these experiments. The reference electrode (SCE) was placed in an electrolyte reservoir, above the Luggin capillary, and separated from the cell by an ungreased and wetted Teflon stopcock. This reservoir had been press fitted into the back of the Teflon securing nut. The Teflon Luggin capillary section was screwed into the cell wall and secured using a Teflon nut fitted with a Viton o - ring. As positioning of the tip of the Luggin capillary, with respect to the working electrode, could not be done visually, the positioning of the reference electrode port in the cell wall was such that using standardised working electrode holders the correct distance of the tip of the Luggin capillary from the working electrode was achieved automatically each time the cell was assembled. For experiments involving two working electrodes, provision had been made for the incorporation of a second reference electrode.

The lid of the cell had five ports and was secured by means of stainless steel screws. The working electrode, contact thermometer and electrode sweeper ports were machined to a minimum clearance. The remaining ports were threaded.

The working electrode holders were the same as those used at lower temperatures. However, when press fitting the epoxy mould of the working electrode into the holder particular care was taken to ensure a tight fit. A Viton o - ring was placed between the holder and the stainless steel retaining ring (used to secure the holder onto the stand - see 11 in Fig. 3.5) to eliminate condensation within the rotating electrode unit. As shown in Fig. 3.5, a Viton o - ring between the working electrode holder and the cell wall was compressed by a stainless steel spacer (10) on which the flange of the PVC spacer tube (12) sits. This

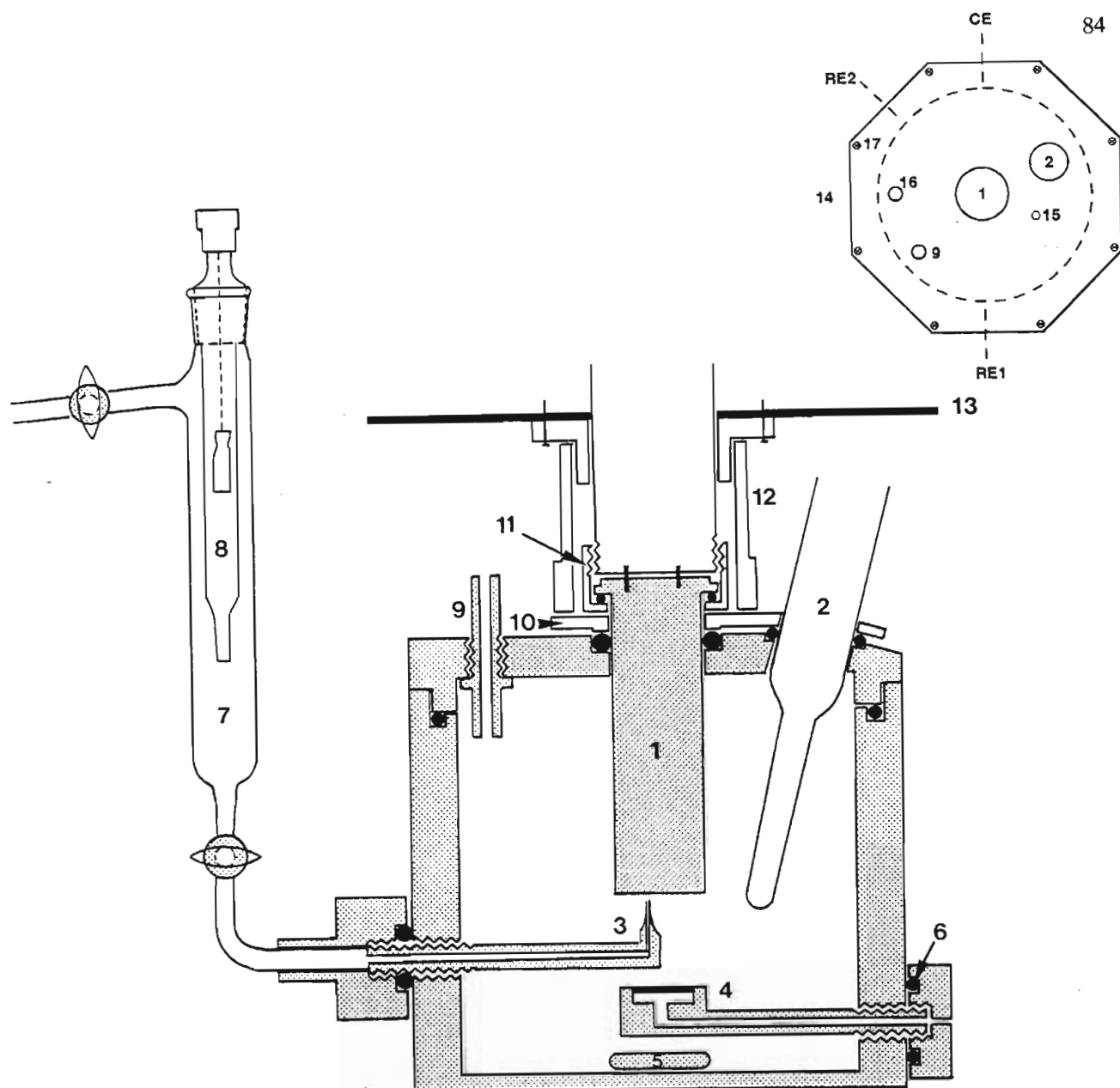


Fig. 3.5 Cross section of Teflon cell

1. Working electrode
2. Contact thermometer
3. Luggin capillary
4. Counter electrode
5. Magnetic stirrer
6. Viton o - rings
7. Electrolyte reservoir
8. Reference electrode
9. Connection for pressure gauge
10. Stainless steel spacer
11. Stainless steel retaining ring
12. PVC spacer
13. 1st tier of rotating electrode unit
14. Top view of lid of cell showing positioning of ports
15. Port for electrode sweeper
16. Port for nitrogen inlet
17. Stainless steel screws

stainless steel spacer also compressed the o - ring around the contact thermometer.

Temperature control was achieved using a contact thermometer inserted through the lid of the cell. The use of a Teflon coated magnetic stirrer bar ensured that temperature gradients were not set up within the cell.

As accumulation of bubbles on the working electrode occurred, particularly after setting up the cell, an electrode sweeper was incorporated in the cell. This consisted of a flanged stainless steel rod, one end of which was welded to a 1cm x 3cm stainless steel plate. This entire assembly was Teflon coated. In order not to scratch the electrode surface a 2mm thick sheet of Viton was secured over the plate. When not in use, the sweeper was withdrawn to the flange and rotated such that the plate was away from the working electrode, so minimising interference.

Threaded Teflon tubes were used for the nitrogen bubbler and to provide a connection for the pressure gauge or manometer. Heavy gauge vacuum tubing, secured by jubilee clips, was used for the connection to the pressure gauge. Thick walled silicone rubber tubing was used for the nitrogen connection.

3.4 ROTATING ELECTRODE UNIT

Controlled rotation of the working electrode was achieved using the rotating electrode unit previously designed and constructed in this laboratory³³⁰ (Fig. 3.6), which is a modification of a design used at MINTEK (Council for Mineral Technology). The rotation rate of the driving motor (12V D.C.) was controlled by a photocell and a stroboscopic disc device controlling a power amplifier / controller. A range of rotation rates were available from 40rad s^{-1} up to 500rad s^{-1} (6.4Hz to 79.6Hz). The motor drove the central shaft of the unit (5) which terminated in an externally threaded steel flange, having two spring - loaded brass plungers in a PVC insert for contact with the wires from the disc (and ring) of the working electrode. Two wires soldered to the brass plungers made contact with two silver plated slip rings on the upper part of the unit. External contact was made with the slip rings through carbon - silver brushes (30% Ag, 70% C, Le Carbon, France) mounted on spring loaded brass arms which were in turn mounted on the electrode stand. Ingress of atmospheric oxygen was controlled by means of a non - rotating pvc cylinder (8) which was machined to a minimum clearance with the rotating unit and has a flange, with an o - ring seal, which rested on that of the flask.

3.5 CONSTRUCTION OF THE WORKING ELECTRODES

3.5.1 Disc Electrodes

An insulated lead was secured to the back of each disc using silver epoxy cement. After contact between

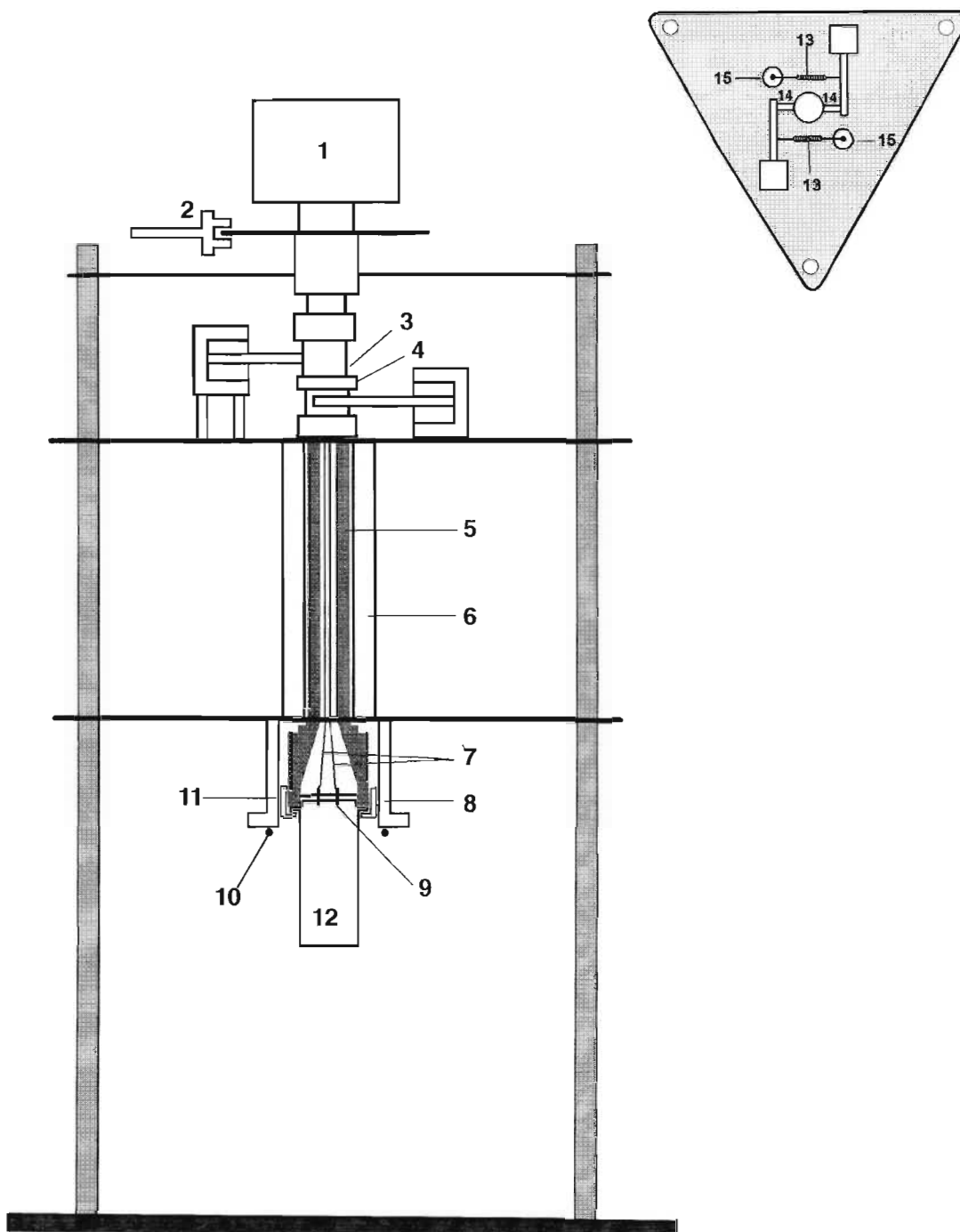


Fig. 3.6 Rotating electrode unit

1. Electric motor (12V D.C.)
2. Photocell speed counter
3. Silver plated slip rings
4. PVC rings
5. Rotating drive shaft
6. Drive shaft housing
7. Insulated wires
8. PVC tube
9. Spring loaded brass plunger
10. o - rings
11. Retaining ring
12. Teflon working electrode holder
13. Tension spring
14. Carbon brushes
15. Spring tension adjusters

the working surface of the disc and the connecting wire had been checked, the disc was ultrasonically cleaned in ethanol for one minute. A Teflon mould was placed concentrically around the disc which was then filled with Araldite M resin. Once cured, the epoxy mould was removed from the Teflon mould and press fitted into a Teflon holder; a completed disc electrode assembly is shown in Fig. 3.7a.

Subsequent to mechanical polishing of the working electrode (see 3.8.1) the Teflon holder was attached to the stand by a retaining ring which screwed onto the external thread of the central shaft. Rapid, easy interchange of working electrodes was accomplished with this system. For XPS or SEM examination, the epoxy mould could rapidly be removed by inserting a metal rod into the central shaft of the Teflon holder and tapping out the epoxy mould.

3.5.2 Ring - Disc Electrodes

The above procedure was used for the construction of ring - disc electrodes with one addition; the Teflon mould was placed concentrically around a platinum ring which was in turn placed concentrically around the disc. The best concentricity possible was aimed for as it is well known that it plays an important role in the behaviour of rotating ring - disc electrodes.³³¹⁻³³³ Fig. 3.7b shows a completed ring - disc electrode assembly.

3.6 INSTRUMENTATION

Electrical connections for experiments having one working electrode are shown in Fig. 3.8. The electrode potential was controlled by a PAR 173 potentiostat programmed by a PAR 175 Universal Programmer. The reference electrode was connected to the potentiostat via a PAR 178 electrometer probe. The current response of the working electrode was monitored using an X-Y recorder (Hewlett - Packard 7044A) and a digital storage oscilloscope (Nicolet 3091) via a linear current to voltage converter (PAR 376). A noise filter (PAR 178/41), which is a 100nF capacitor, was connected between the reference and counter electrodes to reduce AC noise pickup.

For experiments requiring two working electrodes, the necessity for an additional counter and reference electrode had previously been shown.³²⁵ Electrical connections for the rotating ring - disc electrode experiments, in which the ring was held at a fixed potential and the ring current monitored as a function of disc potential, are shown in Fig. 3.8. The potential for each working electrode was controlled by a separate potentiostat, the one working electrode being connected to the PAR 173 potentiostat, the other to a PAR 363 potentiostat which was programmed by a PAR 175 Universal Programmer. The connections for the PAR 173 are as described above. The second reference and counter electrodes were connected to the PAR 363 potentiostat. A 100nF capacitor was inserted between the second counter and reference electrodes to act as a noise filter (capacitance equivalent to that of the PAR 178/41 noise filter). The

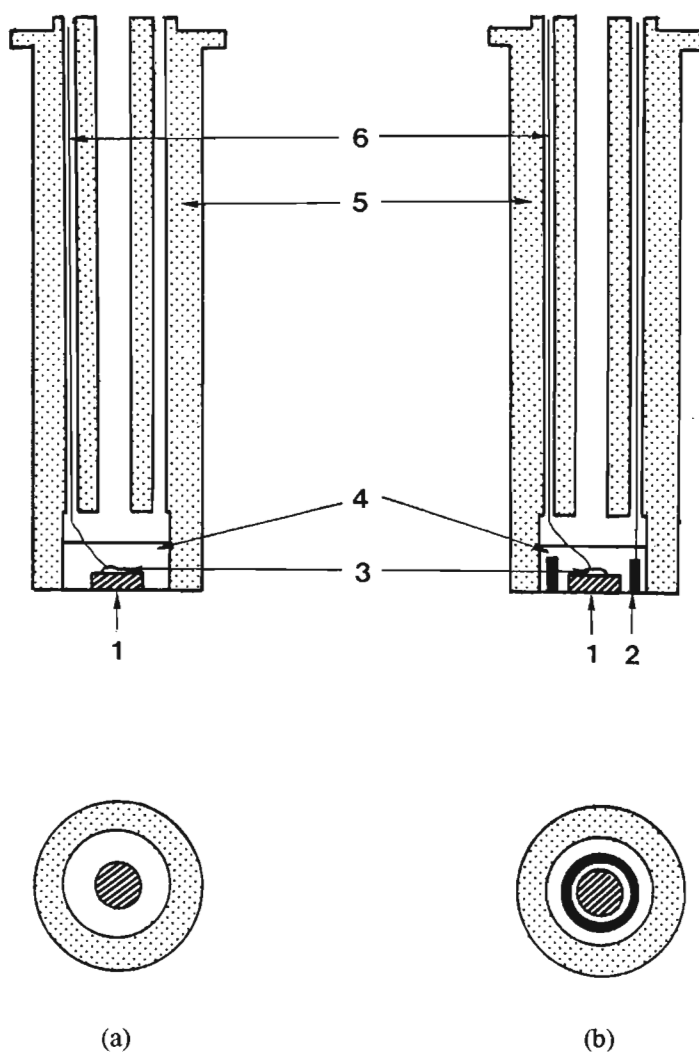


Fig. 3.7 Assembled working electrodes

- (a) Disc electrode
 - (b) Rotating ring - disc electrode
1. Metal working electrode
 2. Pt ring
 3. Silver epoxy
 4. Araldite M epoxy resin
 5. Teflon holder
 6. Insulated contact wires

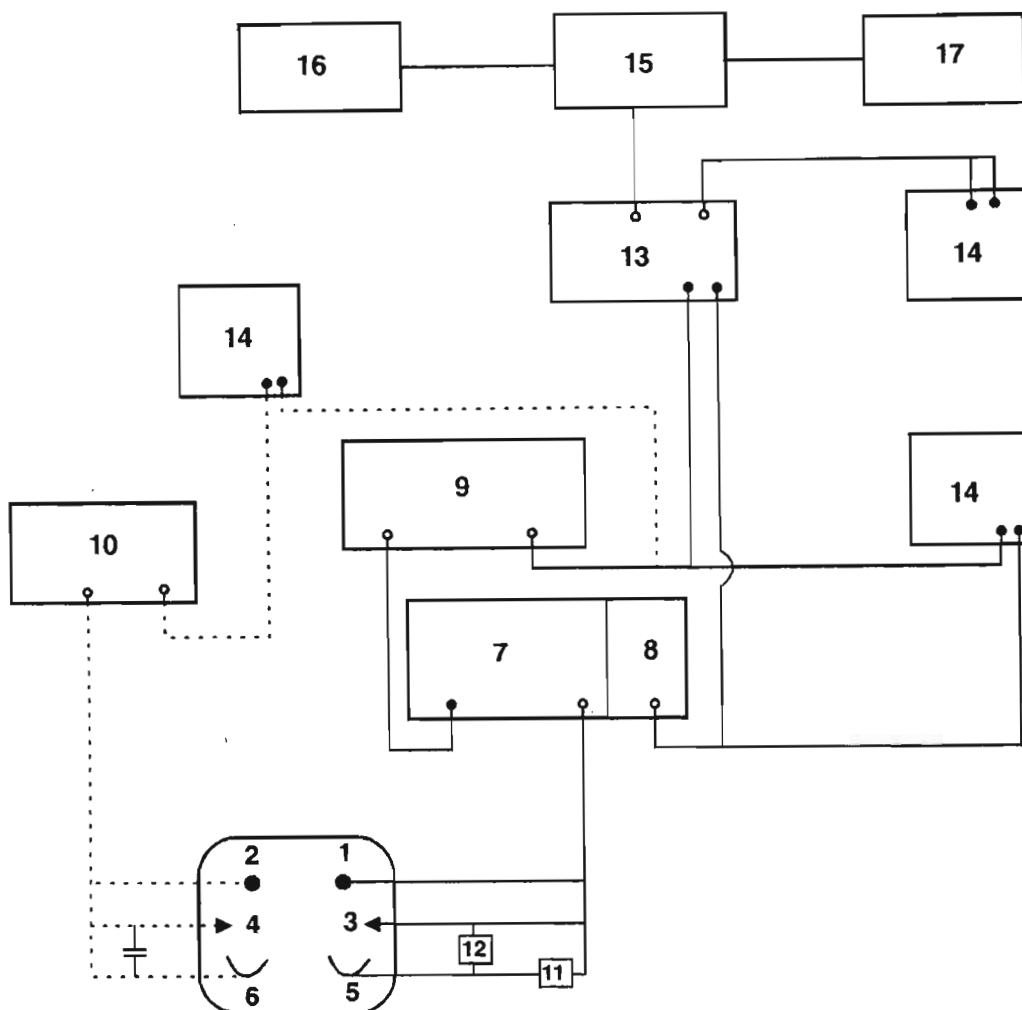


Fig. 3.8 Schematic diagram of electrical connections for experiments having one (—) and two (· · · · ·) working electrodes

1. Working electrode (1)
2. Working electrode (2)
3. Counter electrode
4. Second counter electrode
5. Reference electrode
6. Second reference electrode
7. Potentiostat (PAR 173)
8. I/V converter (PAR 376)
9. Function generator (PAR 175)
10. Potentiostat (PAR 363)
11. Electrometer probe
12. Noise filter (PAR 178/41)
13. Dual channel oscilloscope (Nicolet 3091)
14. X - Y recorder (HP 7044A)
15. Apple II+ computer
16. C.Itoh 8510A printer
17. Plotter (HP 7470A)

current response was monitored on a dual channel oscilloscope (Nicolet 3091) and on X-Y recorders (Hewlett - Packard 7044A).

On completion of an experiment a hard copy of the oscilloscope trace was obtained using the pen function of the Nicolet oscilloscope and an X-Y recorder. In addition, the data was transferred to an Apple II+ computer, via an RS-232C serial interface, and stored on floppy disc for subsequent processing. A numerical listing of the data and experimental parameters was obtained using a C.Itoh 8510A printer while a Hewlett - Packard 7470A plotter was used for plotting the results.

At the time the experimental work was performed, DOS based personal computers (PCs) were prohibitively expensive, in South Africa, and hence the use of an Apple II+ computer. However, as the situation changed, the data collected via the Apple was transferred and converted to DOS format using the program MIRROR II (SoftKlone Distributing Corp.). This enabled subsequent analysis of the data to be performed more efficiently using a 386 PC. LOTUS 1-2-3 (Lotus Development Corp.) was used to this end.

3.7 SOFTWARE

The software package COLLECTION previously written in this laboratory³²⁵ was used for the collection and storage of data.

COLLECTION consisted of three programs, ANODIC POL, CYCLIC and CHRONOAMP, for the collection of anodic polarisation curves, cyclic voltammograms and chronoamperograms respectively. These three programs are variations of a program which initially requests the relevant experimental information. Subsequent to storing an experiment on the Nicolet oscilloscope, channel A data (current data values) is transferred to the Apple followed by channel B data (potential data values). Using the experimental information supplied, the data values are converted into current densities ($A\ cm^{-2}$) and potentials (V). The data from the two channels is then combined and stored on floppy disc as (current / $A\ cm^{-2}$, potential / V).

ANODIC POL and CYCLIC differ only in the experimental information required. CHRONOAMP differs from these two programs in that each channel contains a complete experiment, and the data is stored as (time /s, current density / $A\ cm^{-2}$).

3.8 PROCEDURE FOR ELECTROCHEMICAL MEASUREMENTS

3.8.1 Electrode Pretreatment

Electrochemical measurements can be significantly influenced by the pretreatment of the electrodes,³³⁴ and thus a standard pretreatment was developed. Using a Struers Planpol-2/PdM-Force polishing system the

electrodes were prepared using abrasive paper (SiC) ranging from grade size No. 400 to No. 1200, and then with $7\mu\text{m}$, $3\mu\text{m}$ and $1\mu\text{m}$ Metadi II diamond compound (BEUHLER Ltd.). The electrode was ultrasonically cleaned in deionised water after each change in grade of polishing disc. On completion of polishing, the electrode surface was examined for scratches using an optical microscope. The electrode was then ultrasonically cleaned in ethanol for one minute and was then fitted into the stand. Olmedo *et al.*³³⁵ have shown that when water was used for the final electrode cleaning rapid formation of an amorphous layer of corrosion products occurs while no such layer was found when methanol was used.

All glassware was soaked overnight in Conrad Cleaning Solution, rinsed copiously with deionised water, reagent grade water and finally with the solution to be used. The cell was assembled on the stand with care being taken to ensure that :

- (a) all ground glass joints were suitably greased
- (b) the Luggin capillary was free from air bubbles and was not leaking
- (c) electrical connections between the working electrodes and the appropriate connection points on the stand were satisfactory;

and in the case of the Teflon cell that :

- (d) the Viton o - rings were free of cracks. All o - rings were replaced after a maximum of 10 hours use.
- (e) all Teflon securing nuts and jubilee clips adequately tightened.

Electrical connections were then made (Fig. 3.8) and the solution deaerated with high purity nitrogen (99.998%; $<3\text{ppm O}_2$). The solution resistance between the working and reference electrodes was checked using two independent methods, viz. the ESC Model 800 IR Measurement System (current interrupt method), and with an oscilloscope monitoring the ability of the working electrode to follow an applied square wave signal.³³⁶ Using the IR compensation facility of the PAR 376, compensation was made if necessary.

For experiments not performed at ambient temperature, the electrolyte was preheated prior to inserting the working electrode into the cell. This eliminated the electrode having to stand in the electrolyte for long periods while the required temperature was reached. For experiments performed at the higher temperatures ($T \geq 60^\circ\text{C}$) the electrolyte was frequently changed as the concentration of an electrolyte may change on heating due to evaporation.

As an electrochemical cleaning procedure the electrode was held at a potential 10mV cathodic of the corrosion potential for 10 minutes in order to reduce any air formed oxide.

Reproducible results were obtained from the above procedure.

3.8.2 Anodic Polarisation

The electrode was pretreated as described in 3.8.1, stepped to its corrosion potential and then swept in an anodic direction at 2mV s^{-1} . The current response was simultaneously monitored on an X-Y recorder and on the Nicolet oscilloscope. Data stored in the Nicolet was transferred to the Apple computer using ANODIC POL, and stored on floppy disc.

Subsequent to any addition of anions, the solution was stirred using a magnetic stirrer and nitrogen bubbled for at least one minute to ensure a homogeneous solution before proceeding with the next potential scan. This procedure was adopted for cyclic voltammetric, RRDE and chronoamperometric experiments.

3.8.3 Cyclic Voltammetric Experiments

Following the initial pretreatment, section 3.8.1, the electrode was stepped to the required initial potential and then swept to the required positive limit. The scan direction was automatically reversed, and the electrode swept to the required negative potential. Such cycling was continued for as long as required. Sweep rates used varied from 2mV s^{-1} to 10V s^{-1} , while rotation rates varied from 0 to 256rad s^{-1} .

The cyclic voltammograms were recorded on the Nicolet oscilloscope for all sweep rates, and on an X-Y recorder for the 2mV s^{-1} to 500mV s^{-1} range. Data was transferred from the Nicolet to the Apple computer using CYCLIC.

3.8.4 Rotating Ring - Disc Experiments

In these experiments the ring was polarised at successively more reducing/oxidising potentials, depending on whether processes at oxidation or reduction peaks were being investigated, and the ring current response monitored as a function of disc potential.

3.8.5 Chronoamperometric Experiments

The electrode was pretreated as described in 3.8.1 then held at the initial potential of interest for a specified period before stepping to the final potential. All chronoamperograms were recorded on the Nicolet oscilloscope and the data transferred to the Apple computer, using CHRONOAMP, and stored on floppy disc. A hard copy of the oscilloscope trace was obtained on the X-Y recorder.

Preliminary work had shown the chronoamperograms to be very sensitive to electrode pretreatment, particularly at higher temperature. Thus subsequent to each applied potential step, the electrode was removed from the electrolyte, rinsed in reagent grade water and repolished.

3.9 SURFACE ANALYSIS

3.9.1 SEM Analysis

The electrodes were removed from the Teflon holder, rinsed with reagent grade water and dried using high purity nitrogen. The electrode was stored in an inert nitrogen atmosphere.

For qualitative analysis the electrodes were gold sputter coated using a POLARON SEM coating unit E5100. Sputter coating was found to be necessary to prevent surface charging. The electrodes were then screwed into a custom made holder, which made provision for the contact wires thus eliminating the need for these to be cut off each time an electrode was examined in the SEM.

A Hitachi S520 scanning electron microscope was used for qualitative examination of the electrode surface. A JEOL JSM-35 scanning electron microscope with a KEVEX 7000-77 energy dispersive x-ray spectrometer was used for quantitative analysis of the electrodes.

3.9.2 XPS Analysis

XPS measurements were made using a VG ESCALAB Mk.II. Non - monochromatic Al K α (1486.6 eV) radiation was used from an x - ray gun operated at 15kV and 20mA. The base pressure of the analyser was better than that 2×10^{-10} mbar during analysis. All spectra were recorded using the same spectrometer parameters of 6mm slit width and a constant analyser energy of 100eV for wide scans and 50eV for narrow scans. The precision of binding energy measurements for the latter was ± 0.05 eV.

XPS analyses were performed on the electrochemically prepared samples as well as on standards of the Fe and Cr oxides. Two sets of data were recorded for each of the powder standards - one set on the as-received standard and a second on which a 0.5 - 1nm gold coating had been sputtered. The latter data were used to obtain static charge - corrected binding energies by means of the calibrated energy of 84.0eV for the Au 4f $_{7/2}$ peak. Such charging corrections varied between 2.5 and 3.4eV. These corrections were within 0.1eV of that obtained using the adventitious hydrocarbon C $_{1s}$ at 285.0eV. Therefore on the electrochemically prepared samples, charge referencing was done using the adventitious hydrocarbon peak. Two sets of data were recorded for the electrochemically prepared samples; one on the as - received (unsputtered) electrodes and a second subsequent to 9keV Ar sputtering at $100\mu\text{A cm}^{-2}$ for 40 seconds.

Narrow scan Fe $_{2p}$, Cr $_{2p}$, C $_{1s}$ and O $_{1s}$ spectra were recorded for the electrochemically prepared samples. The Fe $_{2p}$ and Cr $_{2p}$ regions included both the 3/2 and 1/2 doublet peaks, however since sensitivity factors were available for the stronger 3/2 peak, peak fittings were only performed on this peak.

3.9.3 AES Analysis

Auger analysis was performed using a PHI Scanning Auger Microprobe. A primary beam of 3keV was used, having a diameter of between 0.6 and 1 μ m. Sputter cleaning, as well as the AES depth profiles were obtained by sputtering with a 2.5keV Ar⁺ beam, having a current of 25 μ A cm⁻².

CHAPTER FOUR

RESULTS and DISCUSSION

Nucleation and Growth of Anodic Films on Metals in Acidic Electrolytes

In this chapter the formation of anodic films on Fe18Cr electrodes in various electrolytes of $\text{pH} < 7$ (0.1M H_2SO_4 , 0.1M NaHSO_4 , 0.1M Na_2SO_4 , 0.1M NaClO_4 and 0.1M to 1.0M HClO_4) and on alloys Fe16Cr, Fe20Cr, Fe23Cr, 444, 4732, 4733, 304L and 316L in 0.1M H_2SO_4 has been investigated as a function of potential, using chronoamperometry. Current transients were also obtained for Fe, Cr and Mo in 0.1M H_2SO_4 , and for Fe18Cr as a function of temperature. It will be shown that rising current transients similar to those obtained for electrocrystallisation of metals^{225,243-245,246} are obtained for stainless steels at transpassive potentials. With the exception of the previous communication³³⁷ from this laboratory, on Fe18Cr in 0.1M H_2SO_4 , a description and analysis of such transients in terms of the nucleation and growth of anodically formed surface films on ferrochrome steels had not previously been reported.

A Fe18Cr electrode in 0.1M H_2SO_4 was polarised at an active potential (-0.55V) for 5 minutes prior to stepping to passive and transpassive potentials. The resulting current transients (Fig. 4.1) are typical of those obtained in electrocrystallisation studies^{242-245,338,339} and for the nucleation of anodic oxide films on pure metals³⁴⁰ and alloys.³³⁷ At the start of each transient there is a charging current that decays which is followed by an increase in the current, presumably indicating an increase in the electroactive area. On reaching, at time t_m , a maximum current density, i_m , which is potential dependent, the current then decreases to an eventual steady state value. i_m and t_m are potential dependent with i_m increasing linearly and t_m decreasing logarithmically as the final potential was made more positive. The coefficients for these dependencies, for the stainless steels investigated, are given in Table 4.1. At potentials greater than 1.60V, this second decay is followed by further increases in the current, due to oxygen evolution.

These rising current transients provide a very sensitive technique for monitoring the nucleation and growth of surface films, and as will be shown in the following sections, respond sensitively to changes in experimental conditions. Deductions made from these results correlate well with results obtained from other electrochemical and surface analytical techniques.

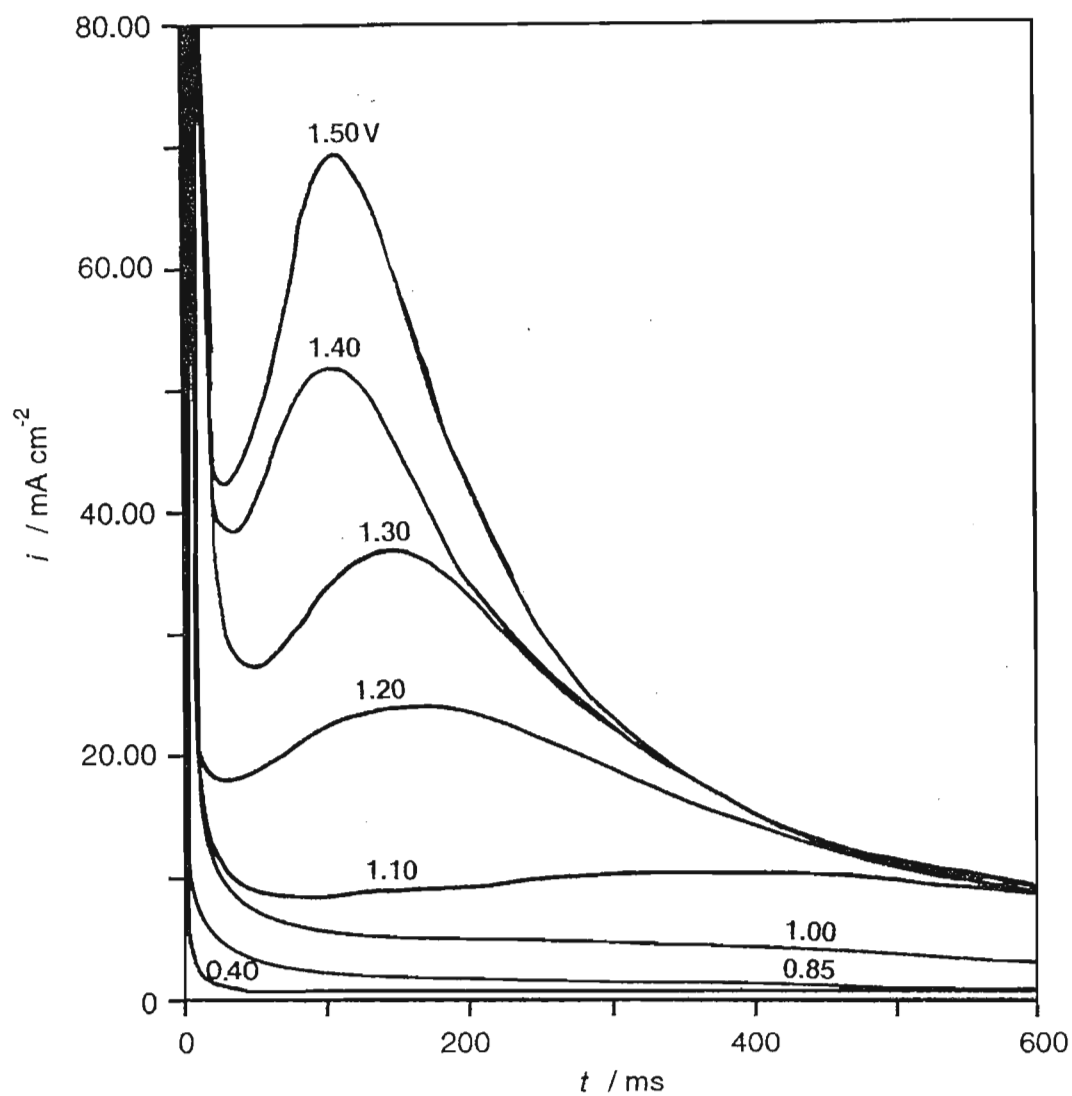


Fig. 4.1 Current transient response of a Fe18Cr electrode in 0.1M H₂SO₄, 20°C, at the indicated potentials.

Table 4.1

Coefficients for the equations below describing the dependence of i_m and t_m on applied potential, E , for various stainless steel alloys in 0.1M H_2SO_4 at 20°C.

$$i_m = a E - b$$

$$\log t_m = c - d E$$

alloy	a	b	c	d
Fe16Cr	129.98	124.03	5.16	2.30
Fe18Cr	112.24	106.00	5.30	2.34
Fe20Cr	93.92	99.77	5.83	2.50
Fe23Cr	85.13	82.90	4.27	1.40
444	74.43	75.53	4.57	1.69
4732	98.21	94.71	4.45	1.52
4733	78.83	78.03	4.54	1.63
304L	114.59	116.00	5.48	2.53
316L	81.36	82.15	4.43	1.51

4.1 INFLUENCE OF ELECTROLYTE COMPOSITION

4.1.1 H₂SO₄

Cyclic voltammograms of a Fe18Cr alloy in 0.1M H₂SO₄ have one oxidation peak (at $\approx 1.15\text{V}$), which will be referred to as peak A, and three reduction peaks at 490mV, 140mV and -50mV (peaks D, E and F respectively).³²⁵ Qualitatively these cyclic voltammograms are the same as those obtained in HClO₄; the latter are presented in Fig. 4.2. It has been shown that the processes responsible for peak A are prerequisites for the appearance of the rising current transients since the latter are only observed for systems in which peak A is present. A synopsis of the facts at present known about peak A are as follows :^{325,341}

Cyclic voltammetric peak A

- occurs at transpassive potentials.
- dependent on electrolyte composition. Peak A is only observed if oxidation of the metal occurs.
- the maximum current density of peak A, $i_{p,A}$, is influenced by the presence of Cl⁻, with $i_{p,A}$ increasing linearly with $\log [\text{Cl}^-]$.
- in the presence of a high Cl⁻ concentration multiple oxidation peaks are observed in the potential region of peak A, suggesting that several reactions are responsible for peak A.
- $E_{p,A}$ is dependent on sweep rate, ν , and $i_{p,A}$ is linearly dependent on $\nu^{1/2}$, for $1\text{mV s}^{-1} \leq \nu \leq 4\text{V s}^{-1}$, suggesting that the processes occurring at peak A are possibly diffusion controlled.
- dependent on the lower potential limit of the cyclic voltammogram. Excluding the reduction peak E from the cyclic voltammogram results in a $\approx 50\%$ decrease in the magnitude of peak A (for $\nu = 100\text{mV s}^{-1}$).
- only $\approx 20\%$ of the oxidation products, of peak A, are reduced on the reverse sweep (at peak E), thus $\approx 80\%$ of peak A's reaction products either diffuse into solution and react further or are electro-inactive.
- addition of Fe²⁺ to the electrolyte significantly increased $i_{p,A}$, while Fe³⁺ additions had very little effect on $i_{p,A}$, but increased $i_{p,E}$.
- from RRDE studies the reaction $\text{Fe}^{\text{II}} \rightarrow \text{Fe}^{\text{III}} + \text{e}^-$ was shown to occur at the potential of peak A and the reduction of the Fe^{III} occurred in the potential region of peak E.
- the magnitude of peak A increases logarithmically with temperature over the temperature range 5°C to 80°C for $5\text{mV s}^{-1} \leq \nu \leq 1\text{V s}^{-1}$.

It is therefore proposed that metal dissolution must occur if rising current transients are to be observed. This is also found for anodic oxidation of iron and certain stainless steel alloys in NaOH where metal oxidation resulted in the appearance of rising current transients due to the nucleation and growth of a duplex surface film (*cf* chapter five).

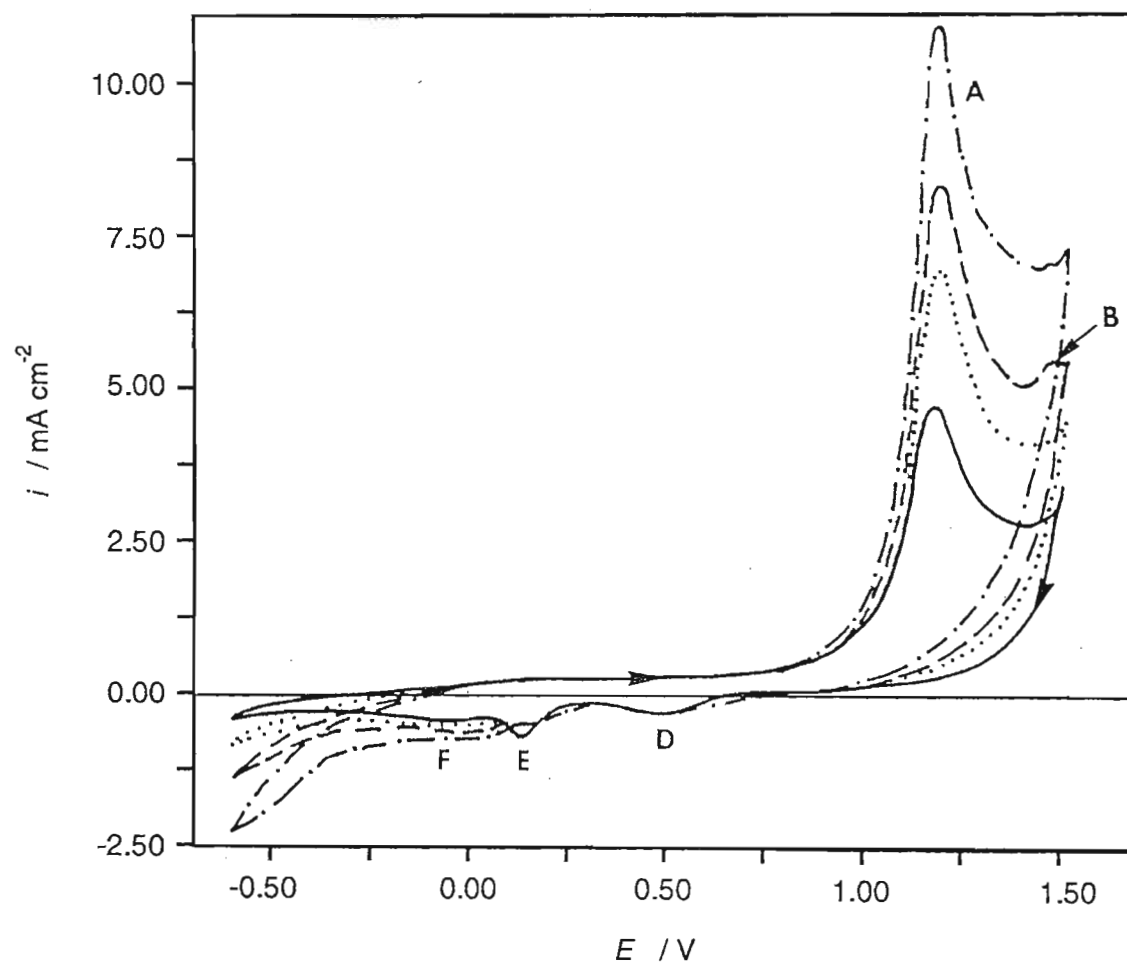


Fig. 4.2

Steady state voltammograms of a Fe18Cr electrode, at 20°C , swept between -0.60V and 1.50V at 100mV s^{-1} , $\omega = 100\text{rad s}^{-1}$.

————— 0.1M HClO_4
 0.3M HClO_4
 - - - - - 0.5M HClO_4
 - · - · - 1.0M HClO_4

4.1.2 NaHSO₄

In 0.1M NaHSO₄ the magnitude of peak A is less (by approximately 26%) than that observed in 0.1M H₂SO₄. On stepping the electrode to transpassive potentials rising transients were indeed observed in 0.1M NaHSO₄, however, they were broader and not as well defined as those in 0.1M H₂SO₄ with $i_{m,H_2SO_4} > i_{m,NaHSO_4}$. It was found that i_{m,H_2SO_4} is proportional to $i_{m,NaHSO_4}$, ie.

$$i_{m,H_2SO_4} = k (i_{m,NaHSO_4})$$

with k varying linearly as a function of applied potential, E , given by the relationship

$$k = 7.04 - 2.74E$$

The elapsed time corresponding to the maximum of the rising $i-t$ transients, t_m , increased by a factor of 1.3, in 0.1M NaHSO₄ compared to 0.1M H₂SO₄ irrespective of the final potential.

4.1.3 HClO₄

A similar result is observed in HClO₄ (0.1M to 1.0M). As can be seen from Fig. 4.2, the height of peak A increases as the HClO₄ concentration is increased with $i_{p,A}$ varying linearly with respect to the logarithm of the HClO₄ concentration according to

$$i_{p,A}/\text{mA cm}^{-2} = 9.95 + 6.08 \log[\text{HClO}_4]$$

Figs. 4.3a and 4.3b show typical rising transients obtained in HClO₄. The transients are broad and not as well defined as those in 0.1M H₂SO₄ (cf Fig. 4.1). As the HClO₄ concentration increased the transients became better defined with i_m increasing and t_m decreasing.

4.1.4 Na₂SO₄ and NaClO₄

Electrolytes in which peak A is not present (0.1M Na₂SO₄ and 0.1M NaClO₄) gave no rising current transients in the potential range -0.60V to 1.40V. Quantitative additions of H₂SO₄ to 0.1M Na₂SO₄ resulted in the appearance and growth of peak A, on the cyclic voltammogram (Fig. 4.4). A linear relationship was found between the increase in $i_{p,A}$ and $\log [\text{H}_2\text{SO}_4]_{\text{added}}$ as given by

$$i_{p,A}/\text{mA cm}^{-2} = 52.3 + 29.2 \log [\text{H}_2\text{SO}_4]_{\text{added}}$$

When the electrode was stepped to transpassive potentials the falling transients observed in pure 0.1M Na₂SO₄ were no longer observed, and instead rising transients were found, as shown in Figs. 4.5a and 4.5b. As the H₂SO₄ concentration increased the transients became more clearly defined as i_m increased and t_m decreased. A linear relationship was found between i_m and $\log [\text{H}_2\text{SO}_4]_{\text{added}}$; eg. for the 1.50V transient

$$i_m/\text{mA cm}^{-2} = 69.2 + 34.7 \log [\text{H}_2\text{SO}_4]_{\text{added}}$$

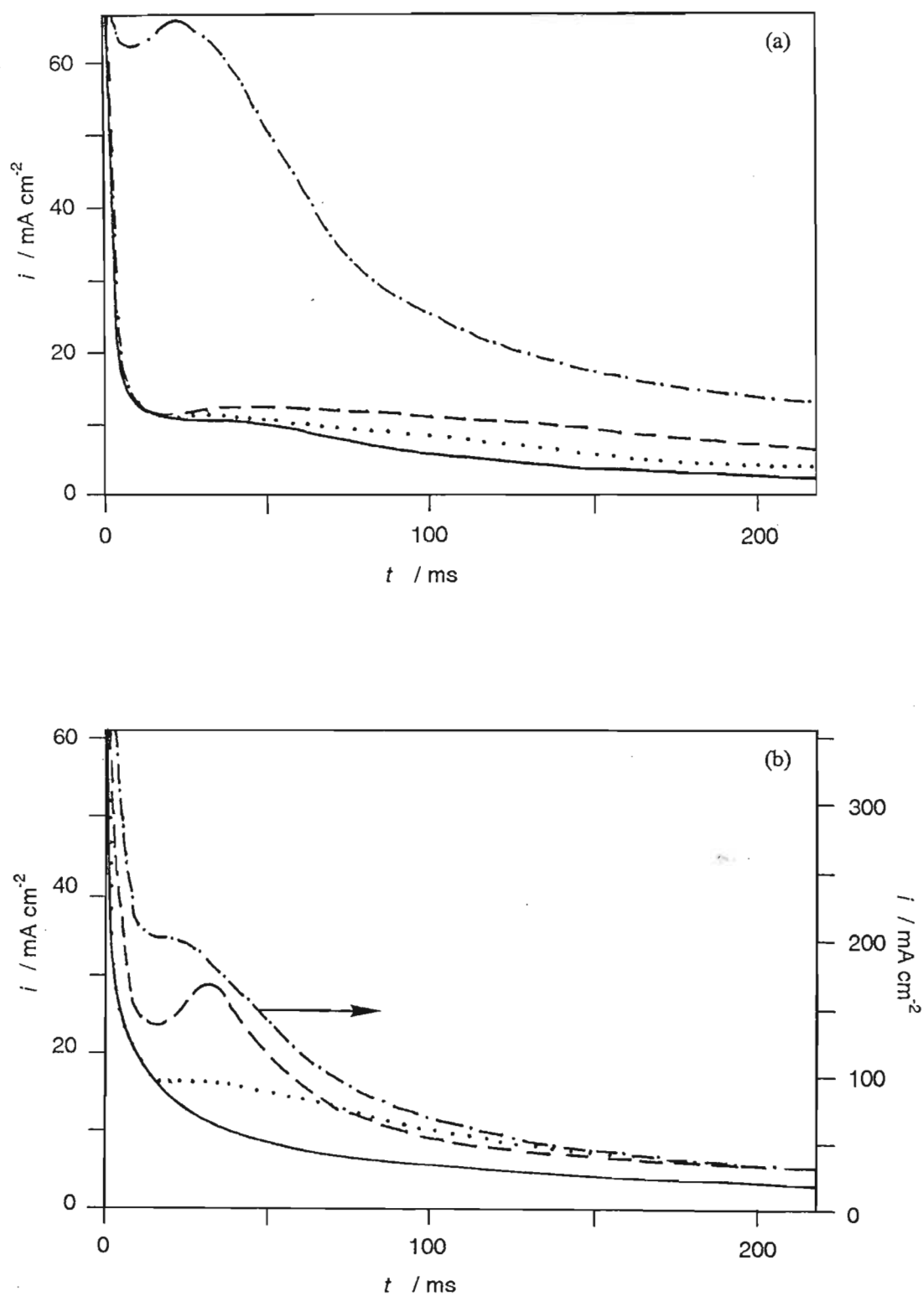


Fig. 4.3a,b Current transient response of a Fe18Cr electrode at (a) 1.30V and (b) 1.50V in

— 0.1M HClO_4
 0.3M HClO_4
 - - - 0.5M HClO_4
 - · - · - 1.0M HClO_4 . $T = 20^\circ\text{C}$.

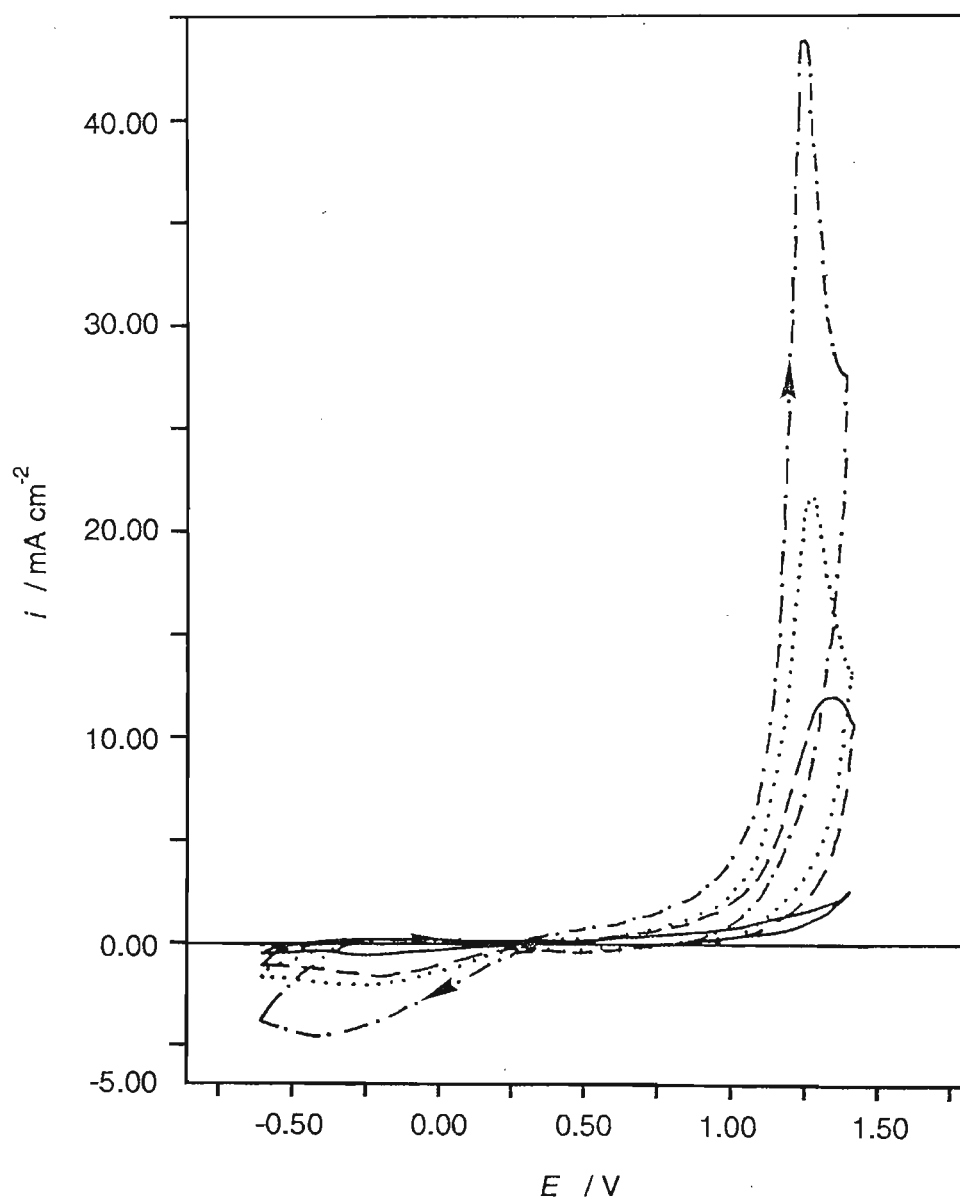


Fig. 4.4 Influence of H_2SO_4 on the steady state cyclic voltammograms of a Fe18Cr electrode, at 20°C , swept between -0.60V and 1.40V at 100mV s^{-1} , $\omega = 100\text{rad s}^{-1}$, in

- 0.1M Na_2SO_4
- 0.1M Na_2SO_4 + 0.04M H_2SO_4
- 0.1M Na_2SO_4 + 0.10M H_2SO_4
- · - · - 0.1M Na_2SO_4 + 0.50M H_2SO_4

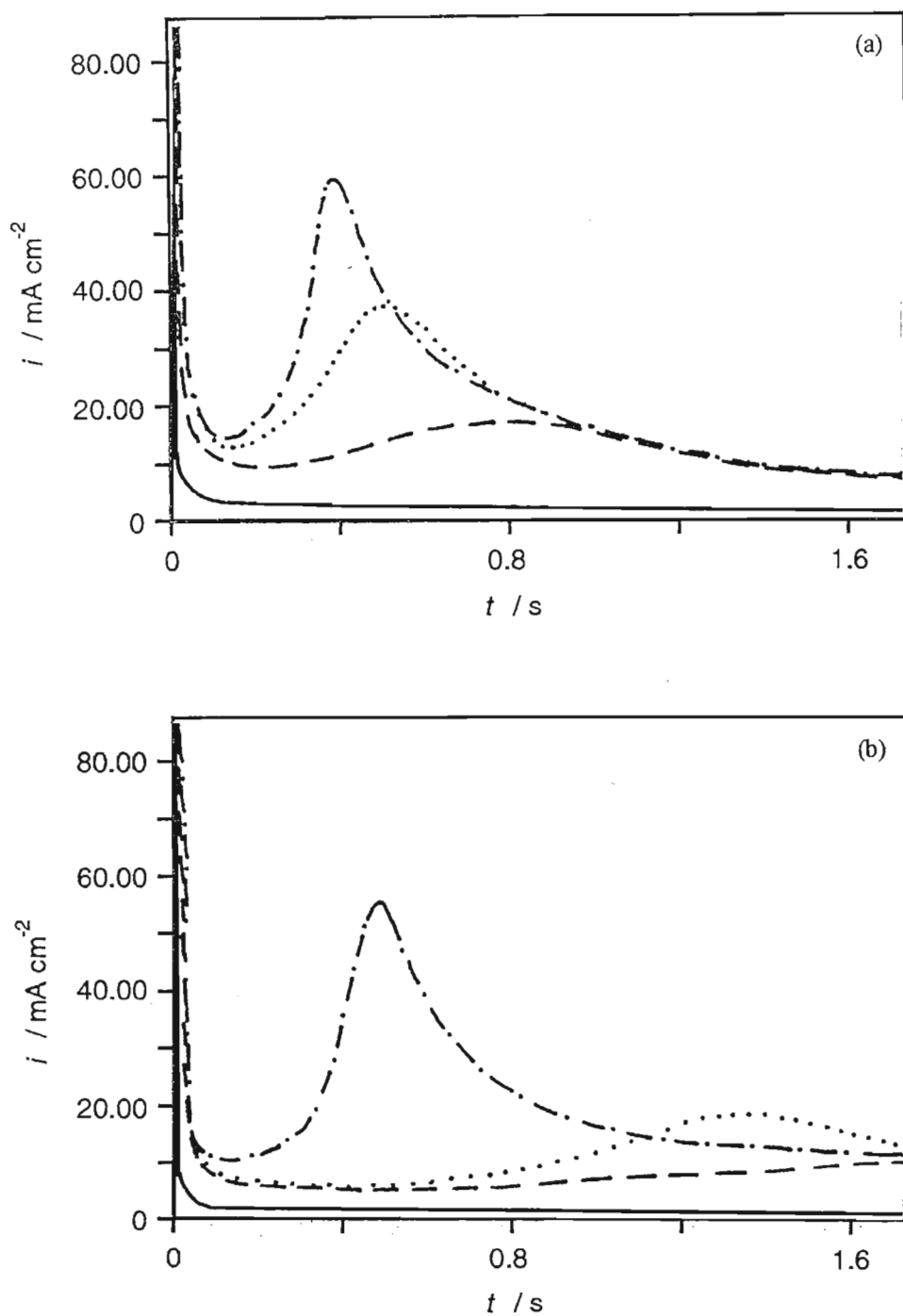


Fig. 4.5a,b

Chronoamperometric response of a Fe18Cr electrode at
(a) 1.30V and (b) 1.40V in

- 0.1M Na_2SO_4
- 0.1M Na_2SO_4 + 0.04M H_2SO_4
- 0.1M Na_2SO_4 + 0.10M H_2SO_4
- · - · - 0.1M Na_2SO_4 + 0.50M H_2SO_4 . $T = 20^\circ\text{C}$.

4.2 INFLUENCE OF ALLOY COMPOSITION

The influence of the substrate alloy composition on the nature and composition of the surface film has been extensively researched and reported on. Thus the alloying elements of a stainless steel should clearly have a significant influence on the nature of the current transients. To further investigate this phenomenon the influence of minor alloying elements and Cr content of the steels on the current transients, as well as the pure alloying elements, were studied.

4.2.1 Iron

Rising current transients were observed for pure iron in 0.1M H₂SO₄, as shown in Fig. 4.6, with the charging current decay followed by an increase in the current to a maximum after the application of a potential step. The time at which the maximum current (i_m) is first attained will be referred to as t_m in subsequent discussions of these Fe transients. Due to the time scale chosen in Fig. 4.6, the charging current decay is not observable. At $t < t_m$ the transient is of the same form as that reported by Bignold and Fleischmann.³⁴² At $t > t_m$ the current decays to a steady state value with the rate of decay increasing and the time at which this steady state current is attained, t_{ss} , decreasing as the final potential is made more positive. It is significant that these rising current transients were observed in the active - passive transition, and passive potential regions (see inset Fig. 4.6), whereas stainless steel alloys required the more positive transpassive potentials, as will be shown in 4.2.4 and 4.2.5. As can be seen in Fig. 4.6, at $t > t_m$ a smooth current decay is not observed, as the current decreases very rapidly to a final value. As the potential, E , to which the electrode was stepped was made more positive i_m increased and t_m decreased as given by the following equations

$$i_m / A \text{ cm}^{-2} = 0.17 + 0.33E$$

$$\log t_m = 2.77 - 0.24E$$

Rotating the electrode at various rotation rates ($0 \rightarrow 288 \text{ rad s}^{-1}$) had a marked effect on the transients, as shown in Fig. 4.7, with both i_m and t_m increasing with increasing rotation rate. For $\omega < 100 \text{ rad s}^{-1}$ t_{ss} increased and the final steady state current was greater than that obtained for a stationary electrode. At $\omega > 100 \text{ rad s}^{-1}$ the current did not decay at $t > t_m$ but maintained a value of approximately i_m .

4.2.2 Chromium

In the potential range investigated (-0.40V to 1.00V) only falling transients were obtained for pure chromium in 0.1M H₂SO₄. This response was not unexpected since no oxidation peaks were present on the cyclic voltammogram over this potential range. However, acquiring the transients more rapidly results in a response very similar to that observed with Fe18Cr at passive potentials (Fig. 4.8) i.e. rapid ($t_m =$

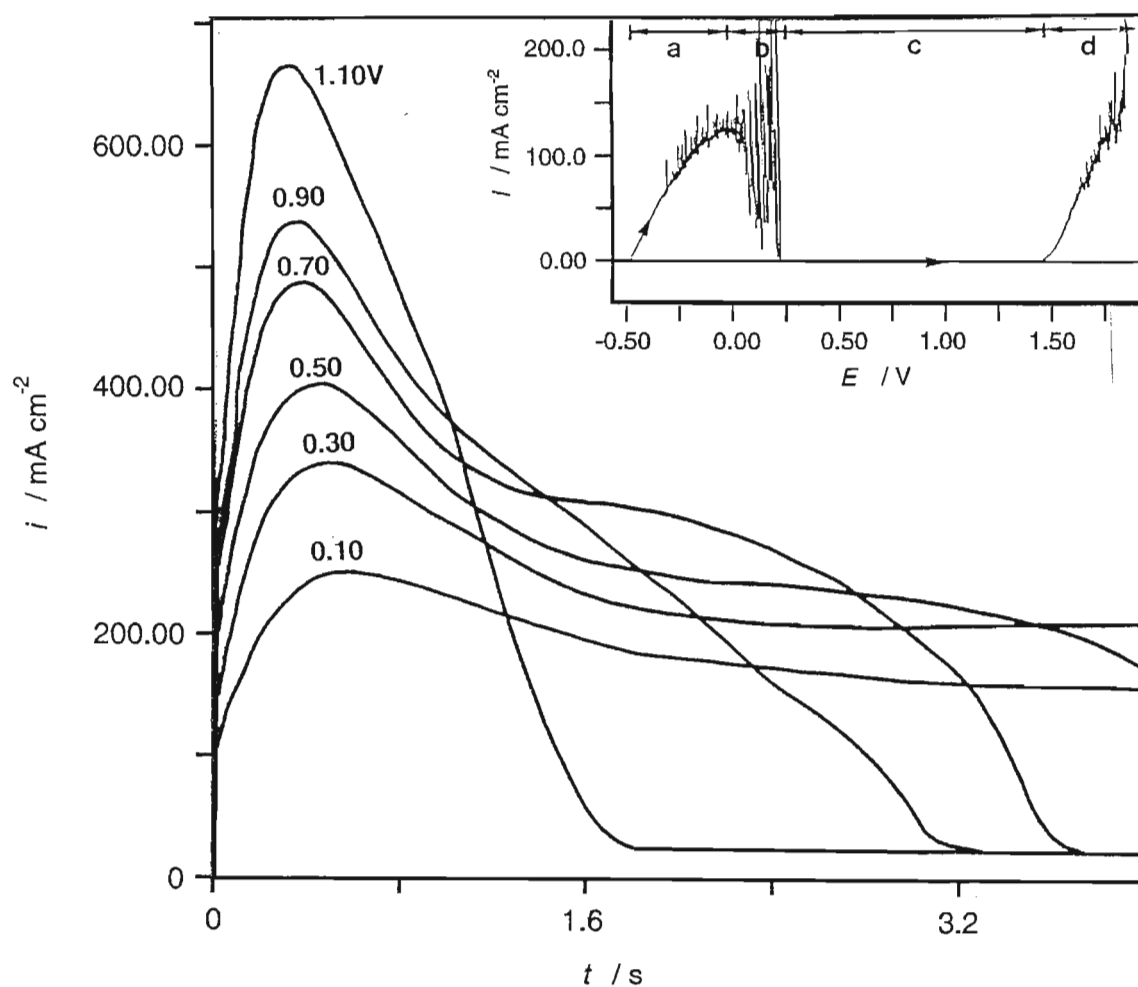


Fig. 4.6 Chronoamperometric response of a pure Fe electrode in 0.1M H₂SO₄, 20°C, at the indicated potentials.

Inset : Anodic polarisation curve of a pure Fe electrode in 0.1M H₂SO₄, swept at 2 mV s^{-1} showing the (a) active, (b) active - passive transition, (c) passive and (d) transpassive potential regions.

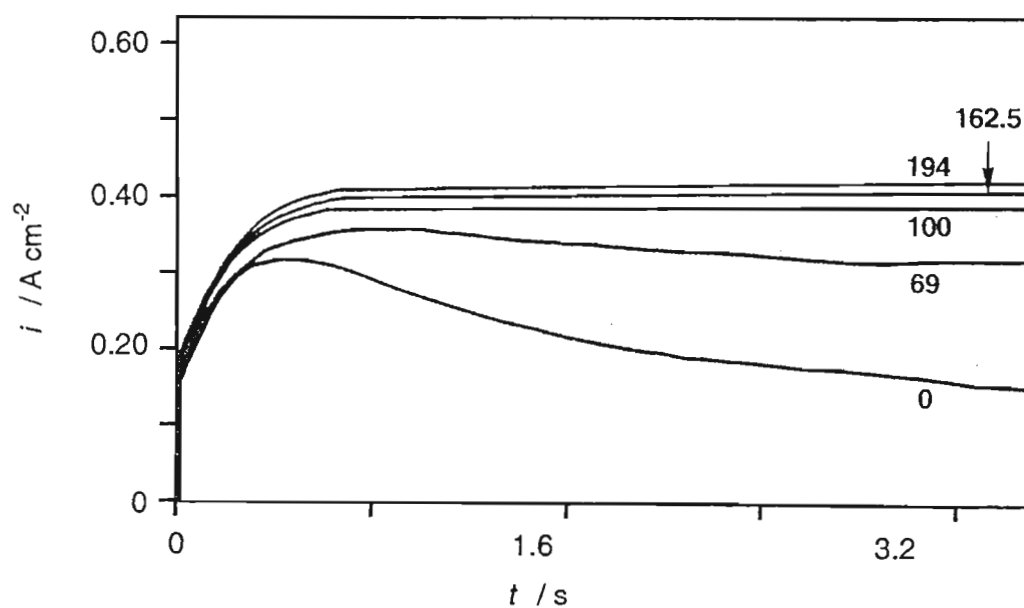


Fig. 4.7 Influence of rotation rate on the current transient response of a Fe electrode in 0.1M H_2SO_4 , 20°C, for the potential step $-0.45 \rightarrow 0.20\text{V}$. Rotation rates given in rad s^{-1} .

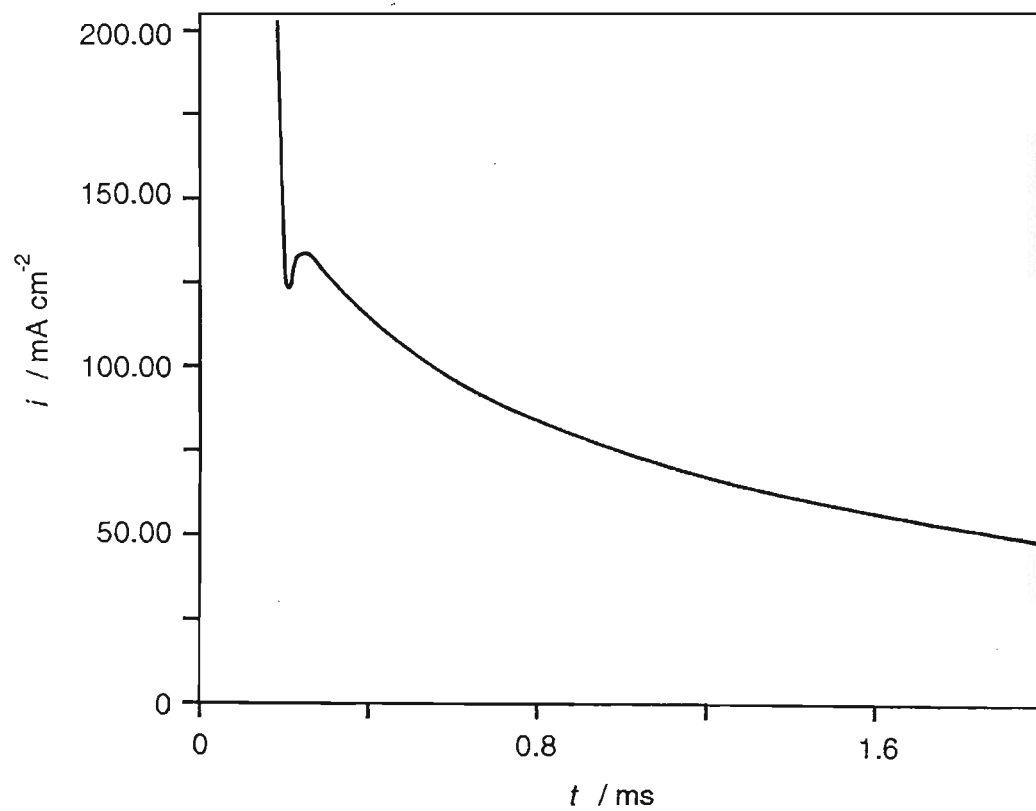


Fig. 4.8 Chronoamperometric response of a Fe18Cr electrode in 0.1M H_2SO_4 , 20°C, for the potential step $-0.60\text{V} \rightarrow 0.60\text{V}$.

150 μ s) rising transients, as shown in Fig. 4.9, due to the very rapid nucleation of a surface film which, together with the solid state passivation reactions, effectively passivates the entire electrode surface.

4.2.3 Molybdenum

The rapid dissolution of pure molybdenum in 0.1M H₂SO₄ results in the formation of a thick black surface deposit and in the appearance of two oxidation peaks at 0.156V and -0.077V on the cyclic voltammogram. Application of a potential step to a pure Mo electrode resulted in rising transients as shown in Fig. 4.10. These transients were unlike those observed with a stationary iron electrode and, as will be shown later, the stainless steel alloys, in that the current did not decay to a final steady state value but maintained a value of approximately i_m — a similar phenomenon to that observed for iron in 0.1M H₂SO₄ with $\omega > 100\text{rad s}^{-1}$ (cf Fig. 4.7).

4.2.4 FexCr

Transients were obtained using Fe16Cr, Fe18Cr, Fe20Cr and Fe23Cr in 0.1M H₂SO₄ in order to investigate the influence of the Cr content of an alloy on the chronoamperograms. At potentials greater than 1.00V rising current transients were obtained for all four alloys. The transients were qualitatively the same and with increasing Cr content of the alloy i_m decreased and t_m increased as demonstrated by the following series, for the 1.40V transient in 0.1M H₂SO₄:

	Fe16Cr	Fe18Cr	Fe20Cr	Fe23Cr
$i_m / \text{mA cm}^{-2}$	56.1	45.6	38.3	36.8
t_m / ms	88	107	151	204

4.2.5 Alloys 444 and 4733

Addition of molybdenum (1.78%) or vanadium (4.08%) to a Fe18Cr alloy resulted in similar rising transient phenomena to that observed with Fe18Cr, viz. at potentials negative to 1.00V falling transients were observed while at potentials greater than 1.00V the chronoamperometric current density increased to a maximum subsequent to the initial decay (Fig. 4.11). One significant difference was the presence of a second broad maximum II preceding the maximum I observed with alloy Fe18Cr. Maximum II was only discernible when the electrode was held at potentials in the range 1.05V to 1.30V. Despite the poorer reproducibility ($\pm 3\text{mA cm}^{-2}$, $\pm 100\text{ms}$) of II, compared to I, it was confirmed that without Mo or V in the alloy II did not appear. Maximum II was more pronounced on imperfectly polished (mechanically) electrodes. The presence of maximum II suggests the occurrence of two processes having different time constants or the presence of at least two types of surface films in this potential region. The charge for maximum II is very much less than that for maximum I indicating that the reaction responsible for I involves direct oxidation of the alloy and not conversion of the initial film to form the final film. AES depth

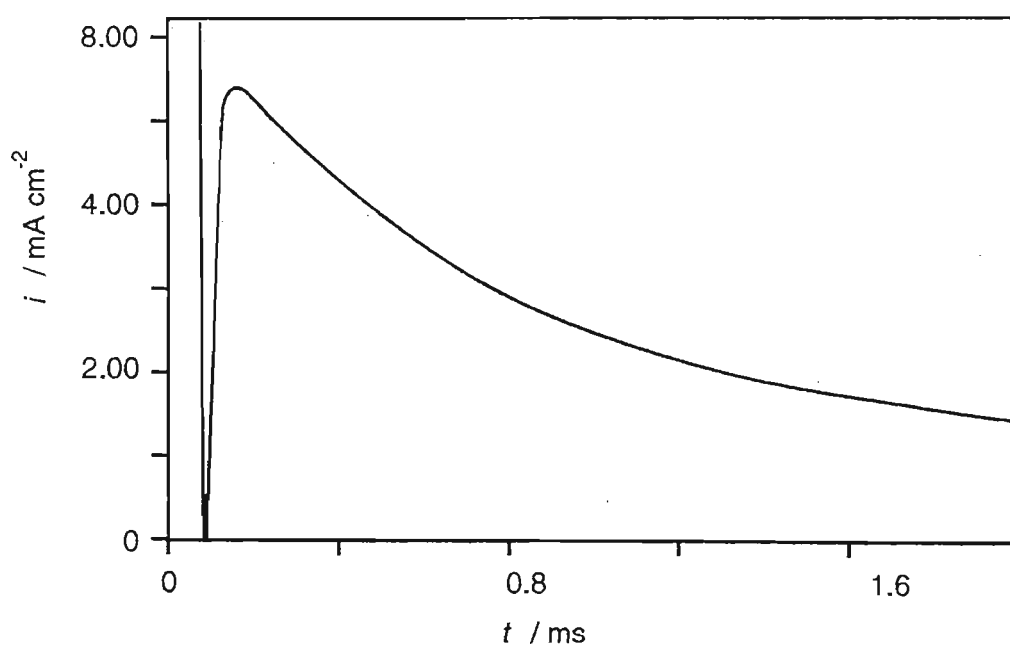


Fig. 4.9 Chronoamperometric response of a Cr electrode in 0.1M H_2SO_4 , 20°C, for the potential step $-0.45\text{V} \rightarrow 0.60\text{V}$.

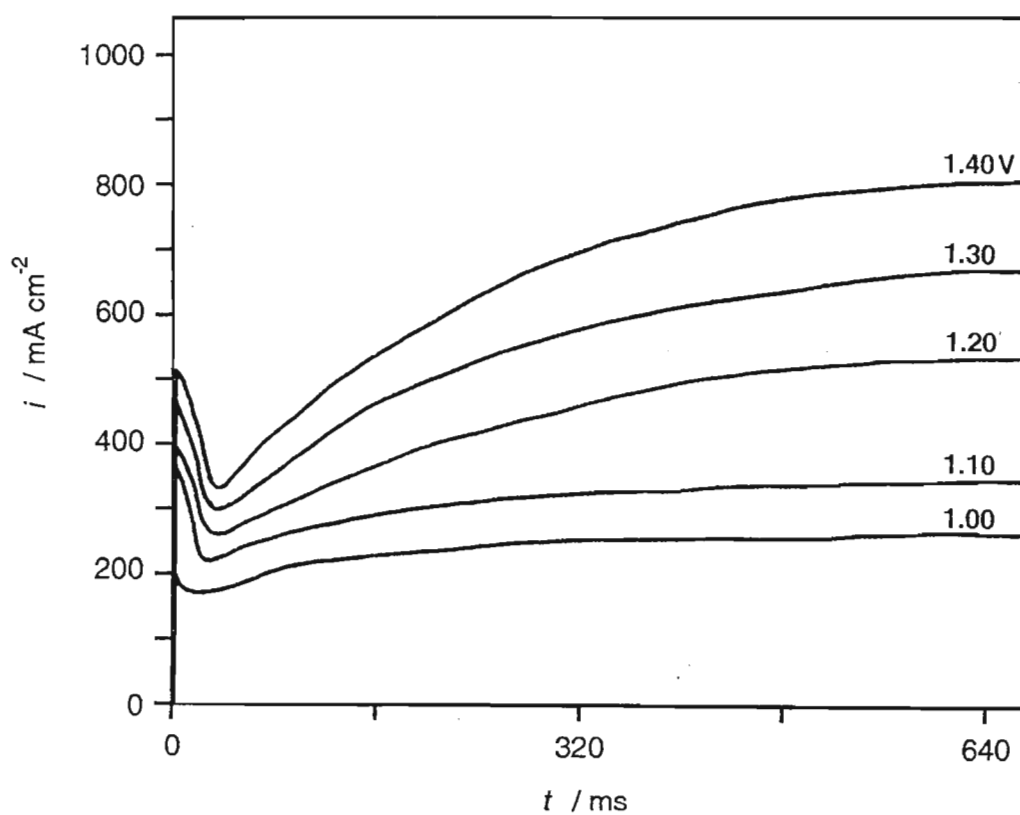


Fig. 4.10 Chronoamperometric response of a pure Mo electrode in 0.1M H₂SO₄, 20°C, at the indicated potentials.

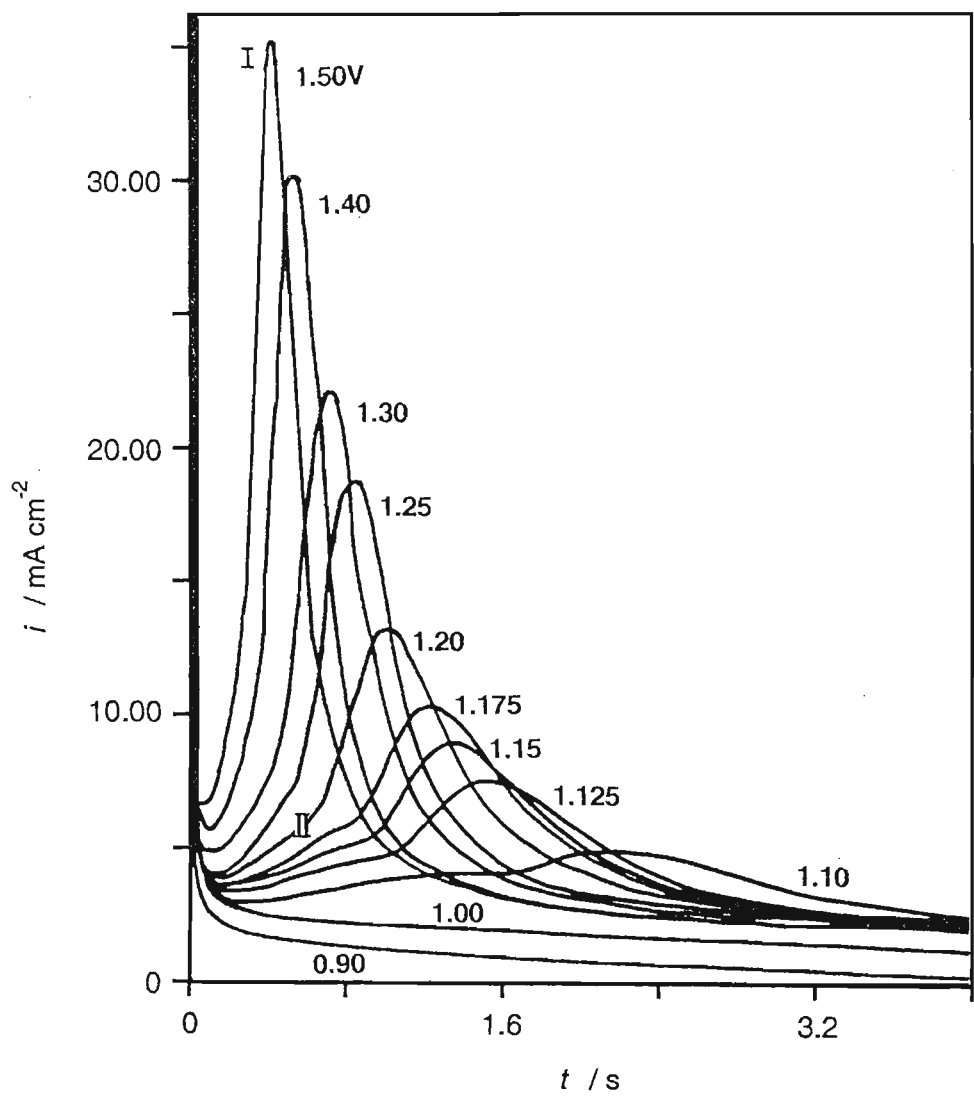


Fig. 4.11 Chronoamperometric response of alloy 444 in 0.1M H₂SO₄, 20°C, at the indicated potentials.

profiling of the two layers formed on a 444 electrode indicated Mo and Cr enrichment to 6.2% Mo and 46% Cr from 1.8% Mo and 18% Cr. A definite decision as to whether the enrichment occurred in the initial or upper or both layers could not be made, but available evidence³³ suggests that the initial surface layer that forms is molybdenum enriched while the subsequent second layer is chromium enriched. This suggestion is supported by the fact that t_m for pure Mo is virtually the same as t_m for maximum II. Since Mo corrodes rapidly in H_2SO_4 maximum II (444) would be expected to be more pronounced on scratched electrodes where dissolution would be expected to occur more extensively and more rapidly — this was found experimentally, as reported above.

The vanadium containing alloy, 4733, resulted in rising current transients that were qualitatively the same as the 444 transients, but in addition had a third, poorly defined maximum preceding the other two maxima as shown in Fig. 4.12. It should be noted that although the final current density of the 1.60V transient is greater than that of the transients obtained at lower potentials, the relative extent of the increase is less than that observed with Fe18Cr (*cf* Fig. 4.1) suggesting that the incorporation of V into the alloys creates a greater overvoltage for oxygen evolution.

4.3 INFLUENCE OF TEMPERATURE

The influence of temperature on the current transient response of alloy Fe18Cr in 0.1M H_2SO_4 was investigated. As can be seen in Figs. 4.13 and 4.14 $i_{p,A}$ increased as the temperature was increased from 5°C to 80°C for $0.005V s^{-1} \leq \nu \leq 1V s^{-1}$ and since a component of peak A involves a dissolution process such an increase is not unexpected. The activation energy for the dissolution process occurring at peak A decreased with increasing sweep rate, as shown in Fig. 4.14, and as given by the equation

$$E_a / kJ mol^{-1} = -7.71 \log(\nu) + 12.63$$

Over the entire temperature range rising current transients were obtained at potentials from 1.00V to 1.60V, and which were qualitatively the same as those observed at ambient temperatures. With increasing temperature t_m decreased logarithmically and i_m increased as shown in Fig. 4.15. This trend has also been observed for Fe and Fe18Cr in 0.5M and 1.0M NaOH, with and without CN^- present (see Chapter 5) and by Shoesmith *et al.*³⁴⁰ for Cu in 1.0M LiOH (with the exception of the 40°C transient in the latter study). While the first rising transient was observed at 1.10V at 10°C it was detected at 1.00V at $T \geq 50^\circ C$. This is as a result of transpassive dissolution commencing at more cathodic potentials as the temperature increases. At $T > 22^\circ C$ falling transients were observed at potentials more positive than 1.50V due to the increased dissolution preventing the formation of a stable film. Activation energies obtained from Arrhenius plots (Fig. 4.15), for surface film formation, decreased with increasing potential, as given below, due to oxidation occurring more readily at the higher potentials; i.e.

E / V	1.10	1.20	1.30	1.40	1.50
$E_a / kJ mol^{-1}$	31.1	26.0	25.5	23.9	24.3

Such values for activation energies are expected for a reaction that is, at least partly, diffusion controlled.³⁴⁰

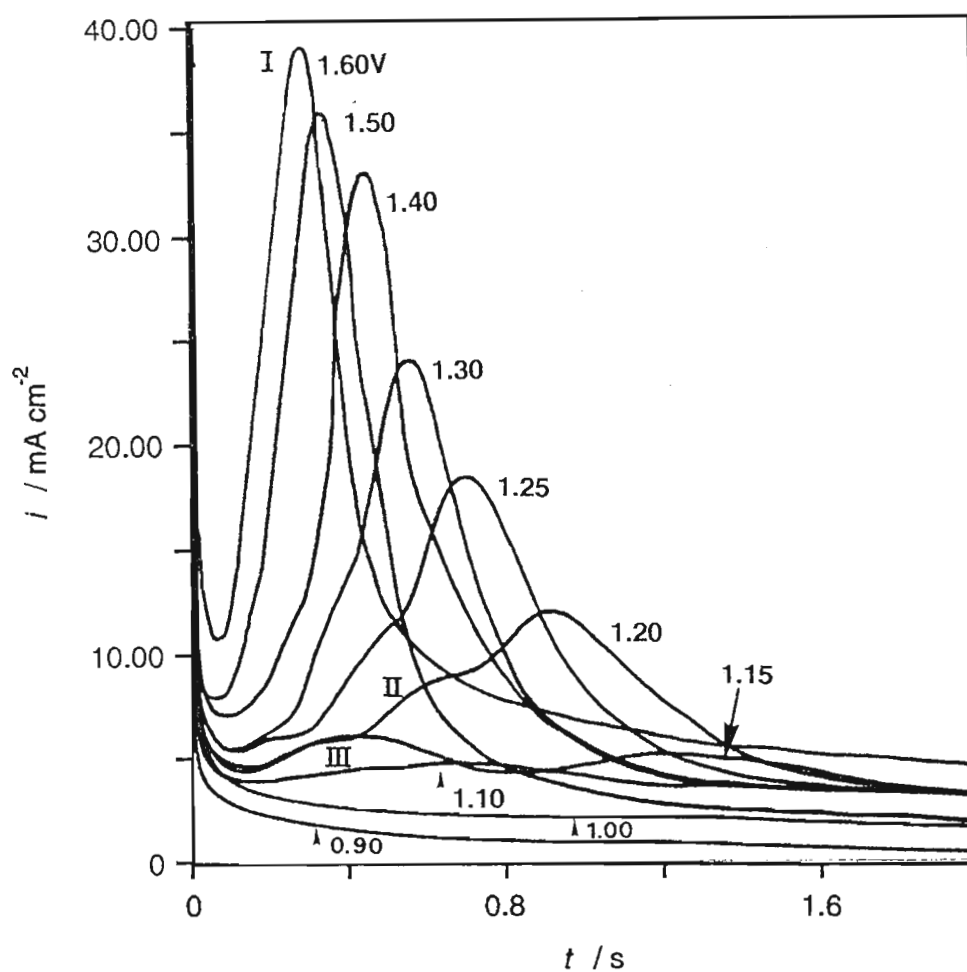


Fig. 4.12 Chronoamperometric response of alloy 4733 in 0.1M H₂SO₄, 20°C, at the indicated potentials.

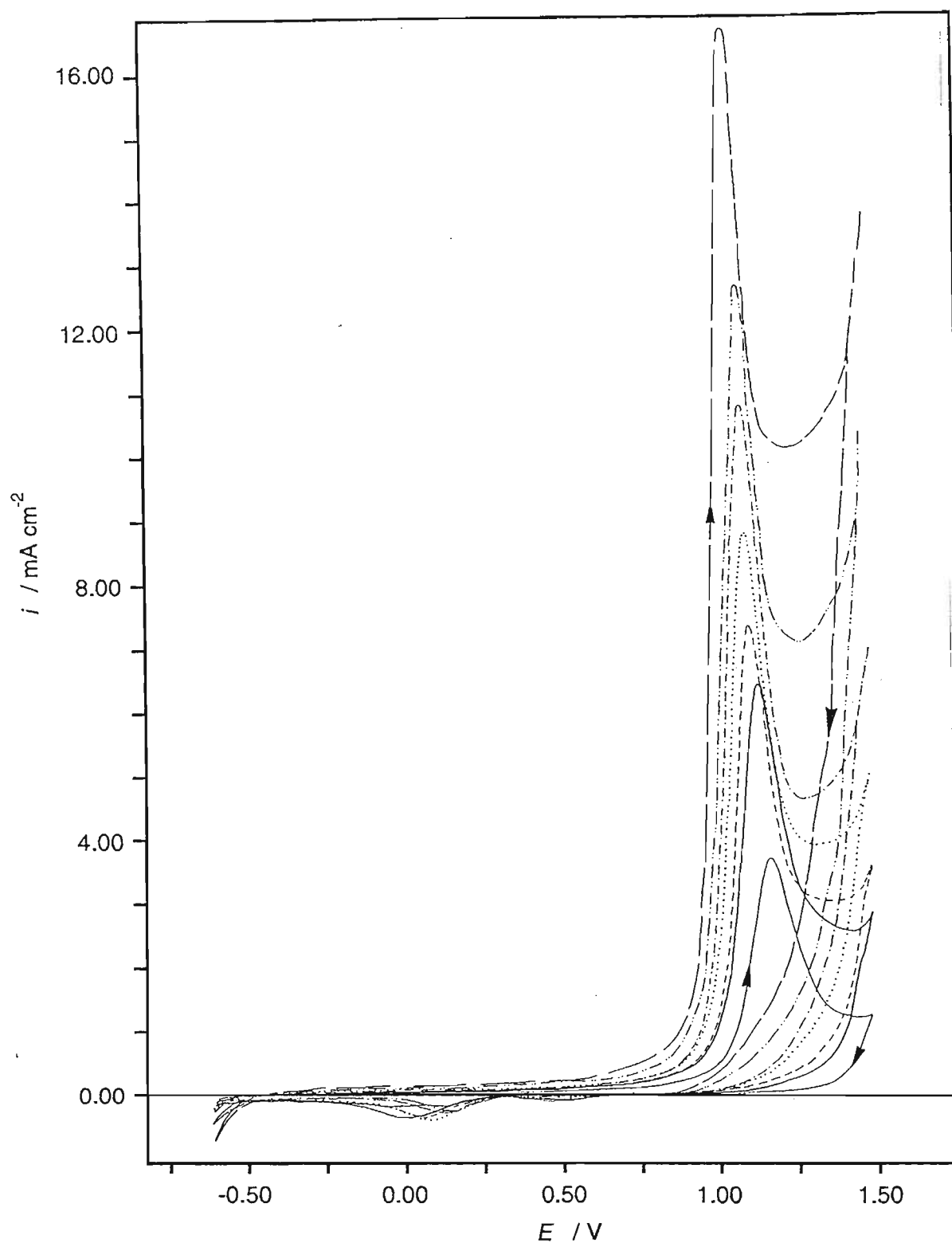


Fig. 4.13 Steady state cyclic voltammograms of a Fe18Cr electrode swept between -0.60V and 1.50V at 100mV s^{-1} , $\omega = 100\text{rad s}^{-1}$, in $0.1\text{M H}_2\text{SO}_4$ at

—	10°C	—	22°C
---	30°C	40°C
-.-.-	50°C	-.-.-	60°C
—	70°C		

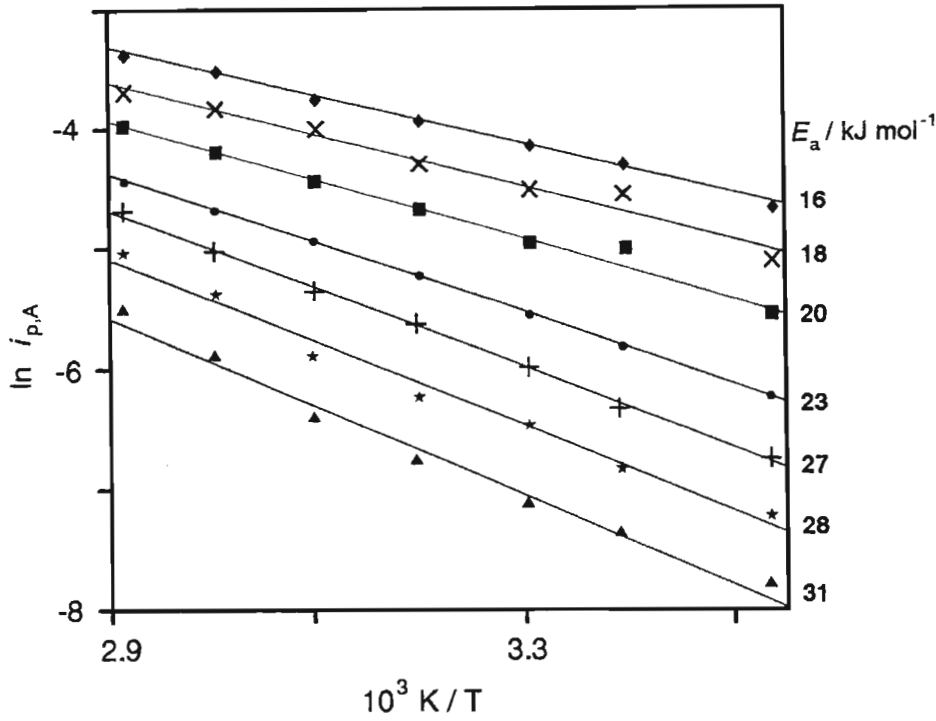


Fig. 4.14 Arrhenius plot for peak A of the cyclic voltammograms of a Fe18Cr alloy electrode in 0.1M H₂SO₄ swept between -0.60V and 1.50V at

- | | |
|-------------------------|------------------------------|
| ▲ 5mV s ⁻¹ | ★ 10mV s ⁻¹ |
| + 20mV s ⁻¹ | • 40mV s ⁻¹ |
| ■ 100mV s ⁻¹ | × 200mV s ⁻¹ |
| ◆ 400mV s ⁻¹ | ω = 100rad s ⁻¹ . |

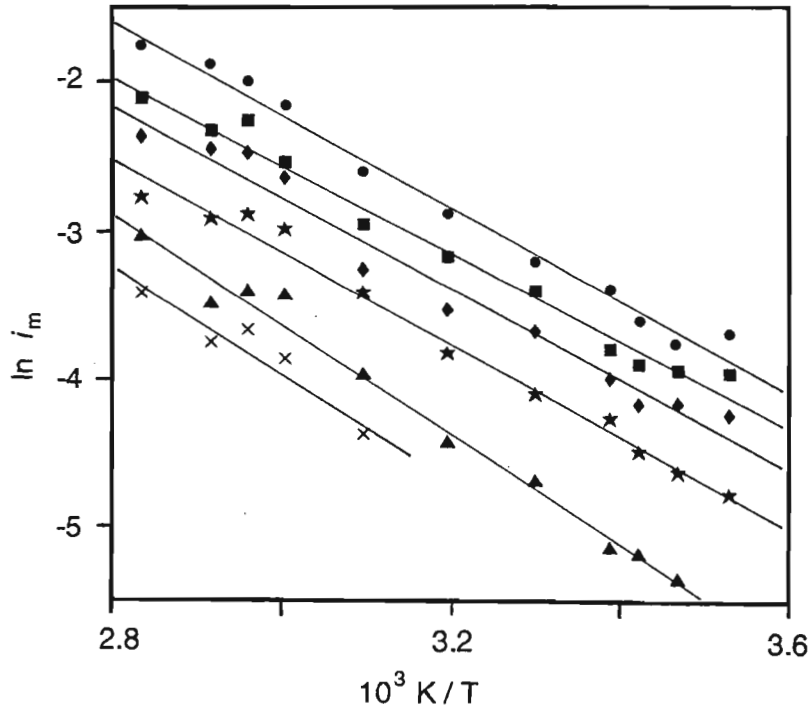


Fig. 4.15 Arrhenius plot of the chronoamperometric current maxima, i_m , for a Fe18Cr alloy electrode in 0.1M H₂SO₄ at

- | | |
|---------|---------|
| × 1.00V | ▲ 1.10V |
| ★ 1.20V | ◆ 1.30V |
| ■ 1.40V | • 1.50V |

4.4 SEM ANALYSIS OF THE ELECTRODE SURFACE

Qualitative SEM analysis of a Fe18Cr electrode surface subsequent to a potential step to transpassive potentials showed three dimensional deposits of differing sizes, corresponding to different stages of growth (Figs. 4.16a, b). The electrode surfaces and deposits thereon were very similar for both the 0.1M H_2SO_4 and 0.1M HClO_4 experiments. Thus the physical nature of the growth centres does not account for the well defined transients obtained with H_2SO_4 compared to the broad and poorly defined ones obtained with HClO_4 . It should be noted that for Fe18Cr electrodes not subjected to a potential step, or which were stepped to potentials at which rising transients were not observed, no surface deposits were evident on the electrode.

SEM examination of the iron electrode in 0.1M H_2SO_4 showed the presence of large surface deposits with a topography very similar to those observed on Fe18Cr electrodes. Numerous smaller deposits, of a fairly uniform size, were also present as can be seen in Figs. 4.17a and 4.17b. Although not evident in Figs. 4.16 and 4.17, at higher magnifications the similarity in the topography of the surface features on the Fe and Fe18Cr electrodes suggests that the anodic film formed on Fe18Cr at transpassive potentials consists predominantly of Fe based compounds — probably an iron oxide or oxyhydroxide.

The dominant features observed on the Mo electrode surface were large deposits, an example of which is shown in Fig. 4.18. Very few smaller deposits were present — as was the case with Fe18Cr but in contrast to Fe.

4.5 FORMATION OF A COMPACT WHITE FILM ON THE SURFACE OF ALLOYS Fe18Cr AND 444

If a number of potential steps (>20), from active to transpassive potentials, are applied successively to a Fe18Cr or 444 electrode in 0.1M H_2SO_4 without polishing the electrode between each potential step, the current response which initially has the expected rising transient form eventually becomes a falling transient. If the electrode is examined at this stage, a white surface film is found to cover the entire electrode surface. As can be seen in Figs. 4.19a and 4.19b, the film is very compact although a number of pit-like indentations are present on the film surface.

It is proposed that this white film is a protective passive film that has formed on the surface. As it is formed by a series of repetitive potential steps to transpassive potentials, it is likely that the number of surface film nucleation sites is such that with their subsequent growth the electrode surface is completely covered with, and passivated by, the surface film. This is supported by the fact that subsequent to the

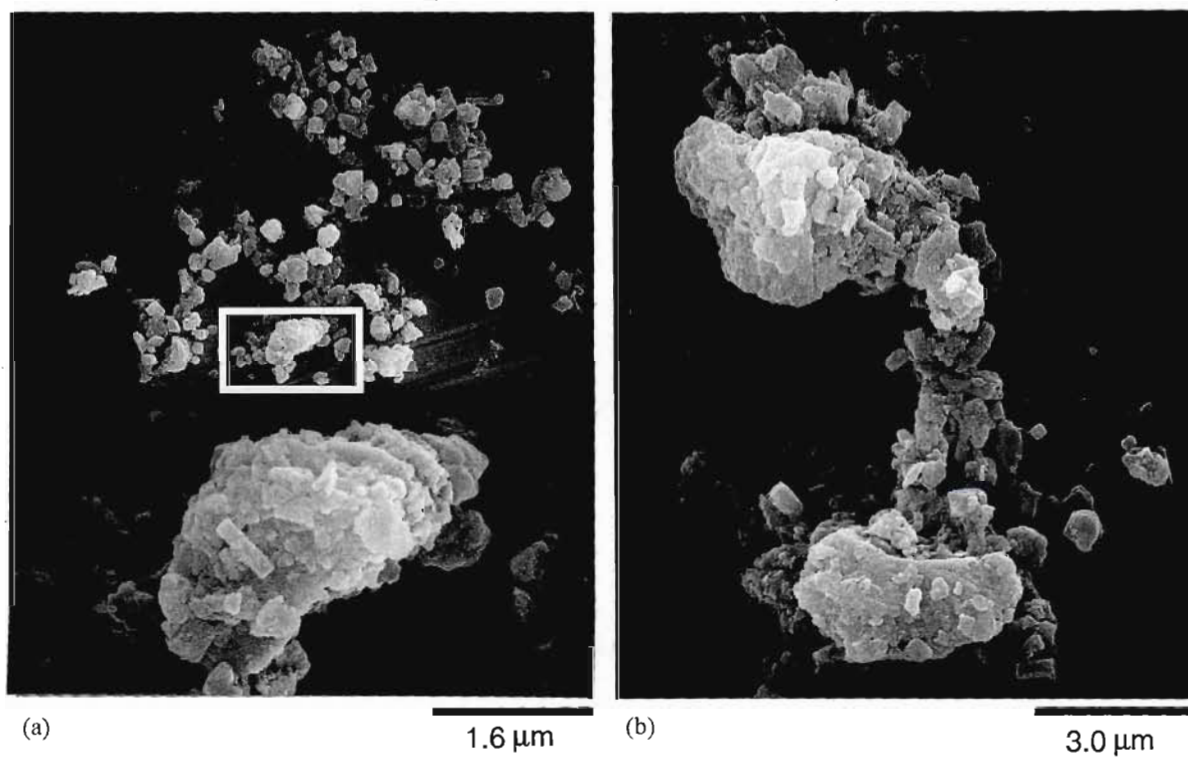


Fig. 4.16a,b SEM micrographs of the growth centres on a Fe18Cr alloy electrode in 0.1M H_2SO_4 , 20°C, obtained subsequent to the potential step $-0.60\text{V} \rightarrow 1.30\text{V}$.

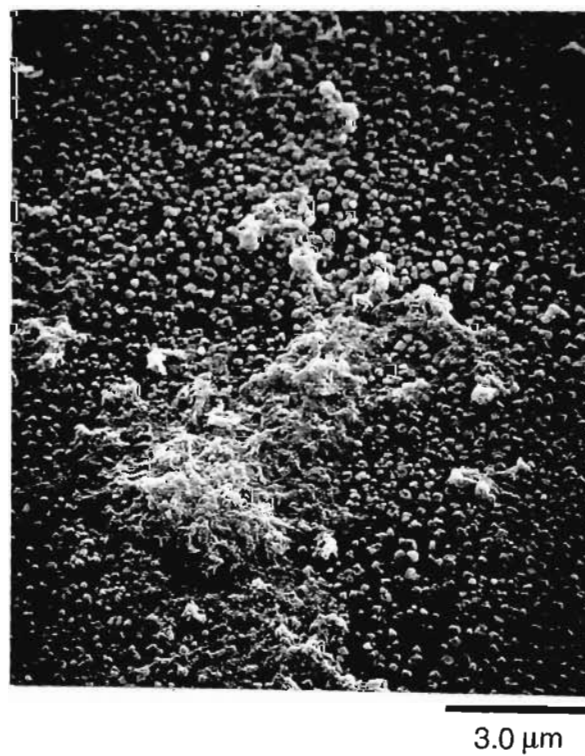


Fig. 4.17 SEM micrograph showing the surface deposits on a Fe electrode in 0.1M H_2SO_4 , 20°C, obtained after the potential step $-0.45\text{V} \rightarrow 0.60\text{V}$.

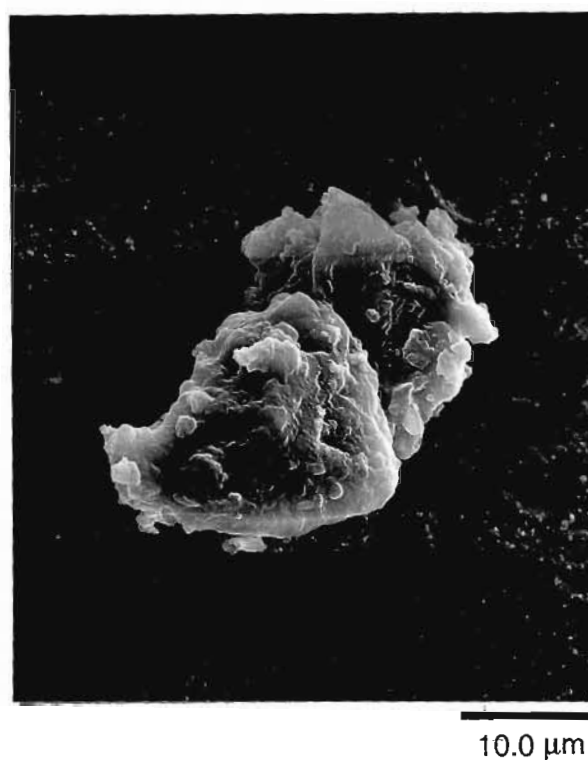


Fig. 4.18 SEM micrograph of a large growth centre on a Mo electrode in 0.1M H_2SO_4 , 20°C, after the potential step $-0.40\text{V} \rightarrow 0.40\text{V}$.

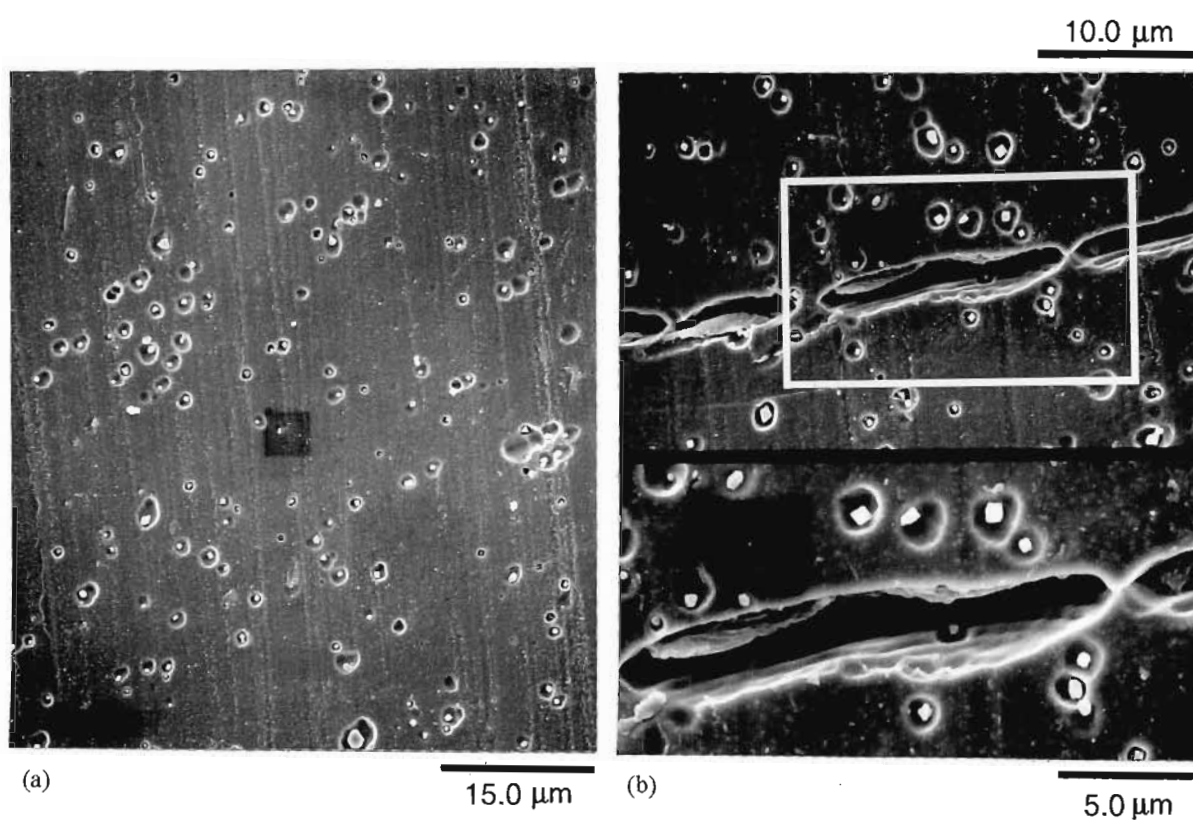


Fig. 4.19a,b SEM micrographs of the white film formed on a Fe18Cr alloy electrode surface in 0.1M H_2SO_4 , 20°C, subsequent to the potential regime $-0.60\text{V} \rightarrow 1.35\text{V}$ (repeated 150 times).

appearance of this white film

- the current response to any further potential steps is that of a falling transient
- if the electrode is left at its rest potential for ≈ 30 min, no significant current fluctuations are observed during this period
- the surface film adheres very well to the electrode (not washed or rubbed off easily)
- SEM evidence of complete coverage of electrode surface with a compact film.

Auger depth profiling of this white film showed that Cr decreased from 52% to 21% while Fe increased from 40 % to 73% and Mo decreased from 8% to 3.5% indicating that the film is enriched in Cr and Mo. As it has been reported that Auger analysis of such surface films tends to underestimate Mo concentrations¹⁸ this last result is particularly interesting since although surface films on Fe18Cr type stainless steels are generally found to be enriched in Cr, contrary findings as to the absence or presence of Mo or molybdenum oxides within the film have been reported in the literature.

From the depth profiles no indication as to the position of Mo within the film is given, nor can any information be obtained from the AES spectra as to whether Mo is present in the elemental or oxidised form. Due to the fact that the surface film is extremely thin and its good adherence to the substrate metal a sufficient quantity of the film could not be removed for x - ray diffraction analysis. Attempts to grow a thicker film were unsuccessful in that breakdown of the film eventually occurred resulting in the onset of general corrosion.

4.6 ANALYSIS OF TRANSIENTS

i vs t^n plots, pertaining to the various nucleation theories, were used for the diagnostic evaluation^{225,243-246,343} of the experimental data. While the nucleation model most likely to account for the SEM observations of the Fe18Cr electrode surface is that of progressive nucleation and three dimensional growth, the situation appears to be more complex for Fe. The large number of smaller surface deposits of similar shape and size suggest an instantaneous nucleation mechanism. However, the presence of several very much larger particles indicates that this is followed by the preferential growth of certain deposits or regions of deposits which suggests a type of progressive mechanism. Subsequent to nucleation, the growth of the active sites is three dimensional.

4.6.1 Fe Transients

With the exception of the data points just prior to the maximum, linear i vs $t^{1/2}$ plots for the rising section of the transients, in Fig. 4.6, were obtained. This suggests that initially nucleation is instantaneous. Dimensionless plots of i/i_m vs t/t_m for the diagnostic evaluation of the transients, as shown in Fig. 4.20, support this suggestion, which is further verified in Fig. 4.17 by the numerous small deposits of similar size

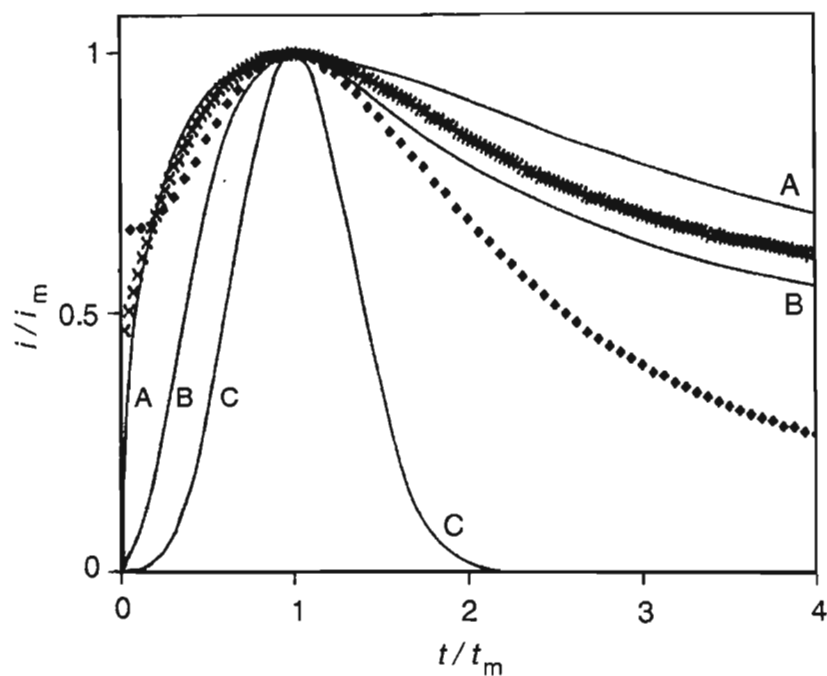


Fig. 4.20

Dimensionless plot of the (x) 0.60V transient in Fig. 4.6 (Fe) and the (♦) 1.30V transient in Fig. 4.1 (Fe18Cr).

The theoretical nucleation curves correspond to

(A) instantaneous nucleation and 3D growth (eqn. 2.19)

(B) progressive nucleation and 3D growth (eqn. 2.18) and

(C) progressive nucleation and 3D growth leading to complete passivation (eqn. 2.40).

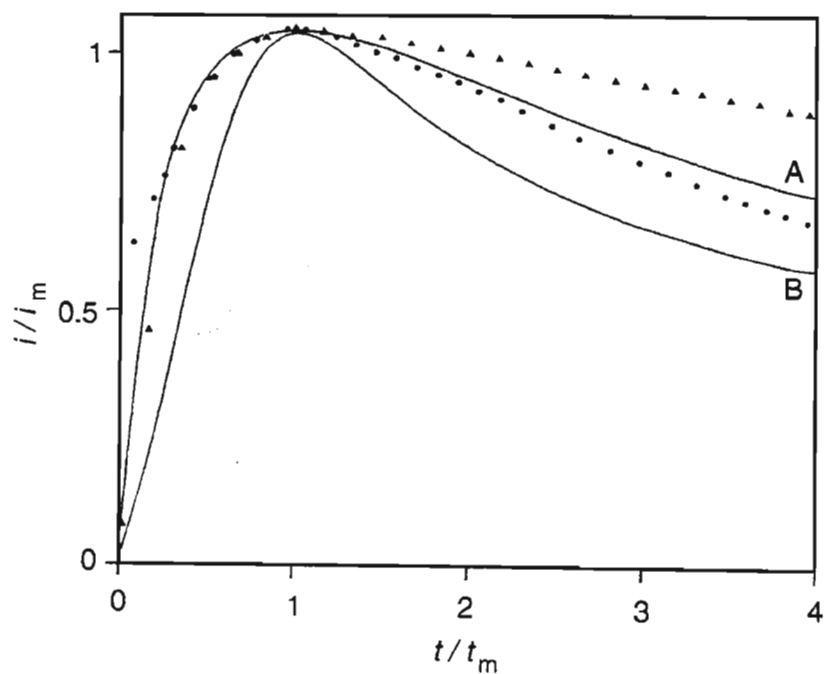


Fig. 4.21

Dimensionless plot of the (•) Fe18Cr transient in Fig. 4.8 and the (▲) Cr transient in Fig. 4.9.

The theoretical nucleation curves correspond to

(A) instantaneous nucleation and 3D growth (eqn. 2.19)

(B) progressive nucleation and 3D growth (eqn. 2.18)

and shape. Deviation of the experimental curve from the theoretical curve (A), in Fig. 4.20, is evident. A possible explanation is provided by the SEM data; the presence of several large surface deposits indicate regions of accelerated growth, which would be described by a progressive nucleation and growth mechanism. The situation is analogous to that of Ostwald ripening whereby the solubility of crystals (in this situation, surface film growth centres) increases with decreasing size resulting in the larger growth centres attracting material from these smaller growth centres. This would result in the experimental curve being lower than the instantaneous curve (A) at $t < t_m$ — as is indeed the case. The progressive nucleation and three dimensional growth of these preferential sites could also account for the fact that at $t > t_m$ the experimental data curve is closer to and has the general shape of curve (B) which is consistent with the previous discussion. Thus it is suggested that the rising current transients obtained for Fe in 0.1M H_2SO_4 are the result of instantaneous nucleation and three dimensional growth which is subsequently replaced or dominated by a progressive nucleation and 3D growth mechanism.

While the fit of the experimental data to the theoretical curves is not conclusive evidence as to the mechanism of anodic film formation, it does however provide a basis for the modelling of the process. It is also noted that the present fit is as good as, and in some cases better than, those presented in the literature,^{225,246,344} even though it is clear that existing nucleation models are inadequate in completely describing the present results.

4.6.2 Fe18Cr Transients

Fe18Cr transients not exhibiting the current maximum, obtained at potentials cathodic of 1.00V (Fig. 4.1) showed a linear $i - t^{-1/2}$ relationship, having a diffusion coefficient of the order of $10^{-9} cm^2 s^{-1}$, possibly indicative of solid state diffusion.^{345,346} At potentials at which rising current transients were obtained, progressive nucleation and three dimensional growth has been suggested³³⁷ as the most likely mechanism for anodic film formation. Fig. 4.16 provides convincing evidence for this proposal. Rejection of the instantaneous nucleation model is supported by the non-linearity of the i vs $t^{1/2}$ plots corresponding to the rising section of the transient. While neither i vs $t^{3/2}$ (progressive 3D) nor i vs t^2 (progressive 2D) plots were linear, for the rising section of the transient, the latter plot exhibited the greater deviation from linearity. Dimensionless i/i_m vs t/t_m plots, while confirming neither instantaneous nor progressive nucleation of a surface film, were of a similar form to the latter having a concave, as opposed to a convex, shape at $t/t_m < 1$ (Fig. 4.20). A possible cause of the discrepancy between the theoretical and experimental curves may be dissolution of the alloy, which will be discussed later. Hence it is proposed that the rising section of the current transient corresponds to progressive three dimensional nucleation of an anodic surface film in the secondary passivation potential region. With the exception of a previous publication from this laboratory³³⁷ such a phenomenon has not previously been reported for Fe18Cr stainless steels.

At $t/t_m > 1$, i/i_m for the experimental curve is lower than the theoretical curve for progressive

nucleation and 3D growth (B) and very much greater than that for three dimensional growth leading to passivation (C), as shown on Fig. 4.20. Deviation from linearity for i vs t^n plots and of the experimental points from the theoretical curves for the dimensionless i/i_m vs t/t_m plots is apparent. Limitations and shortcomings of existing nucleation models have been discussed in section 2.11 and as the present data has shown a more realistic model is necessary to describe anodic film formation on a corroding metal substrate. Initially it had been the intention of this work to provide a realistic, quantitative model to describe the observed current transients. However, after consideration of the complexity of the mathematics involved in such a model, and notwithstanding the comments by other researchers^{255,256,260,263,272} in this regard, a quantitative description of the transients will not be attempted in this thesis as the simplifying assumption required by the mathematics would merely result in a model that is as unrealistic as those presented in the literature. Thus the following phenomenological model is proposed to describe the rising current transients observed in Figs. 4.1 and 4.6.

4.6.3 Nucleation Model

Inhomogeneities and surface defects present on the electrode surface result in active sites which will corrode preferentially or at an accelerated rate with respect to the rest of the electrode surface. These sites are analogous to the nucleation sites reported in electrocrystallisation studies. Imposing a potential step, to an appropriate potential, on a Fe18Cr based stainless steel alloy electrode results in dissolution of the alloy predominantly at these active sites. This results in localised surface roughening and an increase in the electrode surface area with a corresponding increase in the current — as is observed subsequent to the decay of the initial charging current. Preferential dissolution of Fe from Fe18Cr type alloys has been reported extensively in the literature, and atomic absorption analysis of the electrolyte, taken from near the electrode surface using a Teflon sampling tube, with a stationary electrode held at transpassive potentials, confirmed this for the alloys used in the present study. It is generally accepted^{347,348} that transpassive dissolution of iron results in the formation of Fe^{2+} although it has also been reported [references 40 and 41 quoted in reference 348] that at the cathodic end of the transpassive region, below a critical current density, Fe^{3+} was produced. In fact Frankenthal and Pickering³⁴⁹ have shown that for an Fe electrode Fe^{3+} (in solution) can react with the Fe to form Fe^{2+} and thereby polarise the iron to more cathodic potentials which in turn will facilitate further electrode dissolution. Since the solution is quiescent, accumulation of the Fe^{2+} in the diffusion layer near the electrode surface will result in localised regions, in the vicinity of the active sites, with a high Fe^{2+} concentration such that the electrolyte becomes supersaturated with the dissolving species. Once the required level of supersaturation is reached, at time t_{sat} ($t_{\text{sat}} < t_m$), deposition of an anodic surface film will occur. Since this process significantly impedes the dissolution of the electrode, and considering the time scale of events, it is proposed that the deposition occurs on the active sites. By repassivating these sites the active surface area will be reduced resulting in a decrease in the current, as is manifested by the appearance of the maximum i_m of the transient. Once these sites have been passivated, continued deposition and/or growth of the surface film on these sites will continue for as long as the required level of supersaturation is maintained. Such continued growth will further reduce the

active surface area as reflected by the decrease in the current at $t > t_m$. As the oxide is porous, dissolution continues through the pores of the oxide. However, a point is reached at which the rate of dissolution of iron species through the pores is such that a steady state is attained as indicated by the final steady state current.

Such a model would account for the observation that at t_m the electrode surface is not covered entirely by nucleation centres, contrary to that predicted from other electrocrystallisation studies.³⁴³ SEM analysis of the electrodes did not show significant overlap of neighbouring nuclei such as to cover the electrode surface, up to two seconds after stepping to the final potential. As can be seen from Figs. 4.16 and 4.17 the surface coverage by the growth centres is very much less for Fe18Cr than for Fe in keeping with the concept of selected active sites which would be expected to be more limited in number for stainless steels than for iron.

The precondition of supersaturation of a metal salt solution prior to passivation has been well documented and the formation of a salt film having been proposed as a necessary precursor to passivation in many repassivation processes. Beck²⁸ suggested the formation of a salt film, possibly $\text{FeSO}_4 \cdot 7\text{H}_2\text{O}$, on the electrode surface which, once formed, allows the formation of an oxide beneath it. The salt film thins and eventually disappears leaving only the oxide on the surface. The time taken for the salt film to disappear varies considerably depending on the electrode and electrolyte composition and on the experimental conditions. The anodic polarisation curve of Fe (Fig. 4.6, inset) provides evidence for the formation of a salt film with the current fluctuations in the active - passive transition potential region having been associated with salt films.^{28,31} Bartlett and Stephenson³¹ attributed their presence to the formation of the film, while Beck²⁸ proposed that the oscillatory behaviour was due to the changes in pH at the electrode surface, beneath the salt film. Danielson³⁴³ showed that the principal function of a salt film in the passivation process was to provide a region with a sufficient potential drop that the pH at the metal / salt interface can become sufficiently basic that oxide growth is possible.

With the exception of $\text{FeSO}_4 \cdot \text{H}_2\text{O}$ and $\text{Fe}_2(\text{SO}_4)_3$, both of which are only slightly soluble in water, all the other hydrated forms of these two compounds are very soluble in water, as are iron perchlorates (solubility: $\text{FeSO}_4 \cdot 7\text{H}_2\text{O}$ 29.6g/100ml,³⁵¹ $\text{Fe}(\text{ClO}_4)_2 \cdot 6\text{H}_2\text{O} \approx 100\text{g}/100\text{ml}$ ³⁵²). Thus if a salt film (hydrated sulphate or perchlorate) forms on the surface it tends to dissolve, as discussed by Beck, once the oxide has formed. This would account for the similarity of the surface deposits observed in the present H_2SO_4 and HClO_4 experiments. Also, for a given potential t_{m,HClO_4} was less than $t_{m,\text{H}_2\text{SO}_4}$ (cf. Figs. 4.1 and 4.3); since iron perchlorates are more soluble than iron sulphates, the perchlorate salt film will be present on the surface for a shorter period of time than a sulphate film. Thus in perchlorate electrolytes the oxide would not be able to develop to the same extent and have the same stability as an oxide formed in sulphate electrolytes. This would account for the broader, less well defined rising transients observed in 0.1M HClO_4 . The more clearly defined rising transients (higher and sharper) observed at higher concentrations of HClO_4 (eg. 1.0M) could be explained by the fact that as the HClO_4 concentration is

increased, the alloy dissolution will also increase. This will enable the level of supersaturation for iron perchlorate deposition to be maintained more readily, and would delay the dissolution of the salt film, thereby allowing the formation of a more stable oxide film beneath it, and accounting for the better definition of the rising transient.

The above analysis predicts that as the electrode is stepped to more positive potentials in the appropriate potential region supersaturation at the electrode will occur more readily, due to the enhanced dissolution of the alloy. This will result in an increase in i_m and a decrease in t_m , and for Fe a decrease in t_{ss} . This was indeed observed experimentally (cf Figs. 4.1 and 4.6). As existing nucleation theory does not take into account dissolution of the substrate or of the depositing film, the dissolution component could be partly responsible for the differences between experimental and theoretical curves in Fig. 4.20, at $t/t_m < 1$. It would certainly account for the experimental data not starting at the origin of these plots, since although the presence of active sites allows localised dissolution to commence immediately on application of an anodic potential there will be a time delay for the required level of supersaturation to be attained. Any revised theory describing these rising transients requires a term that considers the dissolution of the substrate as well as a term accounting for the film dissolution at $t/t_m > 1$. These terms clearly would be complex since the composition of the substrate needs to be considered.

The influence of the electrode rotation rate on the Fe transients can be explained if localised conditions in and surrounding the active sites are such as to still support the deposition of the anodic film. However, as the rotation rate increases i_m and t_m increase due to the longer time required to reach the necessary degree of supersaturation which in turn provides more time for the iron to dissolve prior to repassivation of the active sites. Also, at $\omega > 100 \text{ rad s}^{-1}$ the current does not decay subsequent to t_m , indicating that the required level of supersaturation cannot be maintained at the electrode surface thereby preventing further deposition and growth of the surface film.

For a given time scale, rising transients are observed at *passive* potentials for Fe and at *transpassive* potentials for Fe18Cr based stainless steels. In the case of Fe, the rising transients observed at passive potentials are due to the ineffectiveness of the surface film in passivating the electrode. For the stainless steels at passive potentials, the major limitation on active area increase, and thus on the appearance of rising transients, is passivation since this reduces the rate of anodic dissolution and the condition of supersaturation is not attained. As an induction period is required for effective passivation, dissolution of the electrode must occur to a limited extent. Therefore, if the current transients are acquired more rapidly, such dissolution, as indicated by an increase in the current, should be observable. This was indeed the case for both Cr and Fe18Cr at passive potentials (cf Figs. 4.8 and 4.9) where rapid rising transients ($t_m \approx 150 \mu\text{s}$) caused by the rapid nucleation of a surface film which, together with any solid state passivation reactions, indicated passivation of the entire electrode surface. Such passivation suggests an instantaneous nucleation mechanism, which is verified in Fig. 4.21 by comparing the shape of the experimental data curves with that

of the theoretical curve for instantaneous nucleation and 3D growth. Both the Fe18Cr and Cr curves are in good agreement with eqn. 2.19, particularly at $t/t_m < 1$.

AES and EDS analysis of surface deposits of the type shown in Figs. 4.16 and 4.17 did not detect the presence of sulphur, suggesting that such deposits could be iron oxides or oxyhydroxides. This in turn indicates that these deposits are not part of the salt film. To further verify this the surface of a Fe18Cr electrode in 0.1M H_2SO_4 was examined subsequent to a potential step to 1.40V, following which the electrode was not rinsed with water prior to SEM examination. As can be seen in Fig. 4.22 large deposits as well as numerous single, oblong deposits were also observed on the electrode surface. These deposits had a completely different topography to those in Figs. 4.16 and 4.17. AES analysis of deposits of the type shown in Fig. 4.22 detected the presence of Fe, S and O. EDS analysis of these deposits showed a high percentage of Fe and S and while EDS analysis cannot yield information about the oxidation state of the elements present, or detect the presence of oxygen, it is proposed that the deposits could be $FeSO_4 \cdot xH_2O$.

The model proposed above explains the SEM observations on the Mo electrode. Molybdenum has a tendency to enter into complex polymerisation reactions, therefore the depositing species may favour interaction with existing nuclei rather than with the electrode surface resulting in the formation of the large surface deposits observed.

The model also explains the results obtained as a function of temperature. As the temperature is increased the rate of dissolution of the alloy will increase correspondingly, resulting in an increase in i_m , and thus the required degree of supersaturation can be achieved more readily as indicated by a decrease in t_m . Arrhenius plots showed that the activation energy for the nucleation of the surface film decreased with increasing potential. This would be in agreement with the model, since dissolution of the alloy would be facilitated as the electrode is stepped further into the transpassive potential region. The required degree of supersaturation would therefore be achieved more readily which in turn would enable the surface film to nucleate more readily.

Further, the above model also provides a means for predicting the influence of alloy composition on the rising current transients. As the alloys become more resistant to dissolution, the rate of transpassive dissolution will decrease resulting in the critical Fe^{2+} supersaturation concentration, and thus t_m , being attained less readily than for a less corrosion resistant alloy. This was demonstrated above with the Fe x Cr alloy series, with t_m decreasing as the Cr content of the alloy decreased. The model also predicts that the more rapid dissolution of the less corrosion resistant alloys will result in $i_{m, \text{less corrosion resistant}} > i_{m, \text{more corrosion resistant}}$. This prediction is verified experimentally, as shown by the following series in 0.1M H_2SO_4 , 20°C, for the 1.00V transient :

alloy	444	4733	316L	Fe23Cr	Fe20Cr	304L	4732	Fe18Cr	Fe16Cr
$i_m / \text{mA cm}^{-2}$	28.8	34.8	35.5	36.8	38.3	42.9	44.0	45.6	56.1

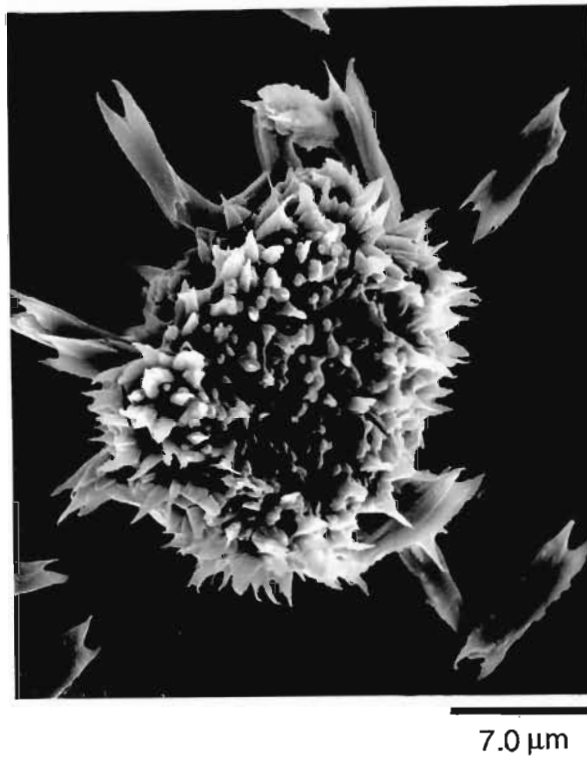


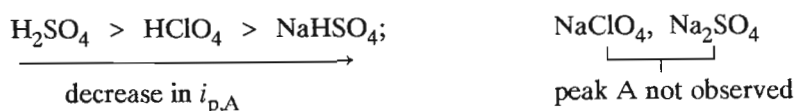
Fig. 4.22

SEM micrograph showing the surface deposits on a Fe18Cr electrode in 0.1M H_2SO_4 after the potential step $-0.60\text{V} \rightarrow 1.40\text{V}$. The electrode was not rinsed with H_2O prior to SEM examination.

The above series can be subdivided into 3 series :

- As the chromium content of the FeCr alloys increases, thereby enhancing the oxidation resistance of the alloy, so i_m decreased; i_m : Fe23Cr < Fe20Cr < Fe18Cr < Fe16Cr.
- Addition of Mo, V and Ni to Fe18Cr further enhances the oxidation resistance, resulting in a decrease in i_m for the series : Fe18Cr < 4732 < 304L < 4733 < 444. This is in agreement with previous electrochemical results^{325,326,353} for Mo and V alloys, which showed the resistance to oxidation, and specifically Cl⁻ induced oxidation, decreased for the series : 444, 4733, 4732, Fe18Cr. Since the incorporation of 9.25% Ni in alloy 304L resulted in only a relatively small decrease in i_m , it is suggested that Ni does not play a major rôle in the initial nucleation and growth of the surface film. This conclusion is further supported by the fact that $i_{m,444} < i_{m,316L}$. If Ni was significantly involved it would have been expected that the current maximum of 316L would be less than that of 444 considering that 316L has an additional 0.22% Mo and 10.19% Ni, and taking the higher 0.85%Cr of 444 into consideration.
- It has been extensively reported in the literature that 316L has superior oxidation resistance to that of 304L, which would lead to the prediction that $i_{m,316L} < i_{m,304L}$ which is indeed verified in the series presented above.

From the above model it is also predicted that since the rate of transpassive dissolution is less for non-aggressive electrolytes, peak A on the cyclic voltammograms will be diminished or non-existent. This was indeed observed³²⁵ when comparing cyclic voltammograms of an alloy in the following 0.1M electrolytes :



This in turn predicts that i_m should decrease and t_m increase for the following series of 0.1M electrolytes :



The experimental results, presented earlier in this chapter, support this prediction.

4.7 INTERPRETATION OF EXPERIMENTAL DATA IN TERMS OF NUCLEATION CONCEPTS

Although classical thermodynamics is often used to describe nucleation and growth processes it is not entirely correct to do so since macroscopic quantities, such as surface tension and bulk density, are used to describe the microscopic process of nucleation. While acknowledging this, it is noteworthy that the present results are qualitatively in agreement with classical precipitation theory. Several examples will be discussed below.

The rate of nucleation has been shown to increase exponentially with degree of supersaturation whereas the

rate of particle growth is approximately linear with respect to supersaturation.³⁵³ Thus at low supersaturations, growth processes will predominate while at high supersaturations nucleation will predominate. This is in agreement the results presented above. Subsequent to the potential step the relative rate of electrode dissolution is high resulting in a high degree of supersaturation; the result is the onset of nucleation. As the active sites are repassivated, supersaturation decreases resulting in growth processes becoming more prominent.

It has been shown above that, subsequent to a potential step to an appropriate potential, alloy dissolution occurs resulting in the appearance of rising current transients. Comparison of the Fe and Fe18Cr transients shows that i_m and t_m are greater for an Fe electrode than for Fe18Cr. This is due to the presence of Cr which retards substrate dissolution by the rapid formation of a protective surface film. The presence of this Cr film is likely to result in precipitation of the Fe species occurring more rapidly (postprecipitation phenomenon) and together with the decrease in the rate of substrate dissolution will result in the concentration of Fe^{2+} in solution being less than in the pure Fe electrode case. Thus at the maximum of the respective transients for Fe and Fe18Cr the relative degree of supersaturation of Fe^{2+} will be greater for Fe than for Fe18Cr. From precipitation theory it would therefore be predicted that Fe would have more nuclei of a relatively small size (nucleation predominating over growth) in comparison to Fe18Cr where fewer, larger particles would be predicted. This was indeed observed as shown in Figs. 4.16 and 4.17.

Experimental evidence³⁵⁴ suggests that the particle size of a precipitate varies inversely with the average degree of relative supersaturation that exists after each addition of the precipitating agent. This leads to the prediction that Fe would have smaller deposits than Fe18Cr. Comparison of Figs. 4.16 and 4.17 shows that this is in fact the case.

The effect of stirring the solution, on precipitation, is reported to be complex with stirring having a marked effect on some systems while having virtually no effect on others.³⁵⁵ A possible generalisation is that the effect of stirring (a) is greater the greater the supersaturation and (b) has a negligible effect on large particles while having a marked effect on smaller particles. This is again in agreement with the electrochemical results; greater supersaturation and smaller nuclei are found with Fe and the marked effect of varying the rotation rate is clearly demonstrated in Fig. 4.7. The rising current transients of Fe18Cr were not significantly influenced by rotation rate as would be predicted from Fe18Cr having fewer but larger nuclei and a lower associated supersaturation.

One of the fundamental theories for crystal growth is the surface diffusion model.³⁵⁵ The basic concept of the theory is that the species move from the bulk solution to the surface, move over the surface and are incorporated at sites where there is a step on the surface. This would be in accordance with our proposal that nucleation occurs at an active site (ie. an inhomogeneity, for example, a step, in the electrode surface).

Nyvt *et al.*³⁵⁵ point out that the precipitation of metal hydroxides from aqueous solutions has not been studied in depth and the solubility products given in the literature are not sufficiently reliable since equilibrium was not attained in many of the studies. However, from available data they concluded that precipitated hydroxides are mostly formed by secondary species (several μm in size) that are composed of primary species. (Secondary species are defined as species that nucleate and grow in the presence of existing nuclei.) Under favourable conditions the secondary species may join to form large, not very robust tertiary clusters that can be broken mechanically. The present electrochemical data is in agreement with Nyvt's conclusions; in particular the Fe18Cr data where it has been concluded above that film formation proceeds via a progressive nucleation and three dimensional growth mechanism and as shown in Fig. 4.16 relatively few, large growth centers of differing sizes are preferred. This would also account for the larger growth centers observed on the Fe electrode.

4.8 SUMMARY

Based on novel chronoamperometric, voltammetric and related SEM data it is proposed that the formation of an anodic surface film on stainless steel alloys in acidic electrolytes at transpassive potentials first requires the formation of a supersaturated salt film at the dissolving electrode followed by progressive three dimensional nucleation and growth as a result of precipitation of solution species initially not present in the homogeneous solution phase. For iron electrodes nucleation is initially instantaneous with three dimensional growth, subsequent to which a progressive nucleation and 3D growth mechanism predominates.

Rising current transients were also observed for Fe18Cr at passive potentials and for Cr, both of which have previously been reported as only exhibiting a falling transient response to an applied potential step. It is proposed that the passive film forms via an instantaneous nucleation and 3D growth mechanism.

Existing nucleation and growth models were shown to be necessarily inadequate in describing the data for oxide formation on an oxidising metal substrate. Clearly a more realistic quantitative model is required, the development of which however, is hampered by mathematical limitations. The proposed qualitative model was able to account for the influence of applied potential, temperature, electrolyte and alloy composition on the observed current transients.

CHAPTER FIVE

RESULTS and DISCUSSION

IRON IN ALKALINE CYANIDE ELECTROLYTES : Cyclic Voltammetry and Rotating Ring - Disc Electrode Experiments

From the literature reviewed in chapter two it can be concluded that a duplex surface film forms on iron in alkaline electrolytes. However, there is little agreement as to the nature, composition or mechanism of formation of this film. Notwithstanding the differences in experimental procedures, it is nevertheless interesting to note the variety of voltammograms presented (*cf* Table 2.1). While some of the work presented in this chapter has been reported in the literature, it was found to be essential to conduct these studies in order to provide a consistent base from which comparisons could be made.

This chapter covers the cyclic voltammetric and rotating ring - disc electrode behaviour of an Fe electrode in

- a) 1.0M NaOH
- b) 1.0M NaOH + 0.4M NaCN
- c) 0.5M NaOH
- d) 0.5M NaOH + 0.4M NaCN

The two cyanide containing electrolytes correspond to the ZADRA and AARL CIP elution solutions.

This chapter focuses on the growth of the surface film and the following chapter will investigate the initial stages of film formation using chronoamperometry. While, initially, it may seem more logical to reverse the order of these two chapters, cyclic voltammetry together with RRDE studies will provide a good qualitative description as to the oxidation and reduction processes occurring under specified electrochemical conditions and these results will expedite the chronoamperometric discussion. Besides, a little hindsight is usually useful!

5.1 Fe in 1.0M NaOH

In 1.0M NaOH the cyclic voltammogram of Fe has four oxidation and two reduction peaks. As shown in Fig. 5.1 the oxidation peaks are A1 (-1100mV), A2 (-950mV), A3 (-720mV) and the broad A4 (-540mV).

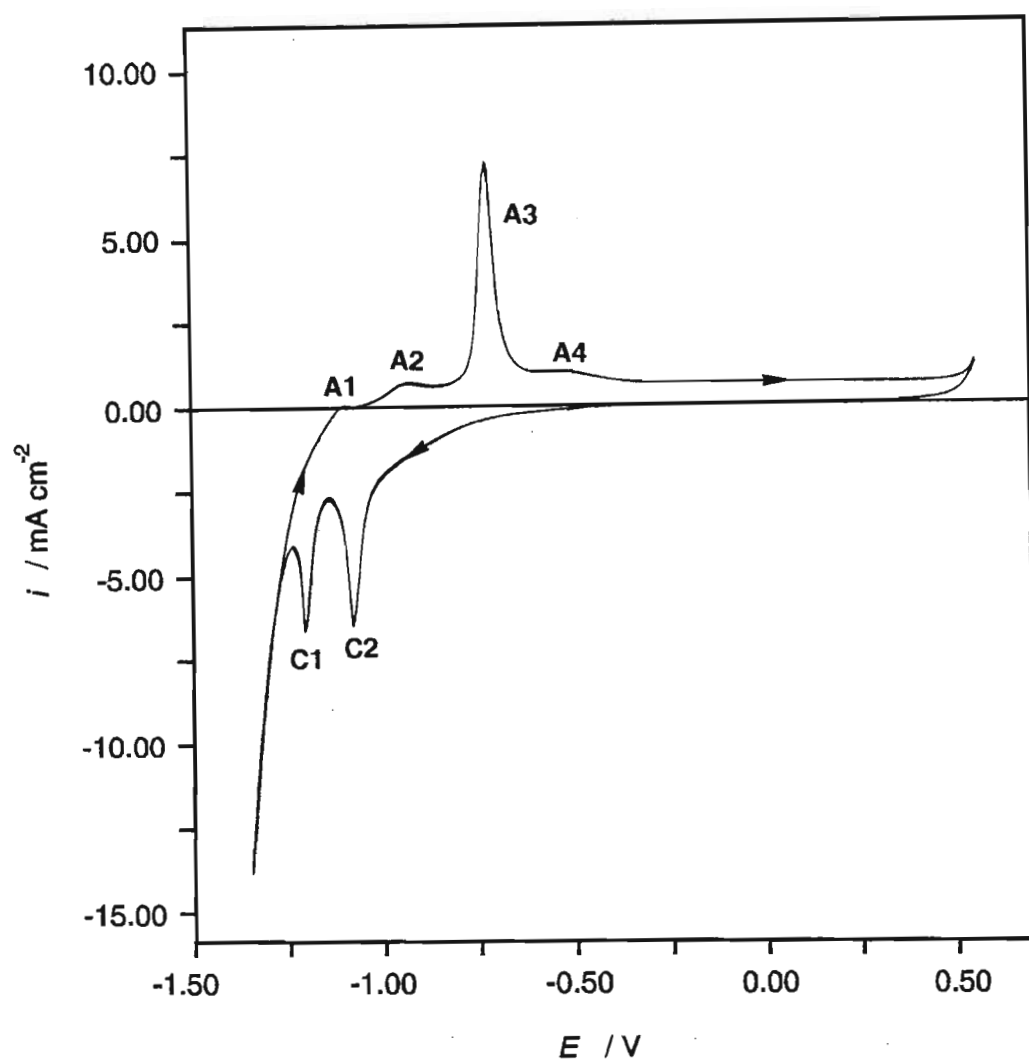


Fig. 5.1 Cyclic voltammogram of the 20th cycle of a Fe electrode in 1.0M NaOH, 60°C, swept at 100mV s^{-1} between -1.35V and 0.55V showing the four oxidation and two reduction peaks. $\omega = 100\text{rad s}^{-1}$

The two well defined reduction peaks are C1 (-1210mV) and C2 (-1080mV). On the forward sweep, after A4 the current density decays to a steady state indicating the passive potential region, which extends to the potential at which the onset of oxygen evolution occurs. Generally voltammograms obtained at slow sweep rates and at higher temperatures gave better definition of the peaks, and hence the use of a 60 °C cyclic voltammogram in Fig. 5.1 to familiarise the reader with all the voltammetric peaks. It will be shown, later in this chapter, that A1 and A2 are due to the formation of the base layer while A3 and A4 are due to upper layer formation.

Steady state voltammograms are not readily obtained in 1.0M NaOH, at ambient temperatures. Using a sweep rate of 100mV s⁻¹ and rotating the electrode at 100rad s⁻¹, 50 cycles were required before a steady state voltammogram was obtained. Fig. 5.2 shows the effect of potential cycling on the voltammogram, with the continual increase in A3 due to the buildup of oxide on the electrode surface. With progressive cycling A1 remained virtually unchanged, C1 increased slightly while A3 and C2 showed the most rapid growth becoming the dominant peaks of the voltammogram. With continued cycling there was a decrease in the relative increase in i_p per cycle. Burke and co-workers^{40,356} have attributed this to the increasing inhibition of water and hydroxide ion transfer to the inner region of the oxide layer with increasing hydrous oxide thickness, resulting in the inner layer remaining largely anhydrous and thereby retaining its protective characteristics. In order to analyse these voltammograms, E_p and i_p data were determined after a specified number of applied potential cycles. The rapid buildup of oxide at A3 resulted in A4 being masked or poorly defined and thereby frequently precluding the acquisition of E_p and i_p for A4.

Fig. 5.2 also shows that A3 and C2 are absent from the first cycle. Haupt and Strehblow³⁴ have attributed this to the absence of a surface film formed prior to the commencement of the cyclic voltammetric applied potential regime. Larramona and Gutiérrez⁴⁹ and Oelkrug *et al.*⁴⁴ also reported the absence of A3 and C2 from the first cycle. As will be discussed later, Fe(III) oxide/hydroxide accumulated during cycling is reduced at peak C2, and therefore as A3 is absent from the first sweep no material is available for reduction, at C2, on the first reverse sweep. The absence of A3 from the first cycle also indicates that A4 is not dependent on the species formed at A3, with A4 most likely being a successive reaction to those occurring at A1 and A2.

A further difference between the first and subsequent ≈ 6 sweeps was that $E_{p,C1}$ moved to more positive potentials. Under certain conditions there was also a decrease in $i_{p,C1}$ after the first sweep. Schrebler Guzmán *et al.*³⁶ have attributed this to the existence of non-equilibrium states related to the participation of the reactant in the reduction reaction indicating that the surface species undergo chemical changes.

In order to verify that A4 is merely masked on subsequent sweeps by the buildup of oxide at A3, 50 potential cycles were applied to a clean Fe electrode resulting in A3 being well defined due to oxide buildup and A4 being completely masked, as shown in Fig. 5.3. The potential sweep was then halted for 1 minute

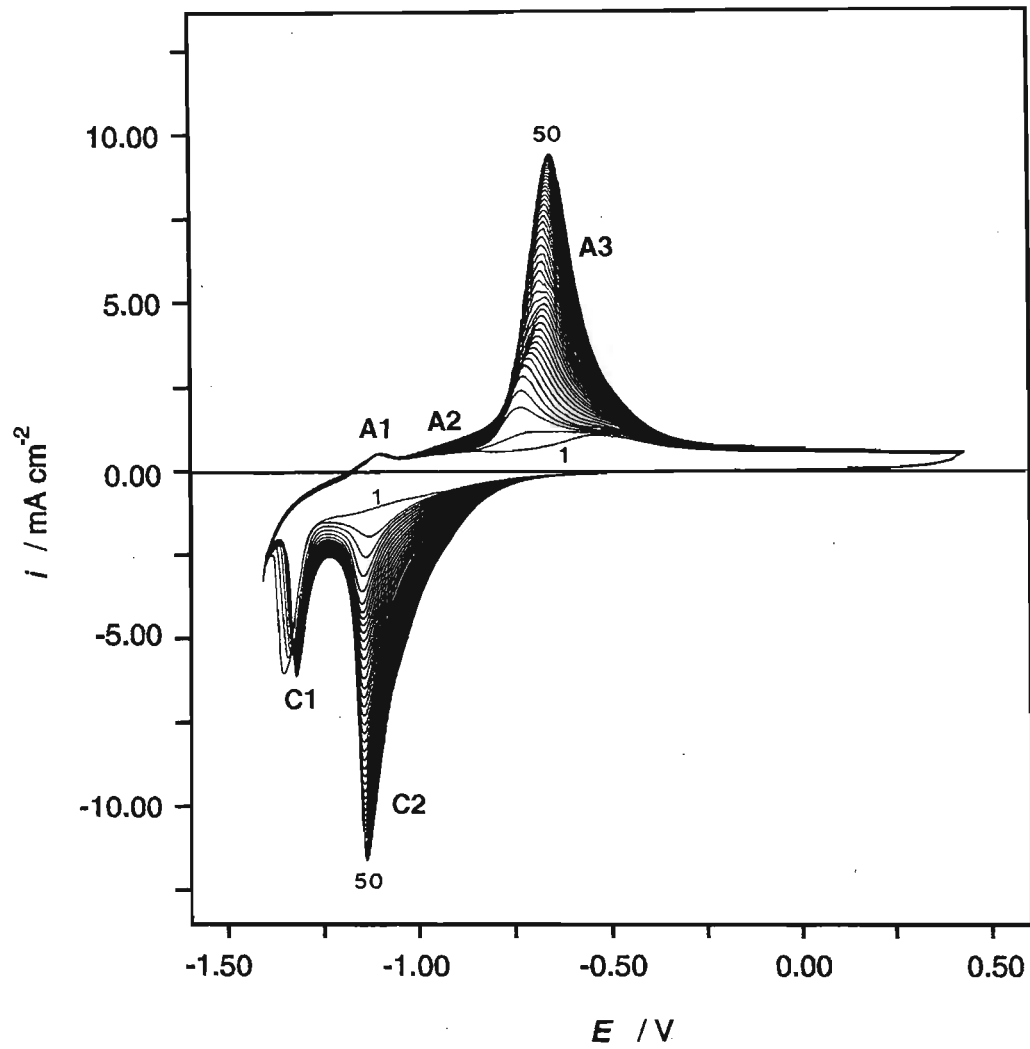


Fig. 5.2 Cyclic voltammogram of the first 50 cycles of a Fe electrode in 1.0M NaOH, 20°C, swept at 100mV s^{-1} between -1.40V and 0.40V showing the buildup of the surface film. $\omega = 100\text{rad s}^{-1}$

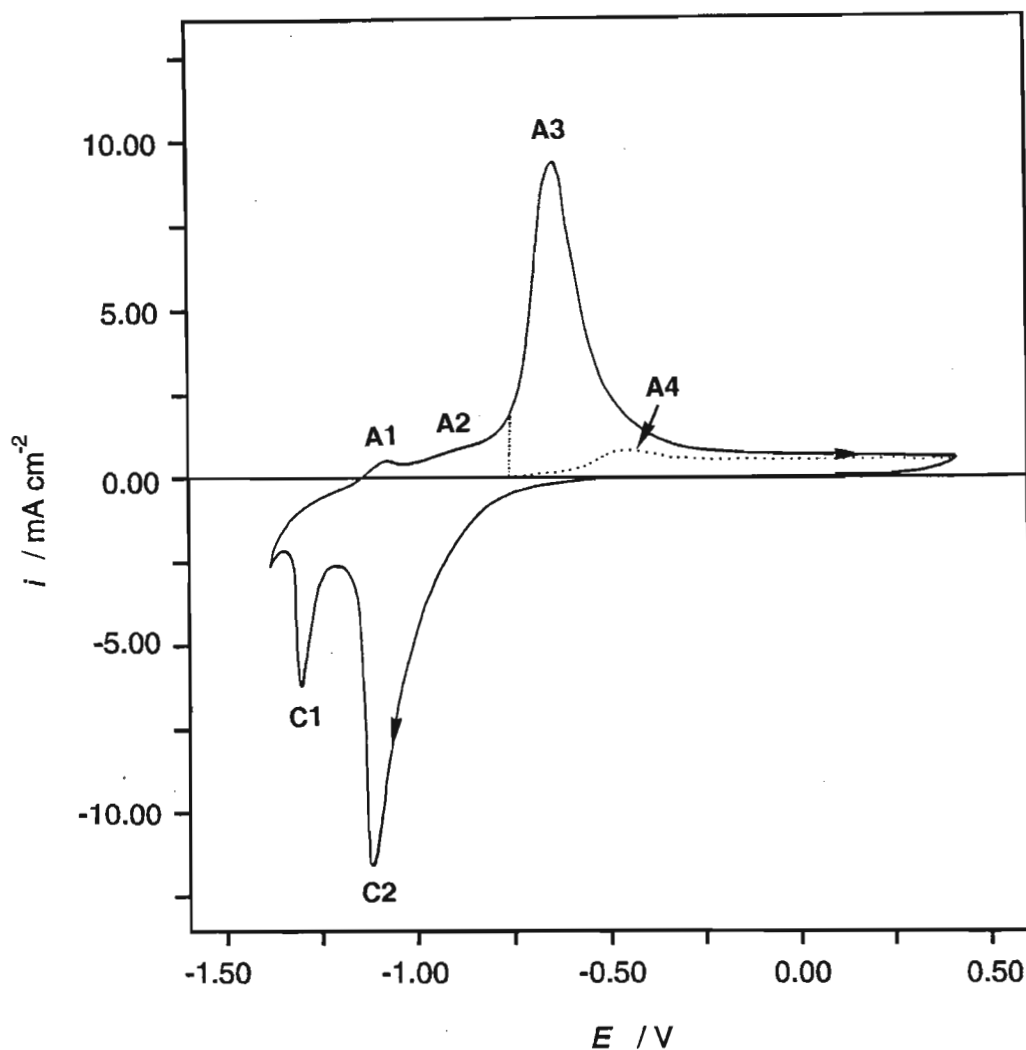


Fig. 5.3 Cyclic voltammogram of a Fe electrode in 1.0M NaOH, 20°C swept between -1.40V and 0.40V at 100mV s^{-1} after 50 cycles (—) and after interrupting the cycling process by holding the applied potential, for 1 minute, at the potential of the dotted vertical line, and then continuing cycling from this potential (·····). $\omega = 100\text{rad s}^{-1}$

at the potential of the dotted vertical line in Fig. 5.3 and the sweep resumed. The section of the voltammogram represented by the dotted curve clearly indicates the presence of A4. If the holding potential was varied between that of the dotted vertical line and $E_{p,A3}$, the same results were obtained on resumption of the sweep, indicating that A4 is not dependent on electroactive species produced at A3.

5.1.1 Sweep Rate and Temperature Dependence

At 20°C, increasing the sweep rate from 4mV s⁻¹ to 1V s⁻¹ resulted in an increase in the magnitude of the peaks with the oxidation peaks shifting to more positive potentials while the reduction peaks shifted to more negative potentials. At $\nu > 10\text{mV s}^{-1}$ a clearly defined peak was not evident for A2. For peaks A1, A3, C1 and C2 i_p increased linearly with sweep rate, while a linear E_p vs $\nu^{1/2}$ relationship was observed for peaks A3, A4, C1 and C2. For A1, E_p increased linearly as a function of ν .

The rate of growth of the surface film was dependent on the applied potential sweep rate since the relative increase per cycle in i_p decreased with increasing sweep rate due to the shorter time spent at the potentials where film growth occurs. With less oxide on the surface there is a greater probability that substrate dissolution can occur. This was indeed indicated by the shift of the oxidation peaks to more positive potentials which in turn means that the onset of passivation occurs later. Thus with more dissolution occurring the overall current density of the voltammogram will be greater — which was observed experimentally.

With increasing temperature (20°C to 120°C) A3 and C2, which were the dominant peaks at the lower temperatures, decreased significantly and were poorly defined at 120°C while A2 which was present as a broad and poorly defined peak at 20°C became the dominant oxidation peak at higher temperatures, as shown in Fig. 5.4. C1 became the dominant reduction peak at higher temperatures. For $T > 40^\circ\text{C}$ i_p increased linearly with ν for A2 and C1 and decreased with ν for C2. With increasing temperature there was also an increase in the passive current indicating, not unexpectedly, that the surface film was not as protective at higher temperatures. A linear i_p vs $\nu^{1/2}$ relationship was observed for A3. At all temperatures investigated, the peak potential of A3, A4 and C1 varied linearly with $\nu^{1/2}$. $E_{p,C2}$ varied linearly with $\nu^{1/2}$ at 20°C and 40°C and with ν at $T \geq 60^\circ\text{C}$. $E_{p,A2}$ was independent of sweep rate up to 60°C, while at higher temperatures a linear E_p vs $\nu^{1/2}$ relationship was observed.

While steady state cyclic voltammograms were not readily obtained at 20°C, with increasing temperature the relative charge increase per cycle decreased such that steady state conditions were attained within ≈ 20 cycles at 80°C and within ≈ 10 cycles at 120°C. This is mainly attributable to the fact that at ambient temperatures upper layer growth predominates, while at higher temperatures growth of the protective base layer predominates. Thus with less upper layer being formed at higher temperatures, there will be less material available for reduction on the reverse sweep which should facilitate the reduction of a greater percentage of the upper layer formed. This in turn means less material available for re-oxidation on the

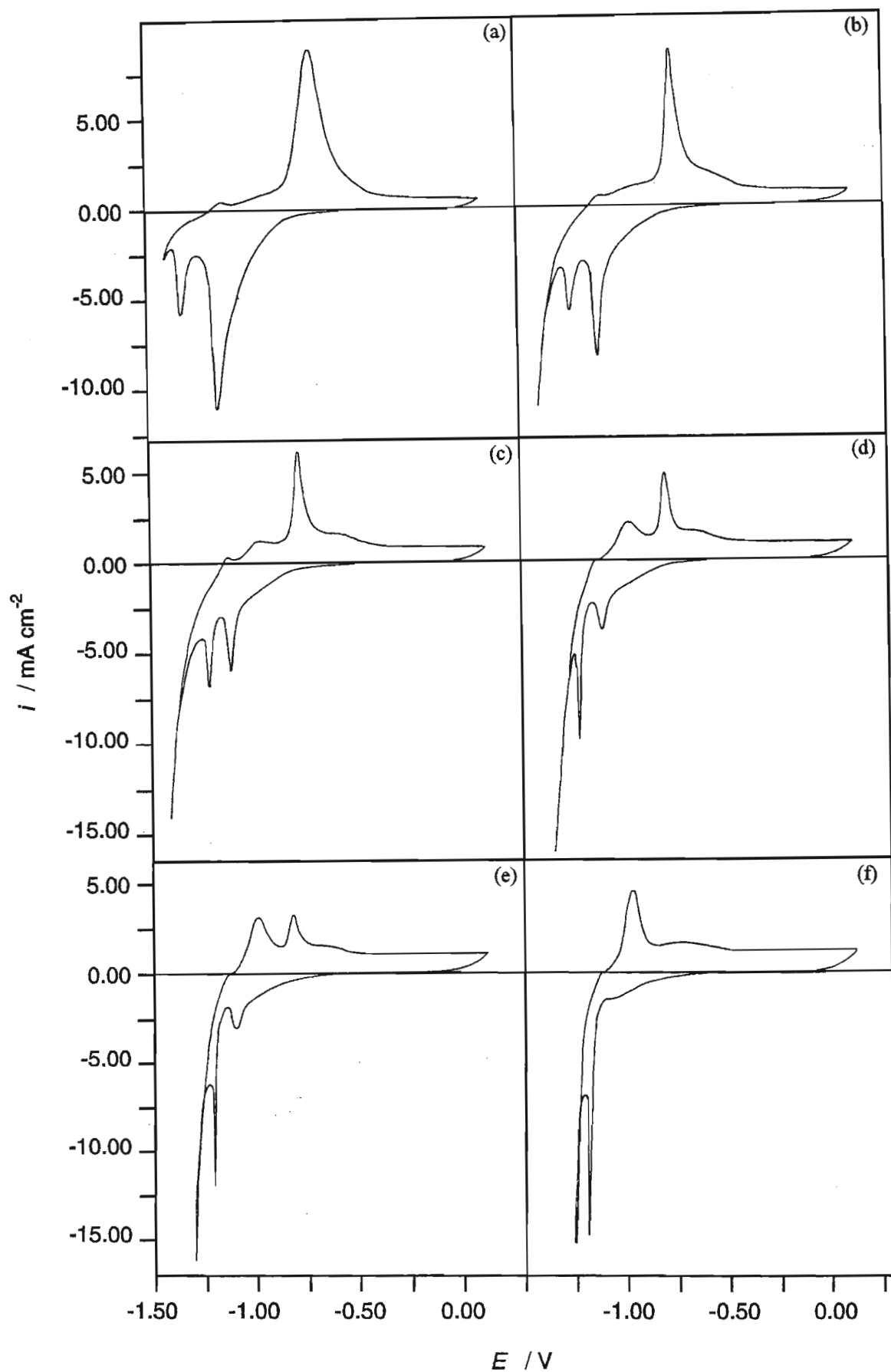


Fig. 5.4 Cyclic voltammogram of the 20th cycle of a Fe electrode in 1.0M NaOH swept at 100 mV s^{-1} between -1.40V and 0.20V at (a) 20°C, (b) 40°C, (c) 60°C, (d) 80°C, (e) 100°C, (f) 120°C. $\omega = 100 \text{ rad s}^{-1}$

subsequent forward sweep, and thereby inhibiting the buildup of the upper layer.

Over the temperature range investigated, E_p for all of the peaks was found to vary linearly with temperature as shown in Fig. 5.5. With increasing temperature C1, C2 and to a very much lesser extent A2 shifted to more positive potentials while A1, A3 and A4 shifted to more negative potentials.

The influence of temperature on i_p , for the 100mV s^{-1} data, in Fig. 5.6 shows that i_p for A2 and C1 increased with temperature according to the Arrhenius equation while A3, A4 and C2 decreased. The activation energies for film growth calculated from Arrhenius plots over a range of sweep rates are presented in Fig. 5.7. These activation energies refer to the overall process occurring at a given peak potential, which in the case of oxidation peaks will be film growth and in the case of reduction peaks, the reduction of the oxide. For A2 and C1 the activation energy decreased with increasing sweep rate which is not unexpected since the substrate dissolution required for film formation can occur more readily at faster sweep rates, due to the poor protective nature of the film formed. It follows therefore that as the reaction(s) at C1 occur more readily at faster sweep rates, there will be less unoxidised Fe(II) species available for reoxidation on the subsequent sweep, and hence the increase in E_a for A3 and C2.

It is interesting to note that despite the extensive work on the Fe/OH⁻ system, there are very few E_a values quoted in the literature and even fewer Arrhenius plots actually presented. Some of the values that are quoted include :

$$E_a = 13.025\text{kJ mol}^{-1} \quad \text{for A2 for Fe in 1.0M NaOH (ref. 42)}$$

$$E_a = 25.52\text{kJ mol}^{-1} \quad \text{at } E = 0.110\text{V for Fe in 10.0M NaOH (ref. 357)}$$

$$E_a = 59.413\text{kJ mol}^{-1} \quad \text{at } E = -0.216\text{V for Fe in 10.0M KOH (ref. 358)}$$

$$E_a = 41.3\text{kJ mol}^{-1} \quad \text{at } E = 0.30\text{V to } 0.80\text{V for Fe in borate buffer, pH 7.4 and pH 8.5 (ref. 359)}$$

$$E_a = 82.84\text{kJ mol}^{-1} \quad \text{at } E = 0.80\text{V for 304 stainless steel in borate buffer pH 9 (ref. 205)}$$

$$E_a = 2.7\text{kJ mol}^{-1} \quad \text{for C2 calculated from M^cKubre's⁵⁴ } 100\text{mV s}^{-1} \text{ data for Fe in 30wt\% KOH}$$

While the conditions quoted above vary widely, the activation energies are the same order of magnitude as the experimental values presented in Fig. 5.7.

A linear dependence of E_p on i_p , as a function of sweep rate, was found for peaks A2, A3, C1 and C2, in this work, which suggests the presence of a resistive surface film.³⁶⁰ The resistance calculated from these plots was found to decrease linearly with temperature for A3 and C1 and to increase for A2 and C2. The increase in resistance of the film formed at A2 is expected since A2 becomes the dominant peak at higher temperatures indicating an increase in the thickness of the base layer and consequently an increase in the resistance. This will reduce substrate dissolution and facilitate the attainment of steady state voltammograms, which were observed experimentally. A3 however, is due to the formation of the non-protective upper layer which is not favoured at higher temperatures. This results in a decrease in the thickness of the upper layer and hence a decrease in the resistance. This, together with the increase in the

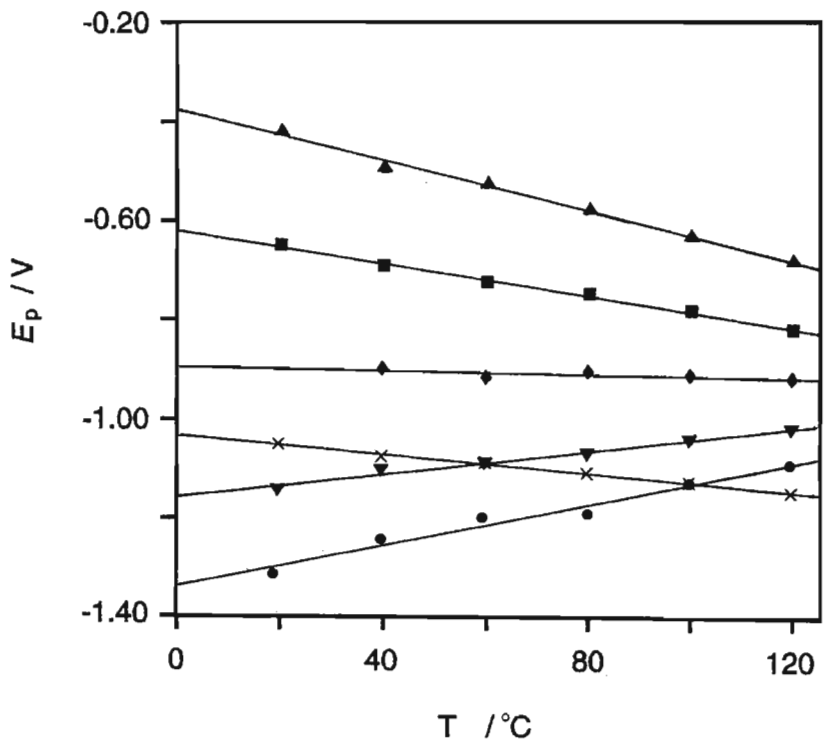


Fig. 5.5 Influence of temperature on the cyclic voltammetric peak potentials of a Fe electrode in 1.0M NaOH. $\nu = 100\text{mV s}^{-1}$, $\omega = 100\text{rad s}^{-1}$.

× A1 ♦ A2 ■ A3 ▲ A4
 • C1 ▼ C2

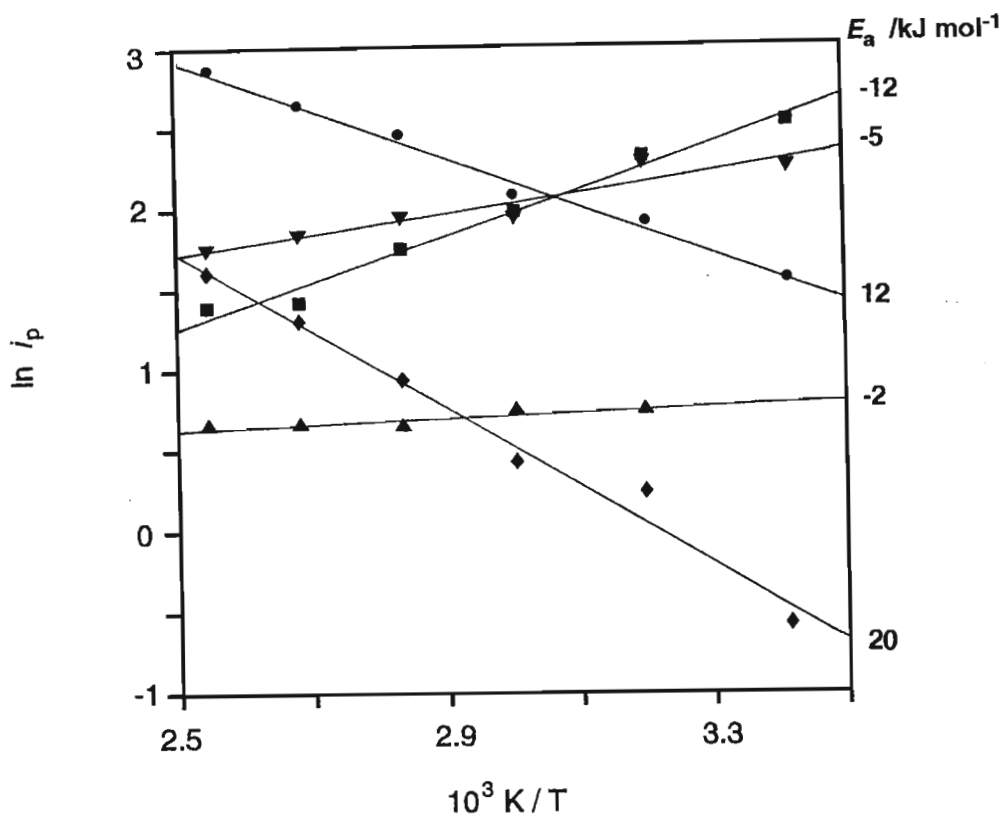


Fig. 5.6 Arrhenius plots for the reactions occurring on a Fe electrode in 1.0M NaOH, at the potentials of the indicated peaks. $\nu = 100\text{mV s}^{-1}$, $\omega = 100\text{rad s}^{-1}$.

◆ A2 ■ A3 ▲ A4
• C1 ▼ C2

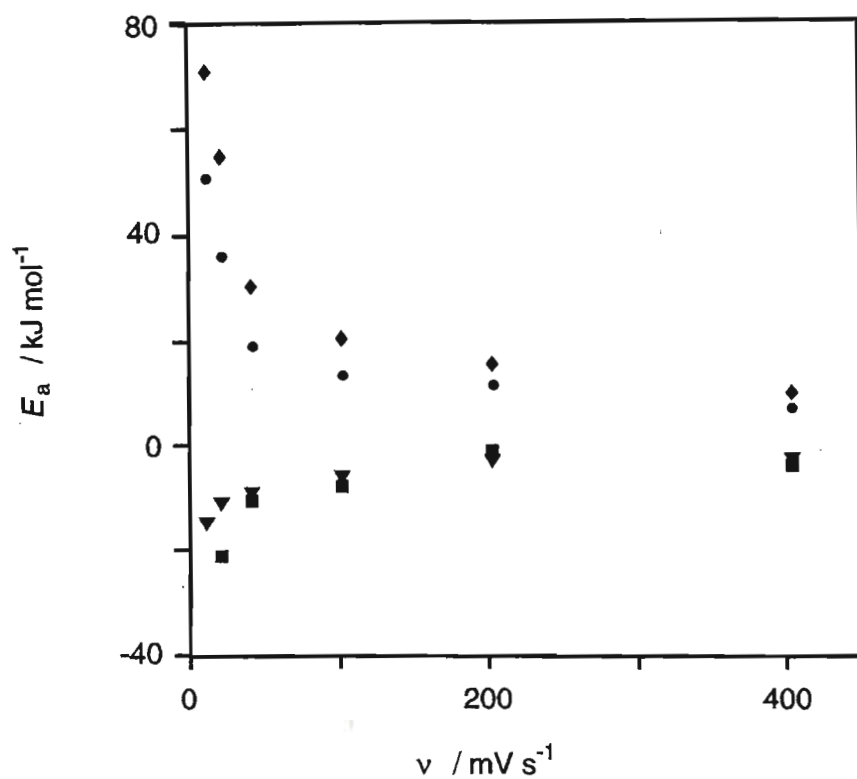


Fig. 5.7 Influence of sweep rate on activation energy of the processes occurring on a Fe electrode in 1.0M NaOH at the potential of peaks

◆ A2 ■ A3
• C1 ▼ C2

activation energy for film formation at A3, resulted in the decrease in magnitude of A3 with increasing temperature.

5.1.2 Growth Laws

Scan rate dependencies of the peak current densities and potentials reported above can be used as a diagnostic for the various growth laws. A brief summary of the relevant equations for the more frequently reported growth laws for the oxidation of iron, and those for which the experimental data was tested, follows :

Pore resistance model^{360,361}

This model assumes that a passivating film of constant thickness forms, during an applied potential sweep, by the random spread of solid film across the electrode until only a small fraction of the substrate remains uncovered. At this point the resistance of the solution in the pores becomes rate controlling and gives rise to a sudden drop in the current. The potentiodynamic peak characteristics for this model are

$$i_p = (n F \rho \kappa / M)^{1/2} A (1 - \theta_m)^{1/2} \nu^{1/2} \quad (5.1)$$

$$E_p = (n F \rho \kappa / M)^{1/2} [(\delta / \kappa) + R_o A (1 - \theta_m)] \nu^{1/2} \quad (5.2)$$

where θ_m is the surface coverage at the peak maximum, ρ is the density of the deposited phase, κ is the specific conductance of the solution, M is the molar mass of the deposited phase, A is the total surface area, δ the thickness of the film, R_o is the resistance of the system without film formation and F is Faraday's constant.

Place exchange mechanism³⁶²⁻³⁶⁴

Film growth proceeds via the field assisted place exchange of metal oxide pairs. In this mechanism, an oxygen or hydroxyl species adsorbed initially on the metal surface exchanges place with an underlying metal atom. A second oxygen / hydroxyl species is then adsorbed, and the two M-O / M-OH pairs rotate simultaneously. This process is repeated, with the number of pairs which exchange increasing with increasing thickness. This leads to a linear increase in E_a with increasing film thickness, if all the place exchanges occur simultaneously. For this mechanism, the following relationship holds

$$i_p = D \gamma \nu \quad (5.3)$$

where $\gamma = 19.5V^{-1}$ and

$$D = 4 n e R T / l^2 E_a$$

with n the stoichiometric number corresponding to the rate determining step, e the electron charge, l is the lattice distance of oxygen in a unit cell of the oxide and E_a is the activation energy for each metal exchange. This type of rate controlling reaction explains the mechanism of anodic oxide formation at the level up to that of a few monolayers, with $E_a = 15 - 20 kJ mol^{-1}$ being consistent with this type of mechanism.

Low field mechanism³⁶⁵

with ion migration through the film as the rate determining step.

For this mechanism it is assumed that ionic defects can occur anywhere within the film, and is therefore sometimes referred to as low field ionic migration with bulk control.

The voltammetric peak current under such conditions is given by

$$i_p = (n F K / V_m)^{1/2} \nu^{1/2} \quad (5.4)$$

where K is a constant dependent on the properties of the film, and V_m the molar volume of the film.

Low field mechanism³¹¹

with ion injection into the film as the rate determining step.

For this mechanism the mobile ionic defects are assumed to be generated entirely at the metal / oxide interface and is therefore sometimes referred to as low field ionic migration with interface control.

The voltammetric peak current under such conditions is given by

$$i_p = (6 F \alpha^{1/2} / V_m) (\nu / i_p^{1/2}) \quad (5.5)$$

where α is the transfer coefficient of electrons exchanged in the rate determining step.

High field mechanism³¹¹

The voltammetric peak current for this mechanism is given by

$$\log i_p = \log A + (6 F B / 2.3 V_m) (\nu / i_p) \quad (5.6)$$

where $A = z e n^{(f)} \nu \exp(-E_a / R T)$

and $B = a z F / R T$

where z is the valency of the moving ion, $n^{(f)}$ the number of charged particles per unit area surmounting the activation energy barrier (E_a) in the forward direction, ν is a single characteristic frequency and a is the half width of the barrier to ion movement.

A variety of relationships have been reported in the literature for E_p and i_p as a function of sweep rate. A selection of these are summarised in Table 5.1 which illustrates that, along with many of the other aspects of the corrosion of Fe in alkaline electrolytes, consensus has not been reached on the effect of sweep rate on the cyclic voltammetric parameters. However, it should be noted that for most of the work presented in the literature specific conditions under which the cyclic voltammograms are analysed, eg. the number of cycles, are not reported. The significance of this becomes apparent when one considers that the thickness of the surface film influences each of the growth mechanisms described above. This is supported by the work of Burke and Lyons⁴⁰ who showed that for a film grown on Fe in 1M NaOH, a linear i_p vs ν relationship was obtained after 120 cycles, whereas for a thick film (360 cycles) the charge capacity decreased by $\approx 50\%$ as the scan rate was increased from 1 to 50 mV s⁻¹, with further increases in the scan rate having little effect on the charge capacity.

Table 5.1

Summary of the relationships presented in the literature of the influence of sweep rate on i_p and E_p for Fe in alkaline electrolytes

i_p	ref.	E_p	ref.
Peak A1			
$\log i_p \propto \log \nu$	37	E_p independent of ν	38,51,54,55
$i_p \propto \nu^{1/2}$ (0°C)	54,55	$E_p \propto \log \nu$	37
$i_p \propto \nu$ (75°C)	54,55		
Peak A2			
i_p weakly dependent on ν	38	E_p weakly dependent of ν	38
$\log i_p \propto \log \nu$	37	$E_p \propto \log \nu$	37,42,43
$i_p \propto \nu^{1/2}$ (0°C)	54,55	E_p independent of ν	51,54,55
$i_p \propto \nu$ (75°C)	54,55		
Peak A3			
$i_p \propto \nu^{1/2}$	38	E_p independent of ν	54,55
$\log i_p \propto \log \nu$	37	$E_p \propto \log \nu$	37
$i_p \propto \nu$	57	$E_p \propto \nu^{1/2}$	38,51
Peak A4			
		$E_p \propto \log \nu$	37
		E_p independent of ν	51,54,55
Peak C1			
$i_p \propto \nu^{1/2}$	38	$E_p \propto \nu^{1/2}$	38
$\log i_p \propto \log \nu$	37	$E_p \propto \log \nu$	37
Peak C2			
$i_p \propto \nu^{1/2}$	38	$E_p \propto \nu^{1/2}$	38
$\log i_p \propto \log \nu$	37	$E_p \propto \log \nu$	37
i_p independent of ν	57		

Using the above relationships to analyse the 10th cycle of the cyclic voltammograms in the present work, the linear i_p vs ν behaviour of A1, A2, C1 and C2, suggests that only surface film formation and reduction processes are involved, with no bulk diffusion processes occurring, which is indicative of a place exchange mechanism. Srinivasan *et al.*³⁶⁶ and Martins *et al.*³⁶⁷ proposed that such a relationship indicated a simple reaction model involving the formation of either a monolayer or of a layer of constant thickness. In the present work the latter would be the more likely. This would support the proposal that A1 and A2 are due to the formation of the base layer. Burke and Lyons⁴⁰ also reported an i_p vs ν relationship for initial film growth.

The linear i_p vs $\nu^{1/2}$ relationship displayed by A3 could be attributed to a purely diffusion controlled process, or as given by eqns. 5.1 and 5.2 to a pore resistance mechanism. However, Macdonald and Roberts³⁸ concluded that the pore resistance mechanism was inadequate in describing the oxidation of carbon steel in 1.0M NaOH. To evaluate this mechanism for Fe in 1.0M NaOH, it was assumed that the surface phase present under A3 would be either Fe₂O₃ or FeOOH (as indicated by the XPS results presented in chapter seven, and the following values substituted into eqns. 5.1 and 5.2 in order to determine the surface film thickness; $n = 3$, $\rho = 4.28 \text{ g cm}^{-3}$ (FeOOH), $\rho = 5.24 \text{ g cm}^{-3}$ (Fe₂O₃), $M = 88.85 \text{ g mol}^{-1}$ (FeOOH), $M = 159.7 \text{ g mol}^{-1}$ (Fe₂O₃), $\kappa = 0.171 \Omega^{-1} \text{ cm}^{-1}$, $A = 0.1963 \text{ cm}^2$, $i_p / \nu^{1/2} = 4.5 \times 10^{-3} \text{ A s}^{1/2} \text{ V}^{-1/2}$, $E_p / \nu^{1/2} = 0.272 \text{ V}^{1/2} \text{ s}^{1/2}$. Eqn. 5.2 yielded a film thickness value of $9.5 \mu\text{m}$ and $11.6 \mu\text{m}$ (assuming FeOOH and Fe₂O₃, respectively, as the film species). It is unreasonable to expect such a film thickness to have formed after 10 cyclic voltammetric cycles between -1.40V and 0.40V at 100 mV s^{-1} . Similar findings were reported by Macdonald and Roberts.³⁸ To further investigate the validity of the δ values, the area under peak A3 was integrated and substituted into the following equation derived from Faraday's Law

$$\delta = (M / n F A \theta_m \kappa \nu) \int_{E_o}^{E_p} i \, dE \quad (5.7)$$

with $E_o = -0.90 \text{ V}$ and $E_p = -0.67 \text{ V}$. More reasonable values for δ of 68 \AA and 99 \AA (assuming FeOOH and Fe₂O₃, respectively) were obtained. The discrepancy between the δ values calculated using eqn. 5.2 and eqn. 5.7 supports Macdonald and Roberts's³⁸ conclusion of the inadequacy of the pore resistance model. Thus, the most likely growth mechanism for the surface film formed at A3, incorporating a surface resistance component, would be the low field mechanism with ion migration through the film as the rate determining step.

None of the cyclic voltammetric peaks yielded linear plots for either $\log i_p$ vs ν / i_p (high field mechanism) or i_p vs $\nu / i_p^{1/2}$ (low field mechanism, with ion injection into the film as the rate determining step).

The comment by Noel and Vasu³⁶⁸ should also be noted; they pointed out that the voltammetric peak current characteristics for a nucleation - growth and diffusion model (NGD) are very similar to the diffusion

controlled process (ie. i_p vs $\nu^{1/2}$) and therefore differentiation between the NGD model and purely diffusion controlled models is difficult. However, one distinguishing feature of the NGD model is the crossing over of the forward and reverse sweeps (as will be shown in Fig. 5.31). The nucleation aspect will be further discussed in chapter six. Therefore it is proposed the initial formation is via a nucleation mechanism with growth being controlled by a low field mechanism with ion migration through the surface film as the rate determining step.

Summarising the conclusions from scan rate dependencies: A1 and A2 are due to the growth of the base layer via a place exchange mechanism while the upper layer forms initially via a nucleation mechanism with subsequent growth being controlled by a low field mechanism with ion migration through the surface film as the rate determining step.

5.1.3 Conjugate Peaks

In order to investigate the relationship between the oxidation and reduction peaks the anodic and cathodic potential limits of the cyclic voltammogram were varied. A typical set of results from such an experiment is shown in Figs. 5.8 and 5.9, with the 60°C data being used since all of the peaks are clearly defined at this temperature.

Increasing the cathodic potential limit such that the rapid current decrease due to the onset of hydrogen evolution was excluded, had very little effect on the voltammogram, as can be seen in Fig. 5.8. If the potential was reversed prior to C1, the peaks A1, A2 and A4 were absent from the voltammogram and there was a marked decrease in the passive current subsequent to A3. Continuing the cycling resulted in a steady decrease in the magnitude of A3 and C2, as indicated by the arrows in Fig. 5.8. This suggests that the growth of the surface film occurs as a result of the electrochemical reactions at potentials more negative than $\approx -1.15\text{V}$. Peaks A3 and A4 were not observed if C2 was excluded from the voltammogram. These results suggest that the products formed on the forward sweep at A3 are reduced at C2 while those formed at the potential of A1, A2 and A4 are reduced at C1.

As shown in Fig. 5.9, decreasing the upper potential limit in the passive potential region resulted in a decrease in the magnitude of C1 and to a lesser extent of A3 and C2. Reversing the potential prior to A4 resulted in a decrease in C2 and C1. Terminating the voltammogram after A2 resulted in C2 no longer being present on the reverse sweep. Reversing the potential prior to A2 resulted in a decrease in the magnitude of C1. From these experiments it can be concluded that A3 is the conjugate peak to C2 while A1, A2 and A4 are conjugate peaks to C1. These results were observed for all temperatures in the range 20° to 120°C. These conjugate peak assignments are in agreement with those reported in the literature^{37,38,42,43} and suggest that A1, A2 and A4 are involved with the formation and growth of the base layer while A3 is due to the growth of the upper layer.

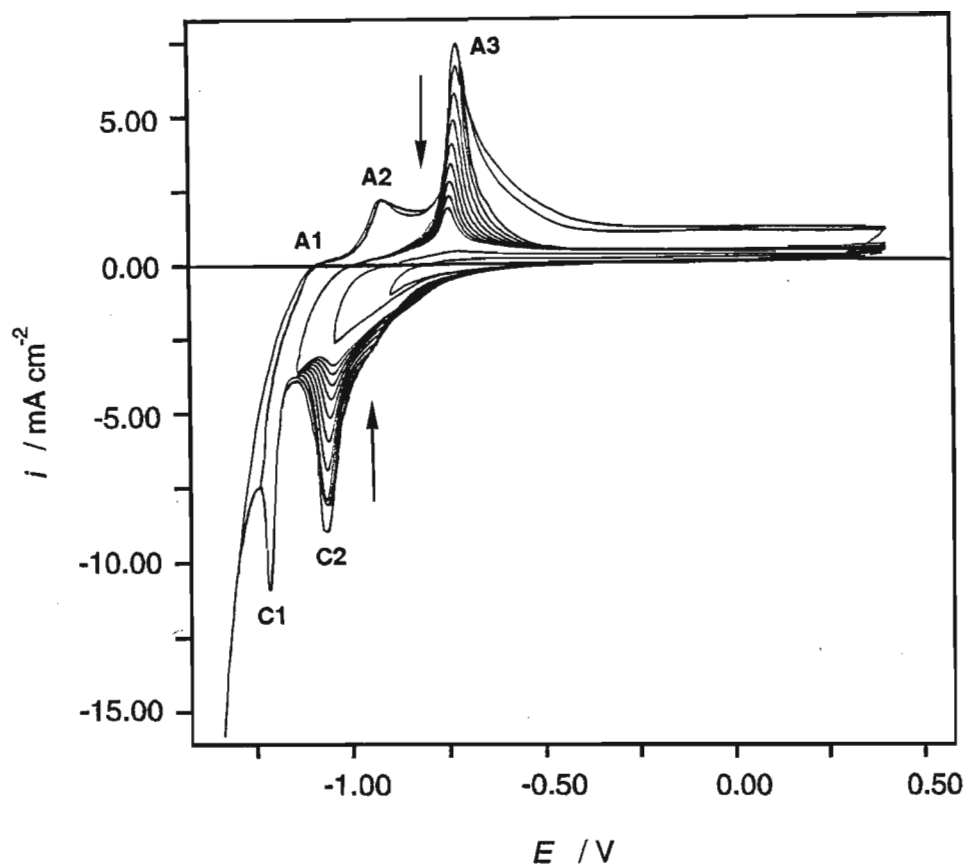


Fig. 5.8 Influence of lower potential limit on the cyclic voltammogram of Fe in 1.0M NaOH, 60°C, swept at 100mV s^{-1} , $\omega = 100\text{rad s}^{-1}$.

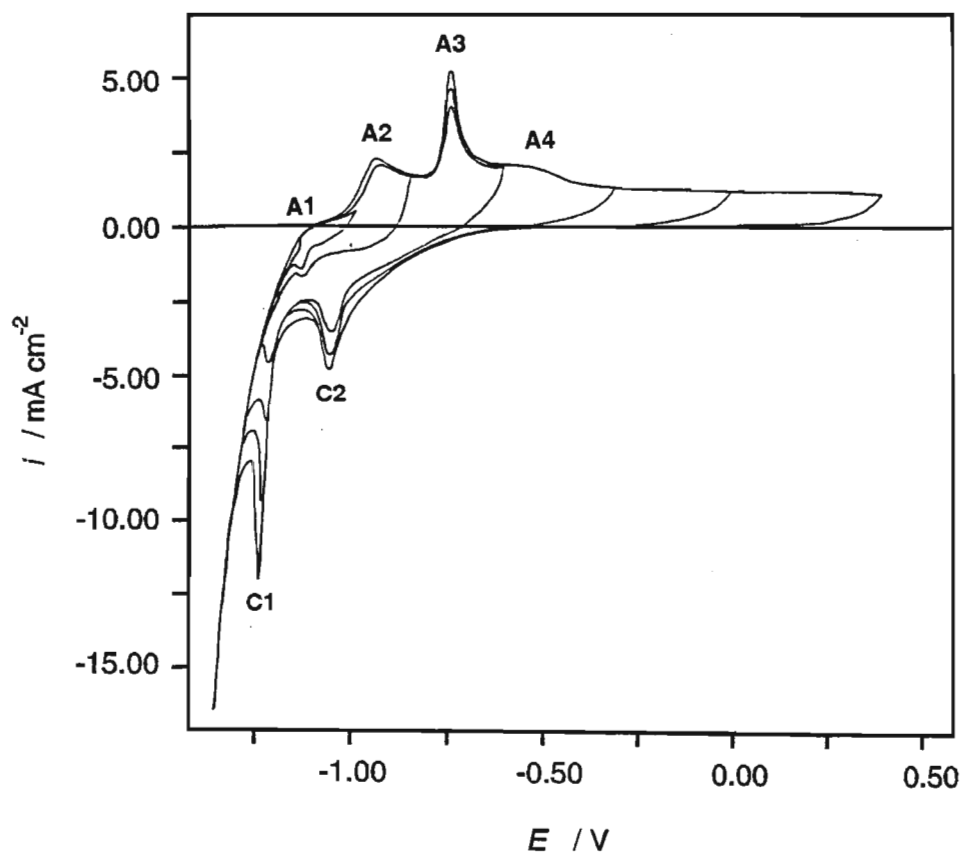


Fig. 5.9 Influence of upper potential limit on the cyclic voltammogram of Fe in 1.0M NaOH, 60°C, swept at 100mV s^{-1} , $\omega = 100\text{rad s}^{-1}$.

The above results are further supported by the cyclic voltammogram shown in Fig. 5.2, where only A1, A2, A4 and C1 are present on the first sweep. It is only on subsequent sweeps that A3 and C2 appear, and with continued cycling there is significant growth of these two peaks, while there is only a slight increase in A1, A2 and C1. Fig. 5.8 supports the earlier proposal that A3 is the result of the re-oxidation of products generated on the previous sweep.

The shape of the reduction peaks are able to provide an indication as to the nature of the surface film formed on the forward sweep, with a sharp symmetrical reduction peak suggesting the reduction of a compact adherent film while a broad peak suggests the presence of a more diffuse film. Thus from the conjugate pairings described above, the sharpness of C1 suggests that A1, A2 and A4 are due to the formation of the compact and adherent base layer while A3 is due to the formation of the non-protective upper layer.

5.1.4 Rotation Rate Dependence

To investigate the rotation rate dependence of the cyclic voltammograms, the rotation rate of the electrode was varied from 0 rad s^{-1} to 256 rad s^{-1} . $i_{p,A1}$ decreased linearly with increasing rotation rate as a function of $\omega^{1/2}$ at 20°C and 40°C and to a lesser extent at 60°C , where greater deviation from linearity was observed. This decrease in current with increasing rotation rate suggests the removal of electrochemically active species from the electrode surface. At all temperatures, the i vs $\omega^{1/2}$ plots did not pass through the origin indicating that the dissolution process is not entirely mass transport controlled, as given by the Levich equation.³⁶⁹ $E_{p,A1}$ was independent of rotation rate at all temperatures and rotation rates.

While no clearly distinguishable peak was evident for A2 at 20°C , at 40°C $i_{p,A2}$ decreased with increasing rotation rate as a function of ω . In agreement with these results Haupt and Strehblow^{34,35} reported that a decrease in the current density with increasing rotation rate, at 20°C . At $T \geq 60^\circ\text{C}$ $i_{p,A2}$ was virtually independent of rotation rate for $68 \text{ rad s}^{-1} \leq \omega \leq 256 \text{ rad s}^{-1}$, however there was increase in the current density at 0 rad s^{-1} . $E_{p,A2}$ was independent of rotation rate at all temperatures and rotation rates.

For peak A3 i_p increased as a function of $\omega^{1/2}$ at 20°C and to a lesser extent at 40°C . This result is at variance with that reported³⁴ for 20°C data where $i_{p,A3}$ was found to be virtually independent of rotation rate. As was observed with A2, at $T \geq 60^\circ\text{C}$ $i_{p,A3}$ was virtually independent of rotation rate, but increased when the electrode was not rotated. The difference in i_p between the stationary and rotating states increased with increasing temperature. Up to 60°C an increase in $E_{p,A3}$ was observed with increasing rotation rate. At higher temperatures $E_{p,A3}$ was virtually independent of rotation rate.

At 20°C and 40°C $i_{p,C1}$ was independent of rotation rate with a decrease in i_p being observed at 40°C when the electrode was not rotated. At $T \geq 60^\circ\text{C}$ $i_{p,C1}$ increased with increasing rotation rate but the precise functional dependence of $i_{p,C1}$ on rotation rate was unclear. Peak C2 increased with increasing ω at 20°C

while at $T \geq 40^\circ\text{C}$ $i_{p,C2}$ was virtually independent of rotation rate, increasing only when the electrode was not rotated. For both reduction peaks E_p was independent of rotation rate.

In order to distinguish between a dissolution - precipitation passivation mechanism and that of a solid state mechanism occurring in parallel with metal dissolution, Armstrong²¹ proposed that for the solid state mechanism i_p was dependent on rotation rate while E_p was independent of the rate of rotation. For the dissolution - precipitation mechanism, both i_p and E_p were dependent on the rotation rate. Applying these diagnostic criteria to the above results it is concluded that a solid state mechanism prevails at the potentials of A1, A2, C1 and C2. At the lower temperatures ($T < 60^\circ\text{C}$) the upper layer formation is ascribed to a dissolution - precipitation mechanism. At higher temperatures, upper layer formation is not favoured (cf Fig. 5.4 showing the decrease in A3 with increasing temperature) and the dissolution - precipitation mechanism no longer holds as indicated by the increasing independence of E_p with respect to sweep rate with increasing temperature.

These results show that the base layer forms via a solid state mechanism while upper layer formation is controlled via a dissolution - precipitation mechanism, with subsequent growth of the upper layer controlled by a low field mechanism of ion migration through the film as the rate determining step (as discussed in section 5.1.2).

5.1.5 Rotating Ring - Disc Electrode Experiments

The purpose of the rotating ring - disc experiments was to determine the presence of solution soluble species formed at the disc by oxidising or reducing them at a platinum ring electrode. In these experiments a potential sweep regime was applied to the disc while the ring was held at a series of oxidising and reducing potentials which enabled the detection of any soluble Fe(II) or Fe(III) species formed at the disc. From the Fe - H₂O Pourbaix diagram,^{206,207} oxidation of Fe(II) \rightarrow Fe(III) will occur at the ring if the ring potential is greater than -0.60V. Ring potentials in the range -1.0V \rightarrow -0.6V will be sufficient to reduce Fe(III) \rightarrow Fe(II), but not enough to reduce Fe(II) to Fe(0). For the later reaction to be observed, ring potentials of less than -1.0V are required. Taking the stability of soluble Fe(I) species and the disc - ring transition time into account, detection of Fe(I) species at the ring is unlikely. The ring response was monitored in the form of i_R vs E_D plots (with the subscripts R and D referring to the ring and disc, respectively).

As shown in Fig. 5.10, with the ring held at reducing potentials, soluble Fe(III) species formed at the disc potential corresponding to peak A3 were observed at the ring on the forward sweep. Both the ring and disc currents tend to limiting values at $E_D > A3$ suggesting that the total anodic process is controlled by either a diffusion controlled reaction or a chemical dissolution reaction. With the ring held at -1.10V, an additional peak was present on the reverse sweep, at a potential cathodic to that of peak C2, which corresponded to the reduction of Fe(II) species produced at C2. No Fe(III) species were detected on the

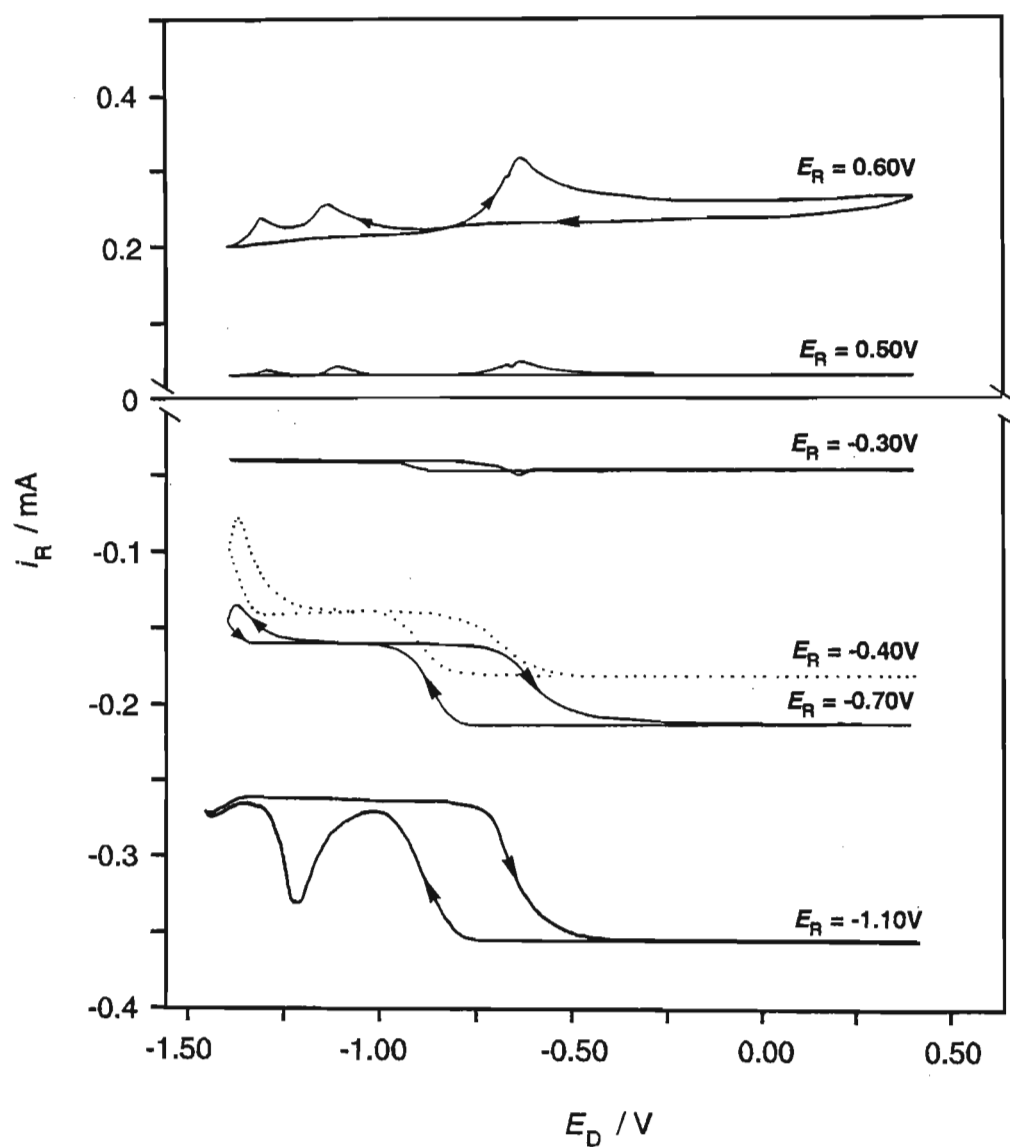


Fig. 5.10 Ring response, at the indicated ring potentials, to a Fe electrode in 1.0M NaOH, 20°C, swept between -1.40V and 0.40V at 100mV s⁻¹, $\omega = 100\text{rad s}^{-1}$.

reverse sweep. Holding the ring at oxidising potentials, a ring oxidation peak was observed on the forward sweep corresponding to A3 and two ring oxidation peaks were observed on the reverse sweep corresponding to C1 and C2. Assuming that the only species present are Fe(II) and Fe(III), it is clear that under oxidising conditions the Fe(II) species produced at the disc are detected at the ring on being oxidised to Fe(III) at potentials corresponding to A3, C1 and C2.

At higher temperatures (60°C) similar results were observed as shown in Fig. 5.11. Holding the ring at reducing potential, the ring reduction current increased to a maximum value at a potential corresponding to A3. With the ring held at oxidising potentials a ring oxidation peak (for $\text{Fe(II)} \rightarrow \text{Fe(III)}$) was observed at potentials corresponding to A3. The current after the peak maximum decreased, then increased, to a plateau at a potential corresponding to A4. On the reverse sweep two ring oxidation currents were observed, which indicated the formation of soluble Fe(II) species at the potentials of C1 and C2.

The above RRDE results are in agreement with those reported in the literature.^{41,370} It is interesting to note that through judicious experimental design and execution, ring currents were readily observed in the present work, while Armstrong^{179,371} investigating Fe in 10.0M KOH, 25°C and in 1.0M KOH, 25°C and 65°C reported that no Fe(II) or Fe(III) were detected at the ring, due to the ring currents being too small for detection, and Haupt and Strehblow³⁴ reported that ring currents start to disappear after the second applied potential sweep of the electrode due to the buildup of the upper layer.

5.2 Fe in 1.0M NaOH + 0.4M NaCN

Addition of 0.4M NaCN to 1.0M NaOH had a significant effect on the cyclic voltammetric behaviour of Fe, as can be seen in Fig. 5.12 with CN^- clearly inhibiting dissolution and surface film formation as indicated by the decrease in the magnitude of the peaks. Steady state voltammograms were obtained from approximately the 5th sweep and a typical steady state voltammogram is shown in Fig. 5.12. The voltammogram consists of a main oxidation peak A5 at -770mV (at 100mV s^{-1}) followed by a broad, poorly defined oxidation peak A6 at -470mV and two reduction peaks C3 and C4 at -1260mV and -1120mV , respectively. Although not shown in Fig. 5.12 a very small oxidation peak A7 (450mV) and reduction peak C5 (-70mV) were also present. These two peaks were better defined at higher temperatures and when the electrode was stationary (*cf* Fig. 5.13). The cathodic current due to hydrogen evolution was also found to be significantly reduced in the presence of CN^- .

The fact that steady state voltammograms are readily obtained suggests adsorption of the highly polarisable CN^- ion, with competitive adsorption between the OH^- and CN^- likely. This suggestion is supported by the results presented by Horányi,³⁷² who demonstrated the strong irreversible chemisorption and electrosorption of CN^- in alkaline media, with elimination of the chemisorbed CN^- from the surface by washing or by varying the potential, in the potential range -240 to 760mV , not being possible although some

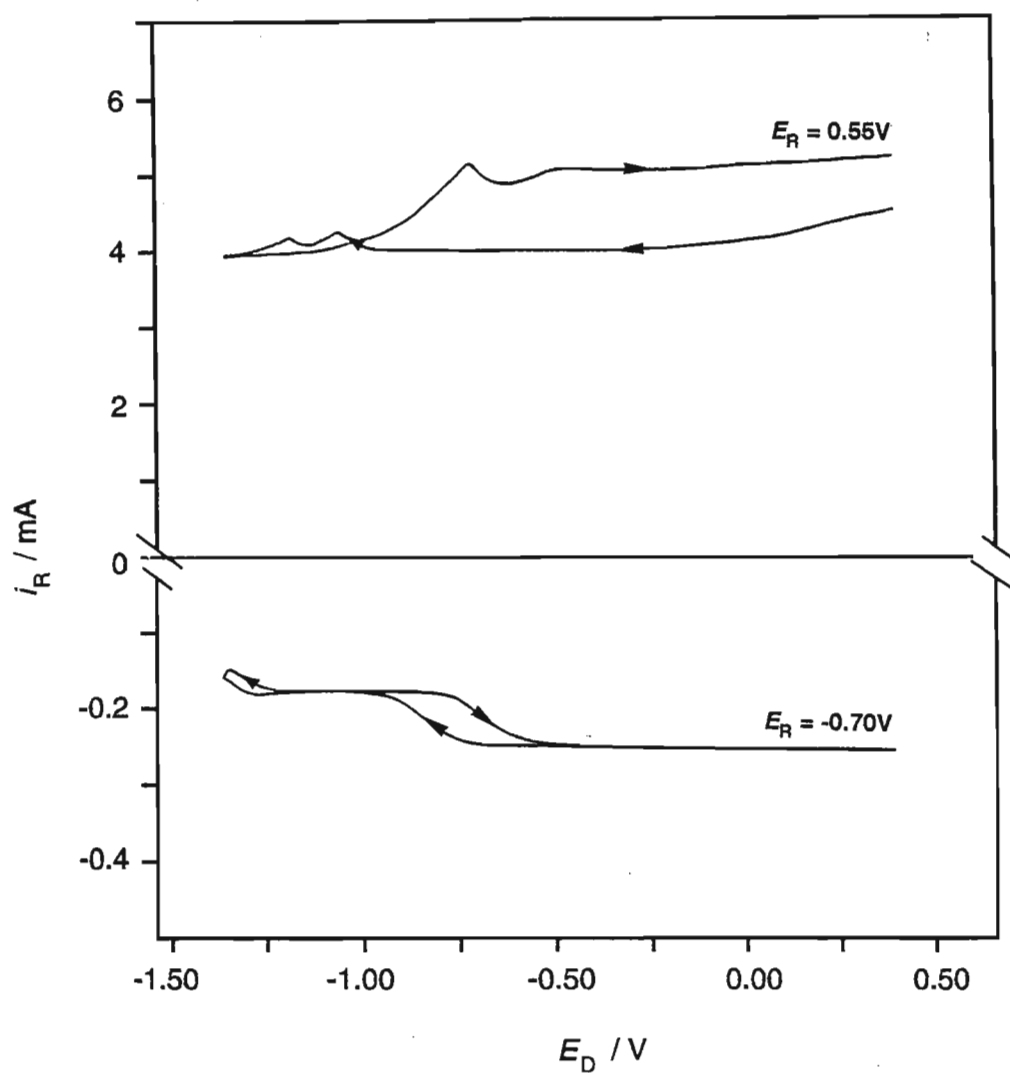


Fig. 5.11 Ring response, at the indicated ring potentials, to a Fe electrode in 1.0M NaOH, 60°C , swept between -1.30V and 0.40V at 100mV s^{-1} , $\omega = 100\text{rad s}^{-1}$.

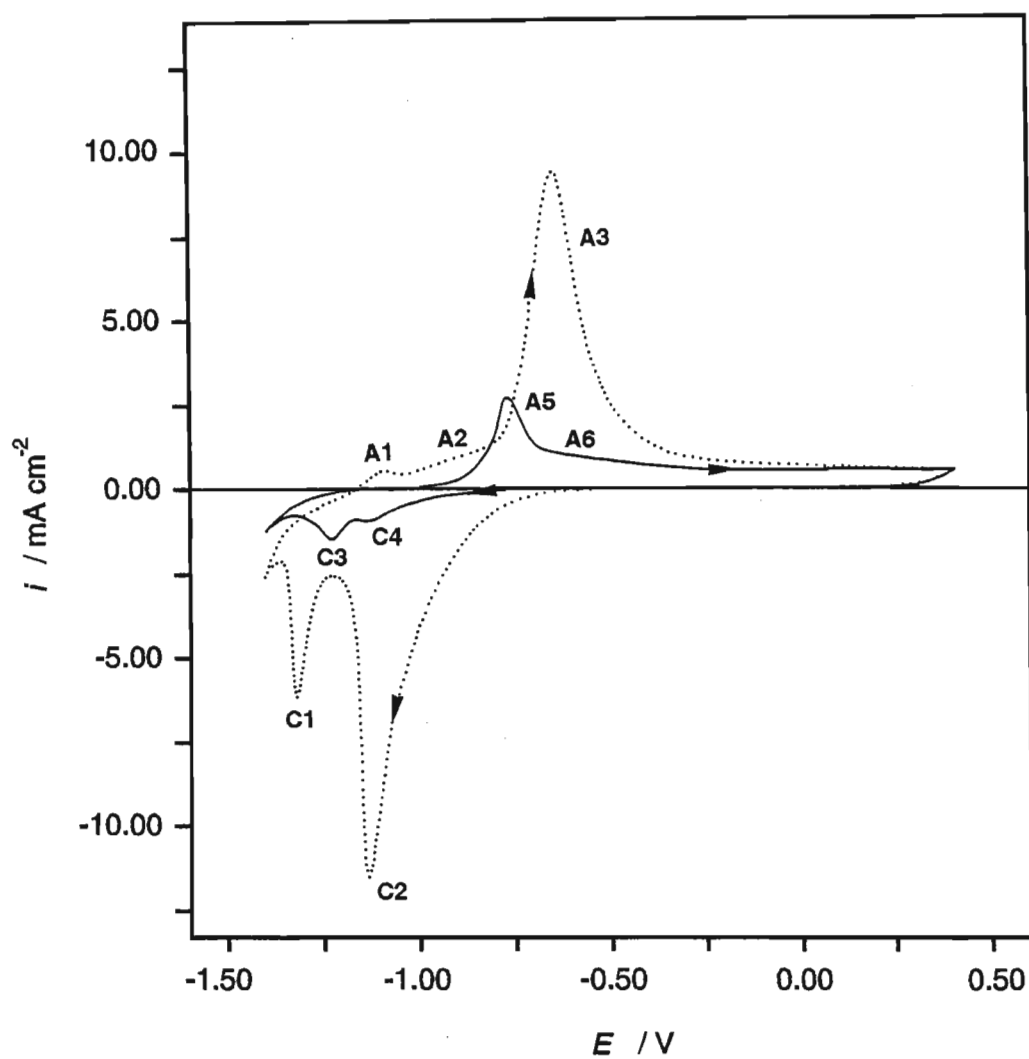


Fig. 5.12 Cyclic voltammogram of the 50th cycle of a Fe electrode in (—) $1.0\text{M NaOH} + 0.4\text{M NaCN}$ and (·····) 1.0M NaOH , 20°C , swept between -1.40V and 0.40V at 100mV s^{-1} , $\omega = 100\text{rad s}^{-1}$.

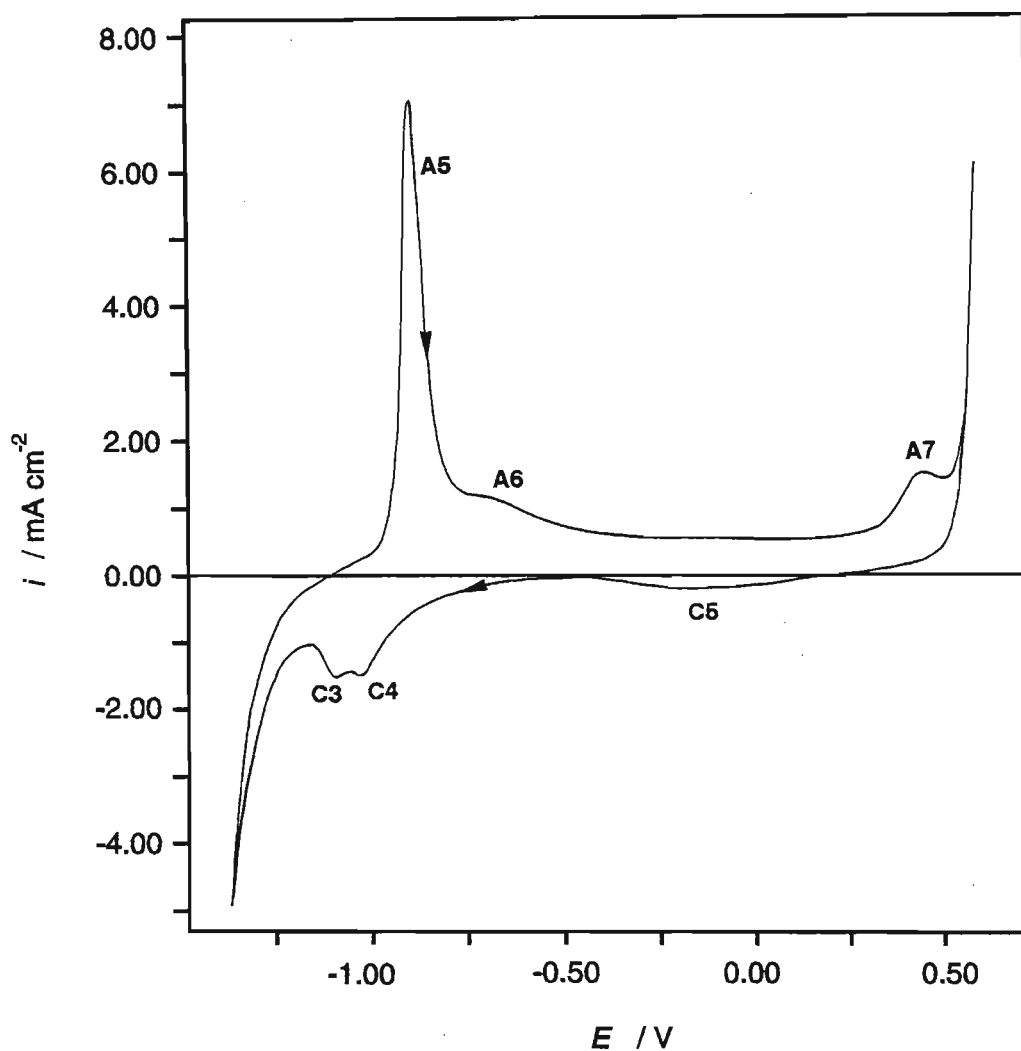


Fig. 5.13 Cyclic voltammogram of the 12th cycle of a Fe electrode in 1.0M NaOH + 0.4M NaCN, 60°C, swept between -1.35V and 0.60V at 100mV s⁻¹, 0rad s⁻¹.

slow desorption occurred at more negative potentials and above 860mV. The likelihood of competitive adsorption is further supported by the work of Shoesmith *et al.*⁵⁰ who reported that the adsorption of highly polarisable anions (SH^- in their case) resulted in steady state cyclic voltammograms for Fe in alkaline electrolytes readily being obtained and also in a significant reduction of the cathodic current due to hydrogen evolution.

As can be seen in Fig. 5.14 the cyclic voltammograms of Fe in 0.5M NaOH + 0.4M NaCN and in 1.0M NaOH + 0.4M NaCN are very similar with the exception of A5 which showed an increase in i_p and a shift of E_p to more cathodic potentials as a result of the increased Fe dissolution in the more concentrated alkali. The increased inhibition of oxide formation and growth with an increasing $[\text{CN}^-]$ to $[\text{OH}^-]$ ratio supports the concept of competitive adsorption.

5.2.1 Sweep Rate and Temperature Dependence

At all temperatures investigated ($20^\circ - 120^\circ\text{C}$), increasing the sweep rate from 2mV s^{-1} to 1V s^{-1} resulted in an increase in magnitude of all the peaks with i_p for A5, A6, A7, C3 and C4 varying as a function of $\nu^{1/2}$ and C5 varying with ν . The peak potential for the oxidation peaks shifted in an anodic direction, with $E_{p,A5}$ and $E_{p,A6}$ changing linearly with $\nu^{1/2}$ and $E_{p,A7}$ varying with ν . E_p for all the reductions peaks shifted in a negative direction as a function of $\nu^{1/2}$.

For a given sweep rate, increasing the temperature from 20°C to 120°C resulted in an increase in magnitude of all the peaks on the voltammogram, as can be seen in Fig. 5.15, with the shift of the reduction peaks to more anodic potentials while A5 and A6 shifted in a cathodic direction. A similar trend was also observed in the absence of CN^- (*cf* Fig. 5.4) with the potential of the oxidation peaks shifting in a cathodic direction while that of the reduction peaks shifted in an anodic direction with increasing temperature. Fig. 5.16 shows the linear E_p vs T relationship exhibited by the peaks.

A linear dependence of E_p against i_p , as a function of sweep rate, was found for all peaks suggesting the presence of a resistive surface film. For all peaks the resistance of the surface film decreased with increasing temperature.

The influence of temperature on i_p is shown in Fig. 5.17. The activation energies for the relevant redox processes calculated from such Arrhenius plots decreased with increasing sweep rate for the reactions occurring at A5, A6 and C3 and increased for C4 (*cf* Fig. 5.18). Over the range of sweep rates 20mV s^{-1} to 200mV s^{-1} there was close correlation between the activation energies calculated for A2 in 1.0M NaOH and for A5 in 1.0M NaOH + 0.4M NaCN. In both of these electrolytes, the E_a vs ν plots for A2 and A5 showed a rapid decrease in E_a at $\nu < 40\text{mV s}^{-1}$ (*cf* Figs. 5.7 and 5.18). In Fig. 5.18 the A5 curve leveled off at $\nu > 100\text{mV s}^{-1}$, while in the absence of CN^- E_a for A2 continued to decrease with increasing sweep rate. This indicates the effectiveness of the CN^- inhibition on oxide formation.

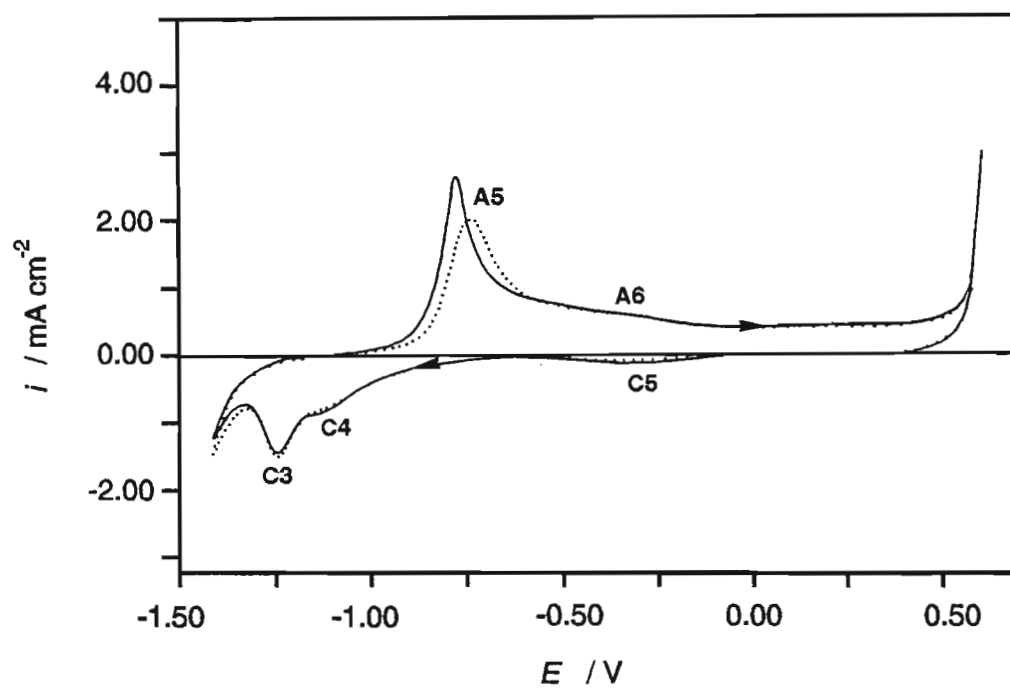


Fig. 5.14 Steady state cyclic voltammogram of Fe in (—) 1.0M NaOH + 0.4M NaCN and (·····) 0.5M NaOH + 0.4M NaCN, 20°C, swept between -1.40V and 0.60V at 100mV s^{-1} , $\omega = 100\text{rad s}^{-1}$.

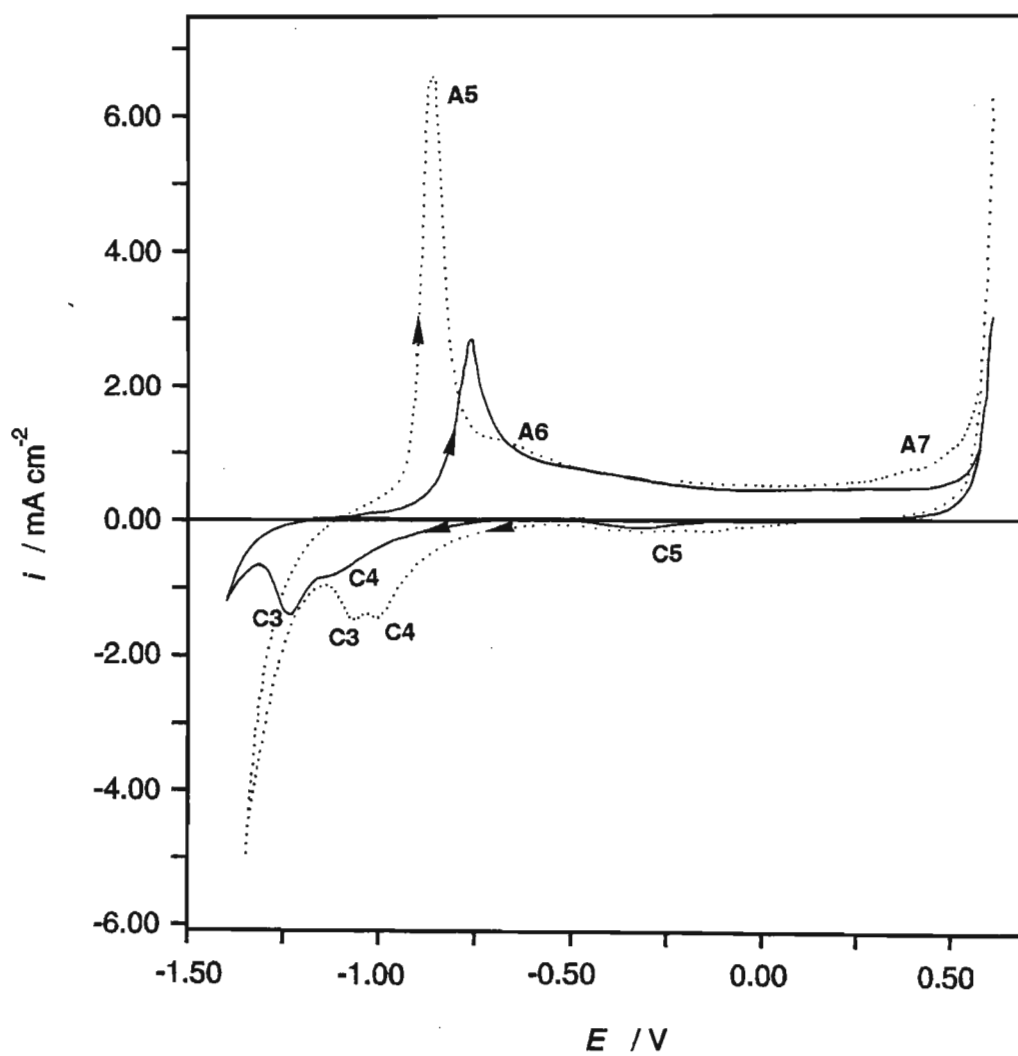


Fig. 5.15 Influence of temperature on the steady state cyclic voltammogram of Fe in 1.0M NaOH + 0.4M NaCN at (—) 20°C and (·····) 60°C, swept between -1.40V and 0.60V at 100mV s^{-1} , $\omega = 100\text{rad s}^{-1}$.

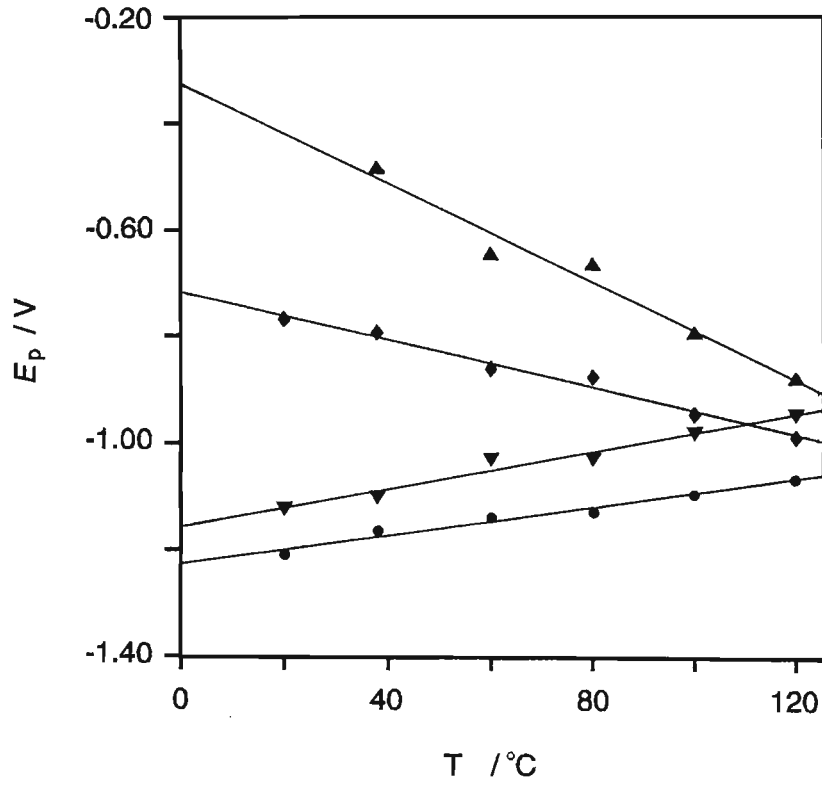


Fig. 5.16 Influence of temperature on the cyclic voltammetric peak potentials of a Fe electrode in 1.0M NaOH + 0.4M NaCN. $\nu = 100\text{mV s}^{-1}$, $\omega = 100\text{rad s}^{-1}$.

◆ A5 ▲ A6
 • C3 ▼ C4

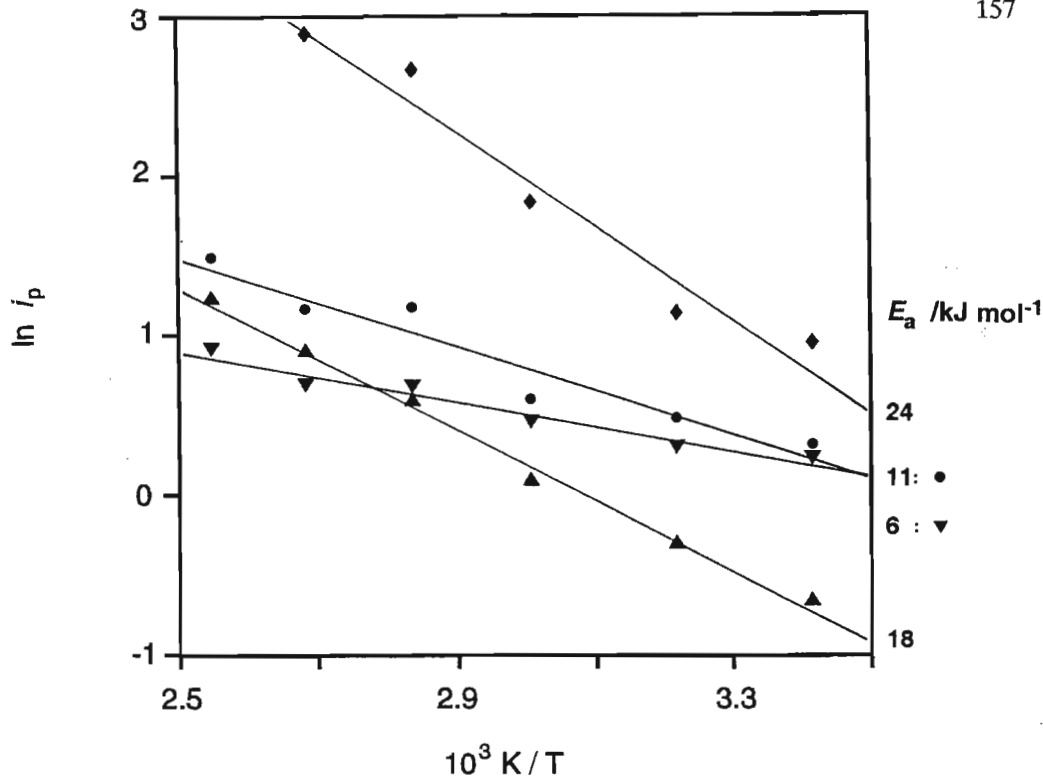


Fig. 5.17 Arrhenius plot for the reactions occurring on a Fe electrode in 1.0M NaOH + 0.4M NaCN at the potentials of the indicated peaks.
 $\nu = 100\text{mV s}^{-1}$, $\omega = 100\text{rad s}^{-1}$
 \blacklozenge A5 \blacktriangle A6
 \bullet C3 \blacktriangledown C4

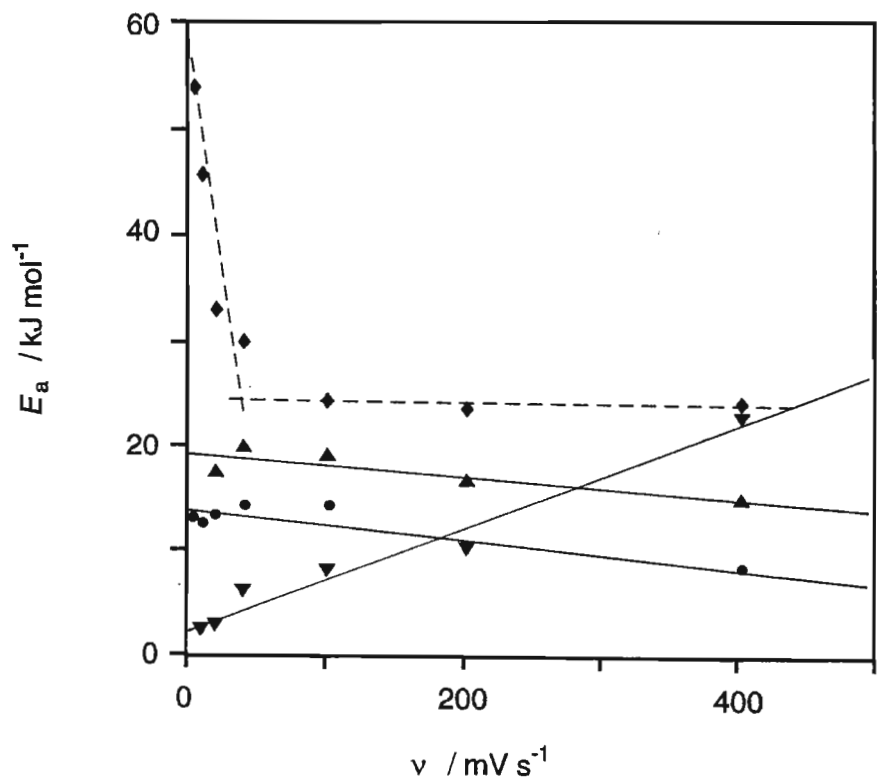


Fig. 5.18 Influence of sweep rate on activation energy of a Fe electrode in 1.0M NaOH + 0.4M NaCN.
 \blacklozenge A5 \blacktriangle A6
 \bullet C3 \blacktriangledown C4

5.2.2 Growth Laws

For temperatures up to 40°C the only plots that showed good linearity were the i_p vs $\nu^{1/2}$ plots which indicated that the low field mechanism prevailed in which ion migration through the film is the rate determining step of oxide growth. With increasing temperature ($T \geq 60^\circ\text{C}$) the linearity of the $\log i_p$ vs ν/i_p plot (high field mechanism) improved such that at 80°C the i_p vs $\nu^{1/2}$ relationship showed only slightly better linearity than the $\log i_p$ vs ν/i_p relationship and at 120°C both relationships showed equally good linearity.

These results indicate that at low temperatures ($T \leq 60^\circ\text{C}$) film growth is controlled by a low field mechanism with ion migration through the film as the rate determining step, and which gradually changes to a high field mechanism at higher temperatures ($T \geq 120^\circ\text{C}$).

5.2.3 Conjugate Peaks

The relationship between the oxidation and reduction peaks was investigated by varying the potential limits of the cyclic voltammogram. As the peaks are better defined at higher temperatures, the 60°C data will be used in this discussion.

As can be seen in Fig. 5.19, reversing the potential prior to C3 halved the peak current density of A5 but had little effect on the rest of the voltammogram. Increasing the lower potential limit such that C4 was excluded, resulted in the disappearance of both peaks A5 and A6. This indicates that the growth of the surface film occurs as a result of the electrochemical reactions at potentials more negative than $\approx -1.0\text{V}$. Similar findings were reported in section 5.1.3 for Fe in 1.0M NaOH suggesting that the surface film formed in CN^- (0.4M NaCN) containing electrolytes is similar to that formed in 1.0M NaOH. C5 remained unchanged, while there was a slight decrease in the magnitude of A7. This trend continued, with further increases in the lower potential limit, and it was only when this potential was greater than -600mV that a decrease in the magnitude of peak C5 was observed. Peak A7 was no longer observed when the potential range of peak C5 was not scanned. Therefore it can be concluded that the conjugate peaks are A5 and C3, peaks A5, A6 and C4, and peaks A7 and C5 indicating that oxidation products from the reaction at A5 are reduced at C3 and C4, while reduction of the surface film formed at A6 is reduced at C4. The experiments were repeated at all temperatures under investigation, with the same conclusions being drawn.

The above conclusions are verified by the results obtained by progressively decreasing the anodic potential limit of the voltammogram. As can be seen in Fig. 5.20 terminating the anodic sweep prior to A7 resulted in the disappearance of C5. Progressively decreasing the anodic potential limit in the passive region resulted in a corresponding decrease in the magnitude of C3 and C4, while A5 and A6 remain unchanged. The two reduction peaks were still present subsequent to A6 being excluded from the voltammogram and it

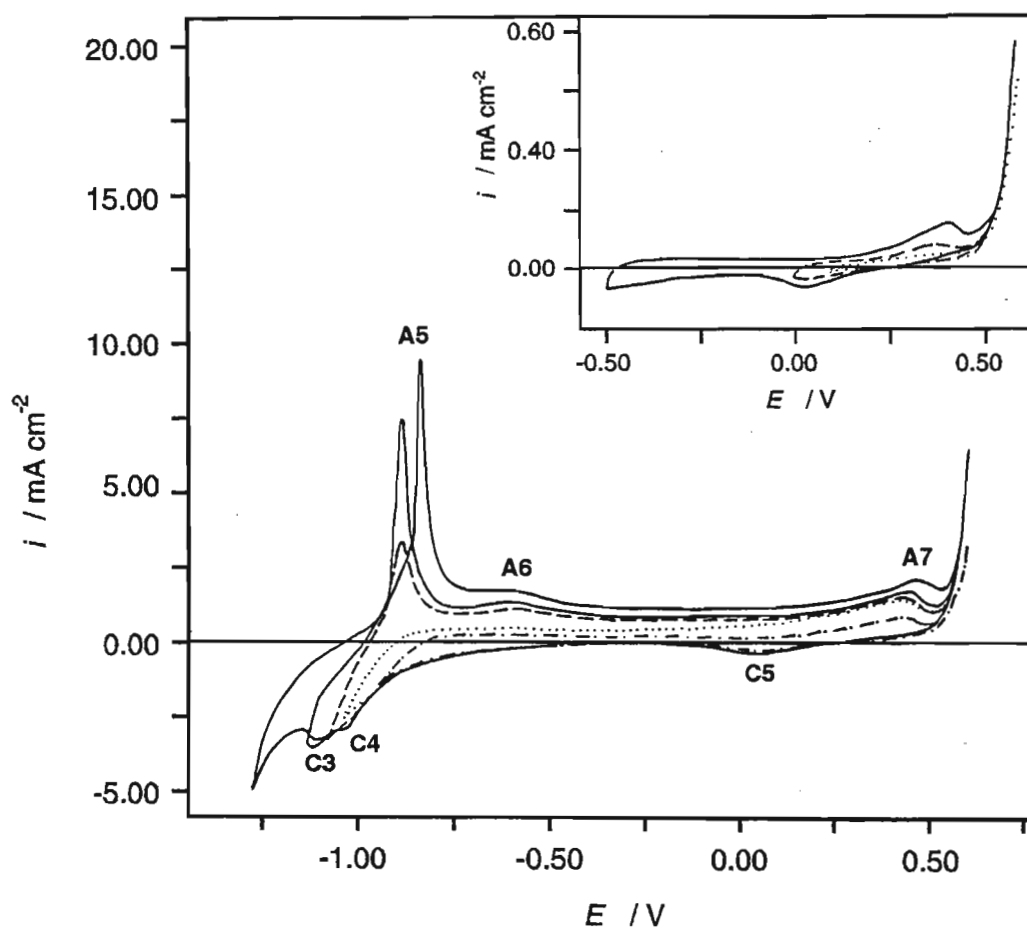


Fig. 5.19 Influence of lower potential limit on the cyclic voltammogram of Fe in 1.0M NaOH + 0.4M NaCN, 60°C, swept at 100mV s^{-1} , $\omega = 100\text{rad s}^{-1}$.

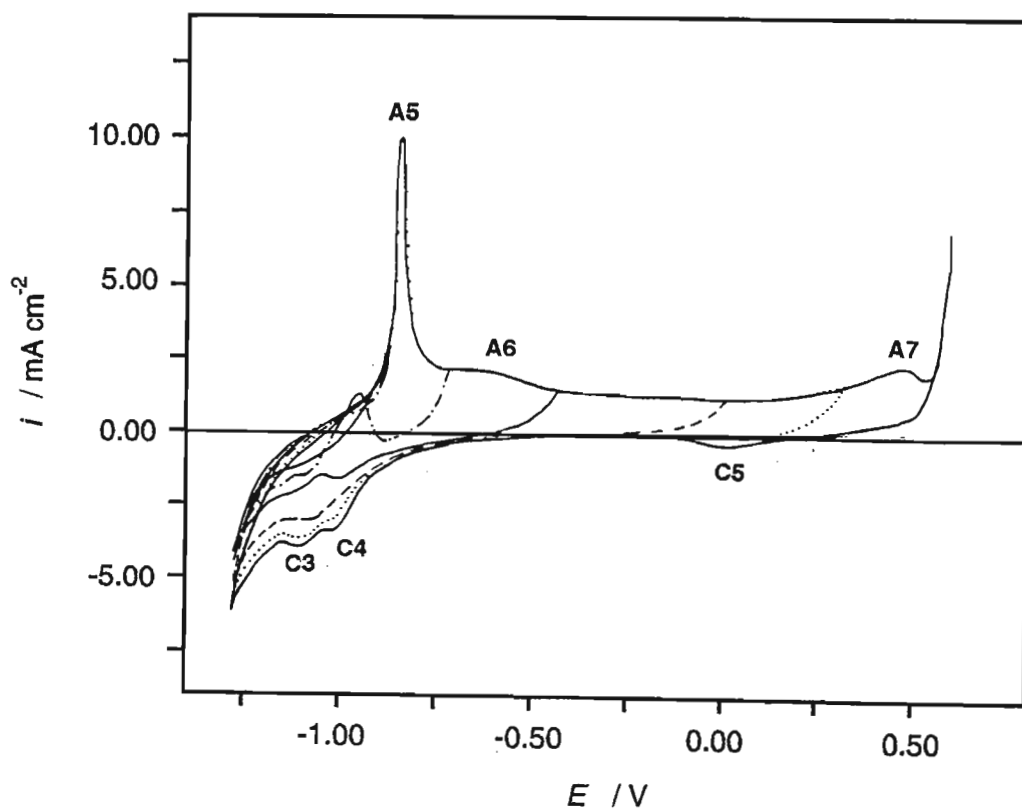


Fig. 5.20 Influence of upper potential limit on the cyclic voltammogram of Fe in 1.0M NaOH + 0.4M NaCN, 60°C, swept at 100mV s^{-1} , $\omega = 100\text{rad s}^{-1}$.

was only after the potential region of peak A5 was no longer scanned that these two peaks were no longer observed. Qualitatively the same results were obtained at all temperatures. In addition, however, the results obtained at $T \geq 60^\circ\text{C}$ showed that the reaction corresponding to A6 is responsible for passivating the electrode surface since when the potential region of A6 was not scanned, effective passivation did not occur, as is demonstrated by the oxidation peak that occurs on the reverse sweep.

The above results showed that the oxidation products formed at the potential of A5 are reduced at C3 and C4 while those formed at A6 and A7 are reduced at C4 and C5 respectively.

5.2.4 Rotation Rate Dependence

With increasing rotation rate the current density of A5 decreased while that of C3 and C4 increased as a function of $\omega^{1/2}$ for $68\text{rad s}^{-1} \leq \omega \leq 256\text{rad s}^{-1}$, at 20°C , indicating the removal of electroactive species from the electrode at A5 and the increase in electroactive species at the electrode surface for the reactions occurring at C3 and C4. E_p for these three peaks was independent of rotation rate. For a stationary electrode a steady state cyclic voltammogram was obtained within six sweeps with C5 having the largest increase in i_p of 26%.

At 38°C the current density of C5 was independent of the rotation rate, while that of A5, C3 and C4 increased linearly as a function of $\omega^{1/2}$, and that of A6 and A7, although varying with rotation rate, showed no clear dependence of i_p vs ω . E_p for all the peaks was independent of rotation rate. For a stationary electrode there is a very slight increase in i_p for C3, C4 and A7 on successive sweeps.

At 60°C i_p for peaks A6, A7, C3 and C4 increased linearly with $\omega^{1/2}$, while $i_{p,A5}$ increased with rotation rate although no trend was apparent. $i_{p,C5}$ and E_p for all the peaks were independent of rotation rate at 60°C . At $T \geq 80^\circ\text{C}$ i_p for C5 and the oxidation peaks, and E_p for all the peaks were virtually independent of rotation rate. C3 and C4 continued to exhibit a linear i_p vs $\omega^{1/2}$ relationship. Based on Armstrong's²¹ analysis of the influence of rotation rate on i_p and E_p , the independence of E_p on ω indicates that a solid state mechanism prevails at A5, C3, C4 and C5.

5.2.5 Rotating Ring - Disc Electrode Experiments

Holding the ring at oxidising potentials two ring oxidation peaks were observed. As can be seen in Fig. 5.21 the one peak (R_1) occurred on the forward sweep at a potential corresponding to peak A5 while the second ring oxidation peak (R_2) occurred on the reverse sweep and corresponded to the disc peak C3. Although not obvious in Fig. 5.21, a shoulder on the leading edge of peak R_2 was evident, indicating that two oxidation processes had occurred at the ring. This shoulder becomes more apparent at elevated temperatures, as can be seen in Fig. 5.22 and Fig. 5.23, and corresponds to the increase in magnitude of C4 with increasing temperature, as was shown earlier in Fig. 5.15. These results indicate the formation of

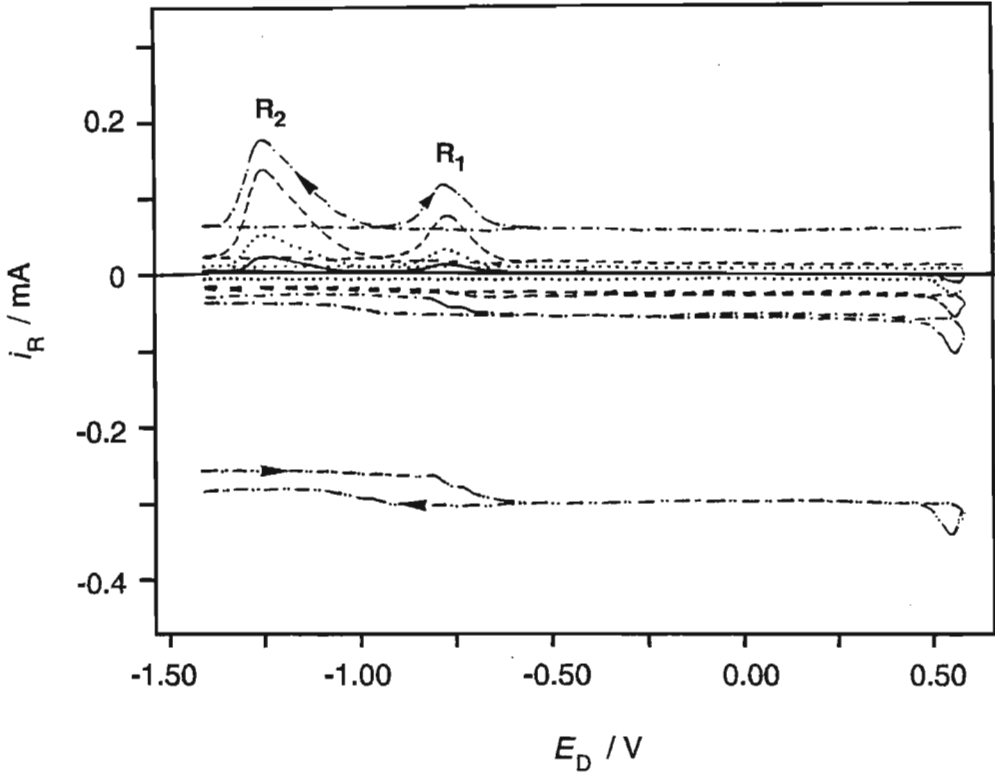


Fig. 5.21 Ring response to a Fe electrode in 1.0M NaOH + 0.4M NaCN, 20°C, swept between -1.40V and 0.60V at 100mV s⁻¹, $\omega = 100\text{rad s}^{-1}$.

Positive ring potentials		Negative ring potentials	
————	0.00V	-0.40V
.....	0.20V	-----	-0.80V
-----	0.40V	— · — · —	-1.00V
— · — · —	0.60V	— · — · —	-1.20V

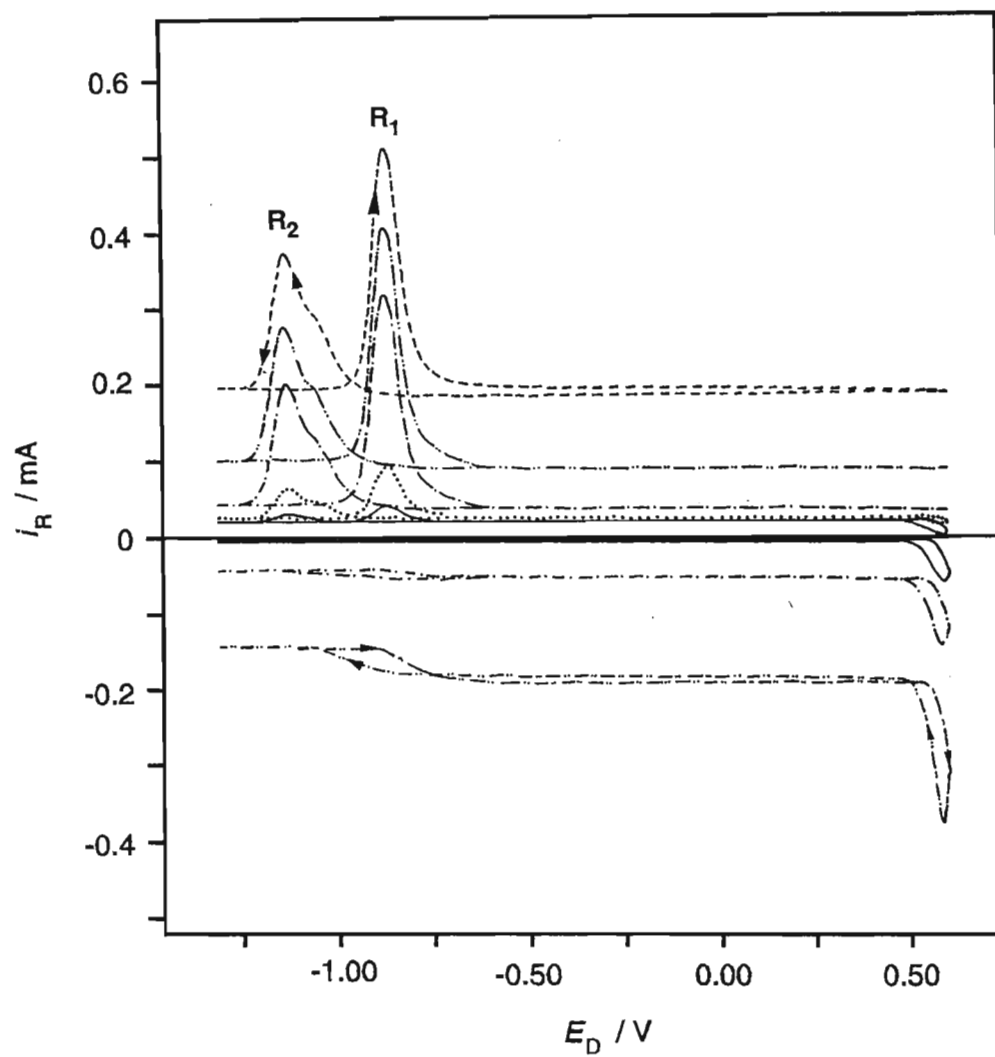


Fig.5.22 Ring response to a Fe electrode in 1.0M NaOH + 0.4M NaCN, 60°C, swept between -1.30V and 0.60V at 100mV s^{-1} , $\omega = 100\text{rad s}^{-1}$.

Positive ring potentials

—— 0.10V
 0.15V
 - · - · - 0.25V
 - · - · - 0.50V
 - - - - - 0.75V

Negative ring potentials

—— -0.20V
 - · - · - -0.60V
 - · - · - -1.00V

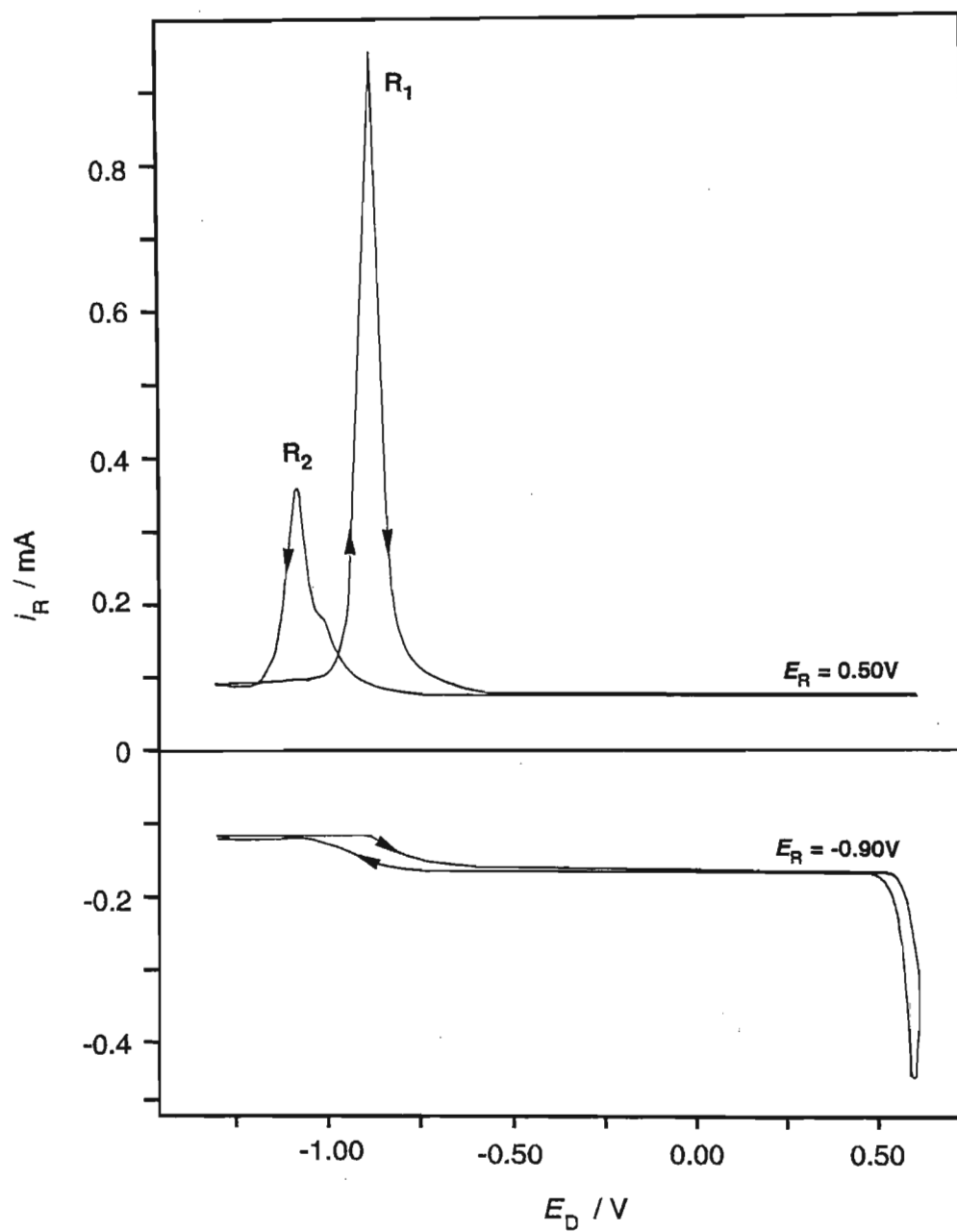


Fig. 5.23 Ring response, at the indicated ring potentials, to a Fe electrode in 1.0M NaOH + 0.4M NaCN, 80°C, swept between -1.30V and 0.60V at 100mV s⁻¹, $\omega = 100\text{rad s}^{-1}$.

soluble Fe(II) species at the disc peaks A5, C3 and to a lesser extent C4.

With the ring held at reducing potentials, a reduction wave was observed at $E_R \leq -0.80V$ as a result of the reduction of Fe(II), produced at A5, to Fe(0). The step in the reduction wave suggests the presence of two processes occurring at A5. No solution soluble Fe(III) species were detected at the ring at 20°C. At $T \geq 60^\circ C$ a very small reduction wave was evident as a result of the reduction of Fe(III), produced at A5, to Fe(II).

Thus it can be concluded that solution soluble Fe(II) is produced at the potential of A5 on the forward sweep and at C3 and C4 on the reverse sweep. At $T \geq 60^\circ C$ very small quantities of Fe(III) were also produced at A5.

5.2.6 Influence of Hexacyanoferrates on the Cyclic Voltammetric and Rotating Ring - Disc Electrode Response of a Fe Electrode

The Fe - CN - H₂O Pourbaix diagram⁶² indicates that although the formation of hexacyanoferrate (III) is thermodynamically unfavourable under present experimental conditions, formation of soluble hexacyanoferrate (II) is favoured at the potential of A5. However, contrary to the Pourbaix diagram, Kenna *et al.*⁶⁰ reported that they could not find any evidence of hexacyanoferrate (II) formation in the pH range of 9 to 10. In order to determine whether hexacyanoferrate (II) or (III) complexes are formed, the influence of $Fe(CN)_6^{2-}$ and $Fe(CN)_6^{3-}$ additions to the electrolyte was investigated.

Addition of $K_4Fe(CN)_6$ to the electrolyte resulted in an increase in A5, C3 and C4, as can be seen in Fig. 5.24. At high anodic potentials an additional oxidation peak was observed in the presence of $K_4Fe(CN)_6$ having a half wave potential of 440mV, after the 5.8mM $K_4Fe(CN)_6$ addition. Wels and Johnson³⁷³ reported a similar voltammetric response for the oxidation of cyanide to cyanate on CuO filmed disc electrodes. For 1mM CN^- they reported $E_{1/2} = \approx 350mV$ with an increase of $\approx 30mV$ per mM CN^- , and concluded that the positive shift of $E_{1/2}$ for increasing cyanide concentrations and also increasing rotation rate was diagnostic evidence for a faradaic process under mixed control by electron transfer and mass transport kinetics.

Fig. 5.25 shows the ring response in the $K_4Fe(CN)_6$ containing electrolytes was very similar to that obtained in the absence of $K_4Fe(CN)_6$ with however the additional reduction wave due to the CN^- oxidation reaction, occurring at the disc, and the increase in the magnitude of the ring oxidation peak, R_1 , on the forward sweep.

As shown in Fig. 5.26, additions of hexacyanoferrate (III) to 1.0M NaOH + 0.4M NaCN resulted in the appearance of an oxidation wave at anodic potentials ($E_{1/2} = 50mV$ after the 4.9mM $K_3Fe(CN)_6$ addition) and a further small oxidation peak at 540mV. This oxidation peak became more prominent when the

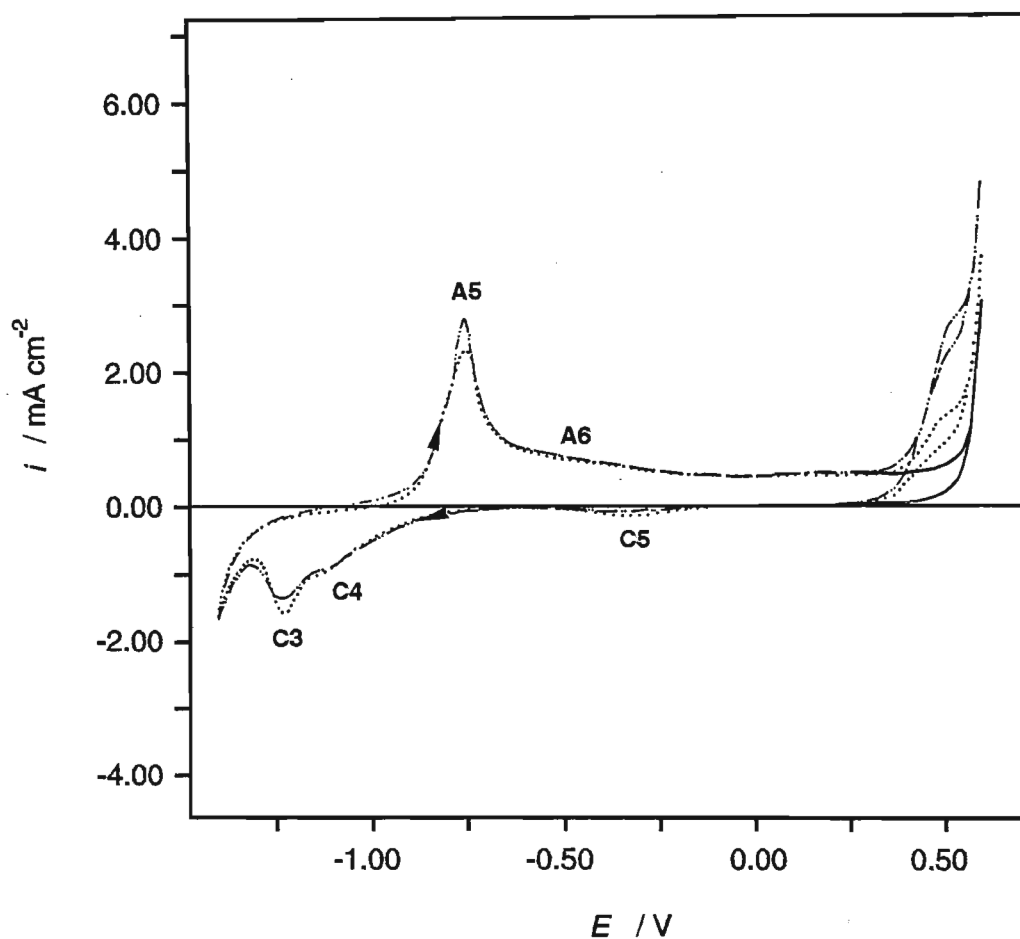


Fig. 5.24 Influence of $\text{K}_4\text{Fe}(\text{CN})_6$ additions on the cyclic voltammogram of a Fe electrode in 1.0M NaOH + 0.4M NaCN, 20°C, swept between -1.35V and 0.60V at 100mV s^{-1} , $\omega = 100\text{rad s}^{-1}$.

- 1.0M NaOH + 0.4M NaCN
- 1.0M NaOH + 0.4M NaCN + 2.0mM $\text{K}_4\text{Fe}(\text{CN})_6$
- · - · - · 1.0M NaOH + 0.4M NaCN + 5.8mM $\text{K}_3\text{Fe}(\text{CN})_6$

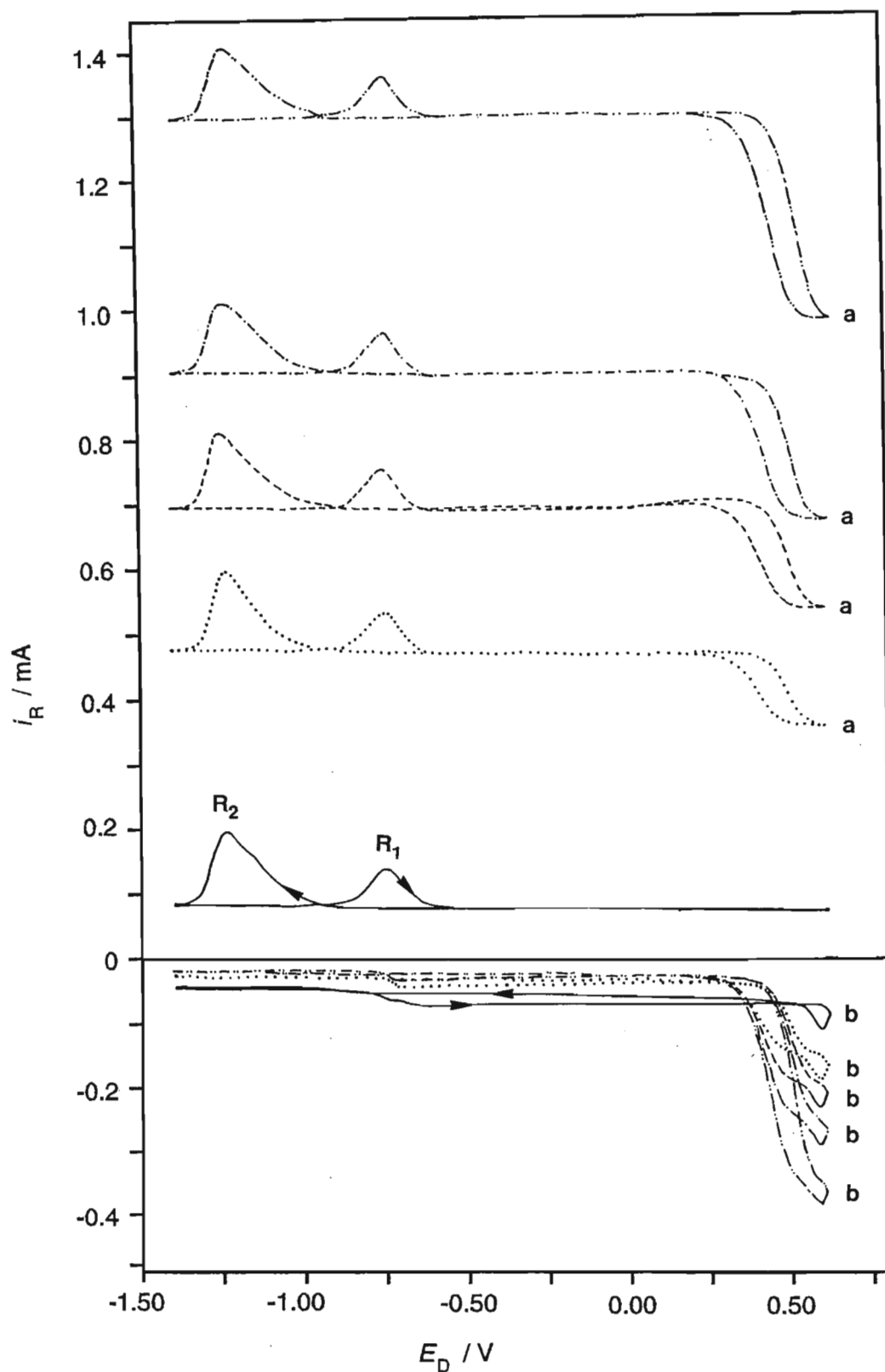


Fig. 5.25 Influence of $\text{K}_4\text{Fe}(\text{CN})_6$ additions on the ring response to a Fe electrode in 1.0M NaOH + 0.4M NaCN, 20°C, swept between -1.40V and 0.60V at 100mV s^{-1} , $\omega = 100\text{rad s}^{-1}$. (a) $E_R = 0.50\text{V}$ (b) $E_R = -1.00\text{V}$

- 1.0M NaOH + 0.4M NaCN
- 1.0M NaOH + 0.4M NaCN + 2.0mM $\text{K}_4\text{Fe}(\text{CN})_6$
- 1.0M NaOH + 0.4M NaCN + 3.0mM $\text{K}_4\text{Fe}(\text{CN})_6$
- · - · - 1.0M NaOH + 0.4M NaCN + 4.0mM $\text{K}_4\text{Fe}(\text{CN})_6$
- · - · - · 1.0M NaOH + 0.4M NaCN + 5.8mM $\text{K}_4\text{Fe}(\text{CN})_6$

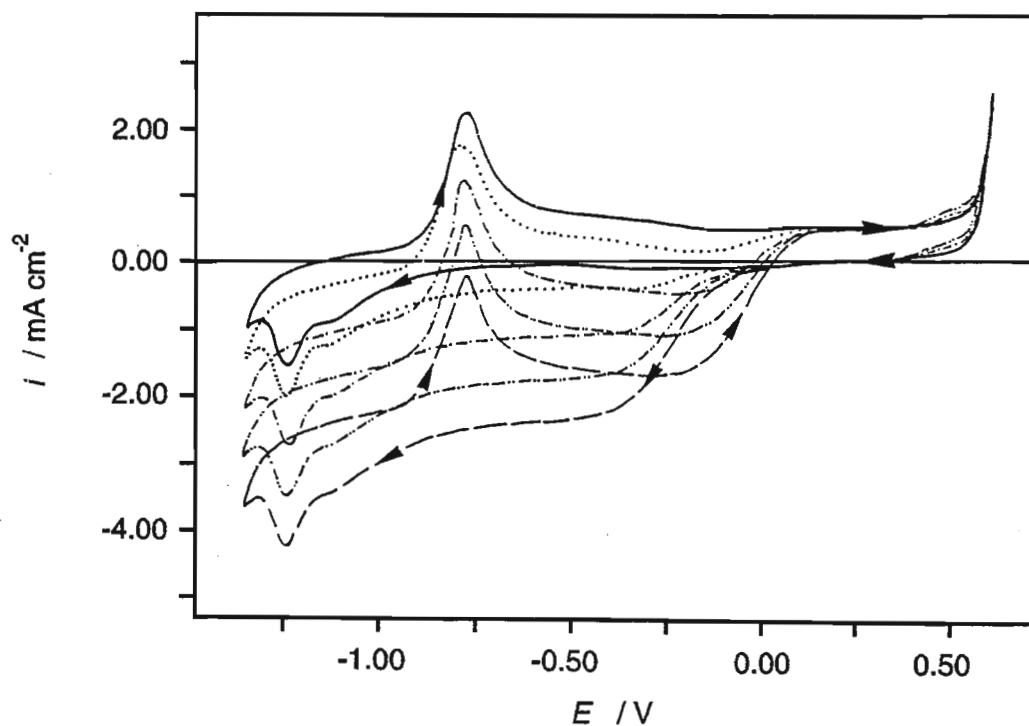


Fig. 5.26 Influence of $\text{K}_3\text{Fe}(\text{CN})_6$ additions on the cyclic voltammogram of a Fe electrode in 1.0M NaOH + 0.4M NaCN, 20°C, swept between -1.35V and 0.60V at 100mV s^{-1} , $\omega = 100\text{rad s}^{-1}$.

- 1.0M NaOH + 0.4M NaCN
- 1.0M NaOH + 0.4M NaCN + 1.0mM $\text{K}_3\text{Fe}(\text{CN})_6$
- · - · - 1.0M NaOH + 0.4M NaCN + 3.0mM $\text{K}_3\text{Fe}(\text{CN})_6$
- · · · - 1.0M NaOH + 0.4M NaCN + 4.9mM $\text{K}_3\text{Fe}(\text{CN})_6$
- - - - 1.0M NaOH + 0.4M NaCN + 6.7mM $\text{K}_3\text{Fe}(\text{CN})_6$

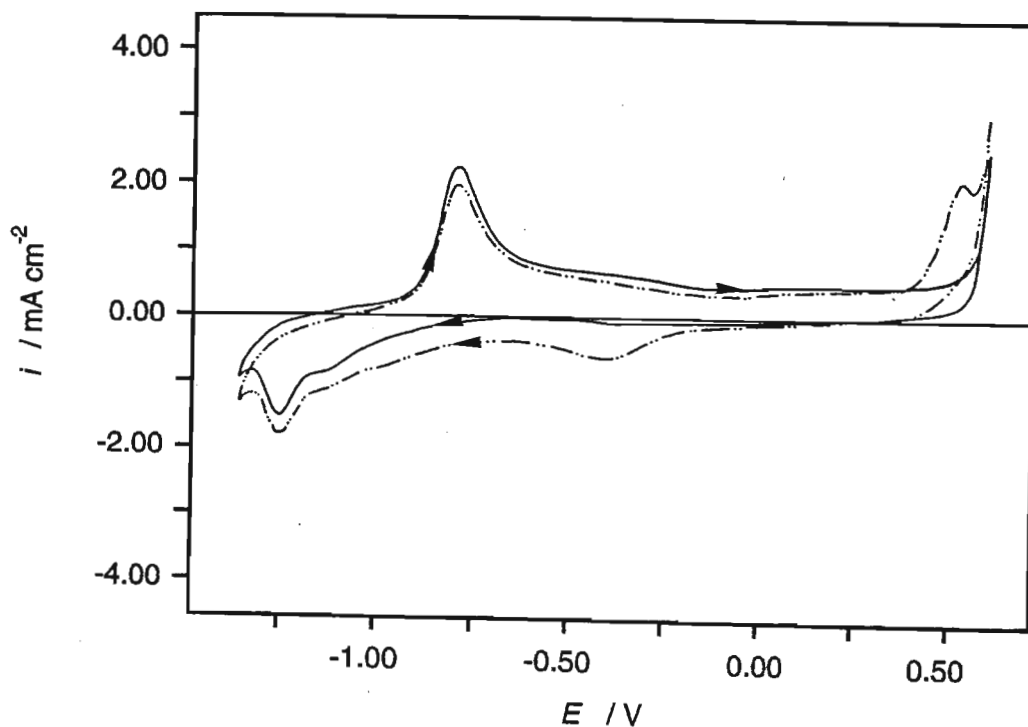


Fig. 5.27 Influence of $\text{K}_3\text{Fe}(\text{CN})_6$ on the cyclic voltammogram of a stationary Fe electrode in 1.0M NaOH + 0.4M NaCN, 20°C, swept between -1.35V and 0.6V at 100mV s^{-1} .

- 1.0M NaOH + 0.4M NaCN
- - - - 1.0M NaOH + 0.4M NaCN + 4.9mM $\text{K}_3\text{Fe}(\text{CN})_6$

electrode was not rotated, as did the reduction peak at -390mV (*cf* Fig. 5.27).

The ring response to the hexacyanoferrate (III) additions (Fig. 5.28) was identical to that of the 1.0M NaOH + 0.4M NaCN system but with the additional responses due to the species produced at the oxidation wave ($E_{1/2} = 50\text{mV}$ after the 4.9mM $\text{K}_3\text{Fe}(\text{CN})_6$ addition) and oxidation peak at $\approx 500\text{mV}$.

Thus these results show that A5 is due or partially due to the formation of hexacyanoferrate (II) and that the oxidation of cyanide to cyanate is responsible for A7. The formation of $\text{Fe}(\text{CN})_6^{4-}$ as opposed to $\text{Fe}(\text{CN})_6^{3-}$ is supported by the fact that despite $\text{Fe}(\text{CN})_6^{4-}$ having a larger dissociation constant than $\text{Fe}(\text{CN})_6^{3-}$, the Fe—CN bond is very much stronger in Fe(II) complexes than in Fe(III) complexes and hence the formation of $\text{Fe}(\text{CN})_6^{4-}$ is favoured. These results are further supported by the Pourbaix diagram for the Fe - CN - H_2O system⁶² which shows that for the present experimental conditions, formation of $\text{Fe}(\text{CN})_6^{4-}$ is favoured while formation of $\text{Fe}(\text{CN})_6^{3-}$ is unlikely.

5.3 Fe in 0.5M NaOH

Decreasing the hydroxide concentration to 0.5M NaOH resulted in a qualitatively similar voltammogram to that obtained in 1.0M NaOH with the exception that at ambient temperatures the main oxidation peak A3 split into three peaks as shown in Fig. 5.29. At 20°C, peaks A3b and A3c appeared on the 8th and 12th sweeps, respectively, and with the exception of peak A1 the current density of all the peaks increased on subsequent cycles, resulting in steady state voltammograms not being obtained at $T \leq 40^\circ\text{C}$. With continued cycling the most pronounced changes in the cyclic voltammogram occurred at A3 and C2. This indicates that the thickness of the base layer remains relatively constant while that of the upper layer (A3) increases with each successive sweep. As was observed in 1.0M NaOH, A3 and C2 are absent from the first sweep of the voltammogram indicating the absence of a surface film prior to the commencement of the cyclic voltammetric applied potential regime.³⁴

It can readily be seen by comparing Figs. 5.2 and 5.29 that the peak current density, particularly of A3 and C2, is greater in 0.5M NaOH than in 1.0M NaOH. Burke and Lyons⁴⁰ reported similar findings and proposed that the protective base layer was anhydrous and that increasing the hydroxide concentration either inhibited rearrangement of the hydrous upper layer, thereby more effectively excluding H_2O and OH^- ions from the base layer, or that the high hydroxide ion activity in the hydrous layer inhibited conversion of anhydrous to hydrous material. XPS data presented later, supports these proposals of an anhydrous base layer and a hydrous upper layer.

The rapid buildup of oxide at the three A3 peaks resulted in A4 being masked and thereby frequently precluded the acquisition of $E_{p,A4}$ and $i_{p,A4}$ data for quantitative analysis of the voltammograms. In order to verify that A4 is indeed masked, an Fe electrode was cycled until all three of the A3 peaks were clearly

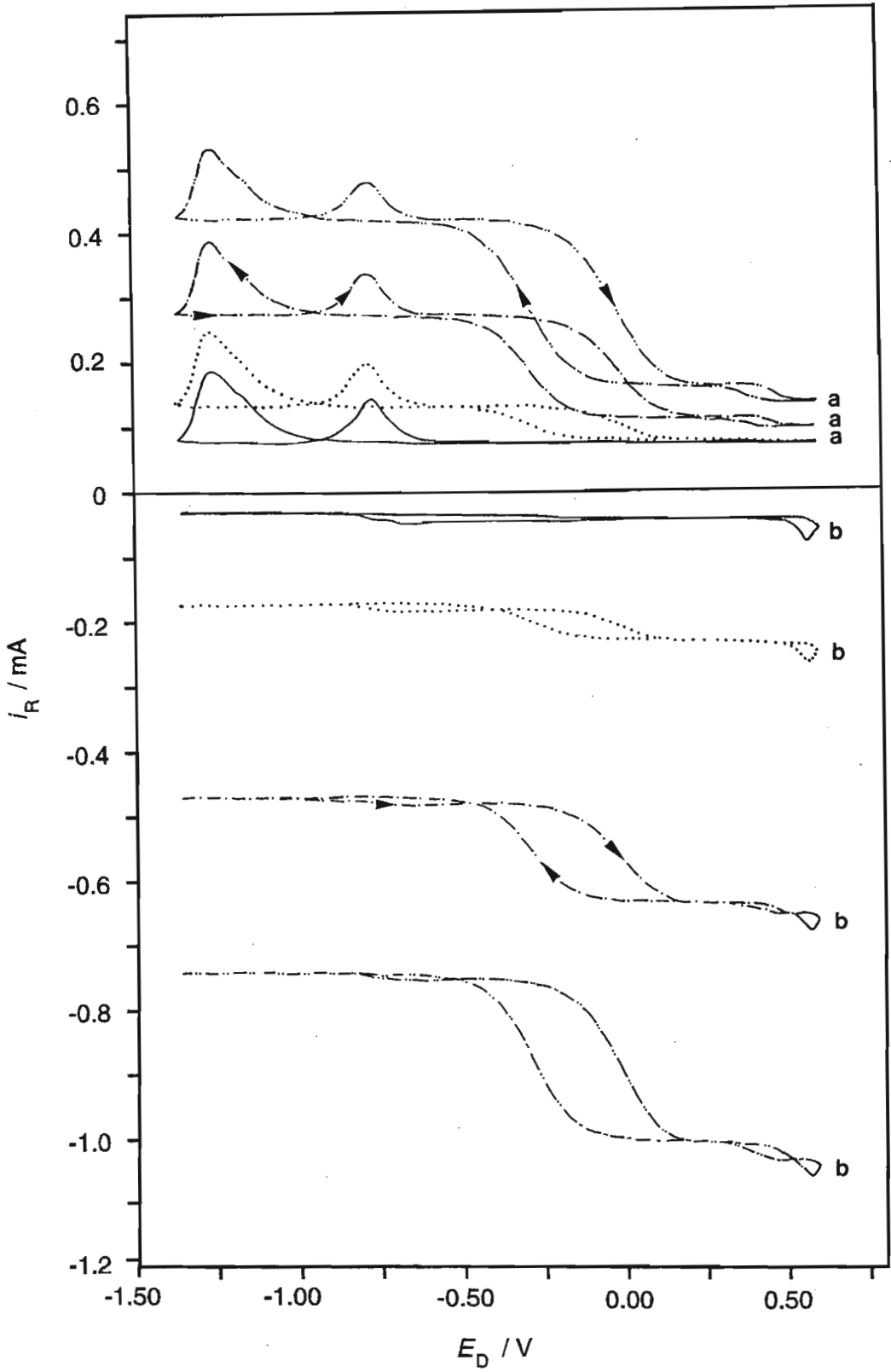


Fig. 5.28 Influence of $\text{K}_3\text{Fe}(\text{CN})_6$ additions on the ring response to a Fe electrode in 1.0M NaOH + 0.4M NaCN, 20°C, swept between -1.35V and 0.60V at 100mV s^{-1} , $\omega = 100\text{rad s}^{-1}$. (a) $E_R = 0.50\text{V}$ (b) $E_R = -0.90\text{V}$

— 1.0M NaOH + 0.4M NaCN
 1.0M NaOH + 0.4M NaCN + 1.0mM $\text{K}_3\text{Fe}(\text{CN})_6$
 - · - · - 1.0M NaOH + 0.4M NaCN + 3.0mM $\text{K}_3\text{Fe}(\text{CN})_6$
 - · · - · 1.0M NaOH + 0.4M NaCN + 4.9mM $\text{K}_3\text{Fe}(\text{CN})_6$

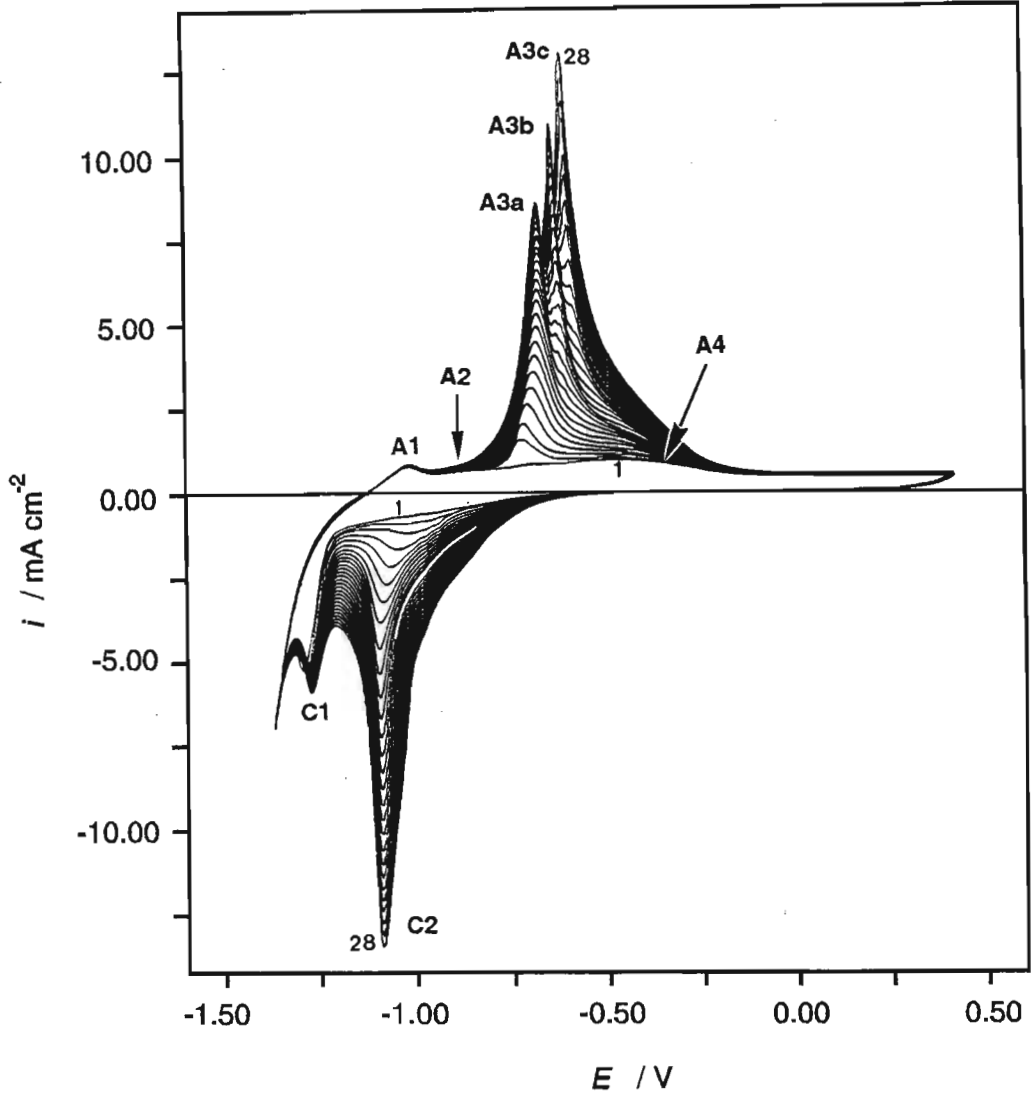


Fig. 5.29 Cyclic voltammogram of the first 28 cycles of a Fe electrode in 0.5M NaOH, 20°C, swept at 100mV s^{-1} between -1.40V and 0.40V showing the buildup of the surface film. $\omega = 100\text{rad s}^{-1}$

defined, as shown in Fig. 5.30, then the sweep was halted for one minute, at a series of potentials from that indicated by the vertical dotted line in Fig. 5.30 to the peak potential of A3c, and then the sweep resumed. The section of the voltammogram represented by the dotted curve in Fig. 5.30 clearly indicates the presence of A4. If the applied potential is held for longer periods eg. 2 to 5 minutes, a decrease in the magnitude of $i_{p,A3c}$ is observed on resumption of the sweep indicating the possible diffusion of reactant species away from the electrode.

5.3.1 Sweep Rate and Temperature Dependence

Increasing the sweep rate from 2mV s^{-1} to 1V s^{-1} resulted in an increase in the magnitude of the peaks. Over the entire temperature range investigated, A3a, C1 and C2 followed a linear E_p and i_p vs $\nu^{1/2}$ relationship, while linear E_p and i_p vs ν plots were obtained for A1. At $\nu > 1\text{V s}^{-1}$ the peaks became very broad and poorly defined. As discussed earlier, in section 5.1.2, a linear i_p vs $\nu^{1/2}$ relationship suggests that film growth occurs via a low field mechanism with ion migration through the film as the rate determining step, while an i_p vs ν relationship indicates a place exchange mechanism.

For $\nu \leq 10\text{mV s}^{-1}$ the voltammograms exhibited a crossing over of the forward and reverse sweep, as shown in Fig. 5.31, which is characteristic of a deposition process.^{302,374} In Fig. 5.31, C2 is analogous to the stripping peak observed in deposition studies and since A3 and C2 are conjugate peaks (as will be shown in section 5.3.2), these results suggest a dissolution - precipitation mechanism is responsible for the formation of the upper layer at A3 with the subsequent reduction of the species occurring at C2.

Increasing the temperature from 20°C to 40°C resulted in an increase in the maximum current density of A3a, A3b, C1 and C2 and a decrease in A1 and A3c. A further increase to 60°C resulted in A3b and A3c no longer being observed, a reduction in the magnitude of A3a and C2 and an increase in A2 (cf Fig. 5.32). This trend continued at higher temperatures (70°C - 120°C) with the result that A3 and C2, which were the dominant peaks at ambient temperatures, decreased such that at 120°C they were present as minor peaks on the voltammogram and A2 which was not evident at 20°C (100mV s^{-1}) was the dominant peak at 120°C .

The peak potential of C1 and C2 increased linearly with increasing temperature while E_p for A1, A2 and A3a showed a linear decrease, as shown in Fig. 5.33. These trends are the same as those observed in 1.0M NaOH. The peak current densities obeyed the Arrhenius equation (as shown in Fig. 5.34) although the poor definition of certain of the peaks resulted in scatter of the data points, particularly at the lower temperatures. It was shown earlier (cf Figs. 5.29 and 5.2) that film formation is inhibited in 1.0M NaOH when compared to that in 0.5M NaOH. This is further indicated by the lower E_a values that are generally obtained in 0.5M NaOH compared to those obtained in 1.0M NaOH.

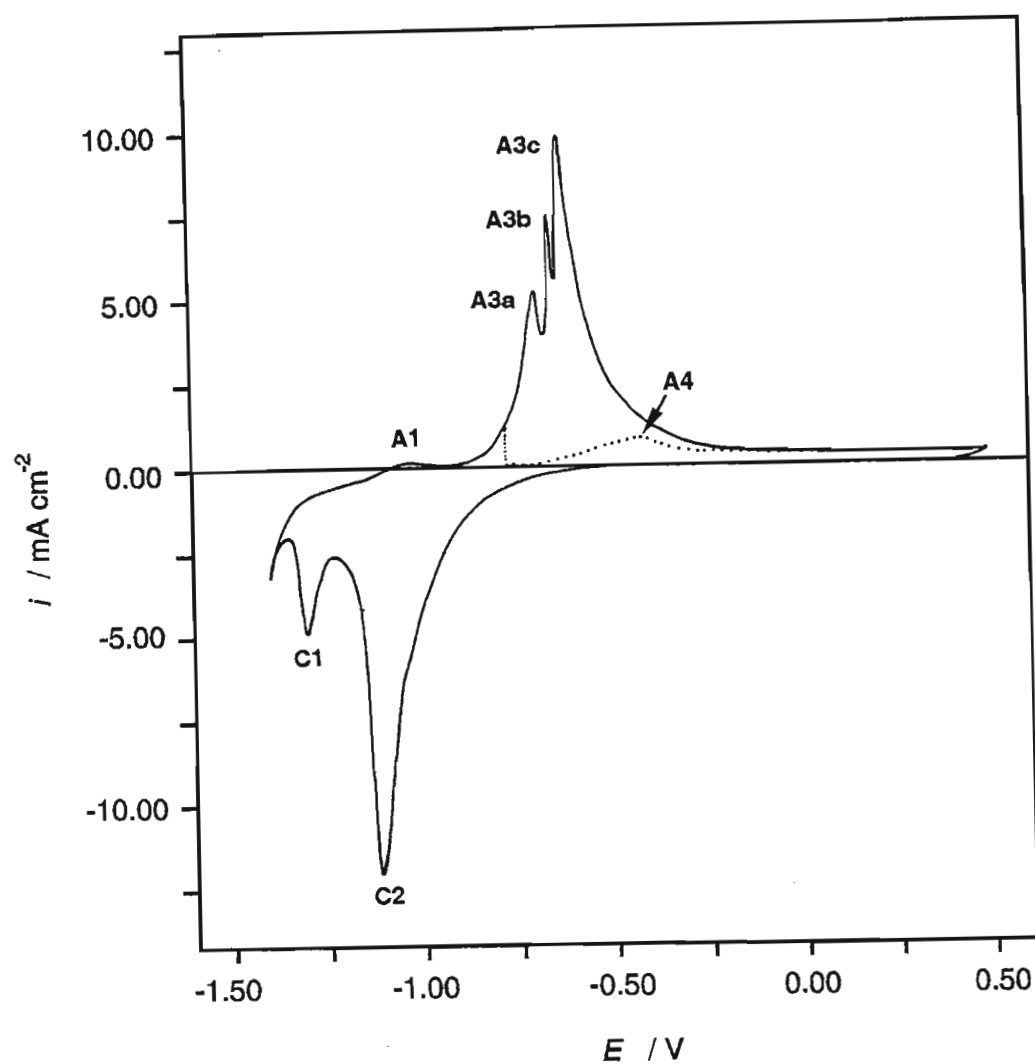


Fig. 5.30 Cyclic voltammogram of a Fe electrode in 0.5M NaOH, 20°C swept between -1.40V and 0.50V at 100mV s^{-1} after 30 cycles (—) and after interrupting the cycling process by holding the applied potential, for 1 minute, at the potential of the dotted vertical line, and then continuing cycling from this potential (·····). $\omega = 100\text{rad s}^{-1}$

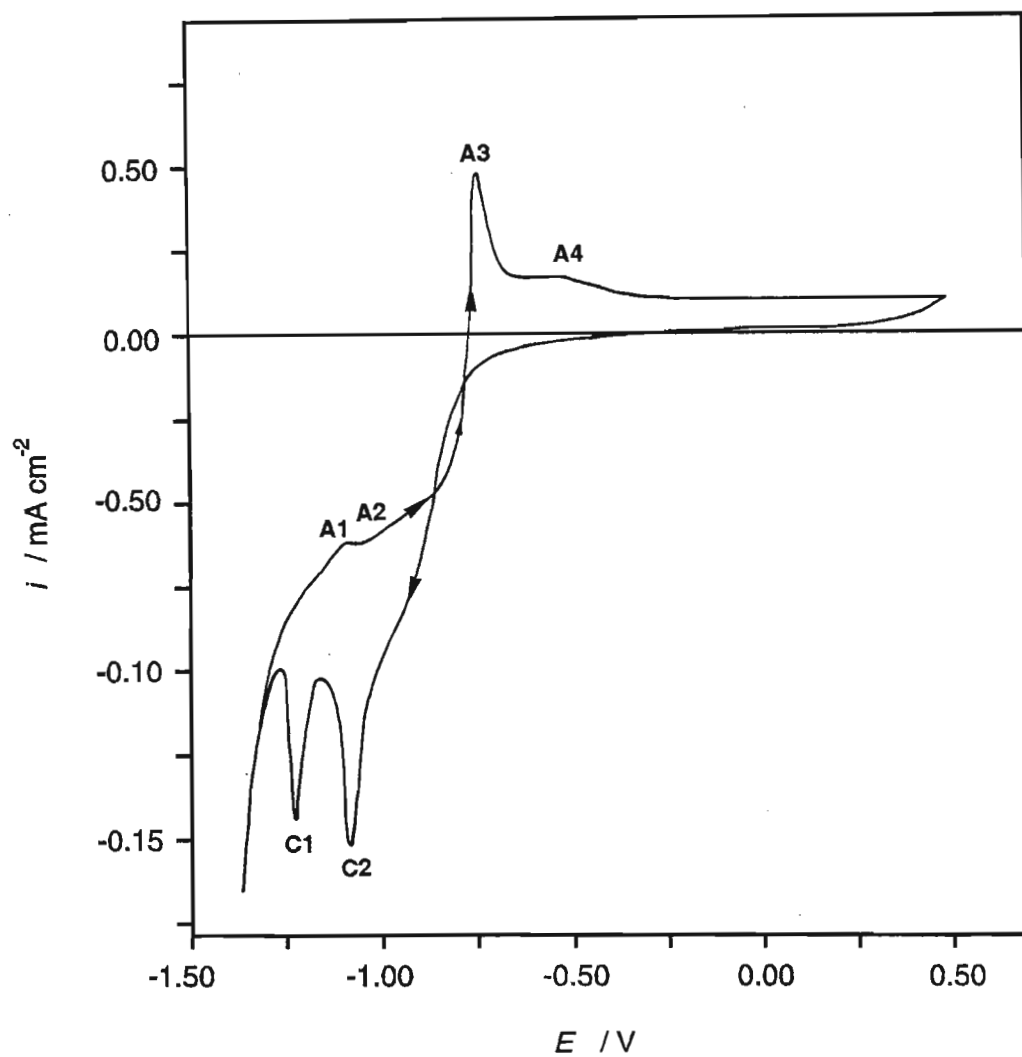


Fig. 5.31 Cyclic voltammogram of the 5th cycle of a Fe electrode in 0.5M NaOH, 20°C, swept between -1.35V and 0.50V at 10mV s^{-1} , $\omega = 100\text{rad s}^{-1}$.

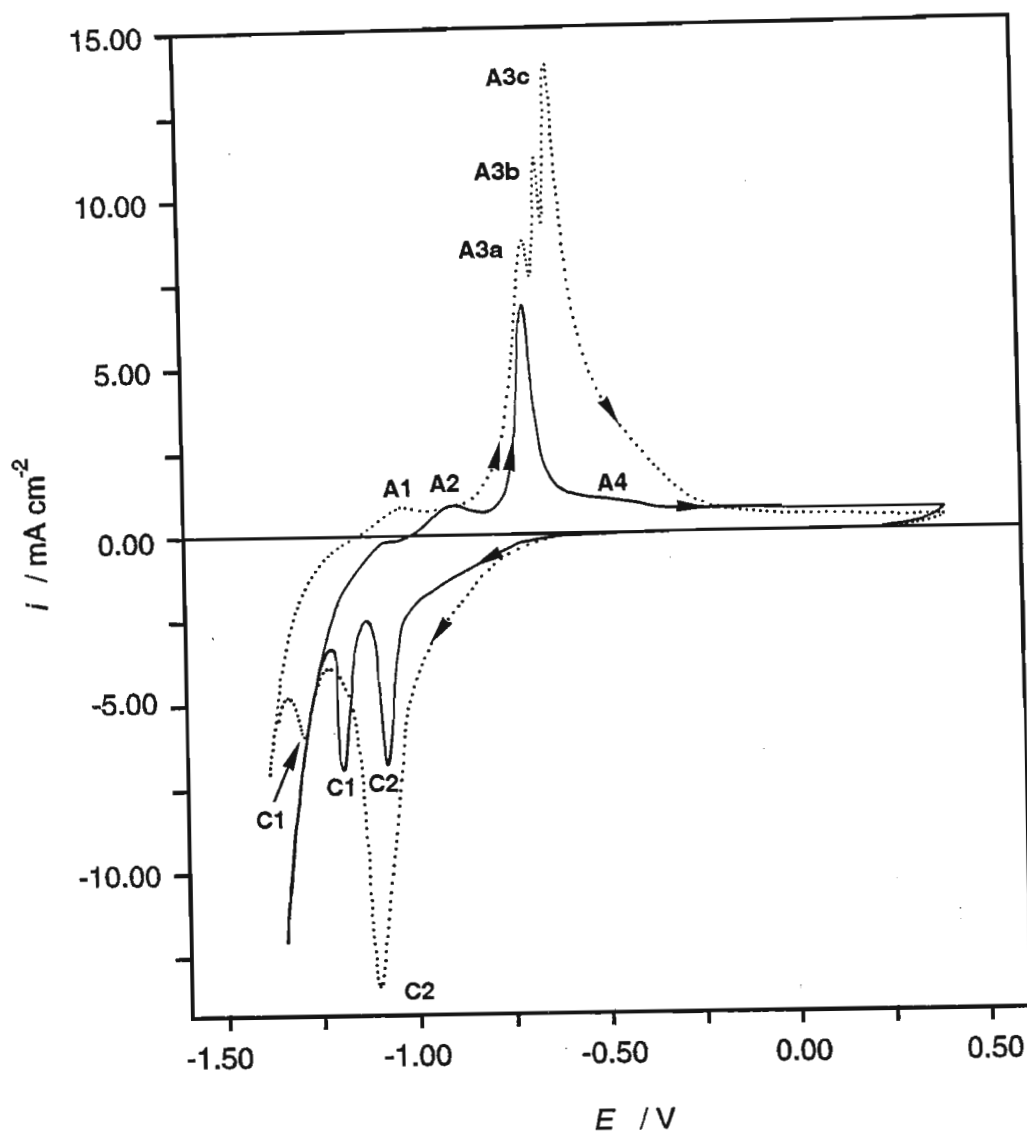


Fig. 5.32 Cyclic voltammogram of the 30th cycle of a Fe electrode in 0.5M NaOH swept at 100mV s^{-1} between -1.40V and 0.40V at (·····) 20°C and (—) 70°C . $\omega = 100\text{rad s}^{-1}$

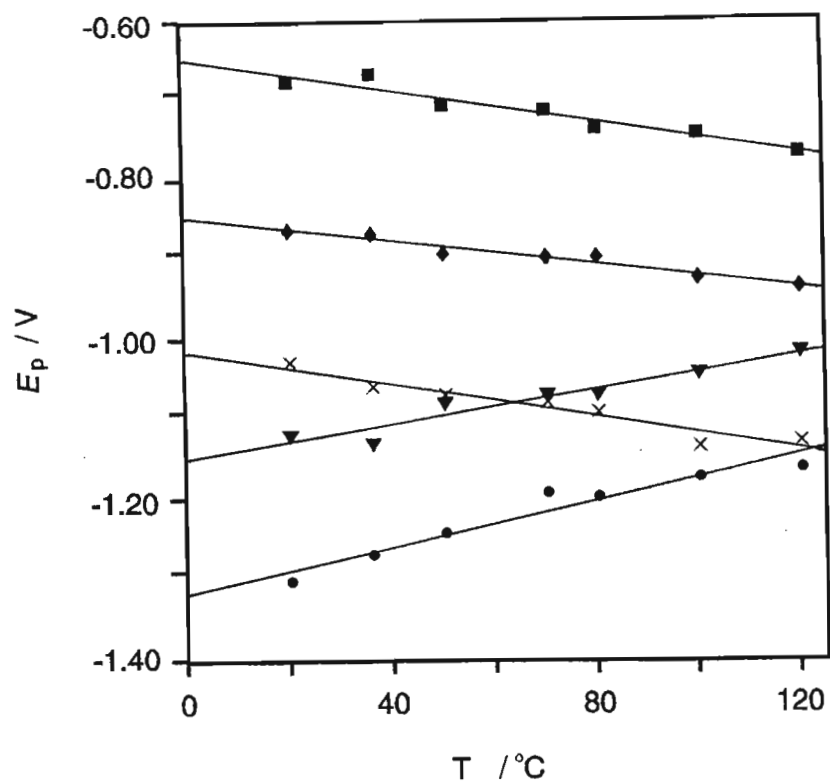


Fig. 5.33 Influence of temperature on the cyclic voltammetric peak potentials of a Fe electrode in 0.5M NaOH. $\nu = 100\text{mV s}^{-1}$, $\omega = 100\text{rad s}^{-1}$.

× A1 ♦ A2 ■ A3a
 • C1 ▼ C2

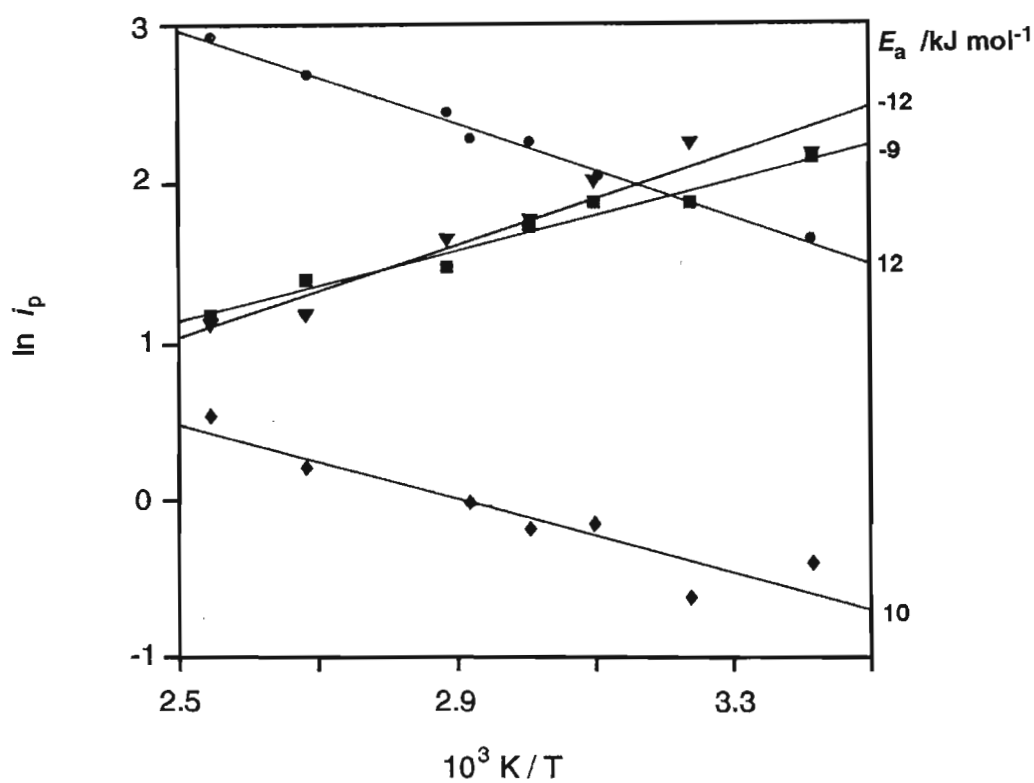


Fig. 5.34 Arrhenius plot for the reactions occurring on a Fe electrode in 0.5M NaOH at the potentials of the indicated peaks. $\nu = 100\text{mV s}^{-1}$, $\omega = 100\text{rad.s}^{-1}$.

♦ A2 ■ A3
 • C1 ▼ C2

5.3.2 Conjugate Peaks

The relationship between the oxidation and reduction peaks was investigated by varying the anodic and cathodic potential limits of the cyclic voltammograms. A typical set of results are shown in Figs. 5.35 and 5.36.

Terminating the voltammogram such that the decrease in the current density due to the onset of hydrogen evolution was excluded, had virtually no effect on the voltammogram (*cf* Fig. 5.35). Reversing the potential prior to C1 resulted in the disappearance of A1, and the current decaying more rapidly subsequent to A3c and to a lower current density in the passive region. The latter could be indicative of A4 no longer being present. Increasing the cathodic potential limit to $E_{p,C2}$ resulted in A3c and A3b no longer being evident and a decrease in A3a and of the passive current density. This demonstrates that the upper layer which forms at A3b, A3c is non-protective and the dissolution occurring from this upper layer results in a greater current density in the passive potential region. Increasing the cathodic potential limit to -860mV resulted in the disappearance of all peaks from the voltammogram.

While Fig. 5.35 shows the effect of cathodic potential limit on the A3 triplet of peaks, the effect on A2 and A4 is not clear due to these peaks being poorly defined at 20°C. Therefore to clarify the conjugate peak assignments, the temperature was increased to 80°C. The results presented in Fig. 5.37 are in agreement with those presented in Fig. 5.35, however they clearly show that excluding C1 from the voltammogram results in A2 and A4 no longer being observed. Fig. 5.35 also shows that the absence of C1, A1 and A2, from the voltammogram, result in a decrease in the quantity of surface film formed at A3 as indicated by the decrease in $i_{p,A3}$ and $i_{p,C2}$ with continued cycling. Thus it can be concluded that A1, A2 and A4 are conjugate peaks to C1 while C2 is the conjugate peak to A3a, A3b and A3c. These results are in agreement with the conjugate peak assignments determined in 1.0M NaOH.

The influence of upper potential limit is shown by the family of voltammograms in Fig. 5.36. Successively decreasing the upper potential limit, in the passive potential region, resulted in a corresponding decrease in the C2 and C1, with a shift of $E_{p,C1}$ to more positive potentials. Successively excluding A4, A3c and A3b from the voltammogram resulted in a continuation of this trend. When the potential region of A3a was not scanned, C2 was no longer present on the voltammogram. Excluding A2 from the voltammogram resulted in a slight decrease in C1 but it is only when the potential region of A1 was not scanned that C1 was no longer evident. These results support the above conclusions regarding the conjugate peaks.

5.3.3 Rotation Rate Dependence

To investigate the rotation rate dependence of the voltammogram, the rotation rate was varied from 68rad s⁻¹ to 225rad s⁻¹. For a stationary electrode at 20°C and 40°C A3c and A1 were more pronounced than when the electrode was rotated and a shoulder to C2 was evident at -0.93V (*cf* Fig. 5.38). $i_{p,A1}$ decreased

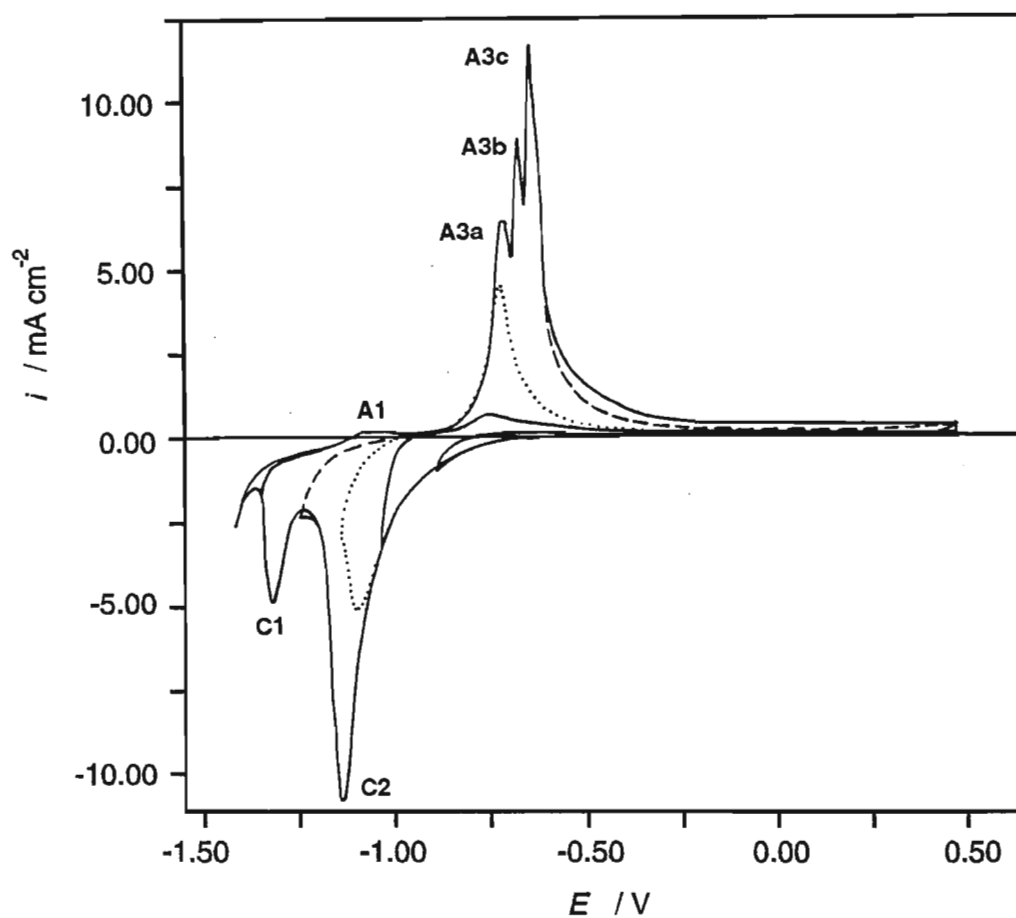


Fig. 5.35 Influence of lower potential limit on the cyclic voltammogram of Fe in 0.5M NaOH, 20°C, swept at 100mV s^{-1} , $\omega = 100\text{rad s}^{-1}$.

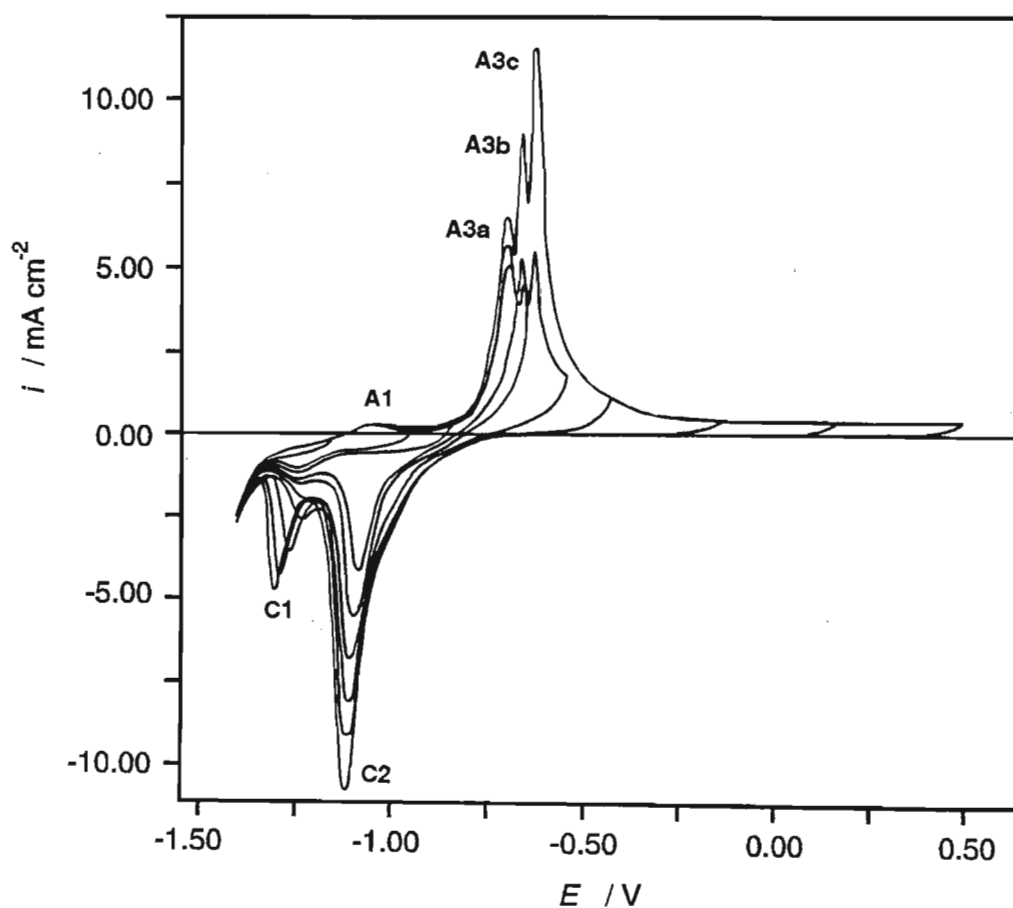


Fig. 5.36 Influence of upper potential limit on the cyclic voltammogram of Fe in 0.5M NaOH, 20°C, swept at 100mV s^{-1} , $\omega = 100\text{rad s}^{-1}$.

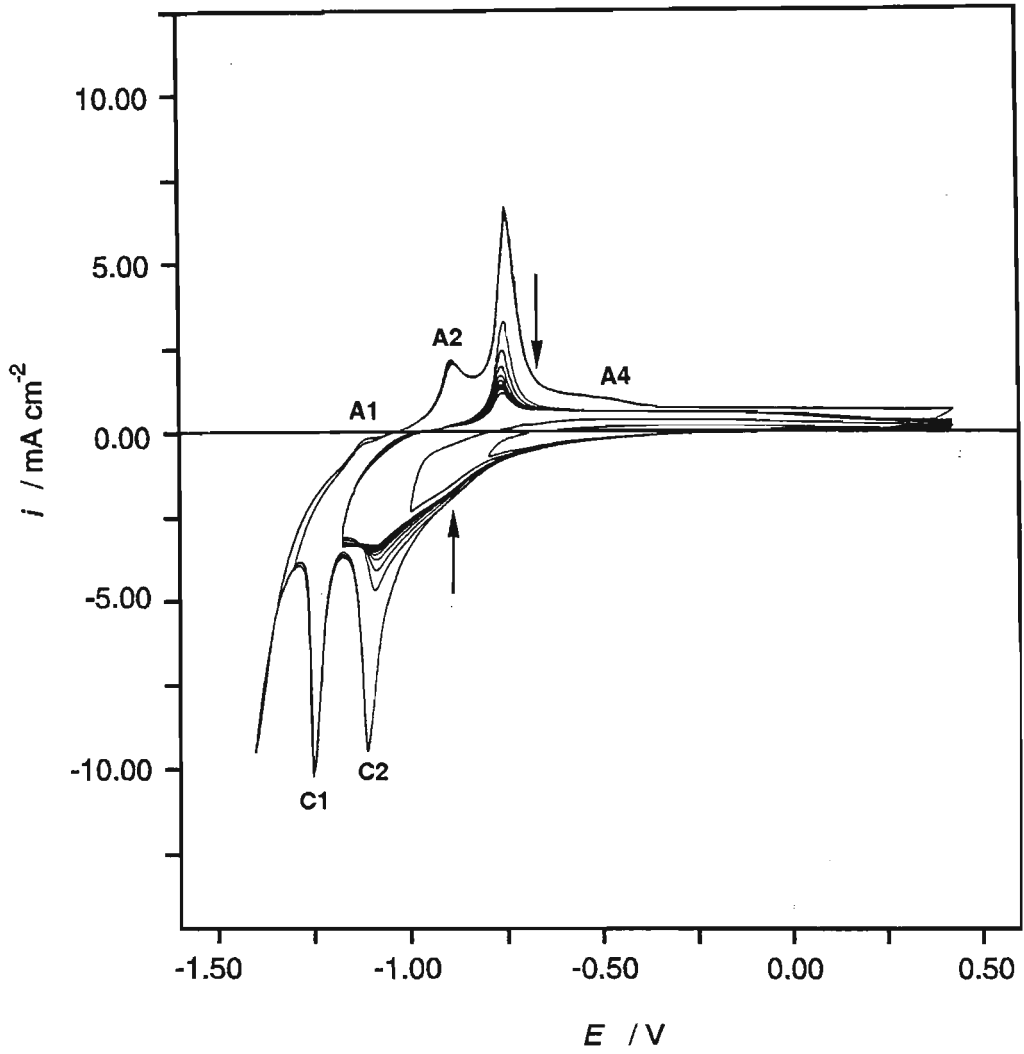


Fig. 5.37 Influence of lower potential limit on the cyclic voltammogram of Fe in 0.5M NaOH, 80°C, swept at 100mV s^{-1} , $\omega = 100\text{rad s}^{-1}$.

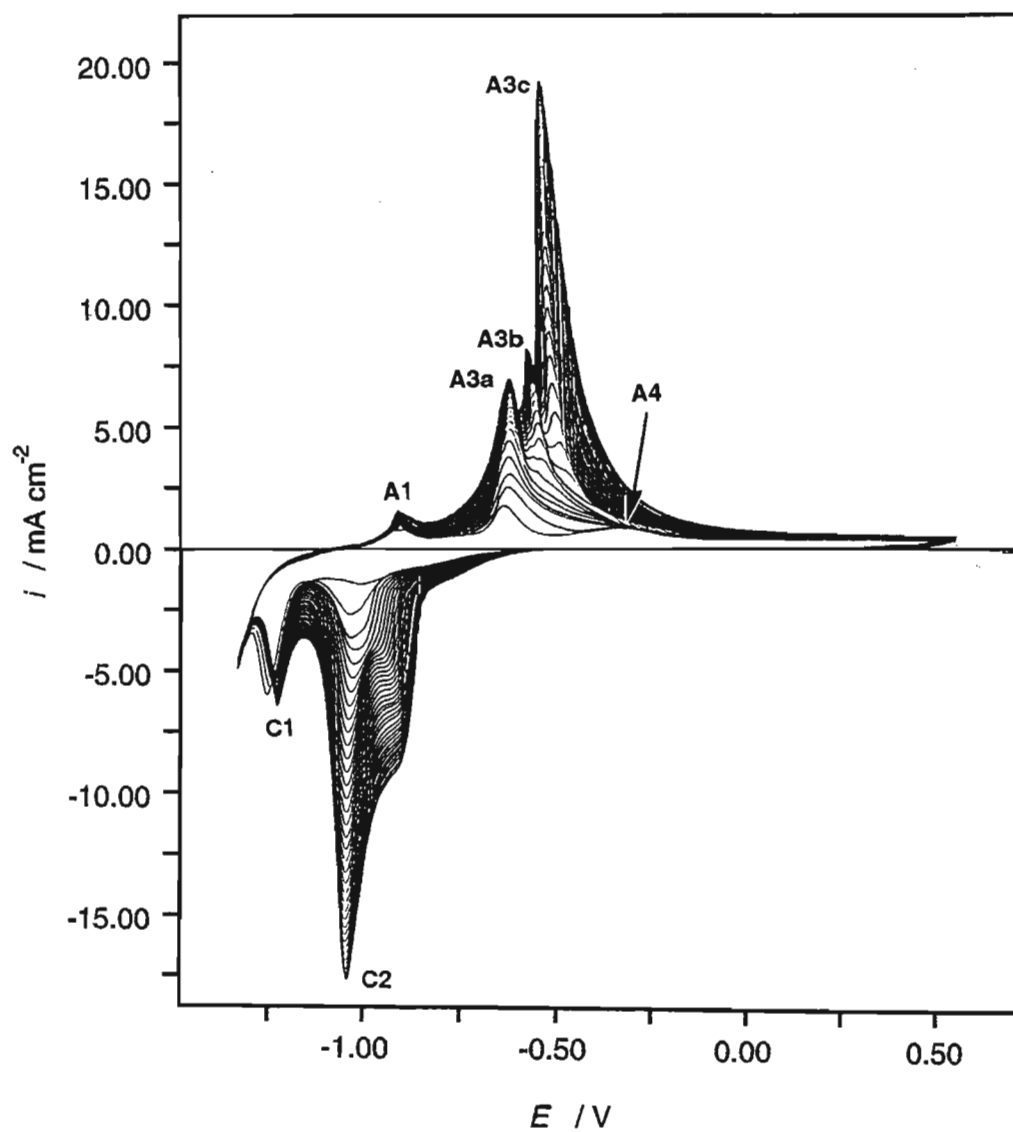


Fig. 5.38 Cyclic voltammogram of the first 40 cycles of a stationary Fe electrode in 0.5M NaOH, 20°C, swept at 100mV s^{-1} between -1.35V and 0.55V showing the buildup of the surface film.

linearly with increasing rotation rate as a function of $\omega^{1/2}$ although at $T > 60^\circ\text{C}$ deviation from linearity was observed. As was reported for the 1.0M NaOH data, at all temperatures investigated the i_p vs $\omega^{1/2}$ plots did not pass through the origin indicating that the dissolution process is not entirely mass transport controlled as given by the Levich equation. $E_{p,A1}$ was independent of rotation rate at all temperatures.

At $T \leq 60^\circ\text{C}$ $i_{p,A2}$ decreased with increasing rotation rate while at higher temperatures $i_{p,A2}$ tended to be virtually independent of rotation rate. $E_{p,A2}$ was independent of rotation rate at all temperatures.

At $T < 60^\circ\text{C}$ i_p for the three A3 peaks increased as a function of $\omega^{1/2}$. At higher temperatures A3b and A3c were no longer present and $i_{p,A3a}$ showed deviation from linearity for the i_p vs $\omega^{1/2}$ plots and at $T > 80^\circ\text{C}$ $i_{p,A3a}$ was virtually independent of rotation rate. $E_{p,A3a}$ increased with increasing rotation rate at all temperatures below 80°C while at higher temperatures $E_{p,A3a}$ was independent of rotation rate.

For both reduction peaks, i_p varied linearly as a function of $\omega^{1/2}$ and E_p was independent of rotation rate, at all temperatures investigated.

Applying Armstrong's²¹ diagnostic criteria to these results it can be concluded that a solid state mechanism prevails for the reactions occurring at A1, A2, C1 and C2. At temperatures below 80°C , upper layer formation (A3a,b,c) can be ascribed to a dissolution - precipitation mechanism, while at higher temperatures this mechanism no longer holds due to the independence of E_p on rotation rate. This dissolution - precipitation mechanism is supported by slow sweep cyclic voltammograms, as shown in Fig. 5.31, which are characteristic of a deposition process with the crossing over of the forward and reverse sweep.

5.3.4 Rotating Ring - Disc Electrode Experiments

At 20°C , and with the ring held at reducing potentials two small reduction peaks were observed at the ring just after the potential of A3a and A3b had been scanned, on the forward sweep. At $E_D \geq A3c$ the ring reduction current increased to a maximum at which it remained for the remainder of the forward sweep (cf Fig. 5.39), indicating the reduction of Fe(III) species formed at the disc. The fact that a limiting plateau is attained suggests that in the passive potential region either a chemical dissolution reaction or a diffusion controlled reaction is occurring. On the reverse sweep a reduction peak is evident at the ring in the potential region between C2 and C1, for $E_R \leq -0.80\text{V}$ and indicates the reduction of soluble Fe(II), produced at C2, to Fe(0).

With the ring held at oxidising potentials a ring oxidation peak was observed on the forward sweep which indicated that soluble Fe(II) species were produced at the potential of A3. On the reverse sweep two ring oxidation peaks were present corresponding to C1 and C2.

It was shown earlier in this chapter that at higher temperatures A3b and A3c are no longer observed (cf.

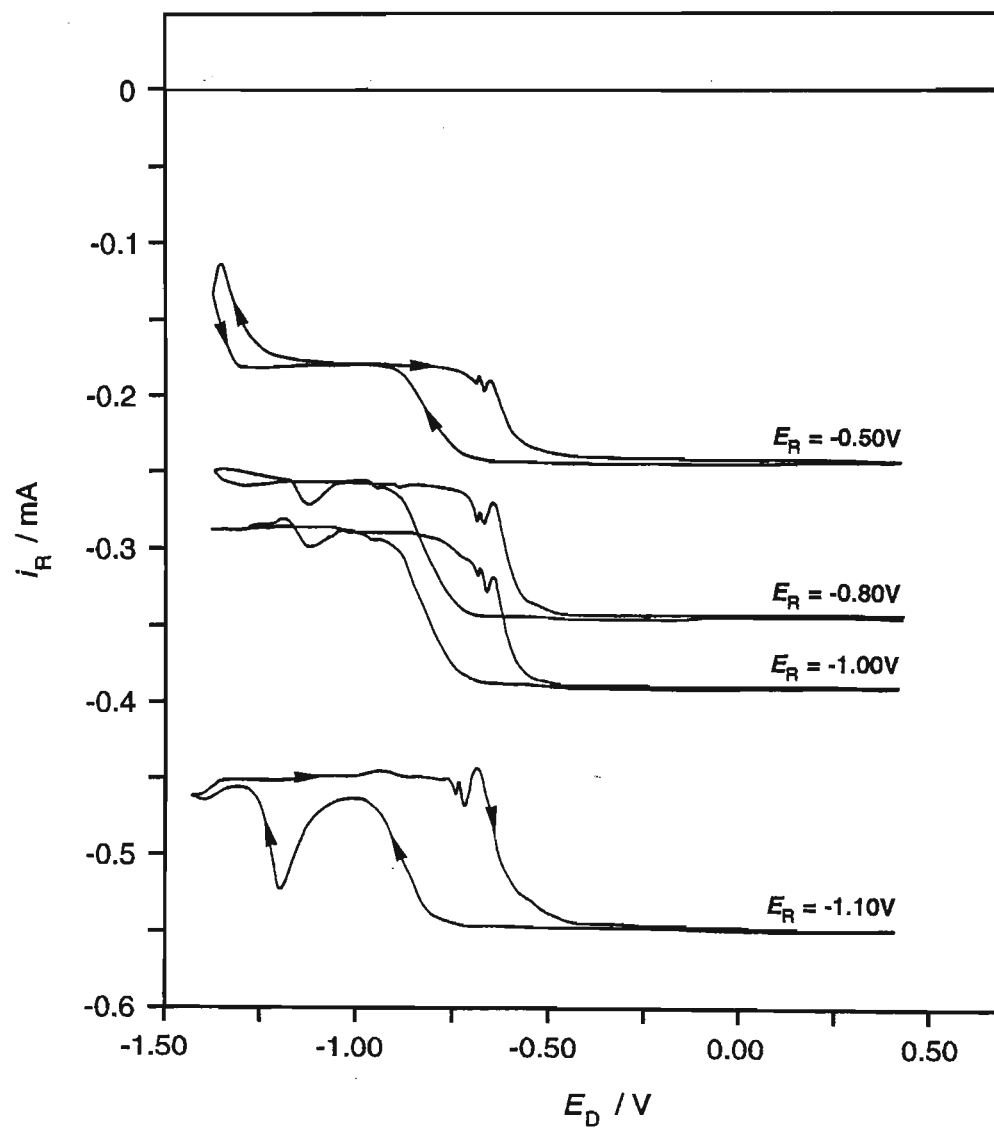


Fig.5.39 Ring response, at the indicated ring potentials, to a Fe electrode in 0.5M NaOH, 20°C, swept between -1.40V and 0.40V at 100mV s^{-1} , $\omega = 162.5\text{rad s}^{-1}$.

Fig. 5.32) and the magnitude of C2 decreased significantly. These changes are reflected in the ring currents as illustrated by the 60°C data in Fig. 5.40. With the ring held at reducing potentials, the ring reduction current reached a maximum plateau current after the potential of A3 had been scanned, indicating the formation of soluble Fe(III) species at this peak. The two small reduction peaks superimposed on this reduction wave at 20°C, were no longer evident. On the reverse sweep no ring reduction peaks were observed, as would be expected from the smaller C2 observed at the higher temperatures.

With the ring held at oxidising potentials a similar ring response to that observed at 20°C, was observed at 60°C. On the forward sweep a ring oxidation peak, corresponding to A3, was present and on the reverse sweep two very small oxidation peaks corresponding to C1 and C2 were observed.

5.3.5 SEM Analysis

SEM examination of iron electrodes prepared in both 0.5M and 1.0M NaOH showed the topography of the surface film to be virtually identical in both electrolytes.

SEM examination of a Fe electrode after seven cycles between -1.40V and 0.40V (20°C) showed that the entire electrode was covered by a surface film, the base layer (BL), as can be seen in Fig. 5.41(a), on top of which were regions where the formation of a second layer, the upper layer (UL), had started (Fig. 5.41(a),(b)). With continued applied potential cycling the size of these upper layer growth centres increased as can be seen in Figs. 5.41(c) and (d), resulting in the overlap of neighbouring clusters and eventually in complete coverage of the electrode by the upper layer (Fig. 5.41(e)). An important feature of the upper layer growth phase is that it was not limited to lateral growth across the electrode surface, although this was the predominant direction of growth. Growth perpendicular to the electrode surface was indicated by, for example, the side view of a growth centre in Fig. 5.41(f) which clearly shows vertical growth, and by the fact that at higher magnifications (*cf* Figs. 5.41(b) and (e)) the micrographs do not indicate a single layer of oxide and also that the base layer was not visible through gaps in the upper layer, which would undoubtedly be present if no vertical growth had occurred.

The cyclic voltammogram in Fig. 5.29 showed that growth of the upper layer became the dominant process with continued cycling. Fig. 5.41(g) shows that when the upper layer was allowed to grow too thick, the increase in volume of the surface film material lead to stresses within the film resulting in rupture, the development of cracks and the possible flaking off of sections of the film. Closer inspection of a typical crack (Fig. 5.41(h)) shows the base layer beneath the damaged upper layer. The current density in the passive region, at $E > A4$, of the cyclic voltammogram recorded during the buildup of the surface film shown in Figs. 5.41(g) and (h) remained constant throughout the experiment indicating that the base layer is responsible for the passivation of the electrode and that the cracking must be limited to the upper layer.

At 40°C, the topography of both the base and upper layers was very similar to that observed at 20°C, as can

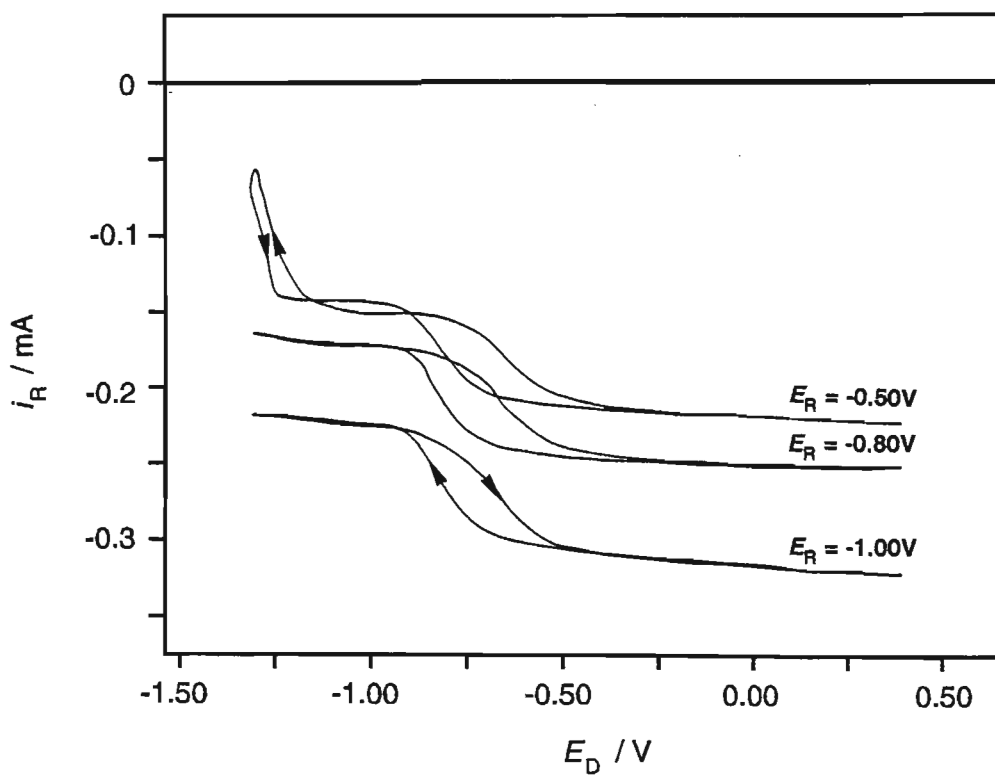


Fig. 5.40 Ring response, at the indicated ring potentials, to a Fe electrode in 0.5M NaOH, 60°C, swept between -1.30V and 0.40V at 100mV s⁻¹, $\omega = 225\text{rad s}^{-1}$.

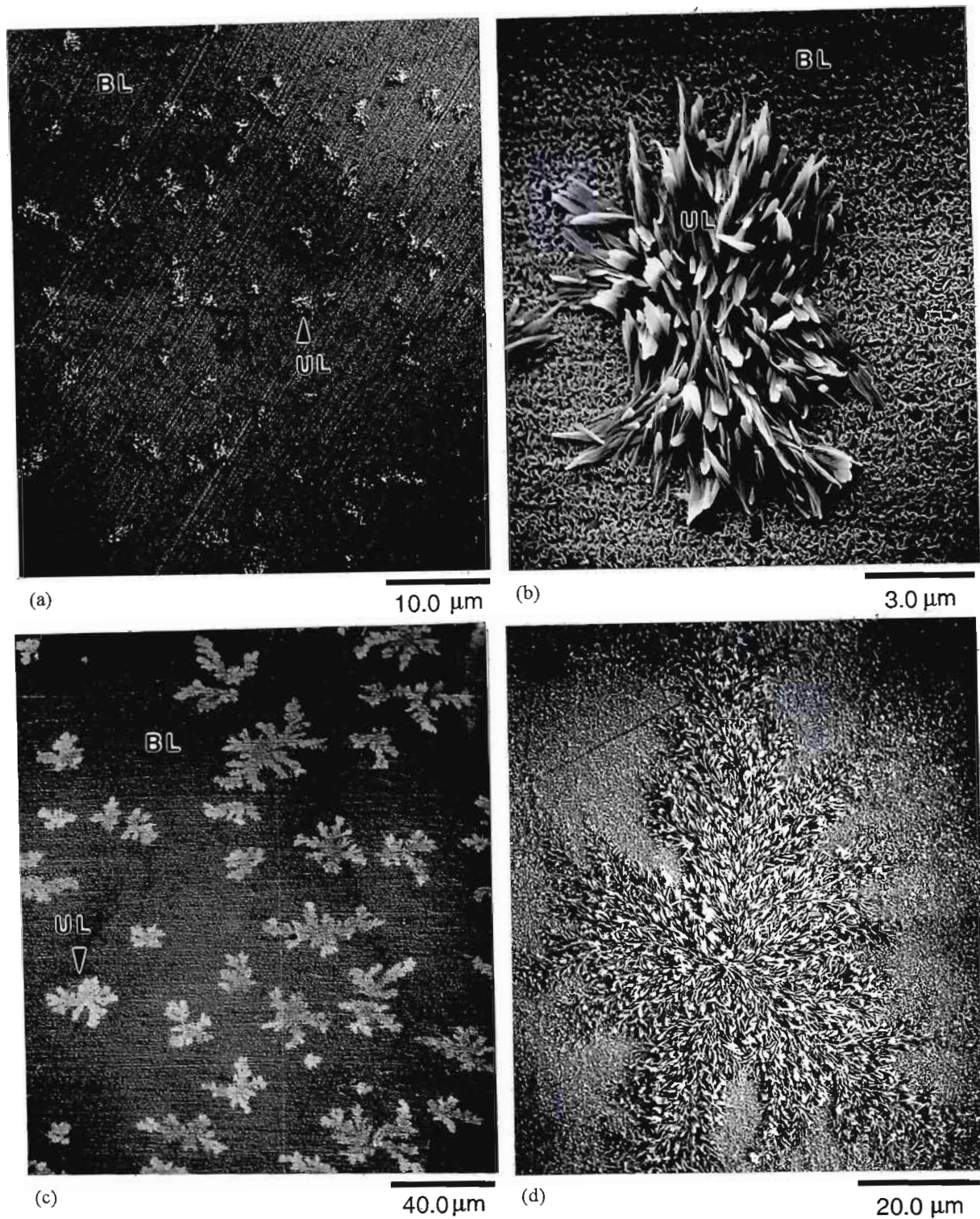


Fig. 5.41 Surface of a Fe electrode in 0.5M NaOH, 20°C, swept between -1.40V and 0.40V at 100mV s⁻¹, 100rad s⁻¹, after :

- (a), (b), (f) 7 cycles showing the coverage of the electrode with the base layer and the start of the formation of the upper layer; (f) side view of upper layer growth centre
- (c), (d) 25 cycles showing the outward growth of the upper layer growth centres on the base layer
- (e) 50 cycles which results in complete coverage of the electrode surface by the upper layer
- (g) 100 cycles showing the development of cracks in the upper layer, thereby exposing the base layer (h).

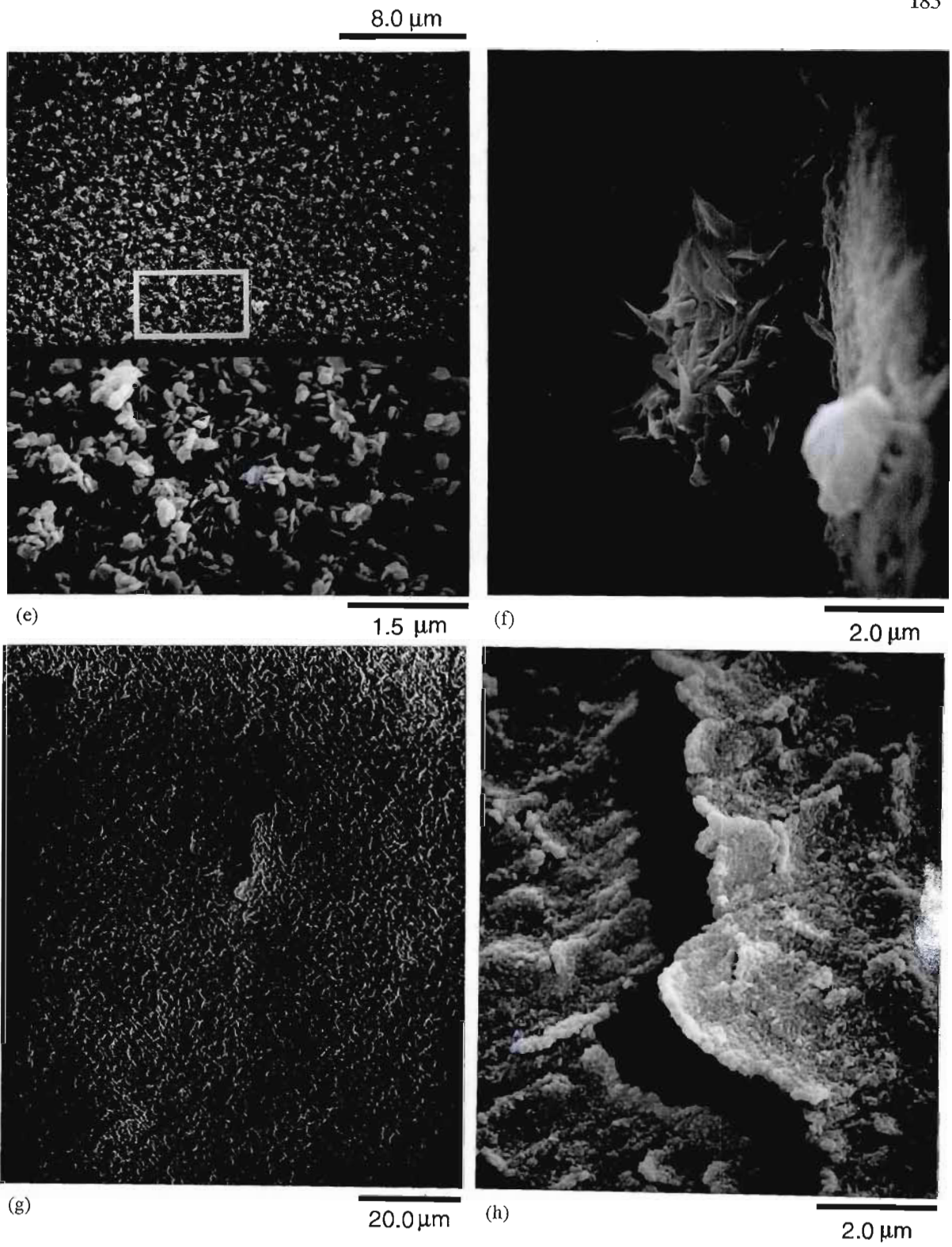


Fig. 5.41 continued

be seen from the micrographs in Figs. 5.42(a) and (b), which supports the electrochemical results presented earlier showing the cyclic voltammograms to be qualitatively similar at 20°C and 40°C.

At higher temperatures, the electrochemical data indicated that base layer growth became the dominant process. Comparison of Fig. 5.43 with the appropriate micrographs in Fig. 5.41 shows that the base layer growth centres are more rounded, a trend that was also observed at higher temperatures (*cf* Figs. 5.44 and 5.45), and that the upper layer growth is not as prolific at the higher temperatures (*cf* Figs. 5.43(b) and 5.41(c)). Figs. 5.43(c) and (d) show a decrease in the upper layer growth both parallel and perpendicular to the electrode surface with the base layer clearly visible beneath the upper layer in Fig. 5.43(d). At 80°C, an unexpected phenomenon was observed with base layer apparently having formed on an upper layer growth centre, as can be seen in Fig. 5.44(b).

At $T > 80^{\circ}\text{C}$, cracking and flaking of the surface film was observed after 50 applied potential cycles, as can be seen in Fig. 5.45. In regions where spalling of the film had occurred, only the outer sections of the film appear to have lifted off the electrode surface, as beneath the spalled sections the electrode was still covered by the base layer, as can be seen in Fig. 5.45(b).

These SEM results indicate a duplex surface film forms on Fe in 0.5M NaOH and 1.0M NaOH, consisting of a protective base layer on which a non-protective upper layer forms. This is in agreement with the literature presented in chapter two.

5.3.6 XPS Analysis

XPS analysis of the surface film formed on Fe in 0.5M NaOH detected the presence of FeO, Fe₂O₃ and FeOOH. It is proposed that the FeO constitutes the base layer while the Fe₂O₃ and FeOOH the upper layer. Details of the XPS analyses will be presented in chapter seven. FeO, as opposed to Fe(OH)₂, as a base layer is supported by recent work by Macdonald⁷ who proposed that protons are excluded from the base layer due to the presence of a large electric field ($\approx 10^6\text{V cm}^{-1}$). This is further supported by the work of Burke and Lyons⁴⁰ who proposed an anhydrous base layer and a hydrous upper layer.

The ratio of the percentage of oxide detected within the surface film was found to be dependent on the extent of applied potential cycling, with the upper layer being largely responsible for this buildup of the film at ambient temperatures. At elevated temperatures (80°C) it was found that the magnitude of the upper layer decreased while that of the lower layer increased. In the initial stages of film growth the film retained its three component structure, while only FeO and Fe₂O₃ were detected for a more well developed film.

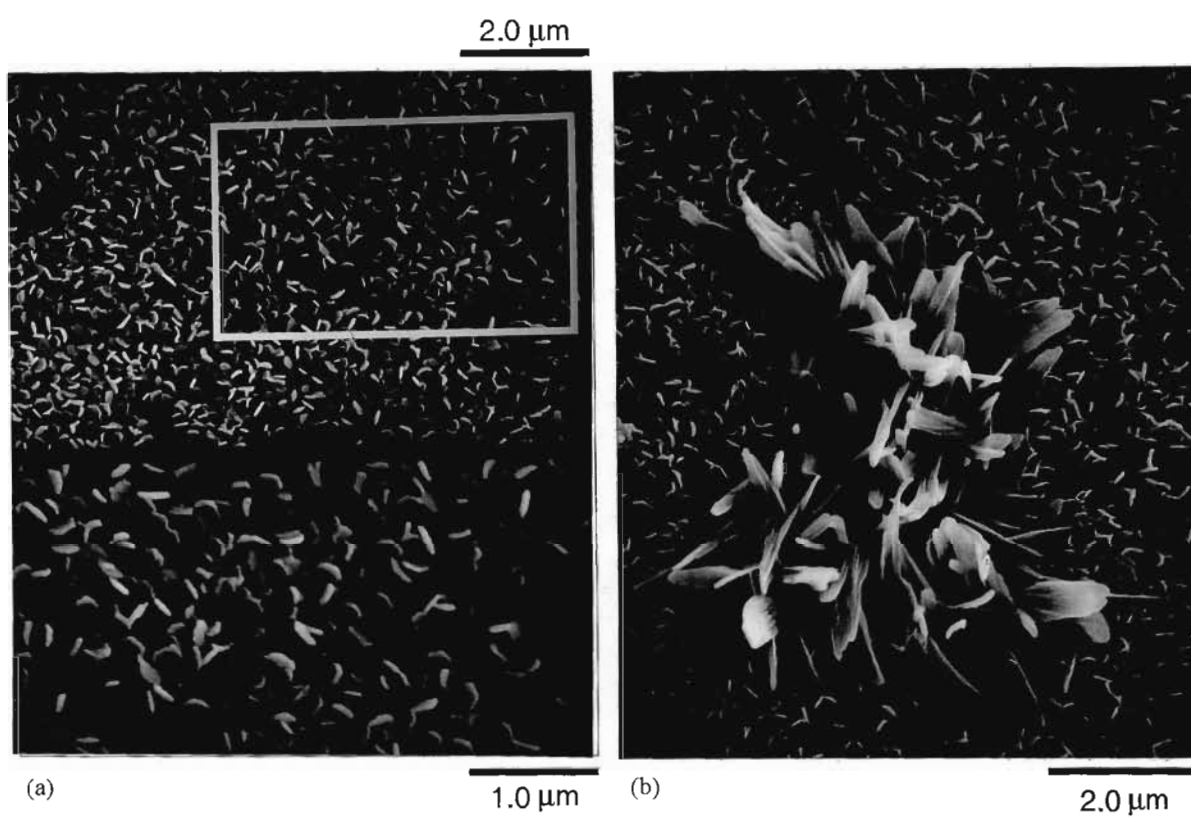


Fig. 5.42 Surface of a Fe electrode in 0.5M NaOH, 40°C, swept between -1.40V and 0.40V at 100mV s^{-1} , 100rad s^{-1} , after 25 cycles showing (a) the base layer and (b) an upper layer growth centre on the base layer.

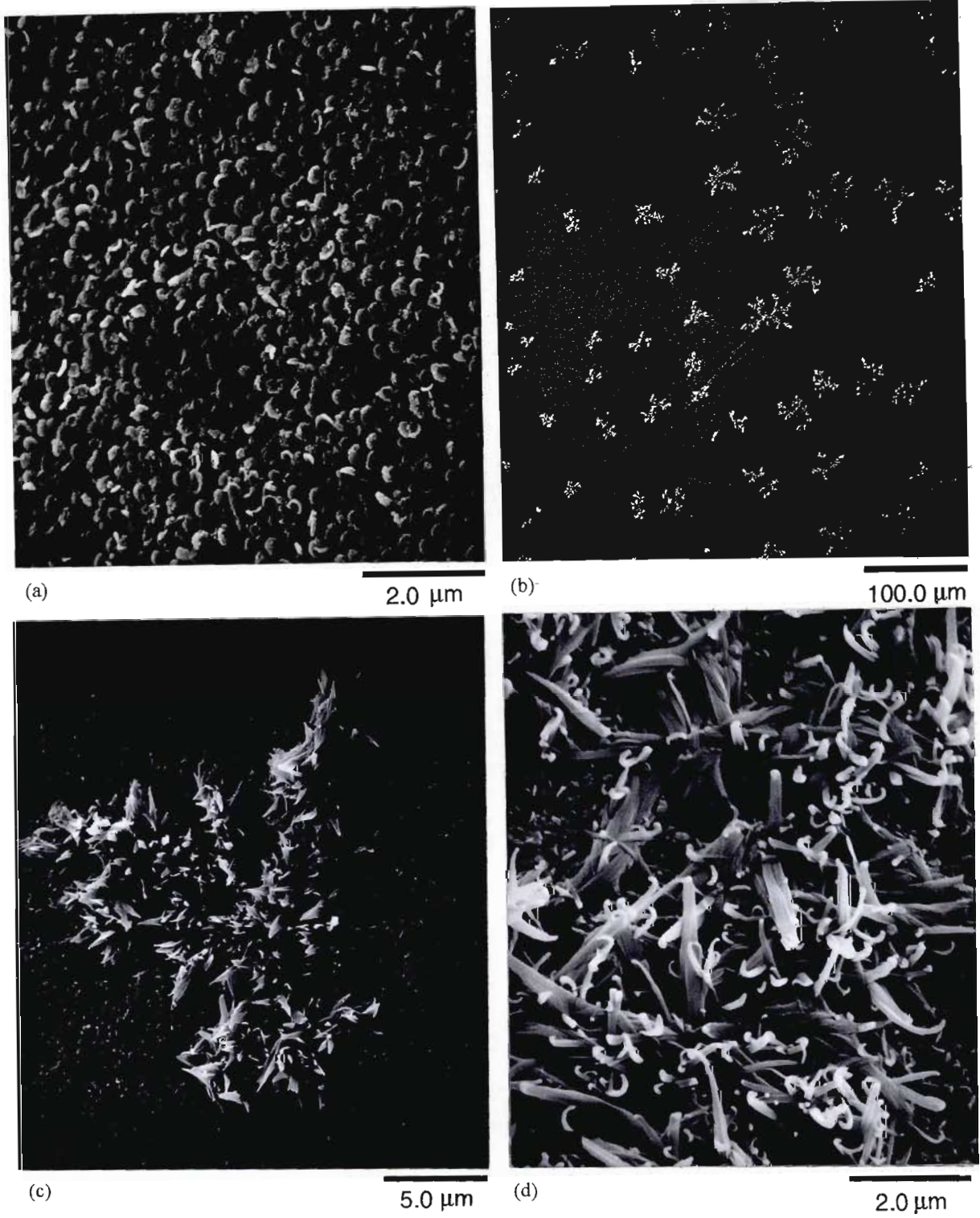


Fig. 5.43 Surface of a Fe electrode in 0.5M NaOH, 60°C, swept between -1.40V and 0.40V at 100mV s⁻¹, 100rad s⁻¹, after 25 cycles showing (a) the base layer (b) upper layer growth centres on the base layer (c) an upper layer growth centre and (d) a higher magnification micrograph of the upper layer, through which the base layer is evident.

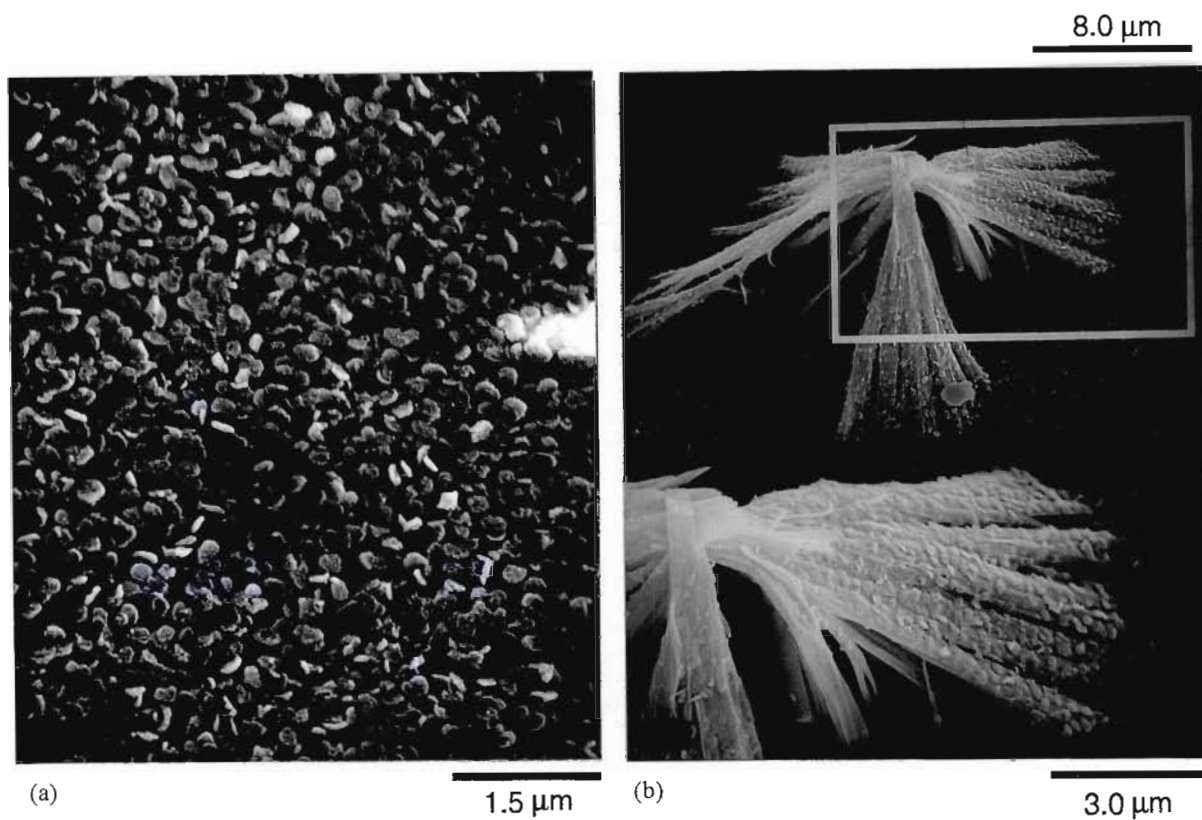


Fig. 5.44 Surface of a Fe electrode in 0.5M NaOH, 80°C, swept between -1.40V and 0.40V at 100mV s^{-1} , 100rad s^{-1} , after 25 cycles showing (a) the base layer and (b) an upper layer growth centre, on the base layer.

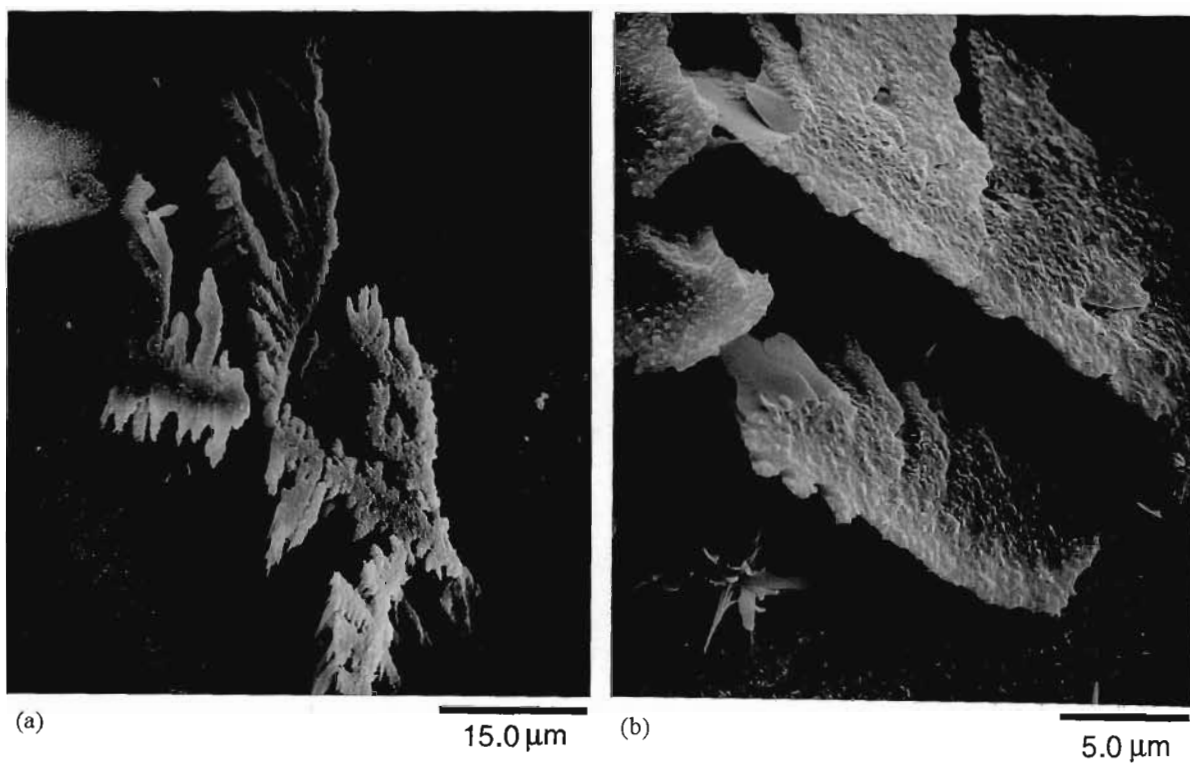


Fig. 5.45(a), (b) Surface of a Fe electrode in 0.5M NaOH, 100°C, swept between -1.30V and 0.40V at 100mV s^{-1} , 100rad s^{-1} , after 50 cycles showing the cracking and flaking of the surface film which occurs at elevated temperatures ($T \geq 80^\circ\text{C}$).

5.4 Fe in 0.5M NaOH + 0.4M NaCN

Addition of 0.4M NaCN to 0.5M NaOH had a dramatic effect on the electrochemistry of the system. From the cyclic voltammograms shown in Fig. 5.46 it can be seen that CN^- reduced the height and number of peaks with only one major oxidation and reduction peak present at -710mV (A5) and -1260mV (C3), respectively. Two broad and poorly defined oxidation and reduction peaks were present at -450mV (A6) and -1100mV (C4), respectively. After ≈ 5 cycles steady state voltammograms were obtained. This indicates the cyanide ion's ability to inhibit the continued activation of the electrode surface, as was observed when the electrode was cycled in 0.5M NaOH, and thereby inhibit surface film growth. Extending the upper potential limit of the voltammogram from 0.4V to 0.6V an additional oxidation and reduction peak was evident at 530mV (A7) and -310mV (C5) respectively, for $T > 60^\circ\text{C}$. A7 and C5 were only observed at 20°C if the electrode was stationary. Thus the cyclic voltammograms obtained in 0.5M NaOH and 1.0M NaOH after the addition of 0.4M NaCN were qualitatively the same. Comparing Figs. 5.12 and 5.46 it is evident that the presence of the 0.4M NaCN had a greater inhibiting effect in 0.5M NaOH than in 1.0M NaOH, which again supports the previous proposal of competitive adsorption between the CN^- and OH^- . The same conjugate peak pairings were obtained in both electrolytes, viz. A5 was the conjugate peak to C3, A5 and A6 were conjugate to C4, and A7 and C5 were conjugate peaks.

To further investigate the influence of CN^- on the surface film formation process, a thick brown film was formed on an Fe electrode in 0.5M NaOH by continuously cycling the electrode between -1.45V and 0.50V at 100mV s^{-1} (cf Fig. 5.47(a)). 1mM NaCN was then rapidly added to the electrolyte. On the first cycle after the CN^- addition there was a slight decrease in A3a and A3b, A3c and C2 remained unchanged, A1 was no longer evident, C1 decreased by 40% and shifted 50mV in an anodic direction and an additional oxidation peak was evident at -0.80V. With continued cycling there was a decrease in the magnitude of all the oxidation peaks and of C2, whilst there was an increase in C1, as indicated by the arrows in Fig. 5.47(b). This figure clearly shows that CN^- has the greatest influence on oxide formation at the A3 triplet of peaks. From these results it can be concluded that CN^- effectively suppresses the reactions occurring at A1 and inhibits the oxide growth at A3.

5.4.1 Sweep Rate and Temperature Dependence

Increasing the sweep rate from 2mV s^{-1} to 1V s^{-1} resulted in an increase in the magnitude of all the peaks, with i_p varying linearly with $\nu^{1/2}$. Linear E_p vs $\nu^{1/2}$ plots were obtained with the oxidation peaks shifting to more positive potentials and the reduction peaks shifting to more negative potentials, with increasing sweep rate. These relationships were obtained at all temperatures investigated, although at 20°C , $E_{p,C3}$ was virtually independent of sweep rate. These results are in agreement with those reported for 1.0M NaOH + 0.4M NaCN and indicate that film growth is controlled by a low field mechanism with ion migration through the film as the rate determining step.

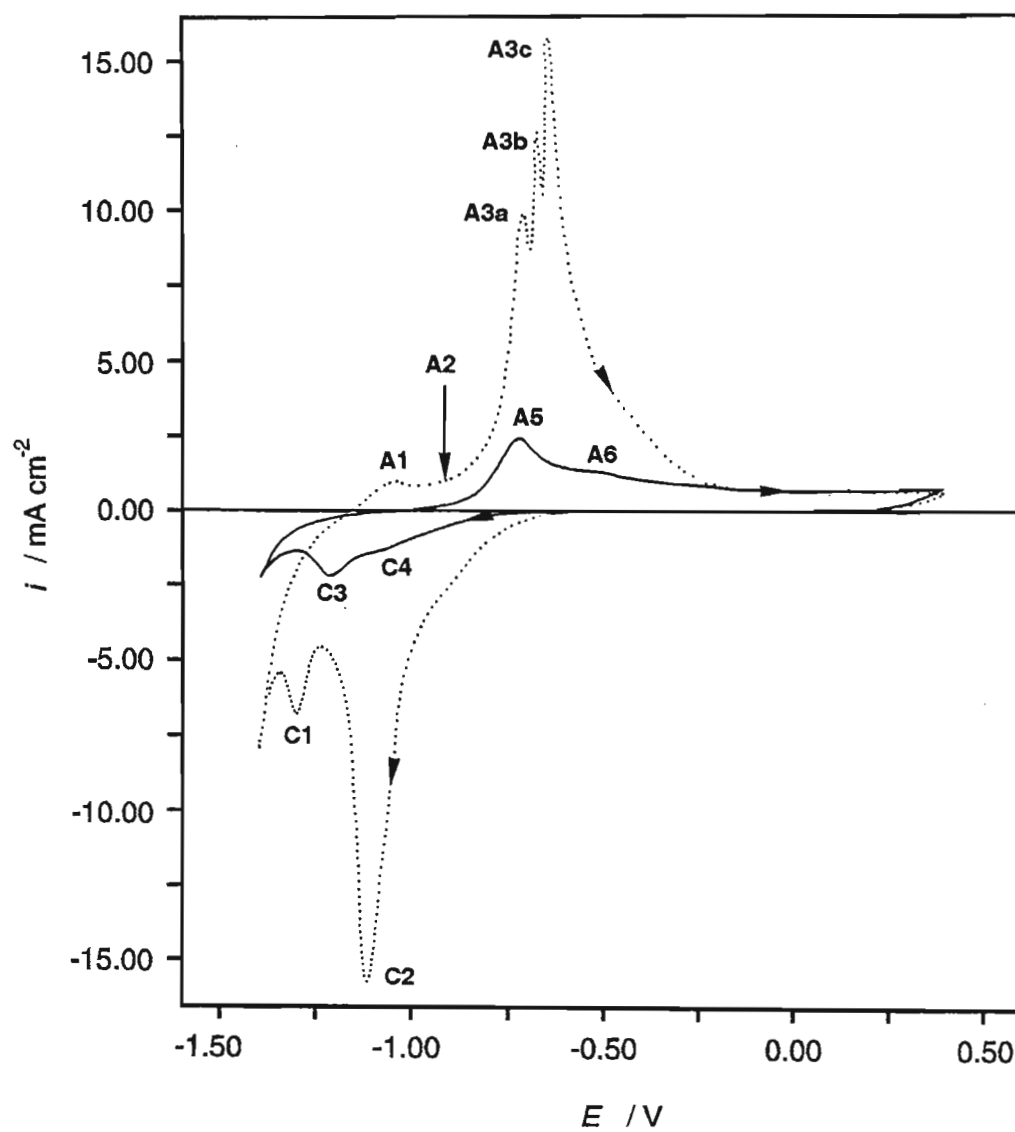


Fig. 5.46 Cyclic voltammogram of the 30th cycle of a Fe electrode in $0.5\text{M NaOH} + 0.4\text{M NaCN}$ (—) and in 0.5M NaOH (·····), 20°C , swept at 100mV s^{-1} between -1.40V and 0.40V . $\omega = 100\text{rad s}^{-1}$

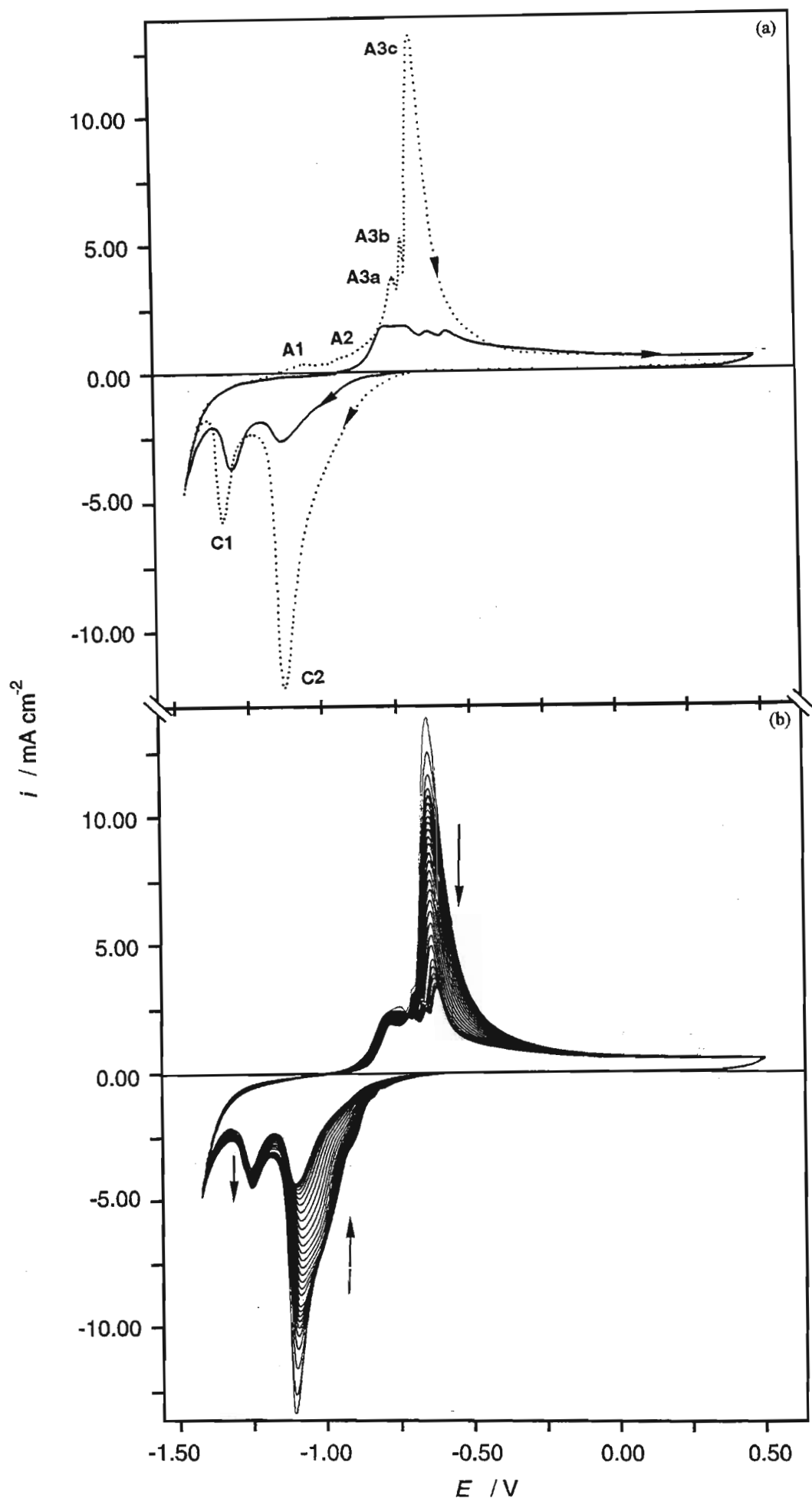


Fig. 5.47(a) Cyclic voltammogram of a Fe electrode in 0.5M NaOH , 20°C , swept at 100mV s^{-1} between -1.45V and 0.50V showing the last cycle (\cdots) before the addition of 0.001M NaCN and the 35th cycle after the CN^- addition (—). The first 32 cycles after the CN^- addition are shown in (b). $\omega = 100\text{rad s}^{-1}$

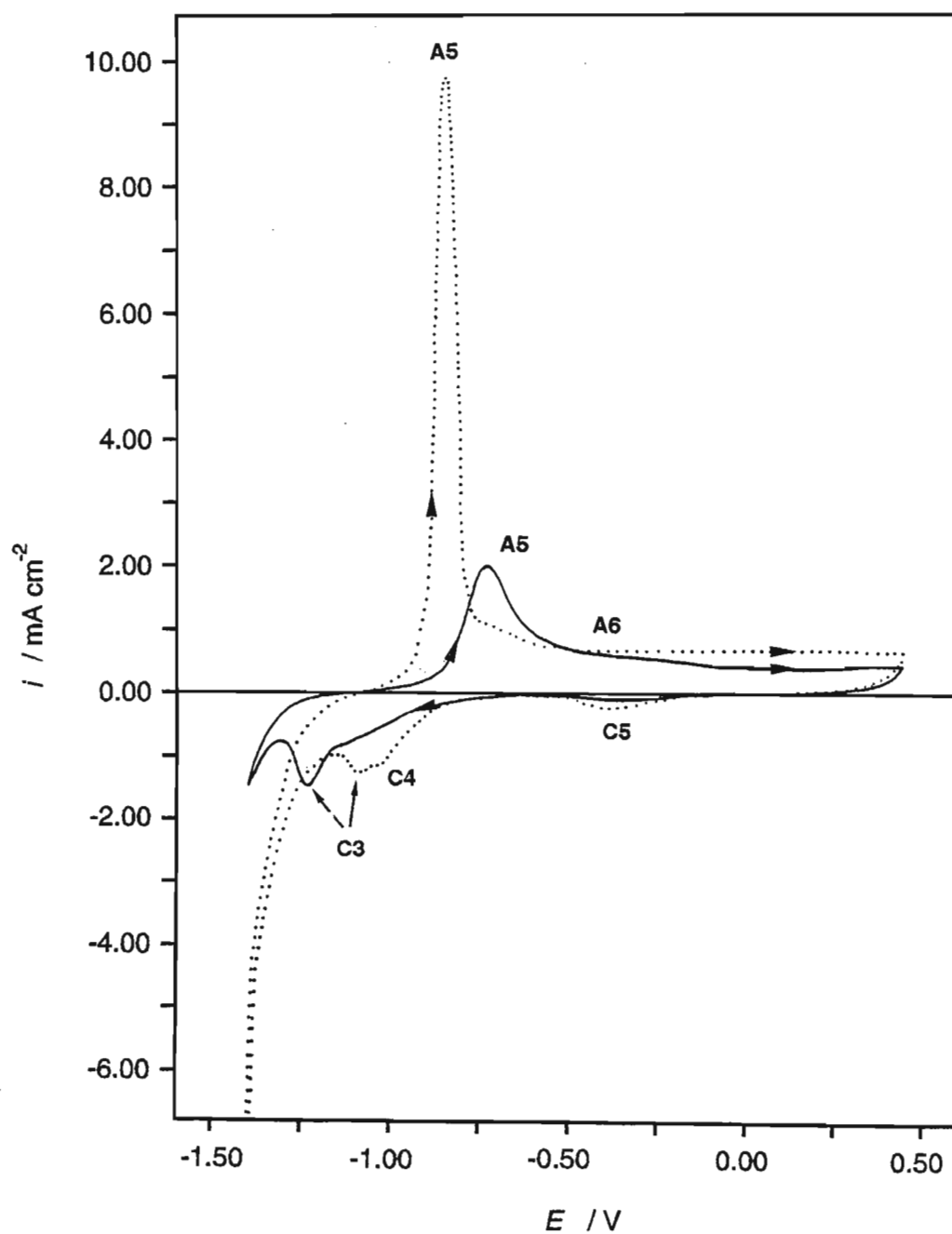


Fig. 5.48 Steady state cyclic voltammogram of a Fe electrode in 0.5M NaOH + 0.4M NaCN swept at 100mV s^{-1} between -1.40V and 0.45V at (—) 20°C and (·····) 80°C . $\omega = 100\text{rad s}^{-1}$.

As demonstrated in Fig. 5.48, for a Fe electrode in 0.5M NaOH + 0.4M NaCN, increasing the temperature resulted in an increase in magnitude of A5, C4 and C5 and a slight decrease in C3. At all temperatures, A6 remained broad and poorly defined. A linear E_p vs T relationship was found for all peaks, as shown in Fig. 5.49, with the oxidation peaks shifting to more negative potentials and the reduction peaks shifting to more positive potentials with increasing temperature. The peak current densities obeyed the Arrhenius equation, as shown by a typical set of data in Fig. 5.50. The activation energy for film growth at the potential of A5 was 21kJ mol^{-1} which is in good agreement with the 25kJ mol^{-1} obtained by de Wet *et al.*⁶³ for mild steel in 0.05M NaOH + 0.2M NaCN.

5.4.2 Rotation Rate Dependence

Varying the rotation rate from 68rad s^{-1} to 225rad s^{-1} resulted in a linear i_p vs $\omega^{1/2}$ relationship being observed for A5, C3 and C4 at all temperatures investigated. E_p was independent of rotation rate. With A6 being poorly defined, quantification of this peak was difficult, however $i_{p,A6}$ appeared to be independent of rotation rate.

5.4.3 Rotating Ring - Disc Electrode Experiments

Similar results to those described in section 5.2.5 were obtained in 0.5M NaOH + 0.4M NaCN. As shown in Fig. 5.51, with the ring held at oxidising potentials two oxidation peaks were observed at the ring. One (R_1) was present on the forward sweep and corresponded to the disc peak A5 while the second (R_2), present on the reverse sweep, corresponded to the disc reduction peak C3. With the ring held at reducing potentials, a ring reduction peak was first evident at $E \leq -1.00\text{V}$. The ring reduction peak present on the forward sweep corresponded to A5, while the ring reduction peak present on the reverse sweep corresponded to C3. Both of these ring reduction peaks were due to the Fe(II) species produced at A5 and C3 being reduced to Fe(0). No solution soluble Fe(III) species were detected at the ring. These results are in agreement with those reported earlier for Fe in 1.0M NaOH + 0.4M NaCN.

It can therefore be concluded that Fe(II) are produced at A5 and C3.

5.4.4 SEM Analysis

It has been shown earlier in this chapter that the addition of 0.4M NaCN to both 0.5M and 1.0M NaOH significantly changes the electrochemical response of Fe. Not unexpectedly, SEM examination of the surface of electrodes prepared in CN^- containing electrolytes showed the surface film to be very different to that observed in the absence of CN^- . Figs. 5.52 and 5.53 show typical regions of a Fe electrode in 0.5M NaOH + 0.4M NaCN. It is evident that a base layer completely covering the electrode surface is not present and that the surface features present, both the larger growth areas (Fig. 5.52) and the mat-like regions (Fig. 5.53(b)), tend to be more filamentous than those observed in the absence of CN^- . Figs. 5.52 and 5.53 are representative of the topography of the surface features observed on electrodes prepared under

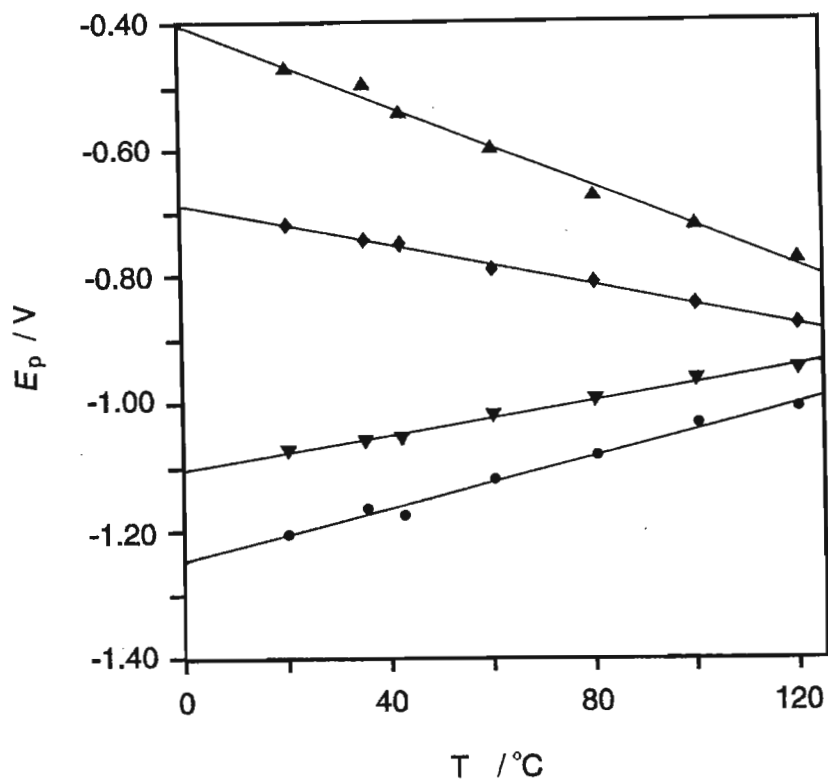


Fig. 5.49 Influence of temperature on the cyclic voltammetric peak potentials of a Fe electrode in 0.5M NaOH + 0.4M NaCN. $\nu = 100\text{mV s}^{-1}$, $\omega = 100\text{rad s}^{-1}$.

◆ A5 ▲ A6
• C3 ▼ C4

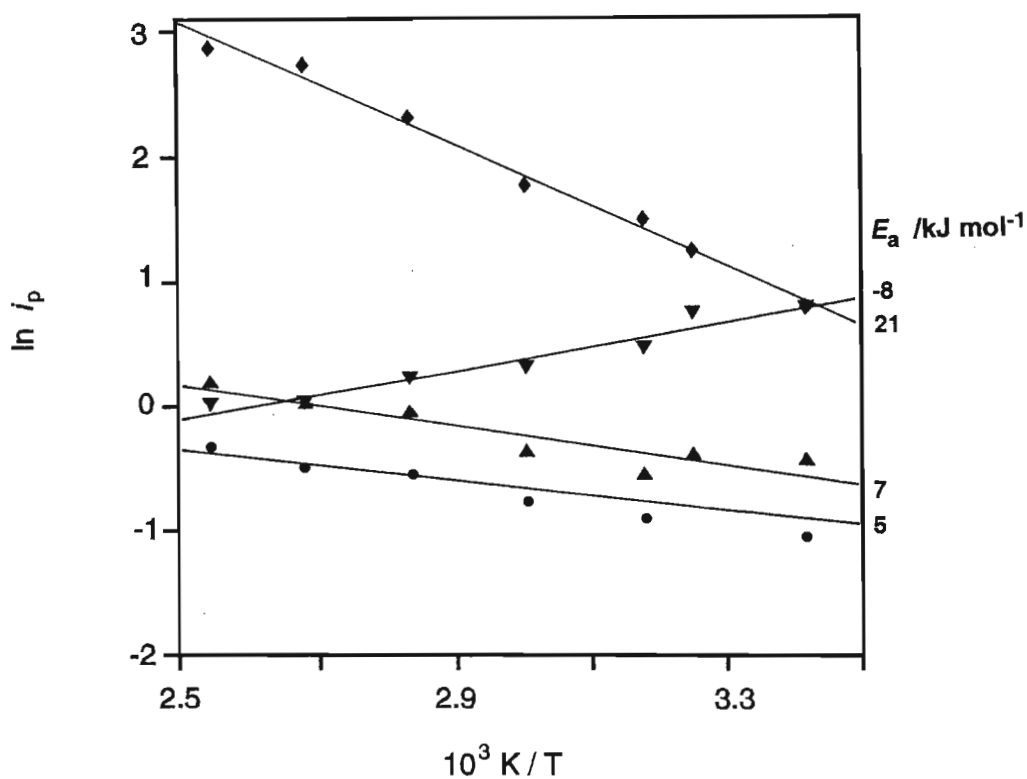


Fig. 5.50 Arrhenius plot for the reactions occurring on a Fe electrode in 0.5M NaOH + 0.4M NaCN at the potentials of the indicated peaks. $\nu = 100\text{mV s}^{-1}$, $\omega = 100\text{rad s}^{-1}$

◆ A5 ▲ A6
• C3 ▼ C4

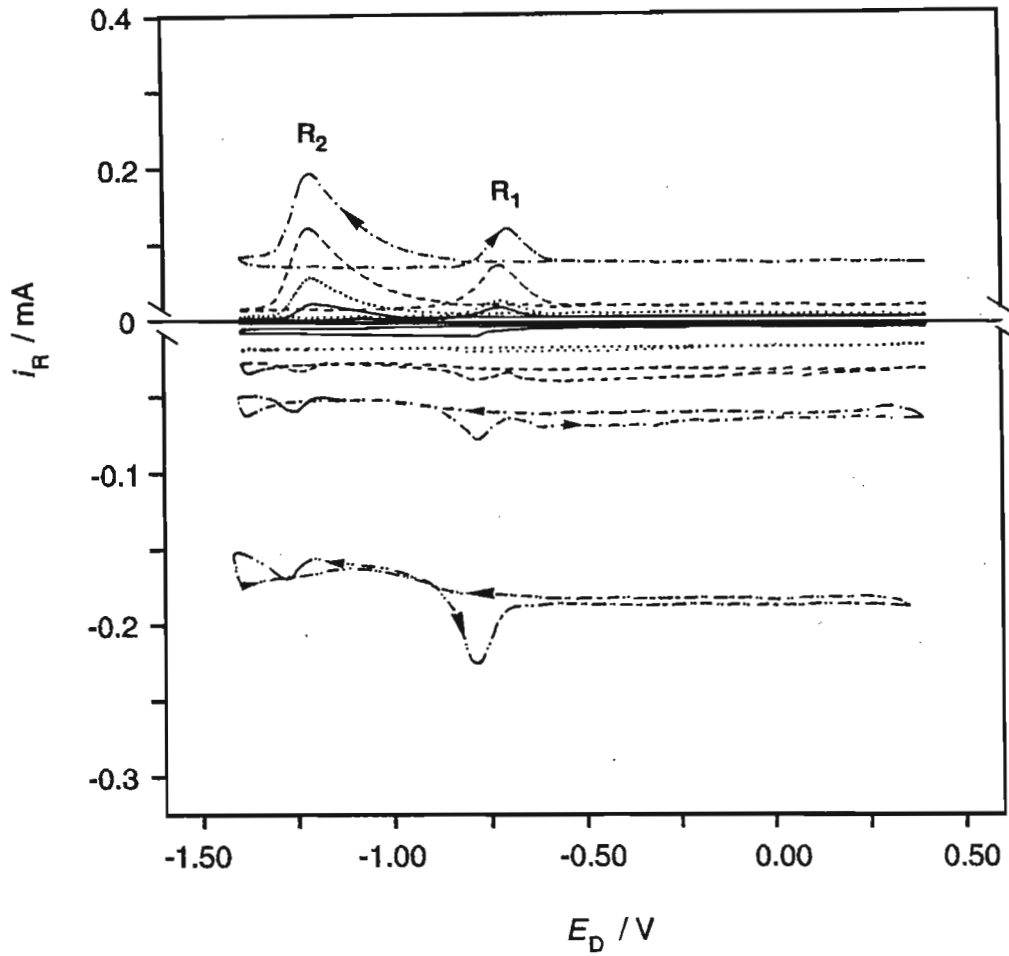


Fig.5.51 Ring response of a Fe electrode in 0.5M NaOH + 0.4M NaCN, 20°C, swept between -1.40V and 0.40V at 100mV s⁻¹, $\omega = 100\text{rad s}^{-1}$.

Positive ring potentials		Negative ring potentials	
————	0.00V	————	-0.60V
.....	0.20V	-0.80V
-----	0.40V	-----	-1.00V
-.-.-.-	0.60V	-.-.-.-	-1.10V
		-.-.-.-	-1.20V

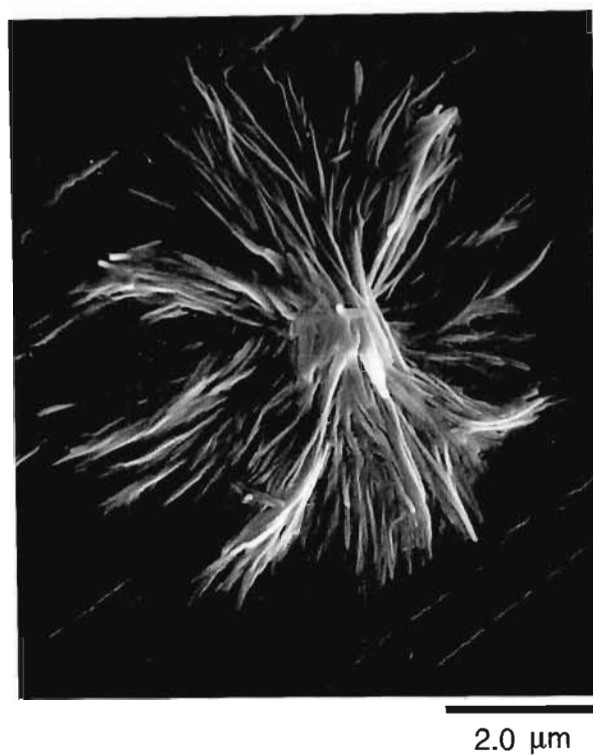


Fig. 5.52 Growth centre on the surface of a Fe electrode in 0.5M NaOH + 0.4M NaCN, 20 °C, after 7 cycles between -1.40V and 0.40V at 100mV s⁻¹, 100rad s⁻¹.

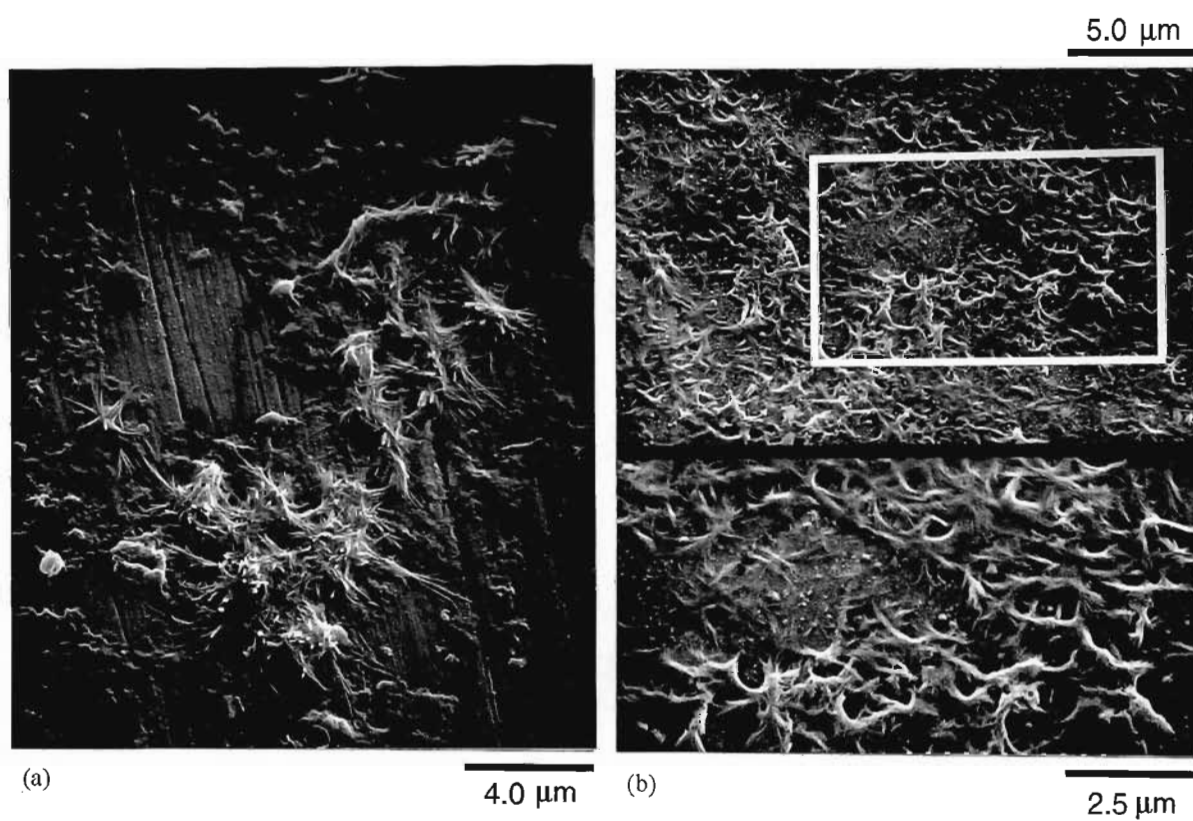


Fig. 5.53 Surface of a Fe electrode in 0.5M NaOH + 0.4M NaCN, 20 °C, after 20 cycles between -1.40V and 0.60V at 100mV s⁻¹, 100rad s⁻¹.

the same conditions, at temperatures up to 80°C. These results support the suggestion, based on the electrochemical data, that CN^- adsorption suppresses oxide formation and growth.

SEM examination of the electrode surface after a 100 cycles at 80°C showed that the surface looked very similar to that observed in 0.5M NaOH, in that cracking and flaking of the surface film which completely covered the electrode was evident, as can be seen in Fig. 5.54. The different topography of the surface film at higher temperatures could be due to the enhancement of the CN^- oxidation at higher temperatures. This would result in disruption of the surface film and in a reduction of the extent of the competitive adsorption between the CN^- and OH^- which would enable oxide formation to occur more readily. After 100 cycles, the increase in volume of the surface film would be such that stresses within the film result in rupture of the film and the appearance of cracks. Where small surface cracks develop (Fig. 5.54(c)) the exposed inner region resembled that of the upper layer formed in 0.5M NaOH (*cf* Fig. 5.41(e)). Fig. 5.54(c) also shows a frequently observed phenomenon of the repair of narrow, superficial cracks, by the formation of an oxide 'patch' (indicated by the arrow) along the crack. Where large cracks develop (Fig. 5.54(d)) two distinct layers can be seen, with the inner layer having a topography very similar to that observed in 0.5M NaOH at elevated temperatures (*cf* Fig. 5.45(a)). No repair of larger cracks was observed. Numerous indentations on the surface of the film were also evident, as can be seen in Figs. 5.54(b) and 5.55(a). It is proposed that these are due to the localised dissolution of the oxide. Repair of these indentations also appears to occur, as indicated by the arrows in Fig. 5.55.

5.4.5 XPS Analysis

XPS analysis showed that the surface film formed at 20°C consisted of FeO and Fe_2O_3 . A small percentage of FeOOH was detected in the outermost part of the film when the temperature was increased to 80°C. Details of the XPS analyses will be presented in chapter seven.

5.5 SUMMARY

5.5.1 0.5M and 1.0M NaOH

At ambient temperatures, four oxidation peaks (A1, A2, A3, A4) and two reduction peaks (C1, C2) were present on the cyclic voltammogram for Fe in 1.0M NaOH. On a clean electrode A3 and C2 were not present on the first cyclic voltammetric sweep, however there was an increase in i_p for these two peaks on subsequent sweeps such that a steady state voltammogram was obtained only after 50 sweeps. At ambient temperatures A3 and C2 were the dominant oxidation and reduction peaks, however at higher temperatures (120°C) these two peaks were poorly defined with A2 and C1 becoming the predominant peaks. A1, A2 and A4 were shown to be conjugate peaks to C1, while A3 was the conjugate peak to C2.

It was proposed that a duplex surface film formed, with the protective base layer forming at the potentials of

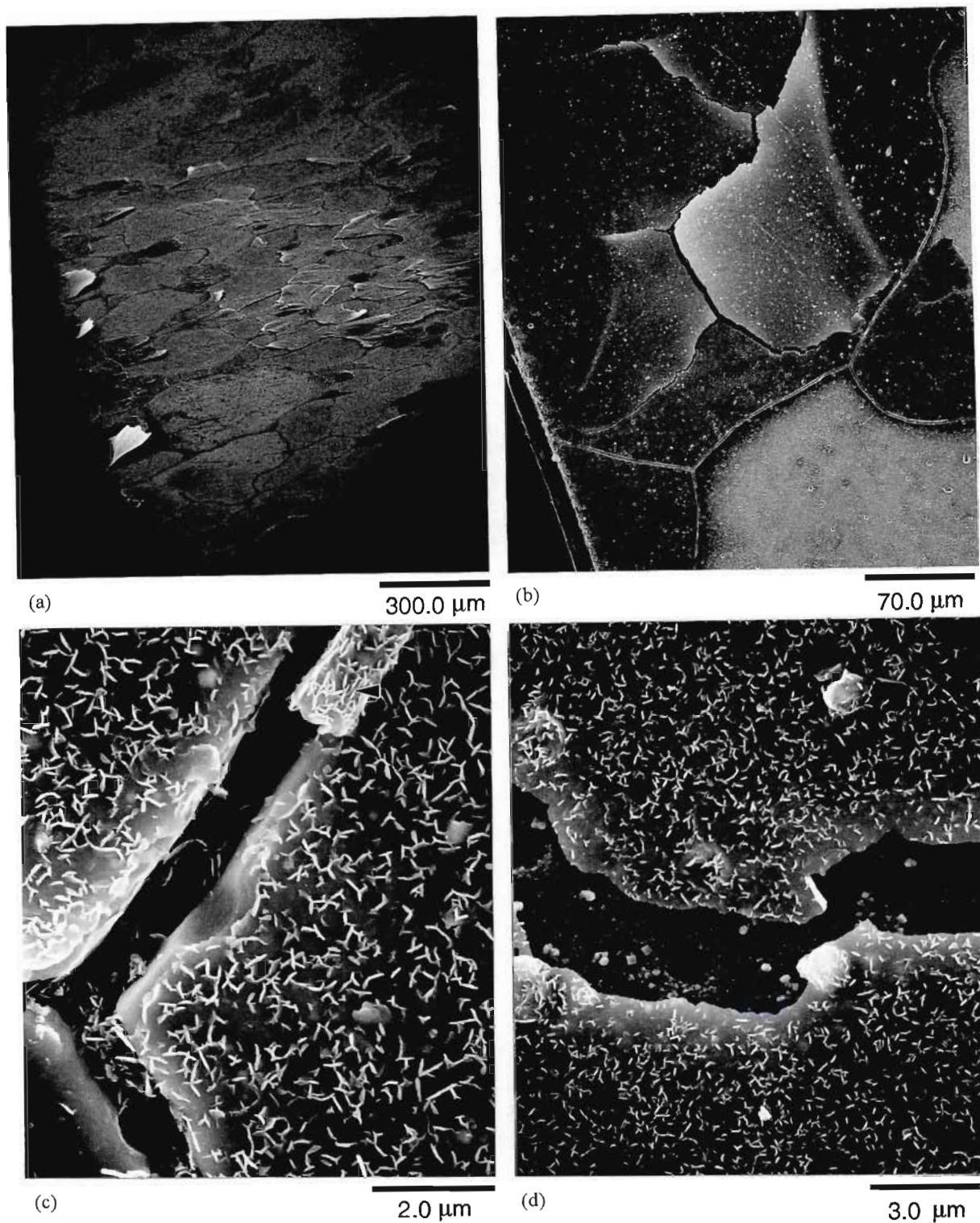


Fig. 5.54 Fe electrode in 0.5M NaOH + 0.4M NaCN, 80°C, after 100 cycles between -1.30V and 0.50V at 100mV s⁻¹, 100rad s⁻¹, showing (a), (b) the development of cracks in the surface film and the consequent flaking of the film revealing (c) the inner regions of the upper layer and (d) the base layer.

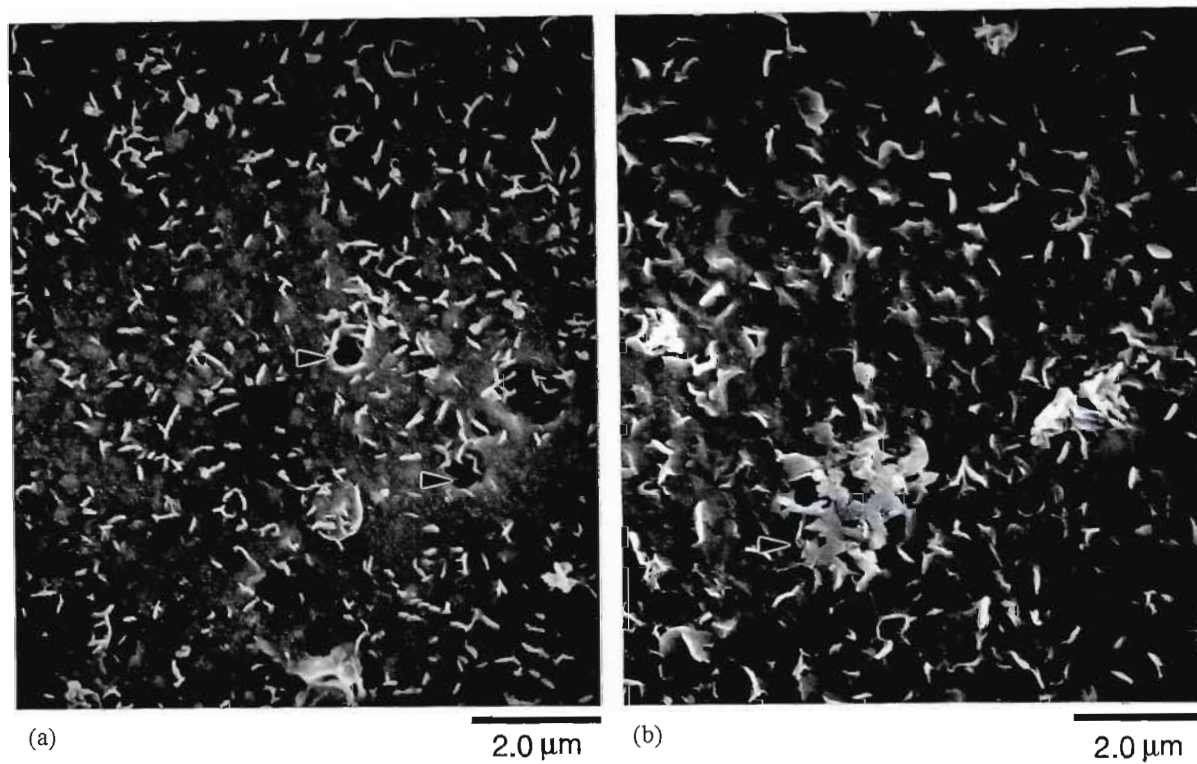


Fig. 5.55 Fe electrode in 0.5M NaOH + 0.4M NaCN, 80°C, after 100 cycles between -1.30V and 0.50V at 100mV s⁻¹, 100rad s⁻¹, showing (a) regions of dissolution of the surface film and (b) the repair of such regions.

A1 and A2 and consisting of FeO, onto which a non-protective upper layer formed (A3) and which was shown to consist of Fe_2O_3 and FeOOH . SEM examination of the electrode surface provided visual evidence of the existence and growth of the two layers.

The influence of rotation rate on i_p and E_p indicated a solid state mechanism prevailed for the reactions occurring at A1, A2, C1 and C2 while a dissolution-precipitation mechanism was applicable to A3 at $T < 60^\circ\text{C}$.

The linear i_p vs ν behaviour for A1, A2, C1 and C2 indicated that only surface film formation and reduction processes were involved with the reactions occurring at the potential of these peaks, with the above relationship suggesting that the base layer growth occurs via a place exchange mechanism. The linear i_p vs $\nu^{1/2}$ displayed by A3 indicated that subsequent to the formation of the upper layer via a dissolution-precipitation mechanism, growth proceeded via a low field mechanism with ion migration through the surface film as the rate determining step.

Finally, the RRDE data showed that soluble Fe(III) species were produced at A3 while soluble Fe(II) species were produced at A3, A4 ($T \geq 60^\circ\text{C}$), C1 and C2.

The voltammetric response of Fe in 0.5M NaOH was very similar to that observed in 1.0M NaOH, with the exception that A3 split into three peaks at $T \leq 40^\circ\text{C}$. At ambient temperatures steady state voltammograms were not obtained. A3 and C2 were again absent on the first sweep indicating that the reaction at A3 is not sequential to that at A2. A1, A2 and A4 were shown to be conjugate peaks to C1 while C2 was conjugate to A3a, A3b, A3c. Soluble Fe(II) species produced were detected at potentials corresponding to A3, C1 and C2 while Fe(III) species produced were detected at A3.

5.5.2 Addition of 0.4M NaCN to 0.5M and 1.0M NaOH

Addition of 0.4M NaCN to both 0.5M NaOH and 1.0M NaOH had a significant effect on the cyclic voltammetric behaviour of Fe with the CN^- inhibiting both dissolution and surface film formation and growth. The voltammograms consisted of a main oxidation peak A5 and two poorly defined peaks A6 and A7. Three reduction peaks, C3, C4 and C5, were observed (*cf* Fig. 5.15) with the latter being broad and poorly defined. The cyclic voltammograms obtained in 0.5M NaOH + 0.4M NaCN and in 1.0M NaOH + 0.4M NaCN were identical, with the exception that $i_{p,A5}$ was lower in the latter electrolyte. A5 was the conjugate peak to C3, peaks A5 and A6 conjugate to C4 and A7 conjugate to C5. In 1.0M NaOH + 0.4M NaCN, solution soluble Fe(II) species were detected at A5, C3 and C4, while Fe(III) were detected at A5 at $T > 60^\circ\text{C}$. In 0.5M NaOH + 0.4M NaCN only Fe(II) was detected at A5 and C3. $\text{Fe}(\text{CN})_6^{4-}$ was shown to be involved in the reaction(s) occurring at A5. A7 was due to the oxidation of CN^- to CNO^- .

The i_p vs $\nu^{1/2}$ behaviour exhibited by A5, A6, A7, C3, C4 and C5 indicated that the low field mechanism

involving ion migration through the film prevailed at the potentials of these peaks.

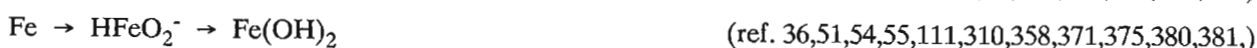
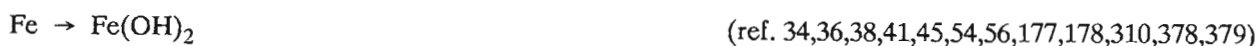
SEM and XPS showed the electrode surface to be sparsely covered with a filamentous type deposit consisting of FeO and Fe₂O₃, at ambient temperatures. At higher temperatures the surface film resembled that observed in the absence of CN⁻ and was shown to consist of FeO, Fe₂O₃ and FeOOH.

5.6 DISSOLUTION MECHANISM

As is evident from the literature review in chapter two, the dissolution mechanism for Fe in alkaline electrolytes has been investigated by a number of authors. Most mechanisms propose that Fe is initially oxidised to the hydrous Fe(OH)₂ at low potentials¹¹¹ and subsequently oxidised to iron (III) oxide or oxyhydroxide at more anodic potentials.^{54,173,178,375} While consensus has not been reached for assignment of the peaks on cyclic voltammograms to specific reactions; some of the more frequent assignments can be summarised by reactions to be described below. (It should be noted that these equations are reported here in the form as presented by the various authors.)

Oxidation peak A1

In weakly alkaline electrolytes iron oxidation has been shown to occur via a solid state oxidation mechanism,^{376,377} while in concentrated alkaline electrolytes it is proposed that the Fe(OH)₂ forms via the soluble intermediate HFeO₂⁻.



Other workers have proposed that the oxide, as opposed to the hydroxide is formed

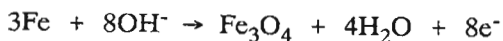


A1 has also been attributed to the oxidation of adsorbed hydrogen

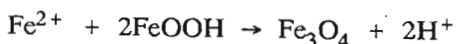


A combination of adsorbed hydrogen oxidation and the formation of an adsorbed FeOH layer has also been proposed.^{39,40}

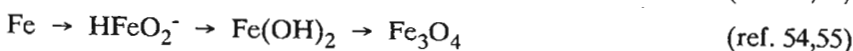
A less frequent assignment of A1 is the formation of Fe₃O₄ (ref. 41,47) via either direct oxidation of Fe

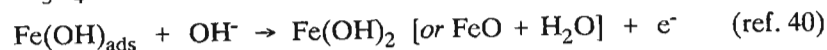
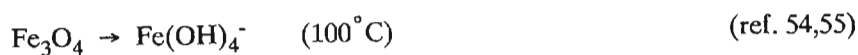


or via chemical reaction of electrogenerated Fe²⁺ with FeOOH

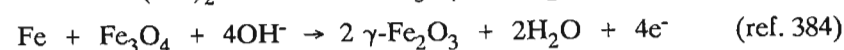
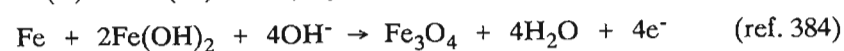
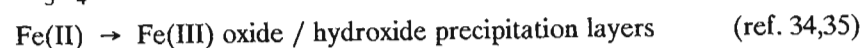
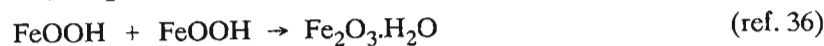


Oxidation peak A2

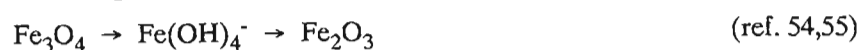




Oxidation peak A3

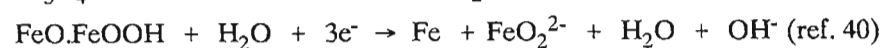


Oxidation peak A4

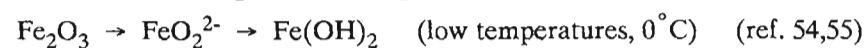
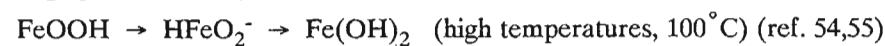
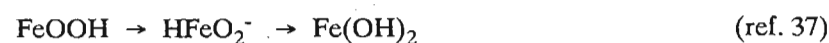


At $E > A4$ the oxyhydroxide FeOOH is reported to form, although consensus has not been reached as to the form of the FeOOH with α ,^{41,45,53,56,95} β ,⁵¹ γ ^{89,100,171,181} and δ ^{41,52,95} having been reported as present.

Reduction peak C1



Reduction peak C2



5.6.1 Dissolution Mechanism of Fe in NaOH Electrolytes

Peak A1

A1 has been attributed to the oxidation of adsorbed hydrogen, however the interdependence of A1 and C1

(cf sections 5.1.3, 5.3.2) suggest that A1 is due to the oxidation of Fe. Since A1 is independent of the number of cycles (Fig. 5.2) and therefore independent of the thickness of the upper layer, A1 must represent the growth of an inner layer. In agreement with what has previously been proposed^{36,40,382} it is suggested that in both electrolytes, at all temperatures, A1 is due to the formation of adsorbed hydroxy species :



Peak A2

Taking into consideration the charge under peaks A1, A2 and C1, together with the fact that A2 is also the conjugate peak to C1 (sections 5.1.3, 5.3.2) it is most likely that A2 is due to the formation of a Fe(II) hydroxide or oxide film. As XPS results (section 5.3.6) have shown the inner layer to consist of FeO, it is proposed that :



The formation of FeO, as opposed to Fe(OH)₂, as the base layer is supported by the work of Burke and Lyons⁴⁰ who proposed an anhydrous base layer and by the work of Macdonald⁷ who proposed that as a consequence of the large electric field ($\approx 10^6 \text{V cm}^{-1}$) protons would be excluded from the base layer.

A2 becomes the dominant peak at higher temperatures (cf Fig. 5.4) however, FeO is reported to be thermodynamically unstable at $T > 60^\circ \text{C}$ and decomposes to Fe₃O₄. As XPS analysis (section 5.3.6) of the surface film formed at 80°C detected the presence of FeO, Fe₂O₃ and FeOOH but not Fe₃O₄, it is suggested that the persistence of FeO at the higher temperatures is due to kinetic factors. The presence of FeO at elevated temperatures is further supported by the work of Schwartz and Simon³⁸⁶ who reported that during anodic polarisation of Fe in 4M KOH at 90°C , Fe dissolves as FeO₂²⁻ which, due to its low solubility, precipitates as Fe(OH)₂ ($\rightleftharpoons \text{FeO} + \text{H}_2\text{O}$).

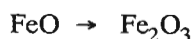
Such a reaction scheme for peaks A1 and A2 holds for the fact that in this work

- no ring currents are detected at the potential of either peak (cf sections 5.1.5, 5.3.4)
- i_p vs ν behaviour indicates a film growth occurs via a place exchange mechanism with bulk diffusion processes not being involved in the rate determining step.
- A1 is not present in CN⁻ containing electrolytes (cf Fig. 5.12) due to non - oxidative adsorption of CN⁻ onto the electrode surface, thereby blocking the surface and resulting in the Fe oxidation occurring at more positive potentials.

Peak A3

With continued applied potential cycling there is a continual increase in the magnitude of A3 while that of A1 and A2 remain virtually constant. It is therefore reasonable to suggest that the species formed at A1

and A2 are not direct precursors for the reaction occurring at A3, which in turn indicates that while the reactions responsible for A1 and A2 may occur consecutively, the reaction at A3 will proceed in parallel to the A1 and A2 reactions. This is further supported by the fact that on a clean electrode, A3 and C2 were not present on the first sweep — if the reaction at A3 was sequential to A2 then A3 should be present on the first sweep. Therefore, it is proposed that reduction, at C1, of the oxide formed on the forward sweep is incomplete and the remaining oxide (FeO) will be oxidised at A3 during the subsequent scan. It is this accumulation that leads to the increase in A3 and C2 with continued cycling (*cf* Figs. 5.2 and 5.29) :



At higher potentials, and with continued cycling, the Fe_2O_3 will convert to FeOOH .

RRDE results (*cf* Figs. 5.10 and 5.11) showed that soluble Fe(II) and Fe(III) species were produced in the potential region of A3. It is proposed that the formation of Fe_2O_3 proceeded via the following intermediate reactions :



The presence of the FeO_2^{2-} intermediate would account for the ring oxidation current while the Fe(OH)_4^- , the ring reduction current.

With increasing temperature the ring oxidation current increased significantly, compared to that of the ring reduction current, as can be seen from comparison of Figs. 5.10 and 5.11. It has been shown^{208-210,387} that HFeO_2^- is the stable species at elevated temperatures. Thus it is proposed that at $T > 60^\circ\text{C}$ the reactions occurring at the potential of A3 are :



Due to the stability of HFeO_2^- at elevated temperatures, the $\text{Fe(II)}_{\text{aq}} \rightarrow \text{Fe(III)}_{\text{aq}}$ will not proceed as readily as at lower temperatures ($T < 60^\circ\text{C}$) resulting in a corresponding decrease in the Fe_2O_3 formed at A3. This will result in a decrease in A3 and C2 (which was observed experimentally, *cf* Fig. 5.4) and in the attainment of steady state voltammograms more rapidly due to the complete reduction of the oxidation products that are produced, and thereby eliminating their buildup.

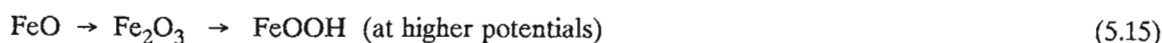
In 0.5M NaOH for a given number of sweeps, $i_{\text{p,A3}}$ was greater than that observed in 1.0M NaOH and at ambient temperatures, multiple peaks were observed in the potential region of A3 (*cf* Fig. 5.29) with A3b and A3c appearing on the 8th and 12th sweeps, respectively. It is therefore suggested that these multiple peaks indicate the presence of $\text{Fe}_2\text{O}_3 \cdot x\text{H}_2\text{O}$ having varying degrees of hydration due to aging processes. This suggestion is supported by the findings of Burke and Lyons⁴⁰ who, investigating Fe in alkaline electrolytes, reported a decrease in $i_{\text{p,A3}}$ with increasing pH, which they attributed to the higher hydroxide

ion concentration inhibiting the rearrangement of the upper layer (hydrous) which would suppress the conversion of anhydrous material of the protective inner region of the oxide to hydrous material. (Burke and Lyons⁴⁰ had proposed that the passivating properties of the film could be attributed to an anhydrous Fe(II) oxide or hydroxide.) Thus, based on the proposals of Burke and Lyons :

- If conversion / rearrangement is allowed to continue (ie. in 0.5M NaOH as opposed to 1.0M NaOH) then it should be more difficult to achieve a steady state cyclic voltammogram in 0.5M NaOH; this was found experimentally (*cf* section 5.3).
- The more hydrous the film is, the broader the peaks should be; again this is supported by the present results; compare Fig. 5.2 (50 sweeps, 1.0M NaOH) and Fig. 5.29 (28 sweeps, 0.5M NaOH), after 50 cycles of the latter the A3 peak will be very much broader than that shown in Fig. 5.2.
- XPS results (section 5.3.6) showed FeO as opposed to Fe(OH)₂ as the inner layer, which is agreement with Burke's proposal that the protective inner layer is more anhydrous than the outer layer.

Peak A4

As discussed in the introduction to section 5.1, A4 is a sequential reaction to A2 (*cf* Fig. 5.3) and does not vary in size with concomitant changes in A3. Thus it is proposed that A4 is due to the oxidation of the FeO to Fe₂O₃.



XPS results did not detect the presence of FeOOH at higher temperatures, therefore it is proposed that at $T > 60^\circ\text{C}$:



Peak C2

It was shown that C2 was the conjugate peak to A3 (sections 5.1.3, 5.3.2) and that the reaction(s) occurring at C2 involved the formation of soluble Fe(II) species, since a ring oxidation current was observed at potentials just negative of C2 on the reverse sweep (sections 5.1.5, 5.3.4). Thus it is proposed that at $T < 60^\circ\text{C}$:



while at $T > 60^\circ\text{C}$, HFeO_2^- will be the preferred intermediate, due to the greater stability of HFeO_2^- at the higher temperatures, ie.



Peak C1

C1 was shown to be the conjugate peak to A1, A2 and A4 (sections 5.1.3, 5.3.4) and RRDE results (*cf* sections 5.1.5 and 5.3.4) indicated the presence of soluble Fe(II) species at the potential of C1. Thus it is proposed that at $T < 60^\circ\text{C}$:





while at $T > 60^\circ\text{C}$:



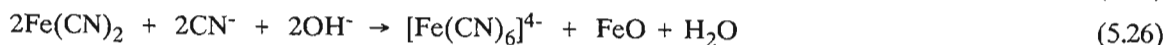
It has been well documented that the reduction of FeO is incomplete, with the remaining FeO being incorporated into the upper layer via an oxidation reaction at A3 on subsequent sweeps.

5.6.2 Dissolution Mechanism of Fe in NaOH/NaCN Electrolytes

In both 0.5M NaOH + 0.4M NaCN and 1.0M NaOH + 0.4M NaCN, CN^- inhibited the adsorption of hydroxide species at A1 (peak A1 not observed), and subsequent oxide formation (SEM observation), and the formation of the upper layer at A3 (A3 not present). It is proposed that the reaction at A1 was suppressed due to CN^- adsorption resulting in the main Fe oxidation reaction being observed at the more positive potential of A5. The fact that the rate of oxide thickening is severely reduced in the presence of CN^- , as indicated by the rapid attainment of steady state cyclic voltammograms, suggests that CN^- is strongly adsorbed on the electrode surface. This behaviour would be expected from the greater polarisability of CN^- compared to that of OH^- . This is supported by the work of Shoesmith⁵⁰ and by the findings of Horányi³⁷² who demonstrated the strong irreversible chemisorption of CN^- ions in alkaline media. In addition, the results presented in Fig. 5.47(b) showed the effects of CN^- on a film formed in 0.5M NaOH. As CN^- inhibits further oxide formation (eg. $\text{FeO} \rightarrow \text{Fe}_2\text{O}_3$, at A3) less oxide will be available for reduction at C2 and reoxidation at A3, resulting in a decrease in the magnitude of these peaks.

It is proposed that CN^- suppresses the formation of FeOH_{ads} at A1 by the non - oxidative adsorption of CN^- on the electrode surface thereby blocking the active sites and inhibiting FeOH_{ads} formation, with the formation of FeO only occurring at the potential of A5. Despite the fact that less oxide was observed on the electrode surface in CN^- containing electrolytes, the charge under A5 was greater in these electrolytes, than in the absence of CN^- . This is due to the formation of $\text{Fe}(\text{CN})_6^{4-}$, as discussed in section 5.2.6 and as indicated by the Fe - CN^- - H_2O Pourbaix diagram.⁶² The following reaction scheme is therefore proposed for Fe in cyanide containing electrolytes :

Peak A5



Two distinct regions were present on the E_a vs ν curve for A2 (cf Fig. 5.18) suggesting the presence of two sweep rate dependent rate determining steps. From the above reaction scheme it is proposed that at $\nu < 40\text{mV s}^{-1}$ (which showed a rapid decrease in E_a with increasing ν) that the formation of FeO is the rate determining step, while at $\nu \geq 100\text{mV s}^{-1}$ the CN^- adsorption is the rate determining step.

Peak A6

The above reaction scheme is then followed by the conversion of the FeO to Fe₂O₃ at the potential of A6



At higher temperatures hydrolysis of CN⁻ and CN⁻ oxidation occurs more readily, reducing the extent of the CN⁻ inhibition on film formation (section 5.4.4 and Fig. 5.54). This would have the effect of allowing the formation of additional iron oxide. Further XPS, results showed that while FeO and Fe₂O₃ were present in the surface film formed in CN⁻ containing electrolytes at 20°C, FeO, Fe₂O₃ and FeOOH were present at 80°C. Thus it is proposed that eqn. 5.27 is followed by the formation of FeOOH at 80°C :

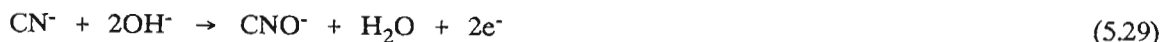


The reaction scheme presented above would account for

- a) the soluble Fe(II) detected at the ring at the potential of A5, (cf Figs. 5.51, 5.21)
- b) Fe(CN)₆⁴⁻ was shown to participate in the reactions occurring at A5 (cf Fig. 5.24) and that
- c) XPS results which showed FeO /Fe₂O₃ present at 20°C and FeO /Fe₂O₃ /FeOOH at 80°C.

Peak A7

At more anodic potentials, A7 has been shown to be due to the oxidation of cyanide to cyanate (cf section 5.2.6 and Fig. 2.12)

**Peak C4**

On the reverse sweep, it is proposed that C4 is due to



Dissolution of the FeO produced must also occur as a ring oxidation current is observed on the reverse sweep at potential negative of C4 (sections 5.2.3, 5.4.3). This oxidation peak becomes more prominent as the temperature increases indicating increased dissolution with increasing temperature; this would not be unexpected.

Peak C3

As C3 is the conjugate peak to A5 (section 5.2.3) it is proposed that C3 is due to



The soluble Fe(II) intermediates in the above two reactions would account for the ring oxidation peaks observed at the potential of C3 (sections 5.2.5, 5.4.3). These reactions must result in the complete reduction of the oxide formed on the forward sweep as steady state voltammograms are readily obtained (cf Figs. 5.12 and 5.46). This is in agreement with the SEM results (section 5.4.4) which showed less oxide was present on the electrode surface.

The thermodynamic viability of the above proposals can be evaluated by considering the appropriate Pourbaix diagram, presented in section 2.10 (particularly those of Pourbaix²⁰⁶ (Fig. 2.5) and Misawa²⁰⁷ (Fig. 2.6) which show the domains of relative predominance of the dissolved species). However, as always, caution must be exercised due to the construction of the diagrams from purely thermodynamic data. The kinetics of the reactions will involve an overpotential thus the criterion of $E_p > E^\circ$ for the oxidation reactions and $E_p < E^\circ$ for the reduction reactions must be met. Nevertheless in all instances where the diagrams display the appropriate reaction given in the proposed mechanism, the above criteria are met thereby confirming the feasibility of the proposed mechanism.

CHAPTER SIX

RESULTS and DISCUSSION

IRON IN ALKALINE CYANIDE ELECTROLYTES : Chronoamperometric Experiments

In chapter four it was shown that chronoamperometry provided a useful means for investigating the nucleation of anodic surface films on various stainless steels and their constituent elemental metals in acidic electrolytes. In this chapter the technique will be used to investigate the initial stages of anodic film formation on Fe in 0.5M and 1.0M NaOH, 0.5M NaOH + 0.4M NaCN and 1.0M NaOH + 0.4M NaCN, over a range of temperatures from 20°C to 120°C.

6.1 Fe in 0.5M NaOH

In these experiments a Fe electrode in 0.5M NaOH was initially polarised at a cathodic potential (-1.20V) for 1 minute, then stepped to the potential of interest. At 20°C, at potentials greater than -0.90V, rising current transients were observed. At the start of each transient there was an initial decrease in the current density followed by an increase, reaching a maximum current density, i_m , at t_m — the rising section of the transient. Subsequent to this, the current decayed to an eventual steady state value. A typical series of rising transients, over a range of temperatures and potentials are shown in Fig. 6.1. From Fig. 6.1 it is evident that certain of the current transients exhibit more than one maximum indicating that more than one process is occurring. At 20°C, in the potential range -0.90V to -0.70V only one very broad maximum was present, with the second maximum, at longer times, first evident at -0.70V. For both maxima, i_m increased and t_m decreased with potential, as given by the following equations :

$$i_m = a + bE \quad (6.1)$$

$$\log t_m = c + dE \quad (6.2)$$

The values for the coefficients a - d are given in Table 6.1.

At ambient temperatures the first maximum was present as a shoulder to the second maximum. Performing a simple deconvolution of the two maxima showed that the charge under the second maximum exceeded that of the first indicating that the second process was unlikely to be a consecutive reaction to the

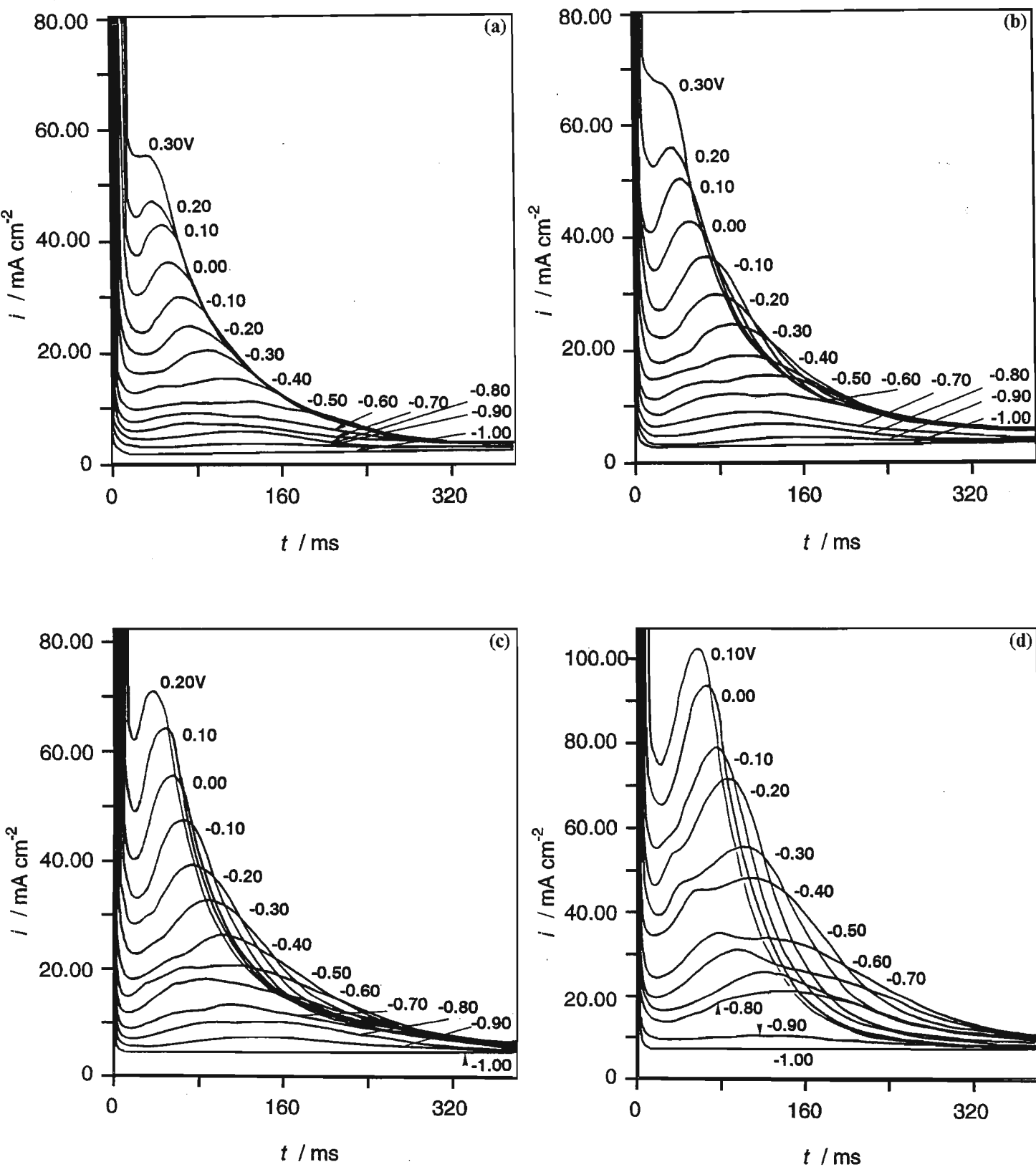


Fig. 6.1 Current transients of a Fe electrode in 0.5M NaOH stepped from -1.20V to the indicated potentials at (a) 20°C, (b) 35°C, (c) 50°C, (d) 70°C, (e) 80°C, (f) 100°C and (g) 120°C.

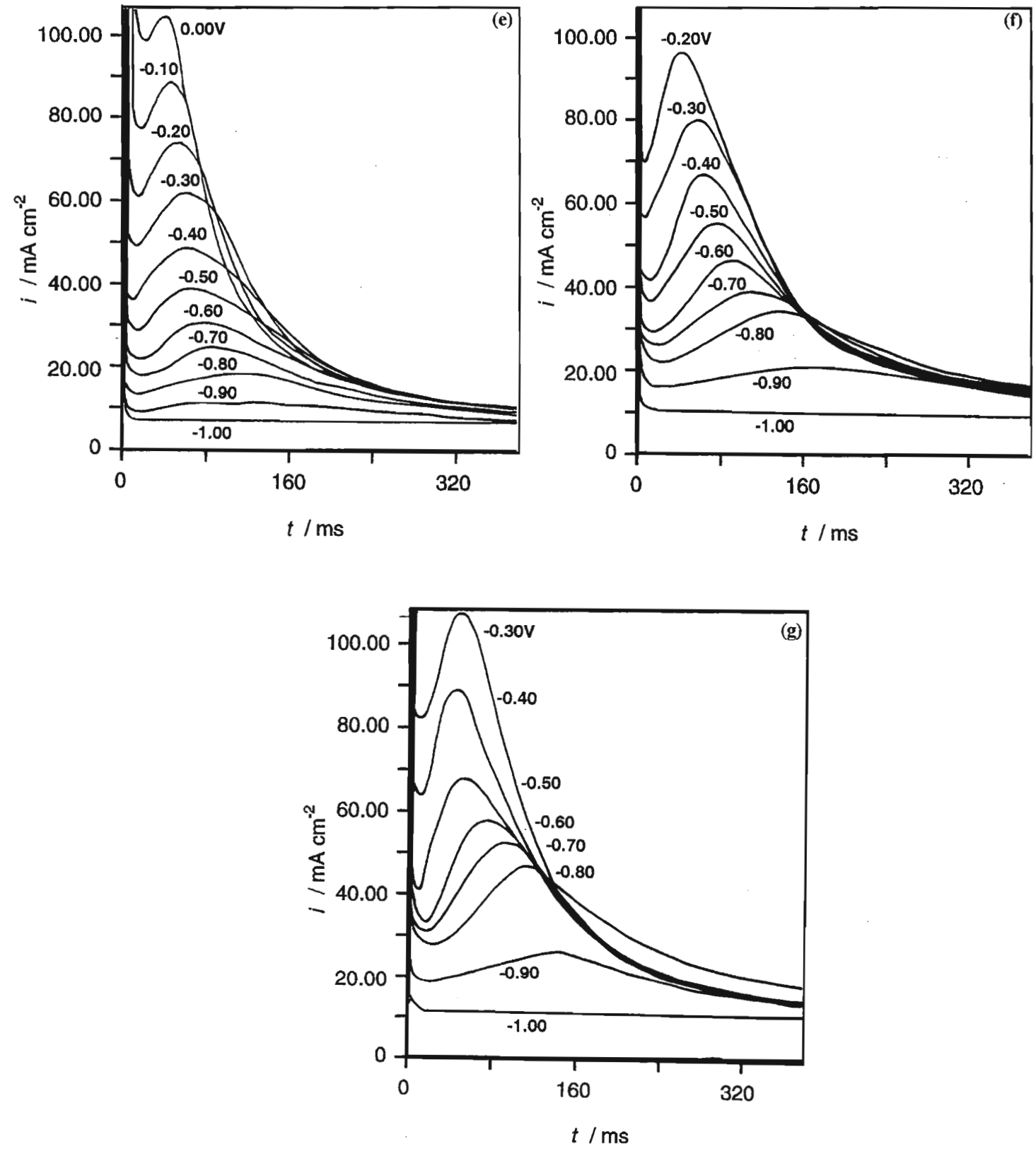


Fig. 6.1 continued

Table 6.1

Values for the coefficients of the relevant relationships given below, for the variation of current maximum, i_m , and corresponding time, t_m , with applied potential.

$$i_m = a + bE \tag{6.1}$$

$$\log i_m = e + fE \tag{6.3}$$

$$\log t_m = c + dE \tag{6.2}$$

Fe in	T/°C	<i>a</i>	<i>b</i>	<i>c</i>	<i>d</i>	<i>e</i>	<i>f</i>
0.5M NaOH (base layer)	20	17.798	18.221	1.084	-1.239	—	—
	35	22.715	23.036	1.273	-1.047	—	—
	50	33.103	26.632	1.231	-1.165	—	—
	70	55.345	45.146	1.271	-1.144	—	—
	80	74.327	79.059	1.442	-1.044	—	—
	100	103.650	90.448	1.553	-0.953	—	—
0.5M NaOH (upper layer)	120	146.820	125.661	1.664	-0.862	—	—
	20	35.487	54.721	1.719	-0.728	—	—
	35	42.684	62.316	1.721	-0.763	—	—
	50	55.398	73.692	1.715	-0.817	—	—
	70	77.815	93.875	1.815	-0.670	—	—
0.5M NaOH + 0.4M NaCN	20	63.749	83.001	1.231	-1.572	—	—
	35	92.937	123.554	1.354	-1.458	—	—
	60	124.828	148.040	1.355	-1.622	—	—
	80	172.909	180.450	1.114	-1.733	—	—
	100	217.700	225.112	1.038	-1.844	—	—
	120	275.677	270.520	0.962	-1.954	—	—
1.0M NaOH (base layer)	40	63.873	58.448	0.449	-1.516	—	—
	60	76.952	68.100	0.404	-2.153	—	—
	80	149.790	155.729	0.873	-1.103	—	—
	100	194.490	205.840	0.778	-1.177	—	—
	120	269.315	298.988	0.965	-0.971	—	—
1.0M NaOH (upper layer)	20	—	—	1.510	-0.406	2.112	1.203
	40	—	—	1.391	-0.507	2.170	1.194
	60	—	—	1.177	-0.752	2.388	1.255
1.0M NaOH + 0.4M NaCN (1st maximum)	20	117.80	156.384	1.522	-0.896	—	—
	35	92.206	115.132	1.331	-1.334	—	—
	60	199.307	242.543	1.309	-1.079	—	—
	80	215.423	232.534	0.641	-1.167	—	—
	100	258.268	272.246	0.305	-1.299	—	—
	120	310.227	312.256	-0.031	-1.431	—	—
1.0M NaOH + 0.4M NaCN (2nd maximum)	20	—	—	2.020	-0.446	1.392	0.696
	60	—	—	1.766	-0.955	1.548	1.125
	80	—	—	1.459	-0.809	2.027	0.827
	100	—	—	1.332	-1.063	2.062	1.041
	120	—	—	1.154	-1.203	2.236	1.110

first. The cyclic voltammetric data presented in the previous chapter, showed that peaks A1 and A2, at -1.14V and -0.92V respectively, were due to the formation of the base layer of the surface film while the triplet A3 peaks (-0.72V to -0.66V) were due to the formation of the upper layer. Further it was shown that the reactions at A3 occurred in parallel to those at A1 and A2. It is therefore proposed that the first current transient maximum is due to the formation of the base layer while the second maximum corresponds to the upper layer. This is supported by the fact that at ambient temperatures the cyclic voltammetric data showed upper layer formation to be the dominant process and which is corroborated by the dominance of the second maximum of the chronoamperometric transients.

The rising current transients observed at 35°C were qualitatively the same as those observed at 20°C (*cf* Fig. 6.1(b)). At 50°C (Fig. 6.1(c)) the first rising transient was detected at more cathodic potentials (-1.00V as opposed to -0.90V) than was the case at lower temperatures. Also, the evidence for base layer formation could still be seen at -0.20V, i.e. 0.20V more positive than at 20°C. A similar situation was observed at 70°C (Fig. 6.1(d)) where the first rising transient was evident at -1.00V and base layer formation was still evident at -0.10V. At 50°C and 70°C the maximum corresponding to the formation of a base layer was a very much more prominent feature of the transient. At $T \geq 80^\circ\text{C}$ there was no longer evidence of the upper layer maximum with base layer formation and growth clearly predominating (*cf* Fig. 6.1(e) - (g)). The trends shown by these rising transients are in agreement with the cyclic voltammetric results presented in the previous chapter, which showed that base layer formation was favoured at the higher temperatures.

For both maxima, the logarithm of t_m decreased and i_m increased linearly with potential over the temperature range 20°C to 120°C, as given by eqns. 6.2 and 6.1 respectively. The coefficients for these equations are summarised in Table 6.1. These coefficients were found to vary with temperature as given by the following relationships :

base layer :	$\log a = -1.08 \times 10^3 T^{-1} + 1.91$
	$\log b = -1.02 \times 10^3 T^{-1} + 1.69$
	$c = 5.53 \times 10^{-3} T + 1.00$
	$d = 4.57 \times 10^{-3} T - 1.41$
upper layer :	$\log a = -0.69 \times 10^3 T^{-1} + 0.90$
	$\log b = -0.47 \times 10^3 T^{-1} + 0.34$
	$c = -1.00 \times 10^{-4} T + 1.72$
	$d = 0.93 \times 10^{-4} T - 0.78$

For the rising transients presented above, it was found that for a given potential, i_m increased with increasing temperature as given by the Arrhenius equation. The activation energies calculated from the Arrhenius plots are summarised in Table 6.2. As these E_a values are determined using i_m , it is proposed that they represent the activation energy for nucleation of the surface film. E_{a1} and E_{a2} , for the base and

Table 6.2

Activation energies, E_a , calculated from Arrhenius plots for Fe in :

- E_{a1} : 0.5M NaOH, base layer
- E_{a2} : 0.5M NaOH, upper layer
- E_{a3} : 0.5M NaOH + 0.4M NaCN
- E_{a4} : 1.0M NaOH, base layer
- E_{a5} : 1.0M NaOH, upper layer
- E_{a6} : 1.0M NaOH + 0.4M NaCN

E/V	E_{a1}	E_{a2}	E_{a3}	E_{a4}	E_{a5}	E_{a6}
-0.90	47.58	—	—	7.71	—	—
-0.80	38.10	—	34.75	8.76	—	37.25
-0.70	31.38	—	26.53	10.29	10.60	28.24
-0.60	27.36	—	23.84	10.77	10.30	19.21
-0.50	25.98	20.66	19.27	11.45	10.26	15.20
-0.40	20.86	19.88	16.66	10.50	9.09	14.03
-0.30	—	16.85	15.92	10.21	8.83	13.18
-0.20	—	16.77	14.84	—	7.07	12.84
-0.10	—	14.85	13.39	—	—	10.05
0.00	—	14.00	12.53	—	—	9.10
0.10	—	12.33	—	—	—	8.25
0.20	—	11.29	—	—	—	8.14

where E_a (kJ mol⁻¹) is the activation energy for nucleation of a surface film growth site.

upper layers respectively, are of the same order of magnitude as those reported for nucleation of surface films on Fe18Cr alloys³⁸⁸ in 0.1M H₂SO₄, Cr deposition,³⁸⁹ film growth on mild steel in a pH 5 electrolyte,³⁹⁰ film growth on Cu in alkali³⁴⁰ and for Cu in borate buffer (pH 9),³⁹¹ and suggest that the nucleation process is at least partially diffusion controlled.³⁴⁰

The activation energy for upper layer nucleation is less than that for base layer nucleation, a trend which was also observed for 1.0M NaOH. This can be explained by the fact that when the upper layer forms it does so under the relatively stable conditions created by the base layer. The latter, however has to form under conditions of more extensive substrate dissolution and has to perform the function of passivating the active sites. Thus a lower activation energy for the upper layer formation is not unreasonable.

E_{a1} and E_{a2} decreased with increasing potential for both the base and upper layers, as given by the following relationships :

$$\text{base layer :} \quad E_{a1} = -49.70E - 0.428$$

$$\text{upper layer :} \quad E_{a2} = -13.54E + 13.80$$

This decrease of E_a with increasing potential can be attributed to the fact that oxidation occurs more readily at higher potentials resulting in more material being available for nucleation.

While it is well established that the oxidation peaks on the cyclic voltammograms, presented in the previous chapter, are the result of the growth of a surface oxide, current transients as presented in Fig. 6.1 have been less extensively investigated. The following multiple potential step / cyclic voltammetric experiment was performed to confirm that such potential step experiments do result in the nucleation and growth of a surface oxide, as reflected by the changes in subsequent cyclic voltammograms. This multiple potential step experiment involved the application of the following potential regime to the electrode (see inset Fig. 6.2). Initially, a single cyclic voltammogram was obtained on a clean electrode surface (-1.4V → 0.40V → -1.40V; $\nu = 100\text{mV s}^{-1}$). This was then followed by a series of potential steps (-1.30V (10s) → -0.10V (10s); repeated 10x in total). The final potential, of the potential step, having previously been shown to result in a rising current transient (cf Fig. 6.1(a)). Another cyclic voltammogram was then recorded. This regime was then repeated, as shown in Fig. 6.2. After the first 10 potential steps peak A3a was evident on the anodic sweep. SEM examination of the electrode surface showed the presence of the base layer. After 20 potential steps the beginnings of peaks A3b and A3c were evident on the cyclic voltammogram and cluster - like deposits, which varied in size, were observed on electrode surface. These deposits were similar to those shown in Fig. 5.41(c). As the total number of applied potential steps increased all the anodic peaks on the cyclic voltammogram became better defined indicating the buildup of an oxide layer on the surface. This was verified by SEM examination of the electrode which revealed that the surface clusters were more numerous and had grown in size, eventually coalescing and covering the entire electrode surface. From this experiment, it may be concluded that the potential step experiments do result in the nucleation and growth of a surface film.

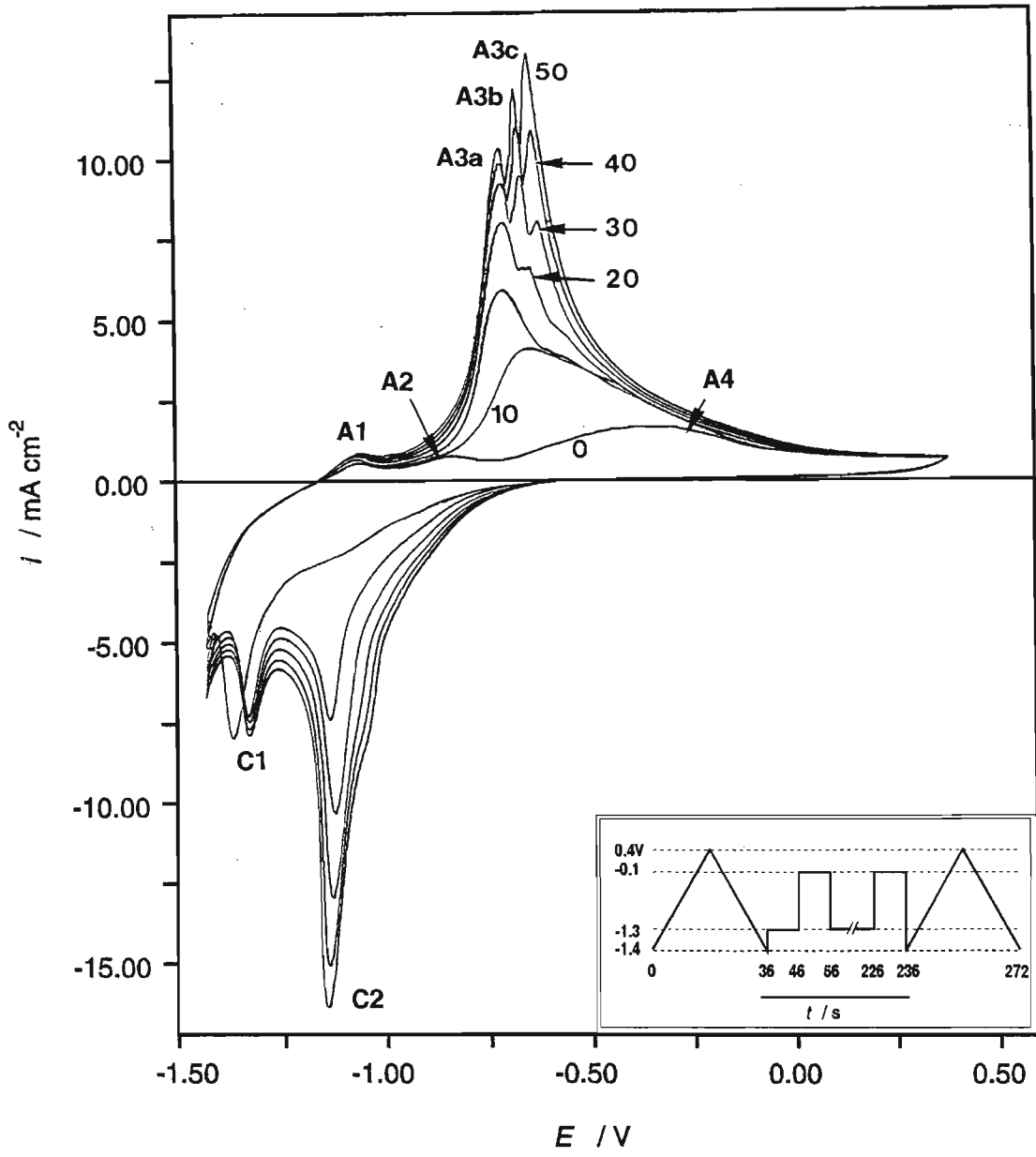


Fig. 6.2 Cyclic voltammogram of a Fe electrode in 0.5M NaOH, 20°C, swept at 100mV s⁻¹ between -1.40V and 0.40V, showing the buildup of surface film as a result of multiple potential steps (the number of steps being indicated on the voltammograms).
Inset : Schematic representation of applied potential regime.

This result was further verified by performing a single potential step experiment, over a range of potentials, and subsequently examining the surface of the electrode using SEM. Fig. 6.3 shows the discrete nuclei present on a Fe electrode surface after the imposition of a single potential step. While the nuclei are relatively uniform in shape and size, there is some variation suggesting that the initial film is formed via a rapid progressive nucleation mechanism. In addition, the size and shape of the nuclei from these potential step experiments corresponds well with those formed using cyclic voltammetric techniques (*cf* Fig. 5.41). The nuclei do not form preferentially along scratches or macro-defects on the electrode surface, as can be seen in Fig. 6.3(a) which shows nucleation on a poorly polished electrode. Reports of nucleation occurring both preferentially^{235,275} along scratches and independent^{44,275} of scratches have appeared in the literature.

There has been debate regarding the influence of potential on the number of nuclei formed. As can be seen from the series of micrographs in Fig. 6.3, potential had a significant influence on the number of nuclei formed. Such visual evidence, for iron or ferrochrome steels, has not previously been reported in the literature. The number of nuclei were found to increase linearly with increasing potential as shown in Fig. 6.4. Comparing the charge required for the formation of the observed number of nuclei with that determined from the appropriate current transient, Fig. 6.5 shows that initially the surface film forms as $\text{Fe}(\text{OH})_2$, since the formation of FeO would require a charge greater than that observed. For the reasons presented in the previous chapter, the $\text{Fe}(\text{OH})_2$ must subsequently dehydrate to FeO . Nuclei formation accounts for 75 - 80% of the transient's charge. The remainder can be accounted for by the fact that in order for a stable nucleus to form, a critical number of atoms must coalesce. If conditions are such that the critical nucleus size cannot be attained the nucleus will not survive.

This visual evidence presented above together with the fact that i_m and t_m vary with potential, indicate that the film forming process is controlled by a potential dependent nucleation mechanism.

Fig. 6.3(c) shows the presence of regular shaped regions devoid of the prevailing shaped nuclei; such zones are referred to as nucleation exclusion zones. These zones were also observed, although to a lesser extent, at 0.20V and 0.40V. For dilute electrolytes it has been proposed that these zones are diffusion zones that develop around the growing nuclei.^{252,259} They have also been attributed to zones of reduced concentration of the electrodepositing species which arise around stable growing nuclei.²⁹⁵ Markov^{290,291} described the nucleation exclusion zones as regions of increased electrical resistance in the electrolyte. In concentrated electrolytes it has been proposed²⁹⁵ that these nucleation exclusion zones are regions of reduced overpotential around the growing clusters, which are the result of local ohmic drop in the electrolyte.

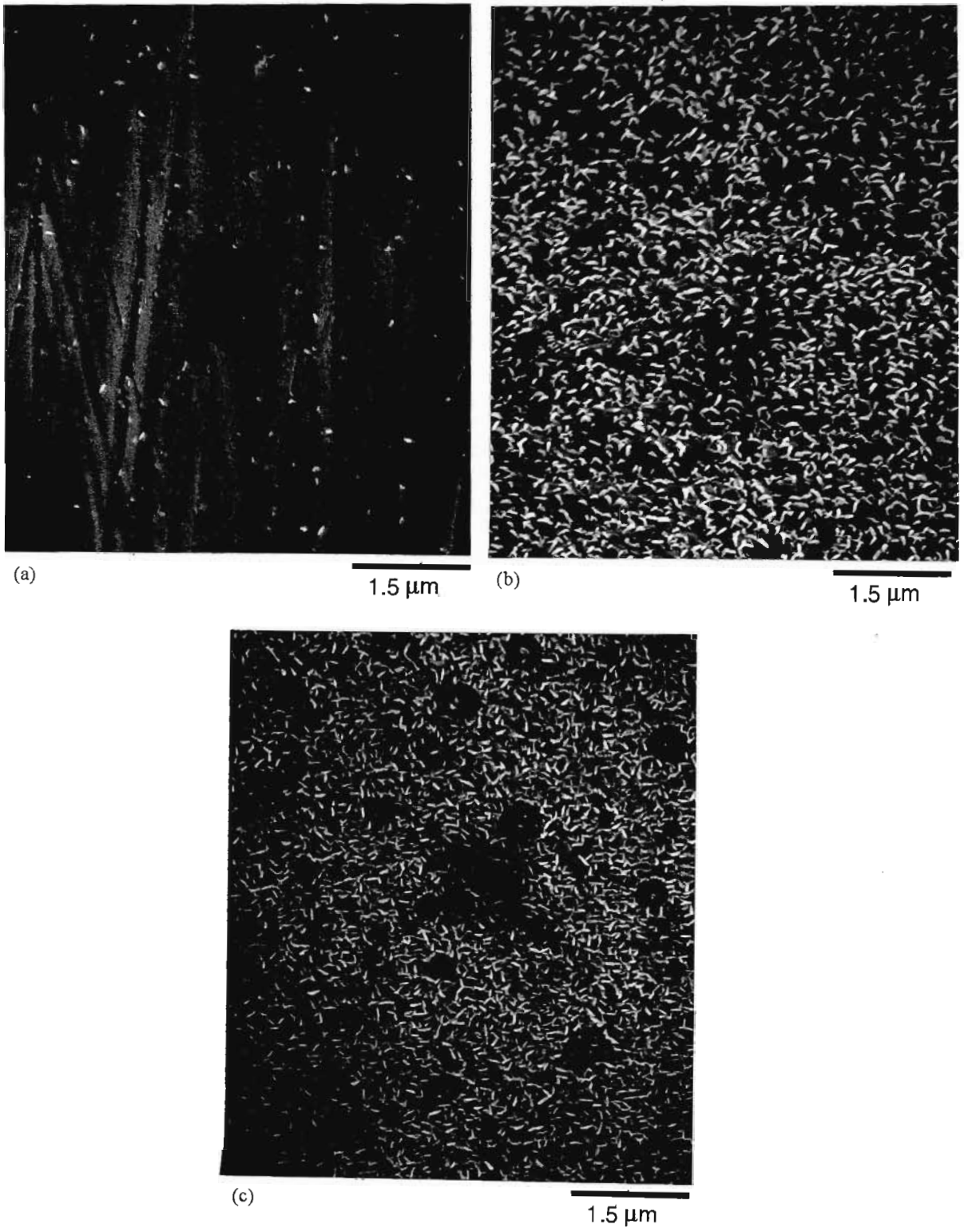


Fig. 6.3 Influence of applied potential on the number of surface film nuclei formed on a Fe electrode in 0.5M NaOH, 20°C, after a single potential step :

- (a) -1.30V \rightarrow -0.60V
- (b) -1.30V \rightarrow 0.00V
- (c) -1.30V \rightarrow 0.30V

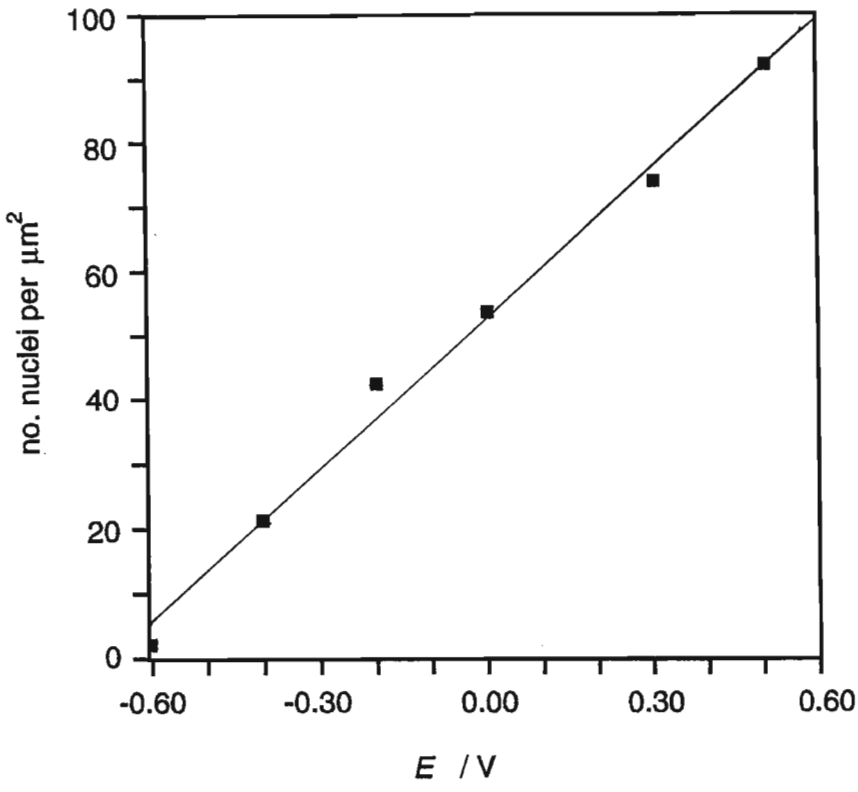


Fig. 6.4 Influence of applied potential on the number of surface film nuclei formed on a Fe electrode in 0.5M NaOH, 20 °C, as determined from SEM micrographs.

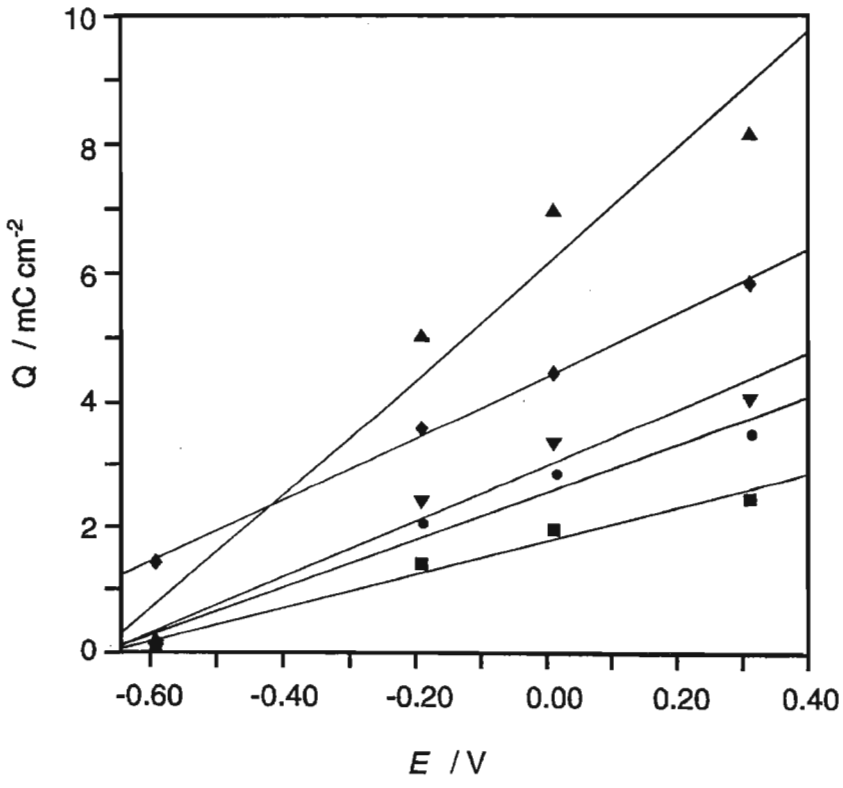


Fig. 6.5 Comparison of the charge required for the formation of the observed number of nuclei, assuming (▼) Fe(OH)₂, (▲) FeO, (■) Fe₂O₃ and (•) FeOOH as the surface film species, and the charge determined from the current transients (◆).

6.2 Fe in 0.5M NaOH + 0.4M NaCN

Rising current transients were observed for Fe in 0.5M NaOH + 0.4M NaCN, as shown by a typical set of curves in Fig. 6.6. In comparison to the transients observed in 0.5M NaOH (*cf* Fig. 6.1) those obtained in the presence of CN^- were very much better defined. For a given applied potential and temperature, t_m for the rising transients obtained in 0.5M NaOH was less than t_m obtained in the presence of CN^- and $i_{m,0.5\text{M NaOH} + 0.4\text{M NaCN}} > i_{m,0.5\text{M NaOH}}$.

Initially these results appear to be contrary to the cyclic voltammetric results which showed that the presence of CN^- inhibits oxide growth with steady state cyclic voltammograms readily being achieved. However, it must be remembered that the chronoamperograms reflect the initial stages of oxide formation whereas the cyclic voltammograms describe the subsequent growth. In CN^- containing electrolytes competitive adsorption between the OH^- and CN^- occurs with the CN^- being preferentially adsorbed on the surface such that dissolution is impeded, resulting in a decrease in the concentration of the species available for nucleation. Thus in CN^- containing electrolytes, it will take longer to reach the required conditions for stable oxide formation, as indicated by $t_{m,0.5\text{M NaOH} + 0.4\text{M NaCN}} > t_{m,0.5\text{M NaOH}}$. As a result of the increase in t_m , a longer period is therefore available for dissolution to occur, accounting for the greater i_m . However, once conditions conducive to nucleation have been achieved, nuclei will form repassivating the active sites. Some growth of the nuclei will occur but as seen from the cyclic voltammograms, the system is readily stabilised with the CN^- inhibiting further oxide growth.

At 20°C the first rising transient was observed at -0.70V. At potentials negative to this, only falling transients were observed. With increasing potential, t_m decreased and i_m increased as given by eqn. 6.1 and 6.2 (*cf* Table 6.1). This can be explained by the increased Fe dissolution that would occur with increasing potential resulting in an increase in i_m . Conditions required for nuclei formation would therefore be achieved more rapidly, as reflected by the decrease in t_m . As can be seen from Fig. 6.6(a) at all potentials the transients are almost symmetrical about i_m , which Armstrong *et al.*²²⁵ have shown to be indicative of progressive nucleation.

At potentials anodic to -0.10V a second maximum was observed at longer times. This maximum followed the same trend with respect to increasing potential as the first maximum, viz. the logarithm of t_m decreased and i_m increased linearly. The potential range in which this second maximum appeared corresponds to that in which the cyanide oxidation and reduction peaks were observed on the cyclic voltammogram. It is proposed that at the higher potentials at which CN^- oxidation occurs, the extent of the competitive adsorption between the OH^- and CN^- will decrease allowing further oxide formation — as is evidenced by the presence of a second maximum on the current transients. This proposal is supported by the fact that CN^- oxidation is favoured at higher temperatures, and it was found that with increasing temperature the second maximum became better defined and a more prominent feature of the transient. Although this phenomenon cannot be seen from the transients presented in Fig. 6.6, it is shown in Fig. 6.8, for Fe in

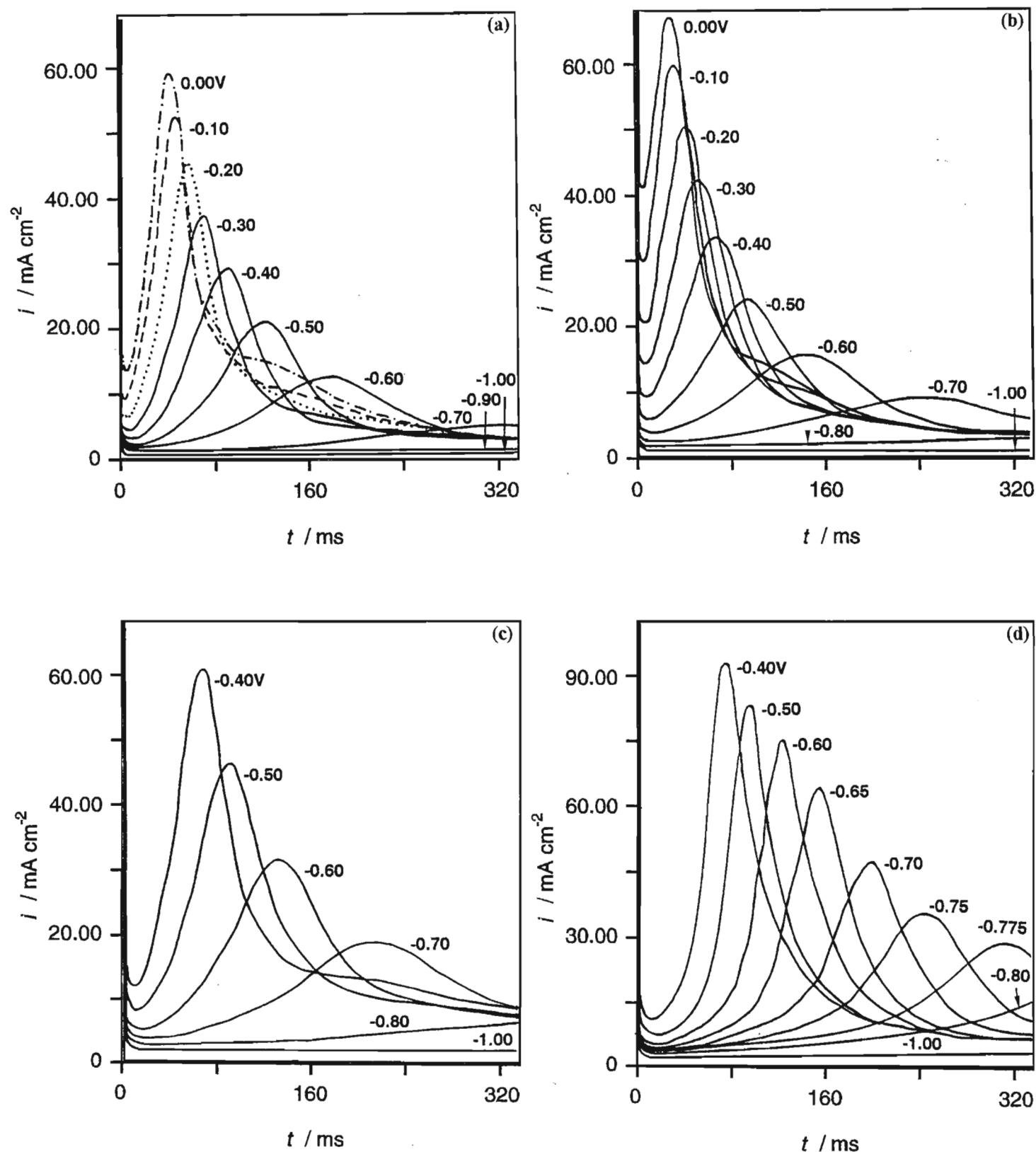


Fig. 6.6 Current transients of a Fe electrode in $0.5\text{M NaOH} + 0.4\text{M NaCN}$ stepped from -1.20V to the indicated potentials at (a) 20°C , (b) 35°C (c) 60°C (d) 80°C (e) 100°C and (f) 120°C .

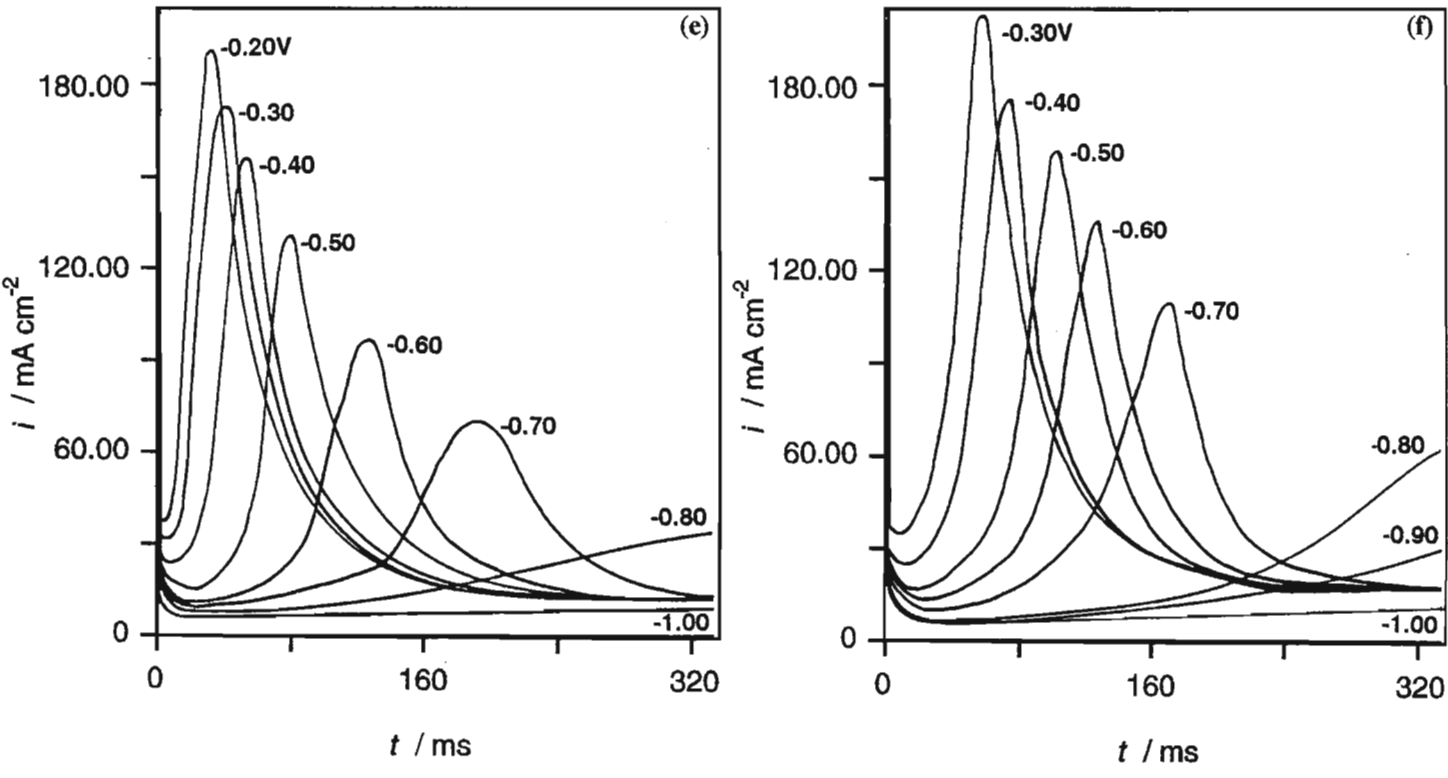


Fig. 6.6 continued

1.0M NaOH + 0.4M NaCN, and discussed in section 6.4 (the higher OH⁻ concentration results in this second maximum being more pronounced and hence the additional figures showing the effect of temperature on this maximum are included in the 1.0M NaOH + 0.4M NaCN section).

This proposal of additional oxide formation is supported by the SEM results presented in section 5.4.4, which showed that at 20°C the surface coverage of the electrode was sparse with the topography of the deposits being very different to that observed in the absence of CN⁻ (cf Fig. 5.53). At higher temperatures where CN⁻ oxidation occurs more readily and there is an increase in the amount of oxide formed resulting in a surface film that is visually similar to that formed in the absence of CN⁻ (cf Fig. 5.54).

The rising transients obtained at 35°C were qualitatively the same as those obtained at 20°C (Fig. 6.6(b)). Increasing the temperature to 60°C and through to 120°C (Fig. 6.6(c) - (f)) showed a continuation of the trend of the rising current transients becoming better defined with increasing temperature, with i_m increasing and t_m decreasing. Over the temperature range investigated, i_m varied linearly while t_m varied logarithmically with applied potential as given by eqns. 6.1 and 6.2. The coefficients for these equations, for this system, are given in Table 6.1. As was observed in 0.5M NaOH, the coefficients were also found to vary with temperature, as given by the following relationships :

$$\log a = -0.74 \times 10^{-3} T^{-1} + 1.32$$

$$\log b = -0.57 \times 10^{-3} T^{-1} + 0.88$$

$$c = -3.82 \times 10^{-3} T + 1.42$$

$$d = -5.54 \times 10^{-3} T - 1.29$$

For a given potential, in the temperature range 20°C - 120°C, it was found that i_m increased with temperature in accordance with the Arrhenius equation. The activation energies for the nucleation of the surface film, E_{a3} , are summarised in Table 6.2. The values for E_{a3} were the same order of magnitude as E_{a1} and E_{a2} , although E_{a3} was slightly lower. E_{a3} was found to vary linearly with potential, as given by the following relationship :

$$E_{a3} = -24.94E + 9.77$$

6.3 Fe in 1.0M NaOH

In the previous chapter it was shown that the cyclic voltammetric response of Fe in 0.5M NaOH and 1.0M NaOH were qualitatively similar. It is therefore not unexpected that rising current transients were also observed in 1.0M NaOH, as can be seen in Fig. 6.7. Comparison of the transients obtained in these two electrolytes showed $i_{m,1.0M NaOH} > i_{m,0.5M NaOH}$ and $t_{m,1.0M NaOH} < t_{m,0.5M NaOH}$. While this result may appear contrary to the cyclic voltammetric data where it was reported that $i_{p,A3}$ was greater in 0.5M NaOH than in 1.0M NaOH, it must again be stressed that the chronoamperograms reflect the initial stages of oxide formation whereas the cyclic voltammograms describe the subsequent growth. The greater

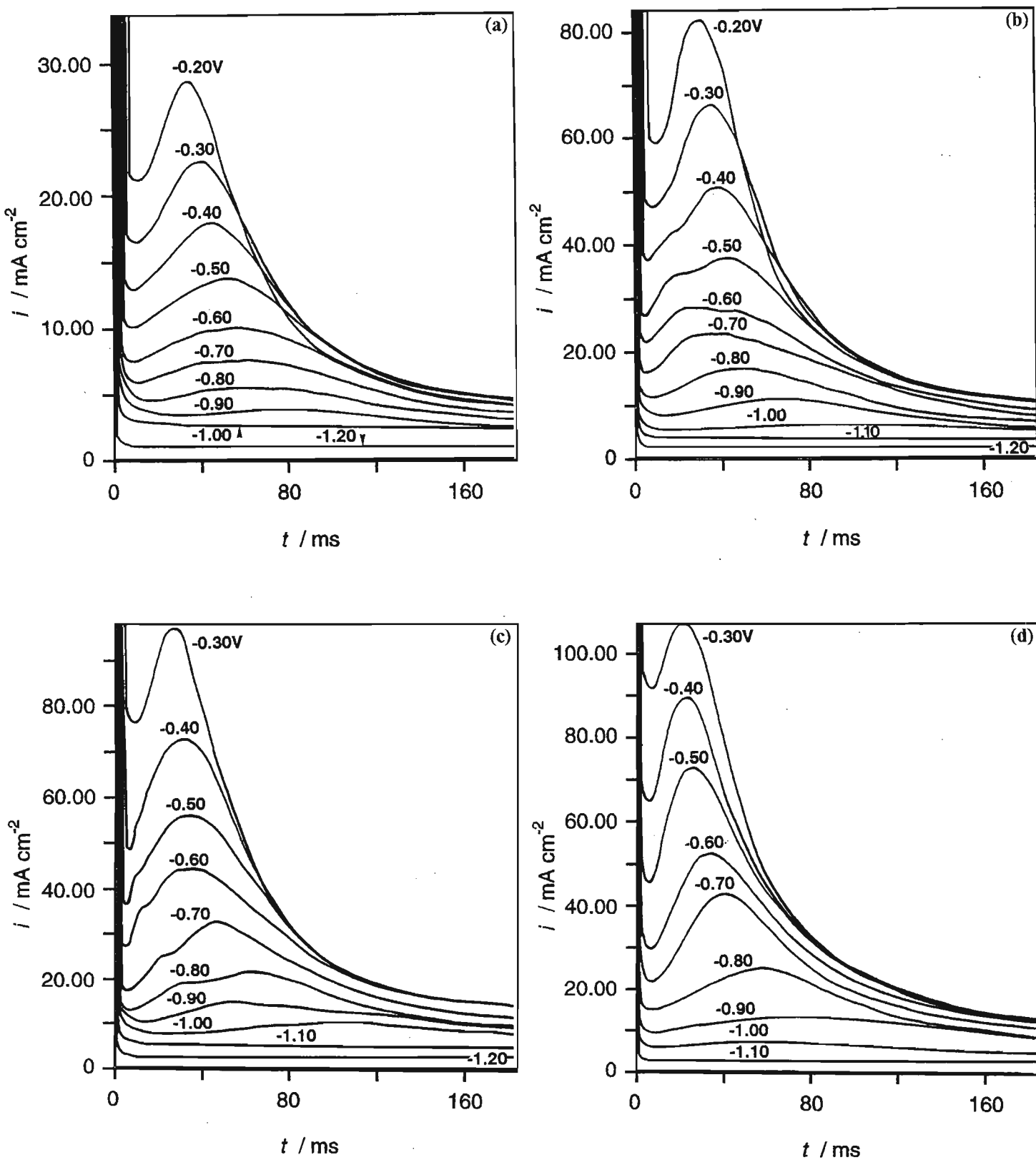


Fig. 6.7 Current transients of a Fe electrode in 1.0M NaOH stepped from -1.20V to the indicated potentials at (a) 20°C, (b) 40°C, (c) 60°C, (d) 80°C, (e) 100°C and (f) 120°C.

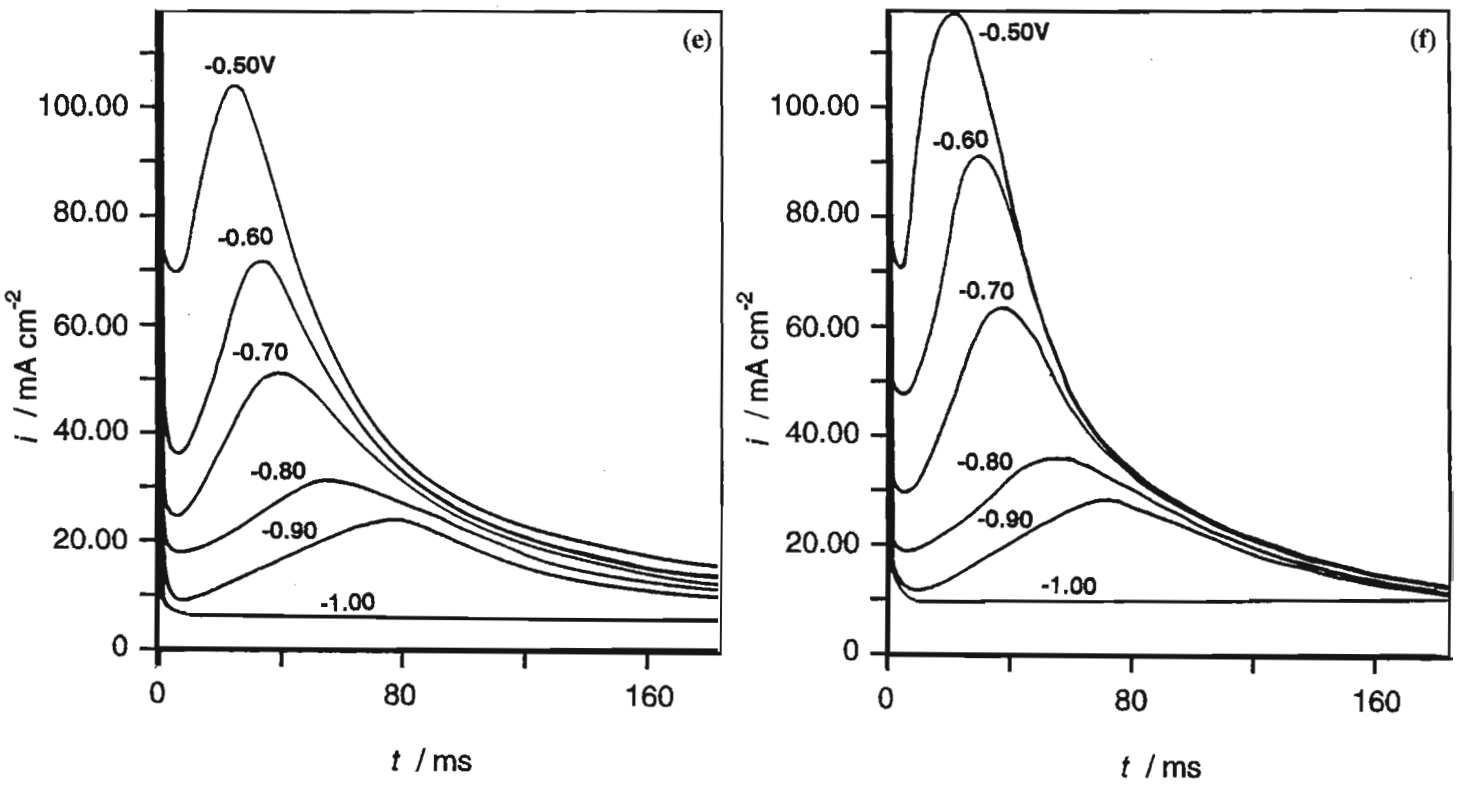


Fig. 6.7 continued

i_m obtained in 1.0M NaOH can be explained by the fact that in the more concentrated alkali greater metal dissolution of the substrate will occur, as reflected by the increase in i_m . This would result in the conditions required for stable nuclei formation to be attained more readily, as indicated by the decrease in t_m . As discussed in section 5.3, it is during the subsequent growth of the oxide that the higher hydroxide ion activity inhibited water and hydroxide ion transfer to the inner regions of the oxide layer thereby creating a more protective film.

At 20°C, the first rising transient was observed at -1.00V. Two maxima were present on these transients corresponding to the base and upper layers. The base layer maximum, distinguishable up to -0.60V, was present only as a very poorly defined shoulder to the upper layer maximum and is in fact not evident in Fig. 6.7(a) due to the scale used in the figure. As can be seen in Fig. 6.7 this first maximum becomes better defined with increasing temperature due to base layer formation becoming the dominant process at higher temperatures (as shown by the cyclic voltammetric data in the previous chapter). At $T \geq 80^\circ\text{C}$ only one maximum was present on the transients (cf Fig. 6.7(d) - (f)), as was observed in 0.5M NaOH. At all temperatures the maxima, particularly the dominant maximum of each transient, became better defined with increasing potential with an increase in i_m and a decrease in t_m as given by the following relationships :

$$\text{base layer :} \quad i_m = a + bE \quad (6.1)$$

$$\text{upper layer :} \quad \log i_m = e + fE \quad (6.3)$$

$$\text{both layers :} \quad \log t_m = c + dE \quad (6.2)$$

The values for the coefficients $a - f$ are given in Table 6.1. These coefficients were found to vary with temperature as given by the following relationships :

$$\text{base layer :} \quad \log a = -1.01 \times 10^3 T^{-1} + 2.00$$

$$\log b = -1.16 \times 10^3 T^{-1} + 2.42$$

$$c = 9.35 \times 10^{-3} T - 0.16$$

$$d = -1.03 \times 10^{-2} T - 2.21$$

$$\text{upper layer :} \quad \log e = -1.28 \times 10^2 T^{-1} - 2.24$$

$$\log f = -4.36 \times 10^1 T^{-1} - 2.78$$

$$c = -8.32 \times 10^{-3} T + 1.69$$

$$d = -8.65 \times 10^{-3} T - 0.21$$

For a given potential, it was found that t_m decreased and i_m increased with increasing temperature. The increase in i_m obeyed the Arrhenius equation and the activation energies calculated from Arrhenius plots are summarised in Table 6.2. The activation energy for base layer formation, E_{a4} , increased with increasing potential while E_{a5} , for upper layer formation, decreased as given by the following relationships :

$$\text{base layer :} \quad E_{a4} = 17.94 E + 24.715$$

$$\text{upper layer :} \quad E_{a5} = -5.041 E + 6.902$$

These activation energies, E_{a4} and E_{a5} , are lower than E_{a1} and E_{a2} obtained in 0.5M NaOH. This is due

to the fact that dissolution of the Fe substrate occurs more readily in 1.0M NaOH than in 0.5M NaOH, which in turn means that more material is available for the formation of the critical nucleus size. Also, the activation energy for upper layer nucleation is less than that for base layer nucleation, a trend which was also observed for 0.5M NaOH, and discussed in section 6.1.

6.4 Fe in 1.0M NaOH + 0.4M NaCN

Rising transients typical of those observed for Fe in 1.0M NaOH + 0.4M NaCN are shown in Fig. 6.8. At 20°C the transients exhibited a single well defined maximum over the potential range -0.75V to 0.20V. At potentials greater than 0.20V a second, less well defined maximum was observed. As can be seen in Fig. 6.8, for a given temperature the maxima became better defined with increasing potential; the logarithm of t_m decreased and i_m increased linearly for the first maximum and logarithmically for the second maximum, as given by equations 6.2, 6.1 and 6.3 respectively. The coefficients for these equations for this electrolyte are given in Table 6.1. These coefficients varied with temperature, as given by the following relationships :

1st maximum : $\log a = -5.69 \times 10^2 T^{-1} + 0.94$

$$\log b = -4.25 \times 10^2 T^{-1} + 0.57$$

$$c = -1.68 \times 10^{-2} T + 1.99$$

$$d = -6.58 \times 10^{-3} T - 0.64$$

2nd maximum : $\log e = -2.59 \times 10^2 T^{-1} - 2.02$

$$\log f = -1.99 \times 10^2 T^{-1} - 2.45$$

$$c = -0.89 \times 10^{-3} T + 2.22$$

$$d = 7.00 \times 10^{-3} T - 0.36$$

As was observed in 0.5M NaOH + 0.4M NaCN, the second maximum becomes very much more prominent with increasing temperature (cf Fig. 6.8). The potential range in which this maximum occurs corresponds to the CN^- oxidation and reduction peaks present on the cyclic voltammograms (0.45V and -0.07V, respectively). As proposed earlier, there is a decrease in the CN^- inhibition of oxide formation and growth due to increased CN^- oxidation at elevated temperatures, resulting in additional oxide formation.

For a given applied potential and temperature, $t_{m,1.0M \text{ NaOH}} < t_{m,1.0M \text{ NaOH} + 0.4M \text{ NaCN}}$ and $i_{m,1.0M \text{ NaOH} + 0.4M \text{ NaCN}} > i_{m,1.0M \text{ NaOH}}$. The same trend was also observed in 0.5M NaOH following the addition of 0.4M NaCN.

With increasing temperature the potential at which the first maximum was evident became progressively more negative, eg. -0.75V (20°C), -0.85V (60°C) and -1.05V (100°C). For a given potential, with increasing temperature the transients became better defined with t_m decreasing and i_m increasing (cf Fig. 6.8). The increase in i_m (first maximum) displayed Arrhenius behaviour, and the activation energies for the nucleation of the surface film, E_{a6} , are summarised in Table 6.2. With the exception of the values obtained at -0.80V and -0.70V, E_{a6} are lower than E_{a3} (0.5M NaOH + 0.4M NaCN). This would have

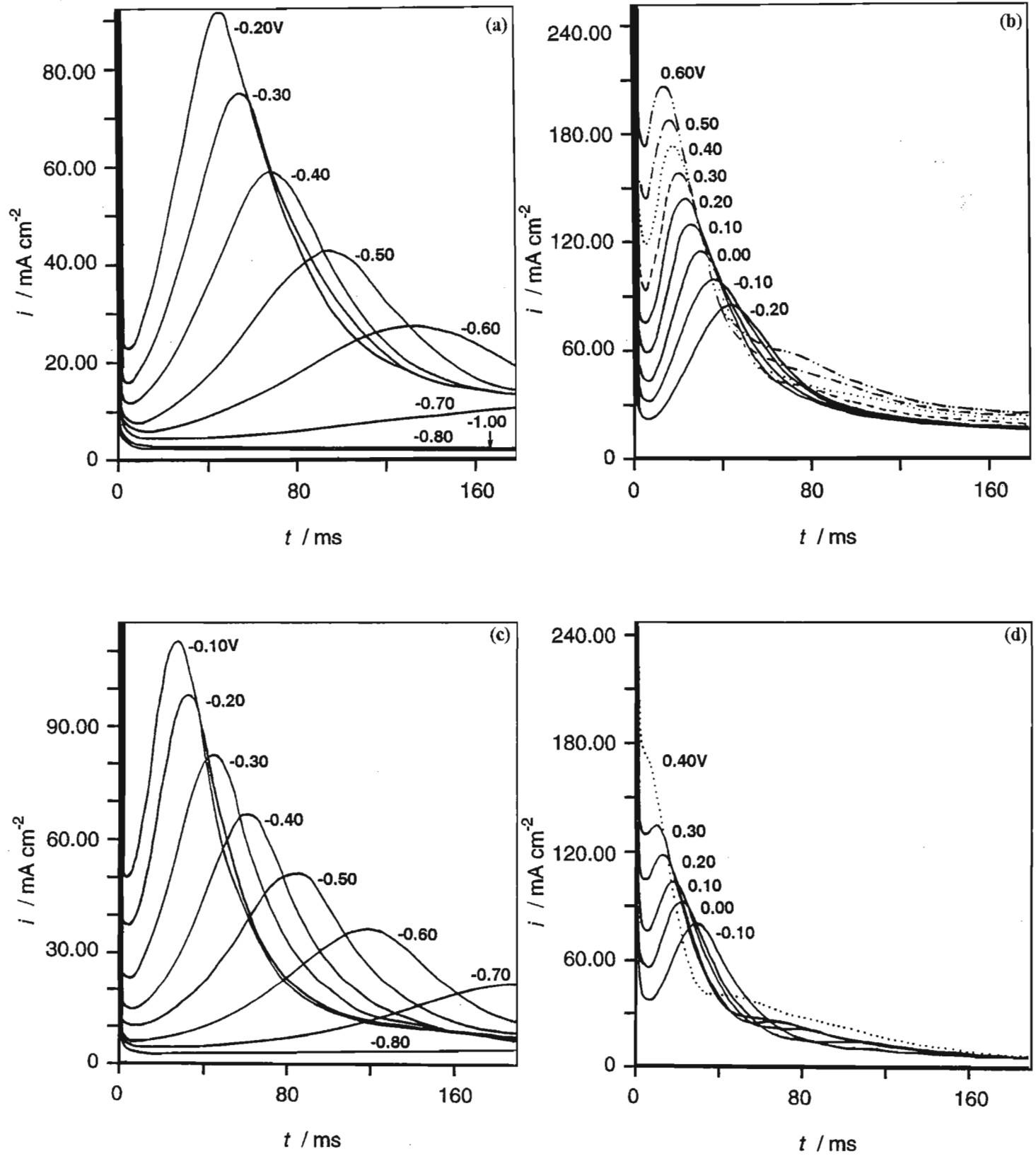


Fig. 6.8 Current transients of a Fe electrode in 1.0M NaOH + 0.4M NaCN stepped from -1.20V to the indicated potentials at (a, b) 20°C, (c, d) 35°C (e, f) 60°C, (g, h) 80°C and (i, j) 100°C.

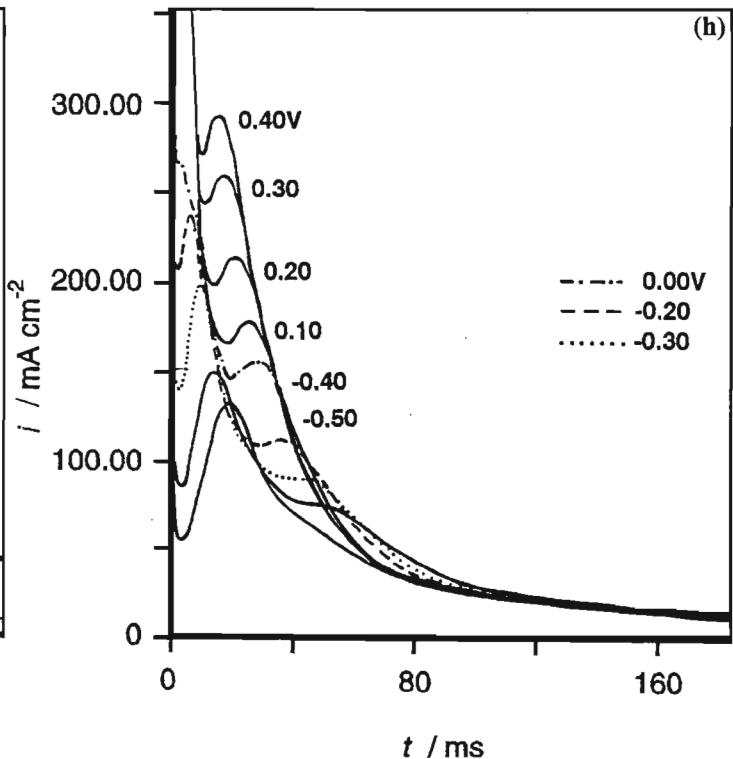
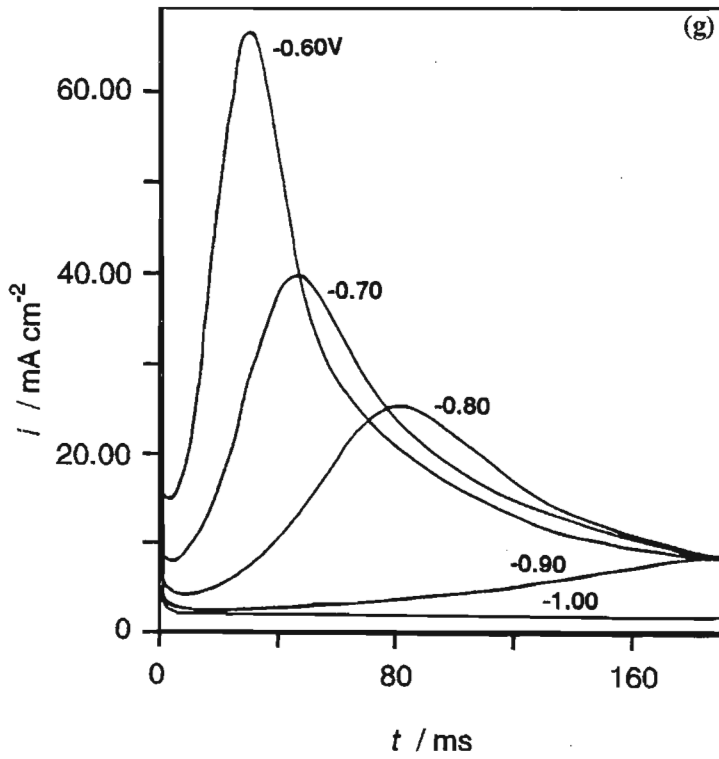
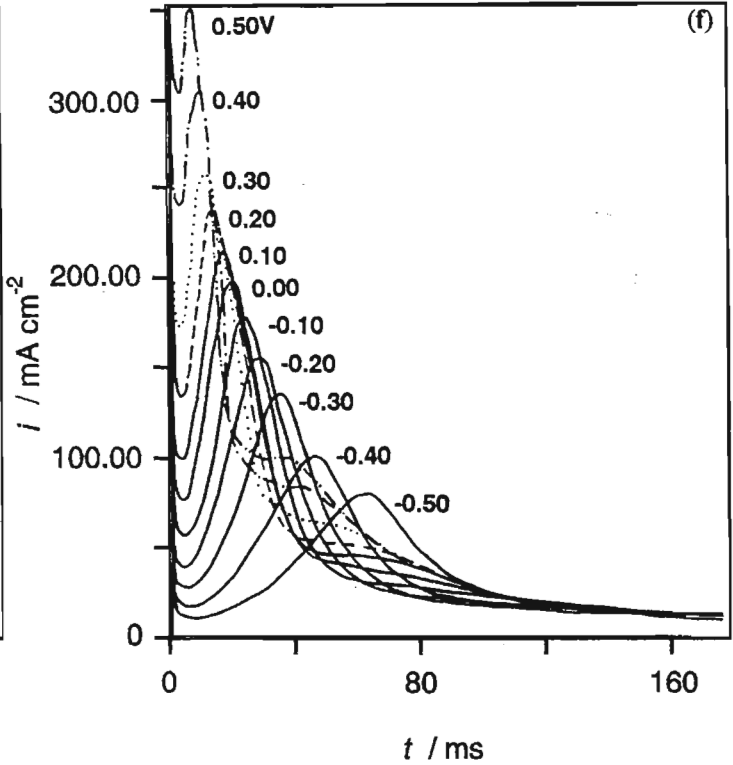
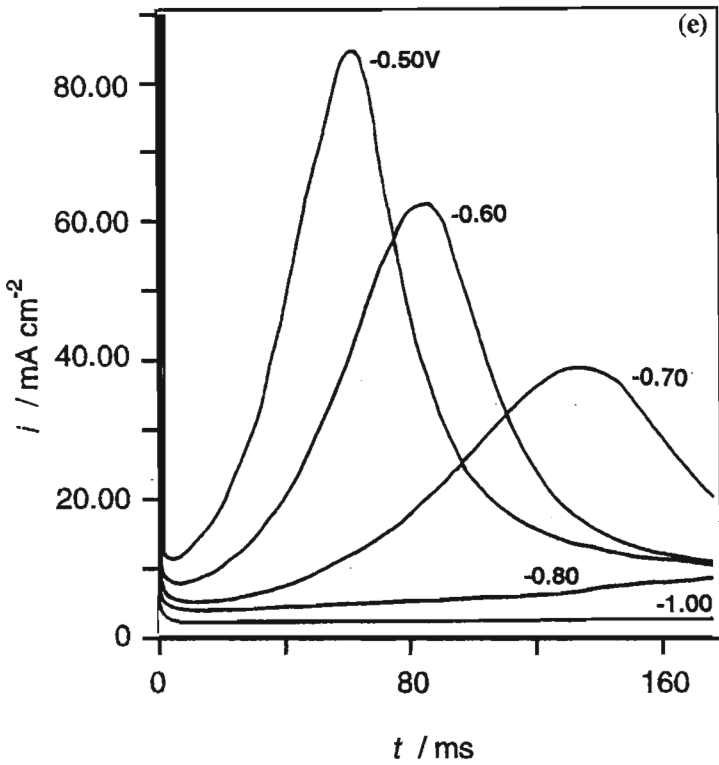


Fig. 6.8 continued

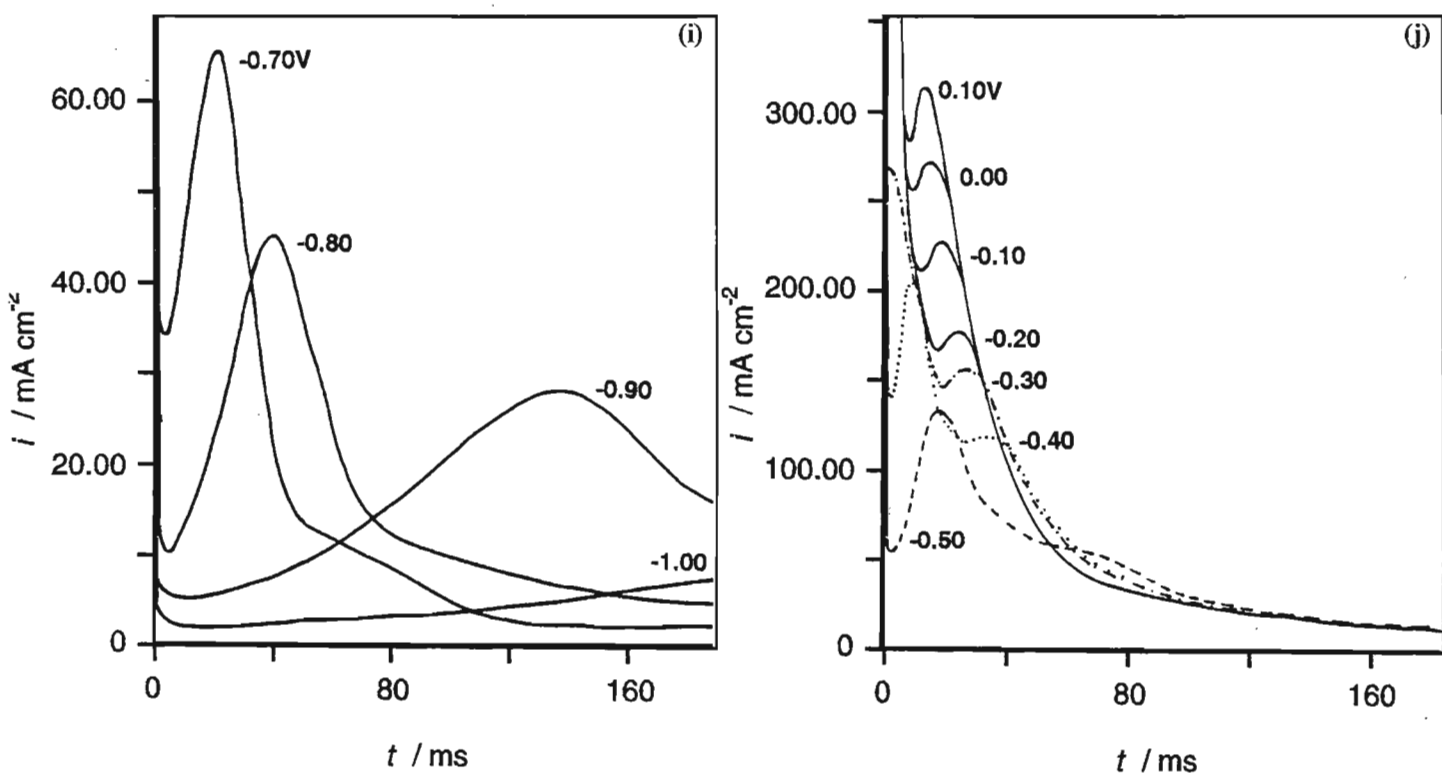


Fig. 6.8 continued

been expected as the higher hydroxide ion concentration will enable the conditions required for oxide nucleation to be achieved more readily.

6.5 ANALYSIS OF THE RISING CURRENT TRANSIENTS IN TERMS OF SURFACE FILM NUCLEATION MODELS

i vs t^n plots, pertaining to the various nucleation theories, were used for the diagnostic evaluation of the experimental data. These plots will give an indication as to the prevailing nucleation mechanism, but not unambiguously define it, for as perusal of the equations in section 2.11 show, several mechanisms yield the same plot. Good correlation between the i vs t^n plots for the various theoretical nucleation models, and the experimental data was not found. This supports the conclusions presented in chapter four for Fe, Fe18Cr and certain Fe18Cr based stainless steels in 0.1M H₂SO₄, of the inadequacy of existing nucleation mechanism and the need for their revision.

The experimental data was further evaluated by means of dimensionless i^n/i_m^n vs t/t_m plots (cf Fig. 2.16). As shown in Fig. 6.9, for Fe in 0.5M NaOH at all temperatures investigated, concave curves were obtained at $t/t_m < 1$ suggesting a progressive nucleation mechanism. At $t/t_m > 1$ there was a decrease in i/i_m for increasing potentials in the range -0.80V to -0.40V. At higher potentials a trend of increasing i/i_m with increasing potential was observed. As can be seen from Fig. 6.9(a), the experimental curves do not correspond to any of the theoretical curves. In the potential ranges $-0.80V \leq E \leq -0.60V$ and $0.00V \leq E \leq 0.20V$ the experimental curves are closest in shape and proximity to the theoretical curve corresponding to progressive nucleation and 3D growth. At potentials in the range $-0.60V < E < 0.00V$ the experimental curves lie between the theoretical curves for progressive nucleation and 3D growth and instantaneous nucleation and 2D growth. This result is supported by the SEM examination of the electrode surface (cf Fig. 6.3) which showed that while most of the nuclei are of a similar size, indicating an instantaneous mechanism, there is a definite variation in the nuclei size suggesting a progressive mechanism. Therefore it is proposed that a rapid progressive nucleation mechanism is operative. With regard to the nature of the growth of the nuclei, the 3D model is based on a hemispherical nucleus geometry, while the 2D model is based on disc shaped nucleus. Fig. 6.3 shows that the nuclei in the present study correspond to neither of these geometries, but rather to that of a flattened ellipse. This would justify the intermediate position of the experimental curve between the 2D and 3D theoretical curves in Fig. 6.9(a). However, evidence precluding the 2D model is that for both base and upper layer nucleation and growth the product $i_m t_m$ varies as a function of potential, which has been shown to be indicative of a 3D process.^{233,243}

Fig. 6.9(b) shows the effect of temperature on the dimensionless plots of transients obtained at a given potential. For all potentials in the range -0.80V to 0.20V, i/i_m decreased with increasing temperature. From the discussion above, it is proposed that at ambient temperatures a progressive nucleation mechanism followed by 3D growth prevails which, at elevated temperatures changes to a progressive nucleation

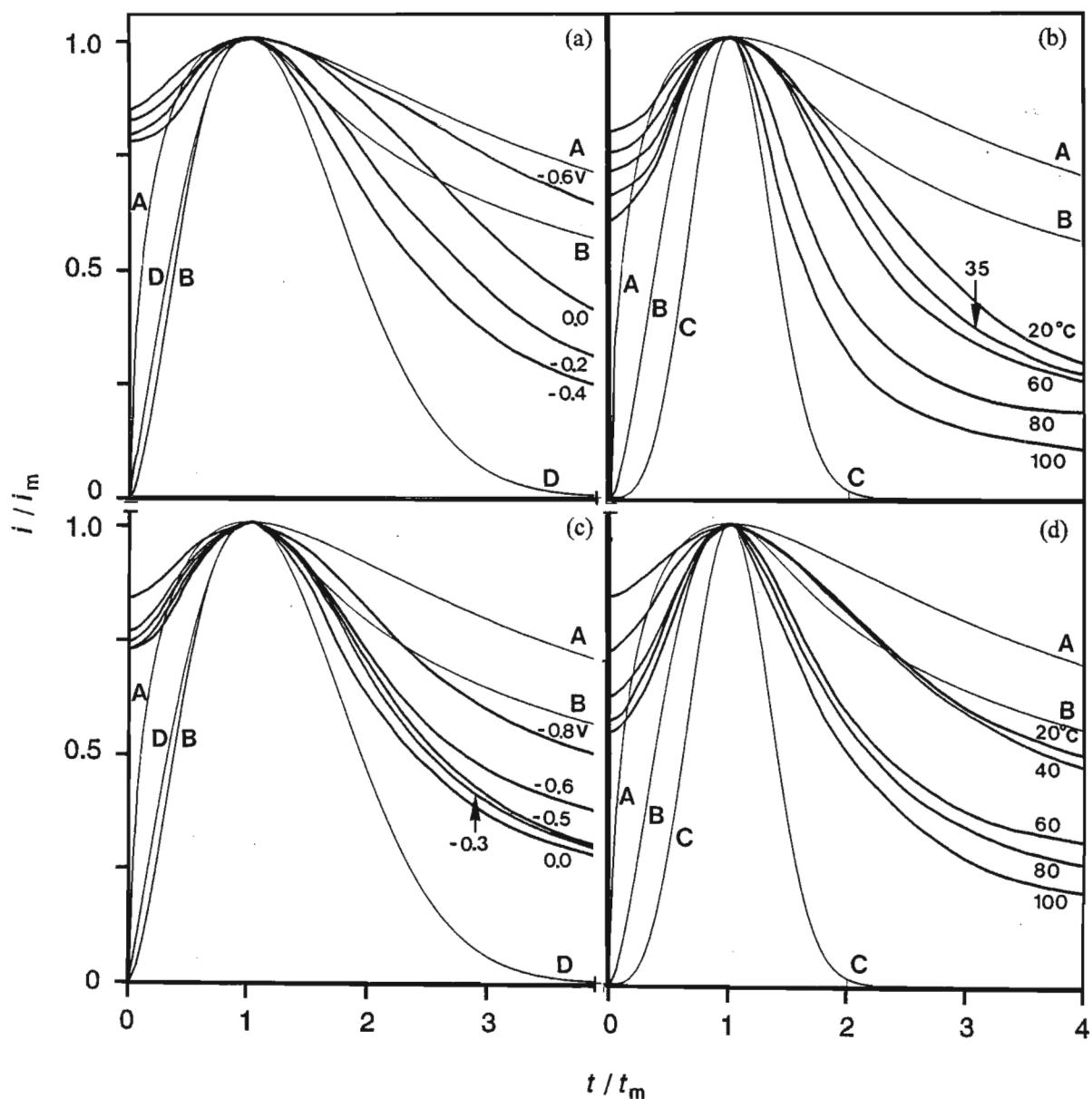


Fig. 6.9 Dimensionless plot of the current transients for Fe in
 (a) 0.5M NaOH, 20°C, at the indicated potentials.
 (b) 0.5M NaOH at the indicated temperatures, for the -0.20V transient.
 (c) 1.0M NaOH, 20°C, at the indicated potentials.
 (d) 1.0M NaOH at the indicated temperatures, for the -0.80V transient.
 Theoretical nucleation curves correspond to (A) instantaneous nucleation and 3D growth, (B) progressive nucleation and 3D growth, (C) progressive nucleation and 3D growth leading to passivation and (D) instantaneous nucleation and 2D growth.

mechanism followed by 3D growth leading to passivation (theoretical curve (C) in Fig. 6.9). This proposal supports the cyclic voltammetric results presented in chapter five, which showed the attainment of steady state conditions occurred more readily at elevated temperatures.

The dimensionless plots of the transients obtained in 1.0M NaOH showed the same trends as those described above for 0.5M NaOH. Comparison of Figs. 6.9(a) and (c) does however show that in 1.0M NaOH i/i_m is less dependent on potential for $-0.60V \leq E \leq 0.00V$. This could be attributed to the greater stability of the surface film in 1.0M NaOH. Fig. 6.9(d) shows the same trend observed in 0.5M NaOH, of a decrease in i/i_m with increasing temperature, for a given potential.

A difficulty encountered in the analysis of the experimental data was the presence of two maxima on the transients. These maxima were generally close together such that deconvolution of the transient was required before they could be analysed. This however provided an additional problem in that the shape of the transient pertaining to a particular maximum was not known. While obviously the shape could be estimated, this would merely reduce the process to a curve fitting exercise. As a result of this, together with the inadequacy of the current nucleation mechanisms, a rigorous evaluation of the transients was not attempted.

Typical dimensionless plots of the transients obtained in the presence of 0.4M NaCN are shown in Fig. 6.10. For both electrolytes there was an increase in i/i_m with increasing potential, for a given temperature. The shape of the curves, particularly those obtained in 1.0M NaOH + 0.4M NaCN show good correlation with the progressive nucleation and 3D growth leading to passivation at the more negative potentials but with increasing potential gradually approached the theoretical curve for progressive nucleation and 3D growth. These results can be explained by the fact that at the more positive potentials CN^- inhibition is not as effective, thereby decreasing the overall passivity of the system and resulting in additional film formation occurring at these potentials. The proposal of a progressive nucleation mechanism is supported by SEM results which showed growth centres of differing size. In addition, the symmetry of the transients about i_m has been shown²²⁵ to be indicative of progressive nucleation.

The effect of temperature on the rate of decay of the i/i_m curve at $t/t_m > 1$ is shown in Figs. 6.10(b) and (c). For transients obtained in 0.5M NaOH + 0.4M NaCN, there was a decrease in i/i_m with increasing temperature while for 1.0M NaOH + 0.4M NaCN i/i_m increased with increasing temperature. These same trends have also been observed for Fe18Cr alloy in 0.5M NaOH + 0.4M NaCN and 1.0M NaOH + 0.4M NaCN.⁵⁰ Chronoamperometric and cyclic voltammetric data presented in this thesis have shown the addition of 0.4M NaCN to 0.5M NaOH to have a greater inhibiting effect on the nucleation and growth of the surface film, than when added to 1.0M NaOH. Thus in 0.5M NaOH + 0.4M NaCN less Fe substrate dissolution occurs, as reflected by $i_{m,0.5M NaOH + 0.4M NaCN} < i_{m,1.0M NaOH + 0.4M NaCN}$. With increasing temperature, the inhibiting effect of CN^- decreases with the result that more material is available for

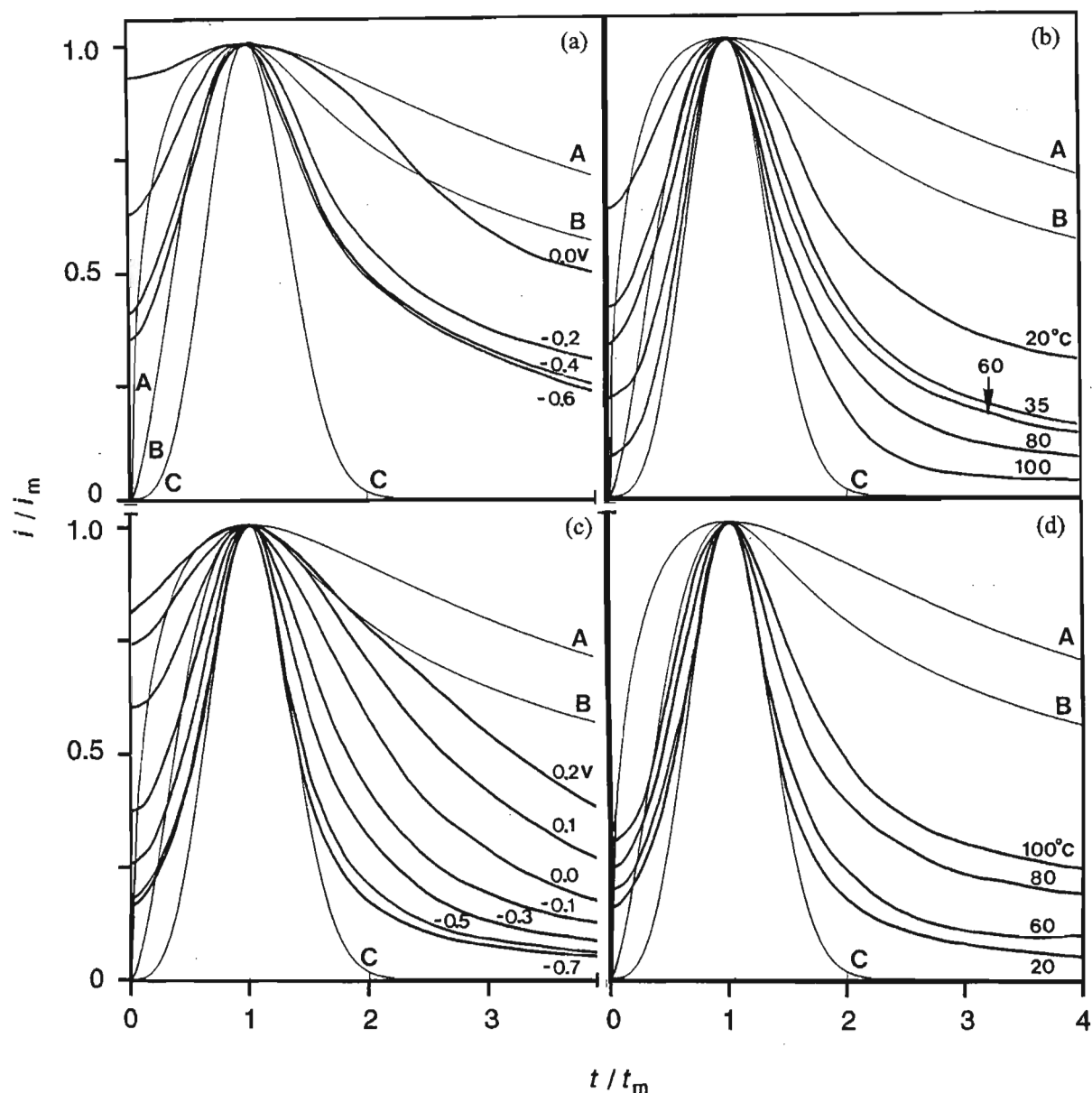


Fig. 6.10 Dimensionless plot of the current transients for Fe in
 (a) 0.5M NaOH + 0.4M NaCN, 20°C, at the indicated potentials.
 (b) 0.5M NaOH + 0.4M NaCN at the indicated temperatures, for the -0.20V transient.
 (c) 1.0M NaOH + 0.4M NaCN, 20°C, at the indicated potentials.
 (d) 1.0M NaOH + 0.4M NaCN at the indicated temperatures, for the -0.60V transient.
 Theoretical nucleation curves correspond to (A) instantaneous nucleation and 3D growth, (B) progressive nucleation and 3D growth and (C) progressive nucleation and 3D growth leading to passivation.

nucleation (as reflected by an increase in i_m) and hence conditions conducive to nucleation will be achieved more rapidly (as indicated by the decrease in t_m) resulting in the rapid passivation of active sites. Therefore it is proposed that with increasing temperature the nucleation mechanism will change from progressive nucleation and 3D growth to that of progressive nucleation followed by 3D growth leading to passivation. This trend is indeed reflected in Fig. 6.10(b) with a decrease in i/i_m with increasing temperature.

For a given potential, in 1.0M NaOH + 0.4M NaCN, i_m is greater and t_m less than that obtained in 0.5M NaOH + 0.4M NaCN. This is as a result of the higher hydroxide ion concentration reducing the inhibiting effect of CN^- , thereby enabling conditions conducive to nucleation to be attained more rapidly. At higher temperatures CN^- inhibition is not as effective due to CN^- oxidation, with the result that additional surface film formation can occur at the higher temperatures. This would result in the change in mechanism from progressive nucleation and 3D growth leading to passivation at ambient temperatures to progressive nucleation and 3D growth at elevated temperatures.

While it is evident that the equations describing the theoretical curves require modification to completely describe the rising current transients presented in this investigation, it should be noted that the present fit is as good as, and in some cases better than, those presented in the literature.^{225,246,344} Gomez Becerra³⁹² investigating oxide formation on Cu in 0.1M NaOH obtained excellent correlation of their experimental data to the theoretical transients for 2D growth under charge transfer control. This was done with the aid of adjustment parameters — the origins or physical meaning of which were not discussed! However, as discussed in chapter four and section 2.11 a realistic quantitative model is not possible at present due to limitations imposed by the mathematics.

6.5.1 Nucleation Model

Existing nucleation models propose that at the maximum of the current transients the nuclei density of the surface film is such that the electrode surface is completely covered, resulting in a subsequent current decay typical of linear diffusion to an effectively planar electrode surface. However, it was shown in chapter four that this was not the case for Fe and Fe18Cr type stainless steels in acidic electrolytes, with no significant overlap of neighbouring nuclei being observed. This led to the proposal of active sites at which the electrode corrodes preferentially or at an accelerated rate and which are analogous to the nucleation sites reported in electrocrystallisation studies. From the results presented in this chapter it is evident that the same situation applies to Fe in alkaline and alkaline cyanide electrolytes. Imposing a potential step, to an appropriate potential, results in dissolution predominantly at these active sites. This results in localised surface roughening and an increase in the electrode surface area with a corresponding increase in the current — as is observed subsequent to the decay of the double layer charging current. The current will continue to increase until conditions at the surface are such that the critical energy for the formation of stable nuclei has been achieved and nucleation of the surface film can take place. As SEM

examination of the electrode surface has shown that complete coverage of the surface by the growing nuclei had not occurred after a single potential step experiment, it is again proposed that nucleation occurs at the active sites. By repassivating these sites the *active* surface area will be reduced resulting in a decrease in the current — which is manifested by the appearance of the maximum i_m of the transient. Once these sites have been passivated, further growth of the surface film on these sites will continue for as long as the required concentration of dissolved species is maintained. Such continued growth will further reduce the active surface area as manifested by the decrease in the current at $t > t_m$. Dissolution of the substrate through the growing nuclei together with dissolution of the uncovered surface will result in localised conditions being conducive to upper layer formation.

This scheme would explain the chronoamperometric results obtained as a function of temperature. As the temperature is increased the rate of dissolution of the alloy will also increase, resulting in an increase in i_m , and thus the required concentration of dissolved species can be achieved more rapidly as indicated by a decrease in t_m .

The above scheme further predicts that as the electrode is stepped to more anodic potentials the required concentration of dissolved species at the electrode surface will occur more readily, due to the enhanced dissolution of the alloy. This will result in an increase in i_m and a decrease in t_m . This was indeed observed experimentally (cf Figs. 6.1 and 6.6). As existing nucleation theories^{225,241,246,343} do not take into account dissolution of the substrate or of the depositing film, the dissolution component could be partly responsible for the differences between experimental and theoretical i/i_m vs t/t_m curves, at $t/t_m < 1$. It would certainly account for the experimental data not starting at the origin of these plots, for although the presence of active sites allows localised dissolution to commence immediately on application of an anodic potential there will be a time delay for the required concentration of dissolved species to be attained. Any revised theory describing these rising transients requires a term that considers the dissolution of the substrate metal as well as a term accounting for base layer dissolution at $t/t_m > 1$. These terms clearly would be complex since the composition of the substrate needs to be considered. In addition, potential and temperature dependent terms must be incorporated, since existing models describing the relatively simple deposition of metals onto effectively unreactive substrates do not completely fit the facts.^{234,256,259}

In this and the previous chapter, it was proposed that CN^- is preferentially adsorbed on the electrode surface. Deutscher and Fletcher²⁷³ predicted that if adsorption is induced preferentially at the electrode / electrolyte interface only, then the specific energy at that point would decrease resulting in a decrease in the nucleation potency (cf section 2.11.2) of the active site, which will in turn result in a decrease in the nucleation rate. Based on the scheme proposed above it would be predicted that if the nucleation rate decreased, t_m and i_m would increase correspondingly (since i_m is due to the repassivation of active sites). These predictions are borne out by the current transients presented in this chapter, with i_m and t_m being greater in 0.5M NaOH + 0.4M NaCN and 1.0M NaOH + 0.4M NaCN than in 0.5M NaOH and 1.0M

NaOH, respectively. This is further supported by the fact that for given experimental conditions the electrode coverage by growth centres is very much less for the CN^- containing electrolytes.

6.6 PRESENCE OF AN INITIAL FILM ON THE ELECTRODE SURFACE

As discussed in section 2.12 the presence of an initial, and unintentional film on the electrode has to be considered and if necessary, incorporated into the nucleation mechanism. The degree of coverage of the electrode by a prefilm together with, for example, inhomogeneities, stability, thickness and electrochemical properties of the film will influence the number and activity of the active sites and hence the nucleation process.

No surface analytical techniques were available in this study that would enable the determination of the presence or absence of a prefilm. However, Haupt and Strehblow³⁴ in a carefully controlled experiment using XPS reported that if no initial oxide / hydroxide film was present on the surface of a Fe electrode then peaks A3 and C2 were absent from the first sweep of the cyclic voltammogram. In the present study this was indeed found to be the case (*cf* Fig. 5.2).

This conclusion is supported by the results of Alonso *et al.*²⁵³ investigating oxide film formation on Ag. Using chronoamperometric techniques, they proposed that the growth of the initial oxide was formed by the diffusion of Ag(I) ions through a primary oxide layer. As a consequence of this the current remained independent of both electrolyte stirring and hydroxide ion concentration. In the present study it was found that i_m was dependent on both the concentration of the electrolyte and rotation rate of the electrode. These results indicate either the absence of a prefilm or that if such a film is present, that it is rapidly oxidised at the commencement of a chronoamperometric experiment such as to have no detectable effect on the nucleation process.

6.7 SUMMARY

The formation of the surface film on Fe in 0.5M and 1.0M NaOH before and after the addition of 0.4M NaCN resulted in the appearance of rising chronoamperometric transients indicating a nucleation and growth mechanism. This was verified by SEM examination of the electrode surface which showed the presence of discrete growth centres. It was proposed that in the absence of CN^- and in 0.5M NaOH + 0.4M NaCN film formation occurred via a progressive nucleation mechanism followed by 3D growth at ambient temperatures which changes to progressive nucleation and 3D growth leading to passivation at elevated temperatures. In 1.0M NaOH + 0.4M NaCN progressive nucleation followed by 3D growth leading to passivation holds at ambient temperatures but changes to progressive nucleation and 3D growth at elevated temperatures.

Existing electrocrystallisation models, presented in section 2.11 were found to be inadequate in quantitatively describing the nucleation and growth of the surface film on Fe in alkaline and alkaline cyanide electrolytes. While a qualitative model was proposed to describe the process a realistic quantitative model was not attempted since work in this regard in the present study, together with evaluation of those models presented in the literature, have shown that the complexity of the mathematics for a realistic model is such as to necessitate the introduction of unrealistic assumption into the model.

CHAPTER SEVEN

RESULTS and DISCUSSION

XPS Investigation of Surface Films Formed on Fe in Alkaline Electrolytes

In the present study, a limited XPS investigation was undertaken to determine the composition of the surface film on Fe in 0.5M NaOH and 0.5M NaOH + 0.4M NaCN at ambient and elevated temperatures.

7.1 STANDARDS

Since information regarding the chemical state of an element is obtained from variations in binding energies, or chemical shifts of the photoelectron lines, the identification of chemical states is dependent on the accurate determination of these line energies. While many attempts have been made to calculate chemical shifts and absolute binding energies, the factors involved, especially in the solid state, are not entirely understood hence the necessity for experimental data to be obtained from standards.

The standards used were FeO, Fe₂O₃, FeOOH, Fe₃O₄, as perusal of the literature showed these were the most likely species to be present in the surface film. Two sets of data were recorded for each of the standards — one set on the as - received standard and a second, onto which a 0.5 - 1nm gold coating had been sputtered. The latter data were used to obtain static charge - corrected binding energies by means of the calibrated energy of 84.0eV for the Au 4f_{7/2} peak. Such charging corrections varied between 2.5 and 3.4eV. These corrections were within 0.1eV of that obtained using the adventitious hydrocarbon C_{1s} at 285.0eV. Therefore on the electrochemically prepared electrodes, charge referencing was done using the adventitious hydrocarbon peak.

Table 7.1 summarizes the binding energies reported in the literature together with those obtained for the standards analysed, the later being used in the subsequent deconvolution of the XPS spectra of the electrochemically prepared electrodes.

Several XPS studies of iron oxides have been reported in the literature.^{120,130,191,393-395} The Fe_{2p} photoelectron spectra of ferric and ferrous oxides are particularly complex, because of the extensive coupling between the core - hole created by photo - emission and the high spin state of iron. However, as

Table 7.1

**Summary of XPS binding energies (BE)
for certain iron species**

Species	line	literature [*] BE/eV	experimental BE/eV
Fe(0)	2p _{3/2}	706.83	706.75
FeO		709.60	709.60
Fe ₂ O ₃		710.94	711.95
FeOOH		711.44	711.20
Fe ₃ O ₄		710.36	
FeCr ₂ O ₄		710.8	
Fe ²⁺		708.77	
Fe ³⁺		710.9	
Fe ⁶⁺		714	

* summary of values presented in Appendix A

spectral line shape is very sensitive to chemical changes, this was also taken into consideration when analysing the spectra.

7.2 GROWTH OF SURFACE FILM IN 0.5M NaOH, 20°C

Cyclic voltammetric data together with subsequent SEM examination of the electrode surface have shown that the surface film on Fe electrodes in 0.5M NaOH at 20°C consisted of two layers, viz. a base layer, adjacent to the metal substrate, onto which an upper layer nucleates and grows. In chapter five it was shown that with continuous applied potential cycling, continued growth of the upper layer occurred. For this XPS investigation three Fe electrodes (numbers 1, 2 and 3, respectively) were prepared by cycling the applied potential between -1.40V and 0.50V at 100mV s⁻¹ such that the base (7 cycles) and upper (50 and 120 cycles) layers were formed (*cf* Table 7.2).

Narrow scan Fe_{2p}, C_{1s} and O_{1s} spectra were recorded for all the electrochemically prepared electrodes. The Fe_{2p} regions included both the 3/2 and 1/2 doublet peaks, however since sensitivity factors were available for the stronger 3/2 peak, peak fittings were only performed on this peak.

A summary of the XPS analyses (reported as atomic percent) is presented in Table 7.3 which shows that with increasing cycling (7 → 50 → 120 cycles) there was a decrease in the Fe₂O₃ (40.5% → 26.5% → 7.4%) and a net increase in the FeOOH (42.0% → 40.1% → 79.1%). Elemental Fe was only detected on electrode 1. These results are in agreement with the cyclic voltammetry and SEM results which have both shown the buildup of the surface film as a function of the number of cycles, starting with a relatively compact base layer onto which an upper layer nucleates and grows, and which becomes increasingly amorphous with continued cycling.

After Ar sputtering, elemental Fe was only detected for electrode 1 (5.6%). This result was as expected since electrodes 2 and 3 would have had a thicker oxide layer present initially and as 40s Ar sputtering is insufficient to remove all of this layer, no elemental Fe was detected for these electrodes. While the percentage of Fe₂O₃ remained virtually constant (36.6% → 36.5% → 37.9%), with respect to the number of sweeps, FeO varied by approximately 5% (50.1% → 45.7% → 55.5%), although no trend with respect to the number of sweeps was evident. FeOOH was only detected for electrode 2; this result was unexpected since it would have been expected to be present on electrode 3, which had the thickest oxide and had the highest percentage FeOOH in the as - received analysis. Results obtained after Ar sputtering of Fe oxides should however always be evaluated with caution since artifacts, as a result of the sputtering, have been reported in the literature.^{35,120,130}

The detection of Fe₃O₄ in surface films by XPS is frequently questioned, due to its structural similarity to γ-Fe₂O₃. Asami and Hashimoto¹⁹² reported that the 2p spectra of α-Fe₂O₃, α-FeOOH, γ-Fe₂O₃ and γ-

Table 7.2

**Experimental parameters for electrode preparation
for XPS analysis**

electrode no.	electrolyte	T /°C	potential limits ^a	no. sweeps
1	0.5M NaOH	20	-1.40 → 0.50	7
2	0.5M NaOH	20	-1.40 → 0.50	50
3	0.5M NaOH	20	-1.40 → 0.50	120
4	0.5M NaOH	80	-1.40 → 0.50	7
5	0.5M NaOH	80	-1.40 → 0.50	50
6	0.5M NaOH + 0.4M NaCN	20	-1.35 → 0.60	50
7	0.5M NaOH + 0.4M NaCN	80	-1.35 → 0.60	50

^a The electrodes were prepared by cycling between the stated potentials at 100mV s⁻¹ for the given number of sweeps.

Table 7.3

Relative atomic percentages of the species detected in the surface film on Fe electrodes (a) before Ar sputtering and (b) after 40s Ar sputtering.

	electrode	Fe	FeO	FeOOH	Fe ₂ O ₃
(a)	1	1.7	6.3	42.0	40.5
	2	0.0	26.4	40.1	26.5
	3	0.0	13.5	79.1	7.4
	4	13.8	32.2	19.7	21.2
	5	4.6	44.2	0.0	47.8
	6	16.2	38.1	0.0	41.6
	7	10.5	35.1	11.5	36.1
(b)	1	5.6	50.7	0.0	36.6
	2	0.0	45.7	9.0	36.5
	3	0.0	55.5	0.0	37.9
	4	28.6	41.2	7.9	20.5
	5	10.6	57.8	0.0	27.8
	6	56.8	31.8	0.0	11.4
	7	39.3	44.4	0.0	12.6

FeOOH were virtually identical but different to that of Fe_3O_4 . They found that the former four spectra have a small broad peak between the Fe $2p_{3/2}$ and Fe $2p_{1/2}$ peaks due to satellite splitting of the Fe $2p_{3/2}$ level. For Fe_3O_4 no such satellite peak was observable. This satellite peak was present on all spectra recorded in the present study. While this cannot conclusively eliminate the presence of Fe_3O_4 it does show that under the conditions of preparation, the surface film never consisted primarily of Fe_3O_4 . Including Fe_3O_4 in the deconvolution, good agreement between the deconvoluted species peaks and the recorded spectrum was not obtained. On these grounds therefore, it was concluded that Fe_3O_4 was not present in the surface films.

From these results it is proposed that a three component surface film is formed on Fe in 0.5M NaOH consisting of a FeO base layer and an upper layer of Fe_2O_3 and FeOOH. As shown in Fig. 7.1(a) - (c), the ratio of the oxides within the surface film was dependent on the extent of cycling.

7.3 INFLUENCE OF TEMPERATURE ON SURFACE FILM GROWTH

Cyclic voltammetric and chronoamperometric data have shown that over the temperature range 20°C to 120°C base layer formation becomes the dominant process with increasing temperature. Electrodes 4 and 5 were prepared with the identical electrochemical pretreatment used for electrodes 1 and 2, respectively, with the exception that the temperature was increased to 80°C (cf Table 7.2). XPS data for these electrodes is given in Table 7.3.

Comparing the XPS results of electrode 1 with those of electrode 4 shows that increasing the temperature from 20°C to 80°C resulted in an increase in Fe (1.7% \rightarrow 13.8%) and FeO (6.3% \rightarrow 32.3%) and a decrease in Fe_2O_3 (40.5% \rightarrow 21.2%) and FeOOH (42.0% \rightarrow 19.7%). This suggests a decrease in the upper layer and an increase in the base layer thickness, with a probable decrease in the overall thickness of the surface film as indicated by the increase in the percentage elemental Fe detected. These XPS results are in agreement with the electrochemical data.

The XPS results obtained for electrodes 1 and 4 after Ar sputtering showed a decrease in FeO (50.7% \rightarrow 41.2%) and Fe_2O_3 (36.6% \rightarrow 20.5%) and an increase in elemental Fe (5.6% \rightarrow 28.6%). While no FeOOH was detected at 20°C , 7.9% was detected at 80°C . The small decrease in FeO, with increasing temperature was unexpected since the electrochemical data has shown base layer formation to predominate at higher temperatures. However, due to the thinner upper layer that forms at the higher temperatures, it is feasible that some of the base layer was also removed in the sputtering process.

The above XPS data suggests that the surface film retains its structure as the temperature is increased from 20°C to 80°C .

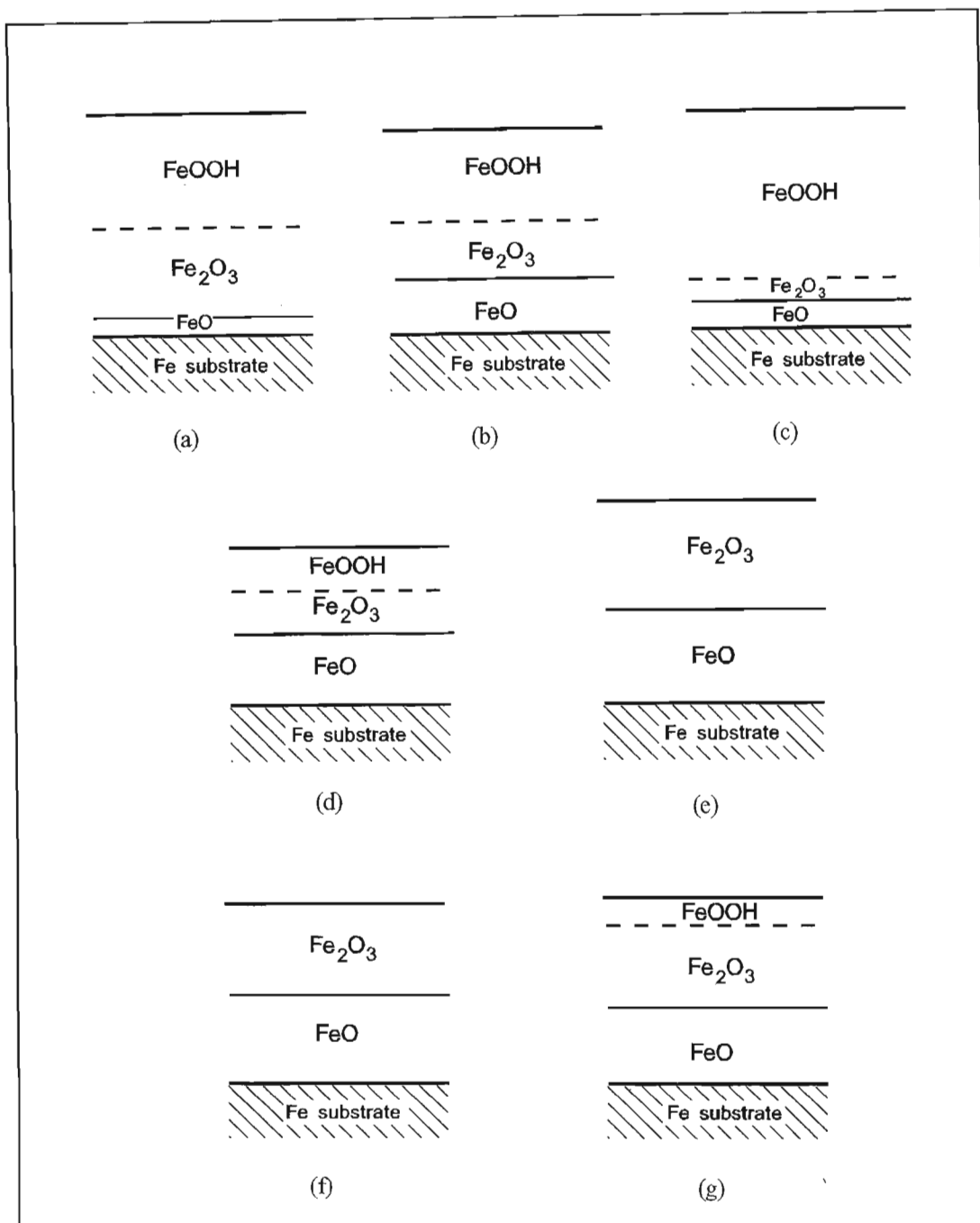


Fig. 7.1

Schematic representation of the composition of the surface film formed on a Fe electrode swept at 100mV s^{-1} between -1.40V and 0.50V for (a) 7 cycles (b) 50 cycles and (c) 120 cycles at 20°C , for (d) 7 cycles and (e) 50 cycles at 80°C in 0.5M NaOH and for 50 cycles between -1.35V and 0.60V in $0.5\text{M NaOH} + 0.4\text{M NaCN}$ at (f) 20°C and (g) 80°C .

Comparing the XPS results of electrode 2 (20°C) with those of electrode 5 (80°C), shows that with increasing temperature there was an increase in the elemental Fe detected (0.0% → 4.6%). This is in agreement with the electrochemical data which has shown that the upper layer formation was suppressed at higher temperatures resulting in a thinner surface film. In agreement with this is the fact that FeOOH was detected at 20°C (40.1%) but not at 80°C and although there was an increase in Fe₂O₃ (26.5% → 47.8%) the total percentage of upper layer decreased with the increase in temperature. The increase in the FeO (26.4% → 44.2%) further confirmed that base layer formation becomes a dominant process at the higher temperature.

The results obtained after Ar sputtering show that with increasing temperature, there is an increase in Fe (0.0% → 10.6%) and FeO (45.7% → 57.8%) and a decrease in Fe₂O₃ (36.5% → 27.8%) and FeOOH (9.0% → 0.0%). A possible explanation for the large decrease in Fe₂O₃ after sputtering, relative to the pre-sputtered value, is that as the Fe₂O₃ forming the upper layer is removed by sputtering.

Thus it is proposed that with increasing temperature the magnitude of the upper layer decreases while that of the base layer increases, and the surface film changes from a three component to a two component film for a well developed film (50 cycles) (*cf* Fig. 7.1(d),(e)).

7.4 INFLUENCE OF CYANIDE IONS ON SURFACE FILM GROWTH AT 20°C

Cyanide ions have been shown to significantly influence the electrochemistry of Fe and Fe18Cr based stainless steels in alkaline electrolytes.³⁹⁶⁻³⁹⁹ Cyclic voltammetry demonstrated that upper layer growth, in particular, is inhibited by the presence of CN⁻ (*cf* Fig. 5.46). SEM analysis of the electrode surface after multiple voltammetric cycles in NaOH, with and without CN⁻ present, showed that the film formed in the CN⁻ containing electrolyte had a completely different topography to that formed in NaOH, the latter being thicker and covering the entire electrode surface, while the former was very thin and only partially covered the surface.

To investigate the influence of CN⁻ on the composition of the film, electrode 6 was prepared in 0.5M NaOH + 0.4M NaCN using the identical electrochemical regime as that used for the preparation of electrode 2 (*cf* Table 7.2). Comparing the XPS results obtained for electrodes 2 and 6, it was found that in the presence of CN⁻ there is an increase in the elemental Fe (0.0% → 16.2%), FeO (26.4% → 38.1%) and Fe₂O₃ (26.5% → 41.6%) and a decrease in the FeOOH (40.1% → 0.0%). This is in agreement with the electrochemistry which showed base layer formation dominates (increase in FeO) while upper layer formation is suppressed (total upper layer, Fe₂O₃ + FeOOH, decreased by 25.0%).

The results obtained for electrodes 2 and 6 after Ar sputtering are also in good agreement with the electrochemical and SEM data. These results indicate less surface film is present with a decrease in FeO

(45.7% \rightarrow 31.8%), Fe_2O_3 (36.5% \rightarrow 11.4%) and FeOOH (9.0% \rightarrow 0.0%) resulting in more elemental Fe being detected (0.0% to 56.8%).

No ferrocyanide complexes were detected on the electrode surface. However, examination of the survey spectra showed an increase in the carbon and nitrogen species for those samples prepared in 0.5M NaOH + 0.4M NaCN electrolytes (see Table 7.4). Although this is not conclusive evidence, it is proposed that this increase in C and N is from the adsorption CN^- .

7.5 INFLUENCE OF CYANIDE IONS ON SURFACE FILM GROWTH AT 80°C

To investigate the influence of CN^- on the surface film formed at elevated temperatures electrode 7 was prepared in 0.5M NaOH + 0.4M NaCN at 80°C (cf Table 7.2).

At elevated temperatures (80°C) CN^- oxidation occurs more readily reducing the extent of CN^- inhibition on film formation and growth. This enables additional oxide to form, particularly in the potential range 400mV to 600mV where CN^- oxidation occurs. FeOOH is the most likely oxide to form at these potentials. Comparing the XPS results for electrodes 5 (20°C) and 7 (80°C) confirms this as an increase in FeOOH (0.0 \rightarrow 11.5%) was observed. The results also show an increase in elemental Fe and a decrease in FeO (44.2 \rightarrow 35.1%) and Fe_2O_3 (47.8 \rightarrow 36.1%). The same trends were observed after sputtering, with the exception that no FeOOH was detected on electrode 7. This suggests the FeOOH is situated at the outer regions of the surface film and therefore readily removed during the sputtering process.

Thus it may be concluded that in the temperature range 20°C to 80°C CN^- inhibited surface film growth particularly that of the upper layer. At ambient temperature (20°C) the inhibition of FeOOH formation results in a duplex layer surface film consisting of FeO and Fe_2O_3 (Fig. 7.1(f)), while at elevated temperatures (80°C) three species were detected in the film, as shown in Fig. 7.1(g).

7.6 INFLUENCE OF TEMPERATURE ON SURFACE FILM FORMATION ON Fe IN 0.5M NaOH + 0.4M NaCN

The influence of temperature on the surface film on Fe electrodes prepared in 0.5M NaOH + 0.4M NaCN can be determined by comparing the XPS data obtained for electrodes 6 (20°C) and 7 (80°C). Electrochemical results indicate an increase in the total film thickness with increasing temperature (cf Fig. 5.48).

XPS data showed that by increasing the temperature from 20°C to 80°C there was a decrease in the percentage elemental Fe (16.2% \rightarrow 10.5%) which suggests the presence of more surface film. While no

Table 7.4**Influence of CN^- on the relative intensity of the C_{1s} and N_{1s} peaks**

sample	temp / $^{\circ}\text{C}$	electrolyte	counts/s $\times 10^{-5}$			
			as - received C_{1s}	N_{1s}	40s Ar C_{1s}	N_{1s}
2	20	0.5M NaOH	0.7	0.4	0.6	0.6
6	20	0.5M NaOH+0.4M NaCN	1.7	0.9	0.9	0.6
5	80	0.5M NaOH	1.5	0.7	0.9	0.9
7	80	0.5M NaOH+0.4M NaCN	1.8	0.9	-	-

FeOOH was detected at 20°C, 11.5% was found at 80°C. As discussed in chapters five and six this is due to CN⁻ oxidation occurring more readily at elevated temperatures resulting in additional oxide formation. Although there was a decrease in FeO (38.1% → 35.1%) and Fe₂O₃ (41.6% → 36.1%) the overall percentage surface oxide increased from 79.7% → 82.7%.

The XPS results obtained after sputtering are in better agreement with the electrochemical data, with a decrease in the Fe (56.8% → 39.3%), an increase in FeO (31.8% → 44.4%) and Fe₂O₃ (11.4% → 12.6%) and an increase of 14% in the overall surface film. No FeOOH was detected at either temperature.

7.7 SUMMARY

The influence of film thickness, temperature of formation and the presence of 0.4M NaCN, on the nature of the surface film formed on pure Fe electrodes in 0.5M NaOH, was investigated using XPS. It has been proposed from electrochemical data that the surface film consists of a protective base layer onto which a non - protective upper layer forms. XPS data showed that the percentage of the various species within the surface film were dependent on the conditions under which the film was formed. The results indicated that the base layer was FeO, with Fe₂O₃ and FeOOH constituting the upper layer. At ambient temperatures the increase in the film thickness was due to additional upper layer formation. Increasing the temperature from 20°C to 80°C favoured base layer formation resulting in a decrease in FeOOH with FeO and Fe₂O₃ becoming the dominant, and in some cases the only, species present.

Addition of 0.4M NaCN to 0.5M NaOH inhibited surface film growth particularly of the upper layer. At ambient temperatures a duplex surface film was formed consisting of a FeO base layer and a Fe₂O₃ upper layer. At elevated temperatures (80°C) where CN⁻ inhibition is not as effective the upper layer was found to consist of Fe₂O₃ with an outer FeOOH layer.

CHAPTER EIGHT

SUMMARY

Surface film formation on Fe and certain FeCr based stainless steels has been investigated using electrochemical and surface analytical techniques.

Single pulse chronoamperometry was used to investigate the nucleation and initial growth of surface films on Fe18Cr alloys in acidic electrolytes as a function of applied potential, electrolyte composition, the addition of minor alloying elements and temperature. Film formation on certain of the constituent alloying elements (viz. Fe, Cr and Mo) was also investigated. In the appropriate potential range rising current transients indicative of a nucleation mechanism were observed, and were shown to be sensitive to variations in the above parameters.

Electrolyte composition. This was the most important experimental parameter, in that dissolution of the substrate metal was found to be a prerequisite for the appearance of rising current transients. For acidic electrolytes ($\text{pH} < 7$) it was found that with decreasing pH there was an increase in the maximum of the chronoamperometric transient, i_m , and a decrease in the corresponding time, t_m .

Potential. In order for rising current transients to be observed, the final potential to which the electrode was stepped had to be such that alloy dissolution could occur. The potential range meeting this criterion would be dependent on the composition of the alloy or metal. For Fe, Cr and Fe18Cr rising current transients were observed in the passive potential region. For Cr and Fe18Cr, these transients were extremely rapid ($t_m \approx 150\mu\text{s}$) due to the rapid passivation of the electrode surface. Analysis of the transients suggested an instantaneous nucleation mechanism followed by 3D growth. For Fe x Cr ($x = 16, 18, 20, 23\%$ Cr), and alloys 444, 4733, 4732, 304L and 316L rising current transients were observed at transpassive potentials. With increasing potential, in the transpassive region, the transients became better defined with i_m increasing and t_m decreasing. Analysis of the Fe18Cr transients suggested a progressive nucleation and 3D growth mechanism prevailed.

Alloy composition. The rising current transients were sensitive to changes in alloy composition with i_m decreasing as the alloys became more corrosion resistant. Further, addition of minor alloying elements eg. Mo, which results in the formation of an initial Mo enriched surface film and which is reflected by the

presence of an additional maximum on the current transient.

Temperature. The rising current transients reflected changes in temperature, with i_m increasing and t_m decreasing with increasing temperature.

Model. A qualitative nucleation model was proposed in which dissolution of the electrode occurs preferentially from localised areas on the electrode surface. Dissolution will continue until the required degree of supersaturation of dissolving species is achieved. Once conditions at the surface are such that the critical energy for the formation of stable nuclei has been achieved nucleation can occur. Growth of the nuclei would continue for as long as conditions are conducive to growth. Existing nucleation models were found to be inadequate in describing surface film formation on an oxidising substrate, and although a more realistic model is required to describe the process, mathematical limitations preclude this at present.

In alkaline and alkaline cyanide electrolytes both the initial stages of nucleation and growth and the subsequent long term growth of the surface film on Fe over the temperature range 20°C to 120°C was investigated. Chronoamperometry showed that in 0.5M NaOH, 0.5M NaOH + 0.4M NaCN, 1.0M NaOH and 1.0M NaOH + 0.4M NaCN the surface film formed via a nucleative mechanism, as indicated by the appearance of rising chronoamperometric transients. This was verified by SEM examination of the electrode surface which showed the presence of discrete growth centres. It was proposed that in the absence of CN^- and in 0.5M NaOH + 0.4M NaCN film formation occurred via a progressive nucleation mechanism followed by 3D growth at ambient temperatures which changes to progressive nucleation and 3D growth leading to passivation at elevated temperatures. In 1.0M NaOH + 0.4M NaCN progressive nucleation followed by 3D growth leading to passivation holds at ambient temperatures but changes to progressive nucleation and 3D growth at elevated temperatures. Existing nucleation models were again shown to be inadequate in describing surface film formation on a corroding substrate.

The growth and thickening of the surface film was investigated using cyclic voltammetry and rotating ring-disc electrode techniques. In 0.5M and 1.0M NaOH four oxidation peaks (A1, A2, A3, A4) and two reduction peaks (C1, C2) were present. A duplex surface film formed with peaks A1 and A2 corresponding to base layer formation and A4 corresponding to the subsequent formation of the upper layer. The reactions occurring at these three peaks were sequential, and in parallel to those reactions taking place at the potential of A3. A3 was also due to upper layer formation resulting from the re-oxidation of incompletely reduced oxide (FeO) from the previous sweep. Consequently A3, and the conjugate peak C2, were absent from the first cyclic voltammetric sweep on a clean electrode. This result also indicates that a preformed and unintentional film is not present on a clean electrode. At ambient temperatures, continued applied potential cycling resulted in the continual increase in $i_{p,A3}$ due to the thickening of the upper layer. In contrast the thickness of the base layer was virtually independent of potential cycling. At ambient temperatures A3 and C2 were the dominant oxidation and reduction peaks however, at higher temperatures

(120°C) these two peaks were poorly defined with A2 and C1 becoming the predominant peaks. RRDE, using a six electrode configuration, showed that solution soluble Fe(III) species were produced at A3 while soluble Fe(II) species were produced at A3, A4 ($T \geq 60^\circ\text{C}$), C1 and C2.

In 0.5M NaOH at ambient temperatures, a triplet of peaks was observed in the potential region of A3 suggesting the presence of $\text{Fe}_2\text{O}_3 \cdot x\text{H}_2\text{O}$ having varying degrees of hydration due to aging processes.

A significant aspect of the work was the SEM data which provided the visual evidence to support the predictions based on the electrochemical data. All stages of surface film formation, from the initial nucleation / early growth centre stage, through to the coverage of the electrode surface by the base layer and the subsequent nucleation of the upper layer on the base layer, and the subsequent thickening and eventual spalling of the upper layer were observed.

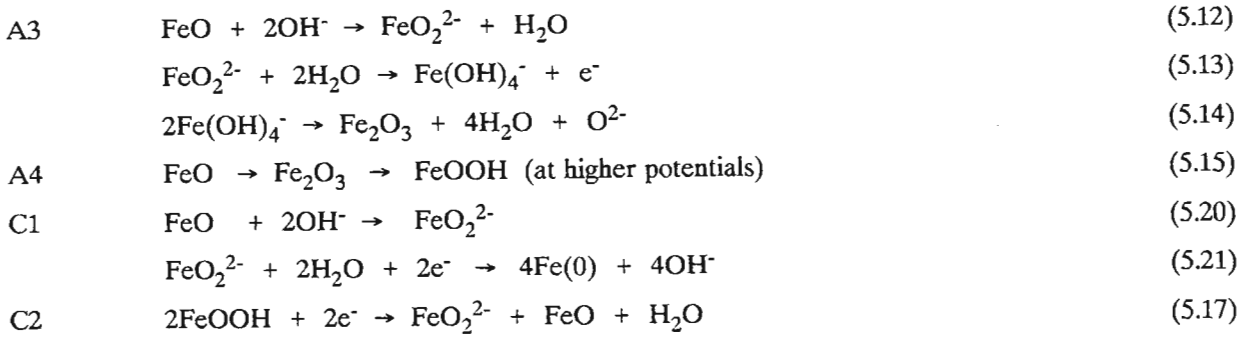
It was proposed that in 0.5M and 1.0M NaOH a duplex surface film forms on a Fe, with a protective base layer consisting of FeO forming at the potentials of A1 and A2 while at more positive potentials (A3) a non-protective upper layer of FeOOH and Fe_2O_3 forms. The initial formation occurs via a nucleation mechanism with subsequent growth of the base layer occurring via a place exchange mechanism while upper layer growth proceeds via a low field mechanism with ion migration through the film as the rate determining step.

Addition of 0.4M NaCN to both 0.5M and 1.0M NaOH significantly inhibits surface film formation and growth, particularly of the upper layer. A competitive adsorption mechanism between CN^- and OH^- suppresses oxide formation by effectively blocking the active sites on the electrode surface. At elevated temperatures the inhibiting effect of CN^- is reduced, due to CN^- oxidation occurring more readily. SEM data again supported the electrochemical results. It was proposed that the surface film forms on Fe in alkaline cyanide electrolytes via a nucleation mechanism with subsequent growth being controlled by a low field mechanism involving ion migration through the film as the rate determining step. While a duplex film structure was not evident from the electrochemical (cyclic voltammetric and chronoamperometric) and SEM data, XPS results did show the presence of FeO / Fe_2O_3 at ambient temperatures.

Following is a summary of the mechanism proposed for Fe oxidation in alkaline and alkaline cyanide electrolytes :

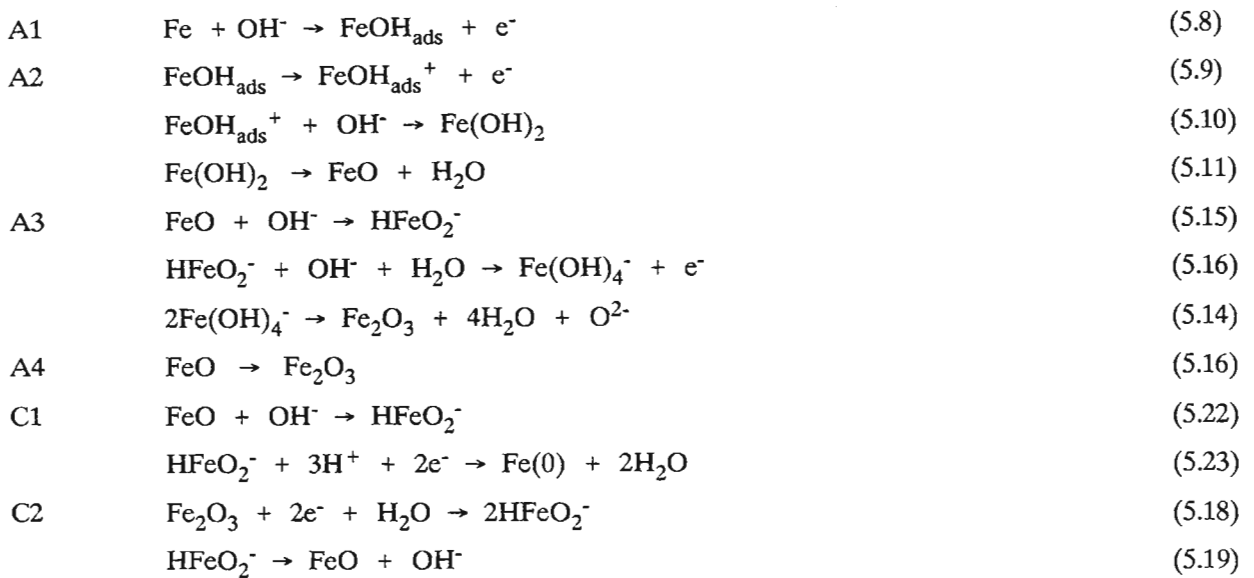
Fe in 0.5M /1.0M NaOH at $T < 60^\circ\text{C}$:





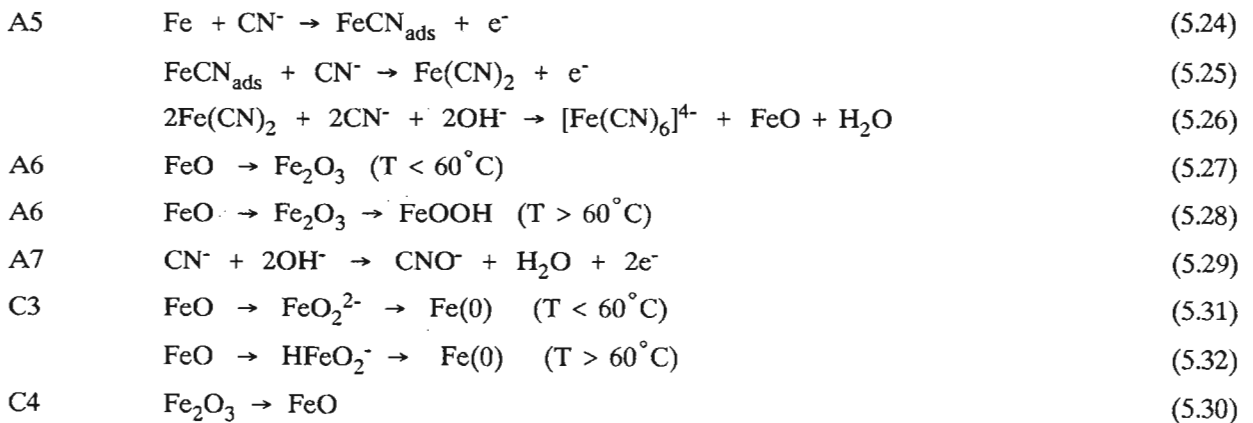
At $T > 60^\circ\text{C}$

peak reaction



In the presence of cyanide the dissolution mechanism modifies to :

peak reaction



REFERENCES

1. K.E. Heusler, *Z. Elektrochem.*, **62**, 582 (1958).
2. J.O'M. Bockris, D.Drazic, A.L. Despic, *Electrochim. Acta*, **4**, 325 (1961).
3. G. Bech - Nielsen, *Electrochim. Acta*, **19**, 821 (1974).
4. A. Akiyama, R.E. Patterson, K.H. Nobe, *Corros. Sci.*, **26**, 51 (1970).
5. W. Lorenz, G. Eichkorn, *J. Electrochem. Soc.*, **112**, 1255 (1965).
6. G. Eichkorn, W.J. Lorenz, L. Albert, H. Fischer, *Electrochim. Acta*, **13**, 183 (1968).
7. D. Macdonald, *J. Electrochem. Soc.*, **139**, 3434 (1992).
8. M. Morsi, Y.A. Elewady, P. Lorbeer, W.J. Lorenz, *Werkst. Korros.*, **31**, 108 (1980).
9. G. Bech - Nielsen, *Electrochim. Acta*, **18**, 671 (1973).
10. G. Bech - Nielsen, *Electrochim. Acta*, **20**, 619 (1975).
11. G. Bech - Nielsen, *Electrochim. Acta*, **21**, 627 (1976).
12. G. Bech - Nielsen, *Electrochim. Acta*, **23**, 425 (1978).
13. G. Okamoto, T. Shibata, *Corros. Sci.*, **10**, 371 (1970).
14. G. Okamoto, *Corros. Sci.*, **13**, 471 (1973).
15. T. Pou, O. Murphy, V. Young, J.O'M. Bockris, L. Tongsen, *J. Electrochem. Soc.*, **131**, 1243 (1984).
16. W. O'Grady, *J. Electrochem. Soc.*, **127**, 555 (1980).
17. Y. Lu, C.R. Clayton, A.R. Brooks, *Corros. Sci.*, **29**, 863 (1989).
18. C. Clayton, Y.C. Lu, *J. Electrochem. Soc.*, **133**, 2465 (1986).
19. A. Brooks, C. Clayton, K. Doss, Y. Lu, *J. Electrochem. Soc.*, **133**, 2459 (1986).
20. Y. Lu, C. Clayton, *J. Electrochem. Soc.*, **132**, 2517 (1985).
21. R. Armstrong, *Corros. Sci.*, **11**, 693 (1971).
22. U. Ebersbach, K. Schwabe, K. Ritter, *Electrochim. Acta*, **12**, 927 (1967).
23. U. Ebersbach, K. Schwabe, P. Konig, *Electrochim. Acta*, **14**, 773 (1969).
24. U. Ebersbach, G. Kreysa, K. Schwabe, *Electrochim. Acta*, **17**, 445 (1972).
25. P. Marshall, G.T. Burstein, *Corros. Sci.*, **23**, 1219 (1983).
26. G. Burstein, P.I. Marshall, *Corros. Sci.*, **24**, 449 (1984).
27. R. Alkire, D. Ernsberger, T. Beck, *J. Electrochem. Soc.*, **125**, 1382 (1978); and references therein.
28. T. Beck, *J. Electrochem. Soc.*, **129**, 2412 (1982).
29. P. Russell, J. Newman, *J. Electrochem. Soc.*, **133**, 59 (1986).
30. H. Kuo, D. Landolt, *Corros. Sci.*, **16**, 915 (1976).
31. J. Bartlett, L. Stephenson, *J. Electrochem. Soc.*, **99**, 504 (1952).
32. H. Isaacs, R. Newman, *Corrosion and Corrosion Protection*, eds. R.P. Frankenthal, F. Mansfeld, Electrochem. Soc. Inc., New Jersey (1981), p. 120.

33. K. Hashimoto, *Passivity of Metals and Semiconductors*, ed. M. Froment, Elsevier, Amsterdam (1983), p. 235, 247.
34. S. Haupt, H.-H. Strehblow, *Langmuir*, **3**, 873 (1987).
35. S. Haupt, H.-H. Strehblow, *Corros. Sci.*, **29**, 163 (1989).
36. R. Schrebler Guzmán, J.R. Vilche, A.J. Arvia, *Electrochim. Acta*, **24**, 395 (1979).
37. V. Muralidharan, M. Veerashanmugamani, *J. App. Electrochem.*, **15**, 675 (1985).
38. D.D. Macdonald, B. Roberts, *Electrochim. Acta*, **23**, 781 (1978).
39. L.D. Burke, M.E.G. Lyons, *Modern Aspects of Electrochemistry*, Vol. 18, eds. R.E. White, J.O'M. Bockris, B.E. Conway, Plenum Press, New York (1986), ch. 4.
40. L.D. Burke, M.E.G. Lyons, *J. Electroanal. Chem.*, **198**, 347 (1986).
41. A. Hugot-Le Goff, J. Flis, N. Boucherit, S. Joiret, J. Wilinski, *J. Electrochem. Soc.*, **137**, 2684 (1990).
42. A. Wieckowski, E. Ghali, H. Ha Le, *J. Electrochem. Soc.*, **131**, 2024 (1984).
43. A. Wieckowski, E. Ghali, *Extended Abstracts*, **83 - 1**, Electrochem. Soc., New Jersey (1983) p. 99.
44. D. Oelkrug, M. Fritz, H. Stauch, *J. Electrochem. Soc.*, **139**, 2419 (1992).
45. J. Dünwald, R. Lossy, A. Otto, *Passivity of Metals and Semiconductors*, ed. M. Froment, Elsevier, Amsterdam (1983), p. 107.
46. D.D. Macdonald, D. Owen, *J. Electrochem. Soc.*, **120**, 317 (1973).
47. C. Melendres, M. Pankuch, Y.S. Li, R.L. Knight, *Electrochim. Acta*, **37**, 2747 (1992).
48. C. Gutiérrez, B. Beden, *J. Electroanal. Chem.*, **293**, 253 (1990).
49. G. Larramona, C. Gutiérrez, *J. Electrochem. Soc.*, **136**, 2171 (1989).
50. D. Shoesmith, P. Taylor, M. Bailey, B. Ikeda, *Electrochim. Acta*, **23**, 903 (1978).
51. C. Chanson, P. Blanchard, A. Wattiaux, J. Grenier, *J. Electrochem. Soc.*, **136**, 3690 (1989).
52. H. Neugebauer, A. Moser, P. Strecha, A. Neckel, *J. Electrochem. Soc.*, **137**, 1472 (1990).
53. W. Tschinkel, H. Neugebauer, A. Heckel, *J. Electrochem. Soc.*, **137**, 1475 (1990).
54. M. McKubre, *The Mechanism of Dissolution and Passivation of Iron and Zinc in Concentrated Potassium Hydroxide Solutions*, Final report to DOE, Contract 450561 (1981).
55. M. McKubre, M. Madou, *Extended Abstracts*, **83 - 1**, Electrochem. Soc., New Jersey (1983) p. 81.
56. O. Albani, L. Gassa, J. Zerbino, J. Vilche, A. Arvia, *Electrochim. Acta*, **35**, 1437 (1990).
57. V. Jovancicevic, R. Kainthla, Z. Tang, *Surfaces, Inhibition and Passivation*, ed. E. McCafferty, R.J. Brodd, **86-7**, Electrochem. Soc. Inc., New Jersey (1986), p. 192.
58. M.D. Adams, *J. S. Afr. Inst. Min. Metall.*, **90**, 37 (1990).
59. J.W. Mellor, *A Comprehensive Treatise on Inorganic and Theoretical Chemistry*, Longmans, Green and Co., London (1923), 3.
60. C.C. Kenna, I.M. Ritchie, P. Singh, *Hydrometallurgy*, **23**, 263 (1990).
61. S.A.I.M.M. School : *Design and Operation of Plants for the Recovery of Gold by Activated Carbon*, S.A.I.M.M., Johannesburg (1986) section 16.
62. K. Osseo - Asare, T. Xue, V. Ciminelli, *Precious Metals, Mining, Extraction and Processing*, eds. V. Kudryk, D. Corrigan, W. Liang, The Metallurgical Society of AIME, New York (1984), p. 173.

63. J.R. de Wet, R.F. Sandenburg, *J. S. Afr. Inst. Min. Metall.*, **93**, 105 (1993).
64. C. Clayton, Y. Lu, *Corros. Sci.*, **29**, 881 (1989).
65. J. Castle, J. Qiu, *Corros. Sci.*, **29**, 591 (1989).
66. C. Clayton, L. Rosenzweig, M. Oversluizen, Y. Lu, *Surfaces, Inhibition and Passivation*, ed. E. McCafferty, R.J. Brodd, **86-7**, Electrochem. Soc. Inc., New Jersey (1986), p. 323.
67. K. Asami, K. Hashimoto, T. Musumoto, S. Shimodaira, *Corros. Sci.*, **16**, 909 (1976).
68. S. Haupt, C. Calinski, U. Collisi, H. Hoppe, H. Speckmann, H.-H. Strehblow, *Surf. Interface Anal.*, **9**, 357 (1986).
69. I. Olefjord, L. Wegrelius, *Corros. Sci.*, **31**, 89 (1990).
70. G. Lorang, M. Da Cunha Belo, J. Langeron, *J. Vac. Sci. Technol. A*, **5**, 1213 (1987).
71. R. Revie, B.G. Baker, J.O'M. Bockris, *J. Electrochem. Soc.*, **122**, 1460 (1975).
72. M. Seo, J.B. Lumsden, R.W. Staehle, *Surface Sci.*, **42**, 337 (1974).
73. J. Lumsden, P.J. Stocker, *Surfaces, Inhibition and Passivation*, ed. E. McCafferty, R.J. Brodd, **86-7**, Electrochem. Soc. Inc., New Jersey (1986), p. 304.
74. N. Ramasubramanian, R. Davidson, N. Preocanin, *Surfaces, Inhibition and Passivation*, ed. E. McCafferty, R.J. Brodd, **86-7**, Electrochem. Soc. Inc., New Jersey (1986), p. 311.
75. A. Yaniv, J.B. Lumsden, R.W. Staehle, *J. Electrochem. Soc.*, **124**, 490 (1977).
76. D. Mitchell, M.J. Graham, *Surface and Interface Analysis*, **10**, 259 (1987).
77. H. Engell, R.A. Oriani, *Corros. Sci.*, **29**, 119 (1989).
78. C. Courty, H.J. Mathieu, D. Landolt, *Electrochim. Acta*, **36**, 1623 (1991).
79. K. Kuroda, B. Cahan, Gh. Nazri, E. Yeager, T. Mitchell, *J. Electrochem. Soc.*, **129**, 2163 (1982).
80. S. Juanto, J.O. Zerbino, J.R. Vilche, A.J. Arvia, *Surfaces, Inhibition and Passivation*, ed. E. McCafferty, R.J. Brodd, **86-7**, Electrochem. Soc. Inc., New Jersey (1986), p. 226.
81. Z. Huang, J.L. Ord, *J. Electrochem. Soc.*, **132**, 24 (1985).
82. J. Ord, D.J. DeSmet, *J. Electrochem. Soc.*, **123**, 1876 (1976).
83. B. Cahan, C.-T. Chen, *J. Electrochem. Soc.*, **129**, 921 (1982).
84. N. Sato, K. Kudo, T. Noda, *Z. Phys. Chem. N.F.*, **98**, 271 (1975).
85. H. Oranowska, Z. Szklarska-Smialowska, *Corros. Sci.*, **21**, 735 (1981).
86. O. Albani, J.O. Zerbino, J.R. Vilche, A.J. Arvia, *Electrochim. Acta*, **31**, 1403 (1986).
87. N. Sato, K. Kudo, T. Noda, *Electrochim. Acta*, **16**, 1909 (1971).
88. Ch.T. Chen, B.D. Cahan, *J. Electrochem. Soc.*, **129**, 17 (1982).
89. M. Brett, K.M. Parkin, M.J. Graham, *J. Electrochem. Soc.*, **133**, 2031 (1986).
90. A. Vértés, I. Czakó-Nagy, *Electrochim. Acta*, **34**, 721 (1989).
91. J. Eldridge, R.W. Hoffman, *J. Electrochem. Soc.*, **136**, 955 (1989).
92. M. Cohen, *Passivity of Metals*, ed. R.P. Frankenthal, J. Kruger, Electrochem. Soc. Inc., Princeton, New Jersey (1978), p. 521.
93. C. Foley, J. Kruger, C.J. Bechtoldt, *J. Electrochem. Soc.*, **114**, 994 (1967).
94. G. McBee, J. Kruger, *Electrochim. Acta*, **17**, 1337 (1972).

95. J. Dünwald, A. Otto, *Z. Anal. Chem.*, **319**, 738 (1984).
96. M. Froelicher, A. Hugot-Le Goff, C. Palotta, P. Dupeyrat, M. Masson, *Passivity of Metals and Semiconductors*, ed. M. Froment, Elsevier, Amsterdam (1983), p. 101.
97. D.D. Macdonald, M. Ben - Haim, J. Pallix, *Corros. Sci.*, **31**, 223 (1990).
98. D. Macdonald, M. Ben-Haim, J. Pallix, *J. Electrochem. Soc.*, **136**, 3269 (1989).
99. J. Kruger, *Surfaces, Inhibition and Passivation*, ed. E. McCafferty, R.J. Brodd, **86-7**, Electrochem. Soc. Inc., New Jersey (1986), p. 210.
100. A. Forty, M. Kerker, J. Robinson, M. Ward, *J. de Physique*, **47**, 1077 (1986).
101. M. Kerker, J. Robinson, A.J. Forty, *Faraday Discuss. Chem. Soc.*, **89**, 31 (1990).
102. G. Long, J. Kruger, D.R. Black, M. Kuriyama, *J. Electroanal. Chem.*, **150**, 603 (1983).
103. A. Benwick, M. Kalaji, G. Larramona, *J. Electroanal. Chem.*, **318**, 207 (1991).
104. C. Calinski, H.-H. Strehblow, *J. Electrochem. Soc.*, **136**, 1328 (1989).
105. R. Frankenthal, D.L. Malan, *J. Electrochem. Soc.*, **123**, 186 (1976).
106. M.G.S. Ferreira, T. Moura e Silva, A. Catarino, M. Pankuch, C.A. Melendres, *J. Electrochem. Soc.*, **139**, 3146 (1992).
107. W. Paatsch, *Surf. Sci.*, **37**, 59 (1973).
108. D.J. Wheeler, B.D. Cahan, C.T. Chen, E. Yeager, *Passivity of Metals*, ed. R.P. Frankenthal, J. Kruger, Electrochem. Soc. Inc., Princeton, New Jersey (1978), p. 546.
109. Ya. M. Kolotyркин, R.M. Lazorenko - Manevich, L.A. Sokolova, *J. Electroanal. Chem.*, **228**, 301 (1987).
110. M. Frolicher, A. Hugot-Le Goff, V. Jovancicevic, *Passivity of Metals and Semiconductors*, ed. M. Froment, Elsevier, Amsterdam (1983), p. 85.
111. L. Öjefors, *J. Electrochem. Soc.*, **123**, 1691 (1976).
112. D.W. Shoesmith, T.E. Rummery, D. Owen, W. Lee, *J. Electrochem. Soc.* **123**, 790 (1976).
113. F-R. Fran, A.J. Bard, *J. Electrochem. Soc.*, **136**, 166 (1989).
114. R.C. Bhardwaj, A. González - Martín, J.O'M. Bockris, *J. Electrochem. Soc.*, **138**, 1901 (1991).
115. J. O'M. Bockris, *Corros. Sci.*, **29**, 291 (1989).
116. I. Olefjord, B. Brox, U. Jelvestam, *J. Electrochem. Soc.*, **132**, 2854 (1985).
117. R. Ansell, T. Dickinson, A. Povey, P. Sherwood, *J. Electroanal. Chem.*, **98**, 69 (1979).
118. M. Graham, J. Bardwell, R. Goetz, D. Mitchell, B. MacDougall, *Corros. Sci.*, **31**, 139 (1990).
119. J. Gui, T.M. Devine, *Corros. Sci.*, **32**, 1105 (1991).
120. P. Mills, J. Sullivan, *J. Phys. D : Appl. Phys.*, **16**, 723 (1983).
121. P. Ho, J.E. Lewis, H. Wildman, J. Howard, *Surface Sci.*, **57**, 393 (1976).
122. H. Andersen, *Appl. Phys.*, **18**, 131 (1979).
123. T. Ishitani, R. Shimizu, H. Tamura, *Appl. Phys.*, **6**, 277 (1975).
124. H. Etzkorn, J. Kirschner, *Nucl. Instr. and Methods*, **168**, 395 (1980).
125. P. Sigmund, A. Gras-Marti, *Nucl. Instr. and Methods*, **168**, 389 (1980).
126. H. Mathieu, D. Landolt, *Appl. Surf. Sci.*, **3**, 348 (1979).

127. R. Goetz, D. Landolt, *Electrochim. Acta*, **29**, 667 (1984).
128. H. Konno, M. Nagayama, *Passivity of Metals*, ed. R.P. Frankenthal, J. Kruger, Electrochem. Soc. Inc., Princeton, New Jersey (1978), p. 585.
129. H. Mathieu, D. Landolt, *Corros. Sci.*, **26**, 547 (1986).
130. N. McIntyre, D. Zetaruk, *Anal. Chem.*, **49**, 1521 (1977).
131. C. Legraf, G. Hultquist, I. Olefjord, B.-O. Elfstrom, V.M. Knyazheva, A.V. Plaskeyev, Ya.M. Kolotyркин, *Corros. Sci.*, **19**, 343 (1979).
132. D. Shoesmith, D. Mancey, D. Doern, M. Bailey, *Corrosion*, **45**, 149 (1989).
133. N. Ramasubramanian, N. Preocanin, R. Davidson, *J. Electrochem. Soc.*, **132**, 793 (1985).
134. I. Olefjord, B. Brox, *Passivity of Metals and Semiconductors*, ed. M. Froment, Elsevier, Amsterdam (1983), p. 561.
135. J. Lumsden, R. Staehle, *Scripta Met.*, **6**, 1205 (1972).
136. J. Castle, C. Clayton, *Corros. Sci.*, **17**, 7 (1977).
137. C. Clayton, A. Brooks, K. Ross, Y. Lu, *Equilibrium Diagrams and Localised Corrosion*, eds. R. Frankenthal, J. Kruger, The Electrochemical Soc. Inc., New Jersey (1984), p. 369.
138. M. daCunha Belo, B. Rondot, F. Pons, J. LeHericy, J. Langeron, *J. Electrochem. Soc.*, **124**, 1317 (1977).
139. I. Olefjord, B.-O. Elfstrom, *Corrosion*, **38**, 46 (1982).
140. K. Asami, K. Hashimoto, S. Shimodaira, *Corros. Sci.*, **16**, 529 (1976).
141. K. Asami, K. Hashimoto, S. Shimodaira, *Corros. Sci.*, **18**, 151 (1978).
142. J. Holliday, R.P. Frankenthal, *J. Electrochem. Soc.*, **119**, 1190 (1972).
143. K. Sugimoto, Y. Sawada, *Corros. Sci.*, **17**, 425 (1977).
144. V. Mitrovic - Scepanovic, B. MacDougall, M.J. Graham, *Corros. Sci.*, **24**, 479 (1984).
145. E. de Vito, M. Keddam, P. Marcus, *Proceedings of the Symposium on Modification of passive Films and Relation to the Resistance to Localised Corrosion*, (1993), p. 19.
146. R.P. Frankenthal, *J. Electrochem. Soc.*, **116**, 1646 (1969).
147. R.P. Frankenthal, *J. Electrochem. Soc.*, **114**, 542 (1967).
148. R.P. Frankenthal, *J. Electrochem. Soc.*, **116**, 580 (1969).
149. S. Tjong, *J. Mat. Sci. Lett.*, **4**, 6 (1985).
150. A. Revesz, J. Kruger, *Passivity of Metals*, ed. R.P. Frankenthal, J. Kruger, Electrochem. Soc. Inc., Princeton, New Jersey (1978), p. 137.
151. K. Asami, M. Naka, K. Hashimoto, T. Masumoto, *J. Electrochem. Soc.*, **127**, 2130 (1980).
152. G. Okamoto, T. Shibata, *Passivity of Metals*, ed. R.P. Frankenthal, J. Kruger, Electrochem. Soc. Inc., Princeton, New Jersey (1978), p. 646.
153. J. Galvele, J. Lumsden, R. Staehle, *J. Electrochem. Soc.*, **125**, 1204 (1978).
154. K. Hashimoto, K. Asami, M. Naka, T. Masumoto, *Corros. Sci.*, **19**, 857 (1979).
155. I. Olefjord, *Materials Science and Engineering*, **142**, 161 (1980).
156. K. Hashimoto, K. Asami, K. Teramoto, *Corros. Sci.*, **19**, 3 (1979).

157. K. Hashimoto, K. Asami, *Corros. Sci.*, **19**, 1007 (1979).
158. Ya. Kolotyrkin, V. Knyazheva, *Passivity of Metals*, ed. R.P. Frankenthal, J. Kruger, Electrochem. Soc. Inc., Princeton, New Jersey (1978), p. 678.
159. P. Bruesch, K. Muller, A. Atrens, H. Neff, *App. Phys. A*, **38**, 1 (1985).
160. I. Olefjord, B.-O. Elfstrom, *Corros. Sci.*, **15**, 697 (1975).
161. A. Streicher, *Corrosion*, **30**, 77 (1974).
162. G. Bianchi, A. Cerquetti, F. Mazza, S. Torchio, *Corros. Sci.*, **12**, 495 (1972).
163. G. Hultquist, C. Legraf, D. Brune, *J. Electrochem. Soc.*, **131**, 1773 (1984).
164. I. Olefjord, B. Brox, U. Jelvestam, *Proc. Electrochem. Soc.*, **84-9**, The Electrochem. Soc. Inc., New Jersey (1984), p. 388.
165. R. Paton, *Stainless Steel*, **28**, 18 (1992).
166. N.D. Tomashov, G.P. Chernova, O.N. Marcova, *Corrosion*, **20**, 166t (1964).
167. F.P.A. Robinson, P. van Biljon, *Corrosion*, **41**, 220 (1985).
168. J. Ord, D.J. DeSmet, *J. Electrochem. Soc.*, **113**, 1258 (1966).
169. V. Mitrovic-Scepanovic, B. MacDonald, M. Graham, *Corros. Sci.*, **24**, 463 (1984).
170. M. Seo, N. Sato, J. Lumsden, R. Staehle, *Corros. Sci.*, **17**, 209 (1977).
171. N. Sato, K. Kudo, R. Nishimura, *J. Electrochem. Soc.*, **123**, 1419 (1976).
172. S. Juanto, J. Zerbino, M. Miguez, J. Vilche, A. Arvia, *Electrochim. Acta*, **32**, 1743 (1987).
173. J. Ord, *Passivity of Metals and Semiconductors*, ed. M. Froment, Elsevier, Amsterdam (1983), p. 95.
174. J. Kruger, *Corros. Sci.*, **29**, 149 (1989).
175. K. Vetter, *Z. Electrochem.*, **62**, 642 (1958).
176. H. Gerischer, *Corros. Sci.*, **29**, 191 (1989).
177. K. Ogura, A. Fijishima, K. Honda, *J. Electrochem. Soc.*, **131**, 344 (1984).
178. M. Vela, J. Vilche, A. Arvia, *J. App. Electrochem.*, **16**, 490 (1986).
179. R.D. Armstrong, I. Baurhoo, *J. Electroanal. Chem.*, **34**, 41 (1972).
180. M. Nagayama, M. Cohen, *J. Electrochem. Soc.*, **109**, 781 (1962).
181. M. Nagayama, M. Cohen, *J. Electrochem. Soc.*, **110**, 670 (1963).
182. G. Foley, J. Kruger, C. Bechtold, *J. Electrochem. Soc.*, **114**, 936 (1967).
183. G. Simmons, E. Kellerman, H. Leidheiser, Jr., *J. Electrochem. Soc.*, **123**, 1276 (1976).
184. P. Sewell, C. Stockbridge, M. Cohen, *J. Electrochem. Soc.*, **108**, 933 (1961).
185. M. Bloom, M. Goldenberg, *Corros. Sci.*, **5**, 623 (1965).
186. M.E.G. Lyons, L.D. Burke, *J. Electroanal. Chem.*, **170**, 377 (1984).
187. H. Yolken, J. Kruger, J.P. Calvert, *Corros. Sci.*, **8**, 103 (1968).
188. K. Heusler, K.G. Weil, K.F. Bonhoeffer, *Z. Phys. Chem. N.F.*, **57**, 149 (1958).
189. C. Wagner, *Ber. Bunsenges. Phys. Chem.*, **77**, 1090 (1973).
190. W. O'Grady, J.O'M. Bockris, *Surface Sci.*, **38**, 249 (1973).
191. G. Allen, M.T. Curtis, A.J. Hooper, P.M. Tucker, *J. Chem. Soc., Dalton Trans.*, **14**, 1525 (1974).
192. K. Asami, K. Hashimoto, reference 11 quoted in reference 128.

193. J. Schultze, *Passivity of Metals*, ed. R.P. Frankenthal, J. Kruger, Electrochem. Soc. Inc., Princeton, New Jersey (1978), p. 82.
194. T.P. Hoar, *J. Electrochem. Soc.*, **117**, 17c (1970).
195. K. Heusler, *Corros. Sci.*, **29**, 131 (1989).
196. N. Sato, T. Noda, K. Kudo, *Electrochim. Acta*, **19**, 471 (1974).
197. I. Olefjord, *Corros. Sci.*, **15**, 687 (1975).
198. K. Hashimoto, K. Asami, *Corros. Sci.*, **19**, 251 (1979).
199. R. Berneron, J.C. Charbonnier, R. Namder-Irani, J. Manenc, *Corros. Sci.*, **20**, 899 (1980).
200. H. Ogawa, H. Omata, I. Otoh, H. Okada, *Corrosion*, **34**, 52 (1978).
201. Z. Szklarska-Smialowska, W. Kozlowski, *J. Electrochem. Soc.*, **131**, 234 (1984).
202. L.L. Wikstrom, K. Nobe, *J. Electrochem. Soc.*, **116**, 525 (1969).
203. W. Schultze, U. Stimming, *Z. Physik Chem. N.F.*, **98**, 285 (1975).
204. J. Vera, S. Kapusta, N. Hackerman, *Surfaces, Inhibition and Passivation*, ed. E. McCafferty, R.J. Brodd, **86-7**, Electrochem. Soc. Inc., New Jersey (1986), p. 165.
205. A.M.P. Simoes, M.G.S. Ferreira, G. Lorang, M. da Cunha Belo, *Electrochim. Acta*, **36** 315 (1991).
206. M. Pourbaix, *Atlas of Electrochemical Equilibria in Aqueous Solutions*, Pergamon Press, London (1966), p. 307.
207. T. Misawa, *Corros. Sci.*, **13**, 659 (1973).
208. V. Ashworth, P.J. Boden, *Corros. Sci.*, **10**, 709 (1970).
209. H.E. Townsend, *Corros. Sci.*, **10**, 343 (1970).
210. L. Öjefors, *J. Electrochem. Soc.*, **123**, 1139 (1976).
211. S.J. Lennon, F.P.A. Robinson, *Corros. Sci.*, **26**, 995 (1986).
212. S. Kesavan, T.A. Mozhi, B.E. Wilde, *Corrosion*, **45**, 213 (1989).
213. A.J. Bard, *Encyclopedia of Electrochemistry of the Elements*, Vol 7, Marcel Dekker, New York (1973), p. 206.
214. M. Fleischmann, H.R. Thirsk, *Electrochim. Acta*, **1**, 146 (1959).
215. R.D. Armstrong, J.A. Harrison, *J. Electrochem. Soc.*, **116**, 328 (1969).
216. R.D. Armstrong, A.E. Metcalfe, *J. Electroanal. Chem.*, **63**, 19 (1975).
217. A. Benwick, M. Fleischmann, H.R. Thirsk, *Trans. Faraday Soc.*, **58**, 2200 (1962).
218. M. Fleischmann, K.S. Rajagopalan, H.R. Thirsk, *Trans. Faraday Soc.*, **59**, 741 (1963).
219. M. Fleischmann, J. Pattison, H.R. Thirsk, *Trans. Faraday Soc.*, **61**, 1256 (1965).
220. R.D. Armstrong, M. Fleischmann, J.W. Oldfield, *J. Electroanal. Chem.*, **14**, 235 (1967).
221. M. Fleischmann, J.A. Harrison, H.R. Thirsk, *Trans. Faraday Soc.*, **61**, 2742 (1965).
222. R.D. Armstrong, D.F. Porter, H.R. Thirsk, *J. Phys. Chem.*, **72**, 2300 (1968).
223. R.D. Armstrong, *J. Electroanal. Chem.*, **20**, 168 (1969).
224. M. Fleischmann, H. Thirsk, in *Advances in Electrochemistry and Electrochemical Engineering*, Vol 3, ed. P. Delahay, C. Tobias, John Wiley and Sons, New York (1963), p. 123.
225. R.D. Armstrong, M. Fleischmann, H.R. Thirsk, *J. Electroanal. Chem.*, **11**, 208 (1966).

226. M. Fleischmann, H.R. Thirsk, *J. Electrochem. Soc.*, **110**, 688 (1963).
227. R.D. Armstrong, M. Fleischmann, *Z. Phys. Chem.*, **52**, 131 (1967).
228. S.K. Rangarajan, *J. Electroanal. Chem.*, **46**, 119 (1973).
229. S.K. Rangarajan, *J. Electroanal. Chem.*, **46**, 125 (1973).
230. J.A. Harrison, W.J. Lorenz, *J. Electroanal. Chem.*, **76**, 375 (1977).
231. M.Y. Abyaneh, B.R. Scharifker, G.J. Hills, *J. Electroanal. Chem.*, **119**, 187 (1981).
232. M.Y. Abyaneh, M. Fleischmann, *J. Electroanal. Chem.*, **119**, 197 (1981).
233. E. Bosco, S. Rangarajan, *J. Electroanal. Chem.*, **134**, 213 (1982).
234. E. Bosco, S. Rangarajan, *J. Electroanal. Chem.*, **134**, 225 (1982).
235. M. Abyaneh, *Electrochim. Acta*, **27**, 1329 (1982).
236. M. Abyaneh, J. Hendrikx, W. Yisscher, E. Barendrecht, *J. Electrochem. Soc.*, **129**, 2654 (1982).
237. M.Y. Abyaneh, M. Fleischmann, *Electrochim. Acta*, **27**, 1513 (1982).
238. M.Y. Abyaneh, *J. Electroanal. Chem.*, **209**, 1 (1986).
239. M.Y. Abyaneh, *Electrochim. Acta*, **36**, 727 (1991).
240. D.J. Astley, J.A. Harrison, H.R. Thirsk, *Trans. Faraday Soc.*, **64**, 192 (1968).
241. G. Hills, D.J. Schiffrin, J. Thompson, *Electrochim. Acta*, **19**, 657 (1974).
242. G. Gunawardena, G.J. Hills, I. Montenegro, *Electrochim. Acta*, **23**, 693 (1978).
243. G. Gunawardena, G. Hills, I. Montenegro, B. Scharifker, *J. Electroanal. Chem.*, **138**, 225 (1982).
244. G. Gunawardena, G. Hills, I. Montenegro, *J. Electroanal. Chem.*, **138**, 241 (1982).
245. G. Gunawardena, G. Hills, I. Montenegro, B. Scharifker, *J. Electroanal. Chem.*, **138**, 255 (1982).
246. B. Scharifker, G.J. Hills, *Electrochim. Acta*, **28**, 879 (1983).
247. V. Tsakova, A. Milchev, *J. Electroanal. Chem.*, **235**, 237 (1987).
248. S. Fletcher, *J. Chem. Soc., Faraday Trans. I*, **79**, 467 (1983).
249. R.L. Deutscher, S. Fletcher, *J. Electroanal. Chem.*, **153**, 67 (1983).
250. B.R. Scharifker, J. Mostany, *J. Electroanal. Chem.*, **177**, 13 (1984).
251. J. Mostany, J. Mozota, B.R. Scharifker, *J. Electroanal. Chem.*, **177**, 25 (1984).
252. V. Tsakova, A. Milchev, *Electrochim. Acta*, **36**, 1151 (1991).
253. C. Alonso, R.C. Salvarezza, J.M. Vara, A.J. Arvia, *Electrochim. Acta*, **35**, 489 (1990).
254. S. Fletcher, *J. Electroanal. Chem.*, **195**, 417 (1985).
255. R.G. Barradas, E. Bosco, *Electrochim. Acta*, **31**, 949 (1986).
256. M. Sluyters-Rehbach, J. Wijenberg, E. Bosco, J. Sluyters, *J. Electroanal. Chem.*, **236**, 1 (1987).
257. P. Bobbert, M.M. Wind, J. Vlieger, *Physica*, **146A**, 69 (1987).
258. P.A. Bobbert, M.M. Wind, J. Vlieger, *Physica*, **141A**, 58 (1987).
259. R.L. Deutscher, S. Fletcher, *J. Electroanal. Chem.*, **239**, 17 (1988).
260. J.W. Jacobs, *J. Electroanal. Chem.*, **247**, 135 (1988).
261. W. Mulder, J. Wijenberg, M. Sluyters-Rehbach, J. Sluyters, *J. Electroanal. Chem.*, **270**, 7 (1989).
262. R. Greef, P.A. Bobbert, J. Vlieger, *J. Electroanal. Chem.*, **280**, 283 (1990).
263. M. Mirkin, A.P. Nilov, *J. Electroanal. Chem.*, **283**, 35 (1990).

264. E. Bosco, S. Rangarajan, *J. Chem. Soc., Faraday Trans. I*, **77**, 1673 (1981).
265. S. Arulraj, M. Noel, *Electrochim. Acta*, **33**, 979 (1988).
266. B. Bhattacharjee, S.K. Rangarajan, *J. Electroanal. Chem.*, **302**, 207 (1991).
267. E.B. Budevski in *Comprehensive Treatise of Electrochemistry*, Vol. 7, ed. B. Conway, J.O'M. Bockris, E. Yeager, S. Khan, R.E. White, Plenum Press, New York (1983), chapter 7, part A.
268. H.R. Thirsk, J.A. Harrison, *A Guide to the Study of Electrode Kinetics*, Academic Press, London (1972), chapter 3.
269. *Electrocrystallisation*, ed. R. Weil, R.G. Barradas, **81-6**, Electrochem. Soc. Inc., New Jersey (1981).
270. A. Benwick, M. Fleischmann, *Proc. Int. Symp. on Topics in Surface Chemistry*, ed. E. Kay, P. Bagus, Plenum Press, New York (1978), p. 45.
271. G. Briggs, M. Fleischmann, D.J. Lax, H.R. Thirsk, *Trans. Faraday Soc.*, **64**, 3120 (1968).
272. J. Wijenberg, W. Mulder, M. Sluyters-Rehbach, J. Sluyters, *J. Electroanal. Chem.*, **256**, 1 (1988).
273. R. Deutscher, S. Fletcher, *J. Electroanal. Chem.*, **277**, 1 (1990).
274. R.L. Deutscher, S. Fletcher, *J. Electroanal. Chem.*, **164**, 1 (1984).
275. M.H.J. Hottenhuis, A.L.M. van den Berg, J.P. van der Eerden, *Electrochim. Acta*, **33**, 1519 (1988).
276. S. Fletcher, *J. Electroanal. Chem.*, **164**, 11 (1984).
277. S. Fletcher, *Electrochim. Acta*, **28**, 917 (1983).
278. S. Fletcher, T. Lwin, *Electrochim. Acta*, **28**, 237 (1983).
279. I. Markov, D. Kashchiev, *J. Cryst. Growth*, **16**, 170 (1972).
280. F. Palmisano, E. Desimoni, L. Sabbatini, G. Torsi, *J. App. Electrochem.*, **9**, 517 (1979).
281. J.W. Jacobs, J.M. Rikken, *J. Electrochem. Soc.*, **136**, 3633, 3641 (1989).
282. R.L. Deutscher, S. Fletcher, *Electrochemistry: Current and Potential Applications, Proc. 7th Australian Electrochem. Conf.*, ed. T. Tran, M. Skylas - Kazacos, Royal Australian Chemical Inst., Melbourne (1988), p. 312.
283. R.L. Deutscher, S. Fletcher, *Electrochemistry: Current and Potential Applications, Proc. 7th Australian Electrochem. Conf.*, ed. T. Tran, M. Skylas - Kazacos, Royal Australian Chemical Inst., Melbourne (1988), p. 308.
284. M.Y. Abyaneh, G. Halvorsen, *J. Electroanal. Chem.*, **149**, 263 (1983).
285. S. Itoh, N. Yamazoe, T. Seiyama, *Surf. Technol.*, **5**, 27 (1977).
286. M. Avrami, *J. Chem. Phys.*, **7**, 1103 (1939).
287. M. Avrami, *J. Chem. Phys.*, **8**, 212 (1940).
288. M. Avrami, *J. Chem. Phys.*, **9**, 177 (1941).
289. U.R. Evans, *Trans. Faraday Soc.*, **41**, 365 (1945).
290. I. Markov, A. Boynov, S. Toshev, *Electrochim. Acta*, **18**, 377 (1973).
291. I. Markov, S. Toshev, *Electrodeposition Surf. Treat.*, **3**, 385 (1975).
292. I. Markov, S. Toshev, *Electrodeposition and Surface Treatment*, **3**, 385 (1975).
293. A. Milchev, *J. Electroanal. Chem.*, **312**, 267 (1991).
294. J. Ambrose, R. Barradas, D. Shoesmith, *J. Electroanal. Chem.*, **47**, 47 (1973).

295. A. Milchev, V. Tsakova, *J. App. Electrochem.*, **20**, 301 (1990).
296. A. Milchev, *J. App. Electrochem.*, **20**, 307 (1990).
297. S. Toshev, A. Milchev, E. Vassileva, *Electrochim. Acta*, **21**, 1055 (1976).
298. A. Milchev, B.R. Scharifker, G.J. Hills, *J. Electroanal. Chem.*, **132**, 277 (1982).
299. M. Noel, S. Chandrasekaran, C.A. Basha, *J. Electroanal. Chem.*, **225**, 93 (1987).
300. G. Hills, I. Montenegro, B. Scharifker, *J. App. Electrochem.*, **10**, 807 (1980).
301. P.M. Rigano, C. Mayer, T. Chierchie, *J. Electroanal. Chem.*, **248**, 219 (1988).
302. M.D. Pritzker, *J. Electroanal. Chem.*, **243**, 57 (1988).
303. A. Milchev, V. Tsakova, T. Chierchie, K. Jüttner, W.J. Lorenz, *Electrochim. Acta*, **31**, 971 (1986).
304. C.P. Jensen, D.F. Mitchell, M.J. Graham, *Electrochim. Acta*, **22**, 1125 (1982).
305. J. Kruger, *J. Electrochem. Soc.*, **110**, 654 (1963).
306. J.O'M. Bockris, M. Genshaw, V. Brusic, *Symp. Faraday Soc.*, **4**, 177 (1970).
307. S. Gojkovic, S.K. Zecevic, D.M. Drazic, *Electrochim. Acta*, **39**, 975 (1994).
308. R. Goetz, B. MacDougall, M.J. Graham, *Electrochim. Acta*, **31**, 1299 (1986).
309. T. Tsuru, E. Fujii, S. Haruyama, *Corros. Sci.*, **31**, 655 (1990).
310. J. Zou, D. Chin, *Electrochim. Acta*, **32**, 1751 (1987).
311. A. Wieckowski, E. Ghali, *Electrochim. Acta*, **30**, 1423 (1985).
312. D. Harrington, A. Wieckowski, S. Rosasco, B. Scharolt, G. Salaita, A. Hubbard, *Corros. Sci.*, **25**, 849 (1985).
313. M.G.S. Ferreira, J.L. Dawson, *J. Electrochem. Soc.*, **132**, 760 (1985).
314. F. Graham, C. Tonkinson, University of Natal, unpublished results.
315. R.P. Wei, M. Gao, *Corrosion*, **47**, 948 (1991).
316. R.P. Wei, M. Gao, P.Y. Xu, *J. Electrochem. Soc.*, **136**, 1835 (1989).
317. R.G. Kelly, R.C. Newman, *J. Electrochem. Soc.*, **137**, 357 (1990).
318. G.S. Frankel, B.M. Rush, C.V. Jahnes, C.E. Farrell, A.J. Davenport, H.S. Isaacs, *J. Electrochem. Soc.*, **138**, 643 (1991).
319. G.T. Burstein, R.J. Cinderey, *Oxide Films on Metals and Alloys*, ed. B.R. MacDougall, R.S. Alwith, T.A. Ramanarayanan, **92-22**, Electrochem. Soc. Inc., New Jersey (1992), p.202.
320. R. Izatt, H. Johnston, D. Eatough, J. Hansen, J. Christensen, *Thermochim. Acta*, **2**, 77 (1971).
321. T. Osterud, M. Prytz, *Acta Chem. Scand.*, **4**, 1250 (1950).
322. J. Marsh, W. Newling, J. Rick, *J. Appl. Chem.*, **2**, 681 (1952).
323. Lux, *Handbook of Preparative Inorganic Chemistry*, 2nd edition, **2**, ed. G. Brauer, Academic Press, New York (1965) p. 1497.
324. H. Weiser, *Inorganic Synthesis*, **2**, 215 (1946).
325. F. Graham, MSc, University of Natal (Durban) (1987).
326. H. Brookes, J. Bayles, F. Graham, *J. App. Electrochem.*, **20**, 223 (1990).
327. F. Graham, H. Brookes, J. Bayles, *J. App. Electrochem.*, **20**, 45 (1990).
328. G. Jones, *High Temperature High Pressure Electrochemistry in Aqueous Solutions*, ed. D. Jones, J.

- Slater, R. Staehle, **NACE-4**, NACE, Houston (1976), p. 265.
329. B.E. Wilde, *High Temperature High Pressure Electrochemistry in Aqueous Solutions*, ed. D. Jones, J. Slater, R. Staehle, **NACE-4**, NACE, Houston (1976), p. 277.
 330. F. Salibas, MSc Thesis, University of Natal (Durban) (1983).
 331. P. Opekar, P. Barren, *J. Electroanal. Chem.*, **69**, 1 (1976).
 332. A.J. Bard, L.R. Faulkner, *Electrochemical Methods - Fundamentals and Applications*, John Wiley and Sons, New York (1980), Ch. 8.
 333. A.C. Riddiford, *Advances in Electrochemistry and Electrochemical Engineering*, Vol. 4, (ed. P. Delahay) Interscience (1966) p. 47.
 334. B. MacDougall, M.J. Graham, *Electrochim. Acta*, **26**, 705 (1981).
 335. A.M.T. Olmedo, R. Pereiro, D.J. Schiffrin, *J. Electroanal. Chem.*, **74**, 19 (1976),
 336. *Model 376 Logarithmic Current Converter, Operating and Service Manual*, EG & G, Princeton Applied Research, New York (1979), p. III-2.
 337. H. Brookes, F. Graham, *Electrochim. Acta*, **33**, 1475 (1988).
 338. M. Ferreira, PhD Thesis, University of Southampton (1979).
 339. G.J. Hills, A. Kaveh Pour, B.R. Scharifker, *Electrochim. Acta*, **28**, 891 (1983).
 340. D.W. Shoesmith, W. Lee, M.G. Bailey, *Electrocrystallisation*, ed. R. Weil, R.G. Barradas, **81-6**, Electrochem. Soc. Inc., New Jersey (1981), p. 272.
 341. F. Graham, J. Bayles, J. Bayles, R. McCrindle, F. Salibas, J. Fourie, *in preparation*.
 342. G. Bignold, M. Fleischmann, *Electrochim. Acta*, **19**, 363 (1974).
 343. Southampton Electrochemistry Group, *Instrumental Methods in Electrochemistry*, Ellis Horwood, England (1985), chapter 9.
 344. J. Ambrose, R.G. Barradas, D.W. Shoesmith, *J. Electroanal. Chem.*, **47**, 65 (1973).
 345. P. Mitchell, N. Hampton, J. Smith, *J. Electroanal. Chem.*, **12**, 13 (1982).
 346. J. Ambrose, R. Barradas, K. Belinko and D. Shoesmith, *J. Colloid. Interfac. Sci.* **47**, 441 (1974).
 347. L. Franke, W. Forker, *Electrochim. Acta*, **20**, 775 (1975).
 348. D. Landolt, *Passivity of Metals*, ed. R.P. Frankenthal, J. Kruger, Electrochem. Soc. Inc., Princeton, New Jersey (1978), p. 484.
 349. R.P. Frankenthal, H.W. Pickering, *J. Electrochem. Soc.*, **119**, 1304 (1972).
 350. M.J. Danielson, *J. Electrochem. Soc.*, **135**, 1326 (1988).
 351. D. Nicholls, *The Chemistry of Iron, Cobalt and Nickel*, Pergamon Press, Oxford (1975), p. 1011.
 352. *Handbook of Chemistry and Physics*, 62nd edition, ed. R. West, M. Astle, CRC Press Inc., Florida (1981), p. B-108.
 353. H. Brookes, F. Graham, *Corrosion*, **45**, 287 (1989).
 354. D. Skoog, D. West, *Fundamentals of Analytical Chemistry*, 3rd edition, Holt, Rinehart and Winston, New York (1976), p. 126.
 355. J. Nyvlt, O. Söhnel, M. Matuchová and M. Broul, *The Kinetics of Industrial Crystallisation*, Elsevier, Amsterdam (1985), Chapters 3, 4, 6.

356. L.D. Burke, D.P. Whelan, *J. Electroanal. Chem.*, **135**, 55 (1982).
357. A. Agrawal, K.G. Sheth, K. Poteet, R.W. Staehle, *J. Electrochem. Soc.*, **119**, 1637 (1972).
358. J. Zou, D. Chin, *Electrochim. Acta*, **33**, 477 (1988).
359. K.E. Heusler, B. Kusian, D. McPhail, *Ber. Bunsenges Phys. Chem.*, **94**, 1443 (1990).
360. D.D. Macdonald, *Transient Techniques in Electrochemistry*, Plenum Press, New York (1977).
361. A.J. Calandra, N.R. DeTacconi, R. Pereiro, A.J. Arvia, *Electrochim. Acta*, **19**, 901 (1974).
362. N. Sato, M. Cohen, *J. Electrochem. Soc.*, **111**, 519 (1964).
363. A.H. Lanyon, B.M. Trapnell, *Proc. Roy. Soc.*, **227A**, 387 (1955).
364. J.T. Law, *J. Phys. Chem. Solids*, **4**, 91 (1958).
365. D.E. Williams, G.A. Wright, *Electrochim. Acta*, **21**, 1009 (1976).
366. S. Srinivasan, E. Gileadi, *Electrochim. Acta*, **11**, 321 (1966).
367. M. Martins, A.J. Calandra, A.J. Arvia, *Electrochim. Acta*, **17**, 741 (1972).
368. M. Noel, K.I. Vasu, *Cyclic Voltammetry and the Frontiers of Electrochemistry*, Aspect Publications, London (1990), p. 386.
369. Southampton Electrochemistry Group, *Instrumental Methods in Electrochemistry*, Ellis Horwood, England (1985), chapter 4.
370. E.B. Castro, J.R. Vilche, A.J. Arvia, *Corros. Sci.*, **32**, 37 (1991).
371. R.D. Armstrong, I. Baurhoo, *J. Electroanal. Chem.*, **40**, 325 (1972).
372. G. Horányi, E. Rizmayer, *J. Electroanal. Chem.*, **215**, 369 (1986).
373. B. Wels, D. Johnson, *J. Electrochem. Soc.*, **137**, 2785 (1990).
374. Southampton Electrochemistry Group, *Instrumental Methods in Electrochemistry*, Ellis Horwood, England (1985), p. 210.
375. H. Neugebauer, G. Nauer, N. Brinda-Konopik, G. Gidaly, *J. Electroanal. Chem.*, **122**, 381 (1981).
376. J.O'M. Bockris, M.A. Greshaw, V. Brusic, M. Wroblowa, *Electrochim. Acta*, **16**, 1859 (1971).
377. J.O'M. Bockris, A. Reddy, *Modern Electrochemistry*, Vol. 2, Plenum Press, New York (1970), p. 1080.
378. D.D. Macdonald, B. Roberts, *Electrochim. Acta*, **23**, 557 (1978).
379. D. Poa, J. Miller, N. Yao, *Extended Abstracts*, **83 - 2**, Electrochem. Soc., New Jersey (1983) p. 17.
380. D. Drazic, C.S. Hao, *Electrochim. Acta*, **27**, 1409 (1982).
381. Y. Geronov, T. Tomov, S. Georgiev, *J. App. Electrochem.*, **5**, 351 (1975).
382. D. Geana, A.A. El Miligy, W.J. Lorenz, *J. App. Electrochem.*, **4**, 337 (1974).
383. H.G. Silver, E. Lekas, *J. Electrochem. Soc.*, **117**, 5 (1970).
384. R. Kirchheim, B. Heine, H. Fischmeister, S. Hofmann, H. Knote, U. Stolz, *Corros. Sci.*, **29**, 899 (1989).
385. L.D. Burke, O.J. Murphy, *J. Electroanal. Chem.*, **109**, 379 (1980).
386. W. Schwartz, W. Simon, *Ber. Bunsenges Phys. Chem.*, **67**, 108 (1963).
387. M. McKubre, *The Mechanism of Dissolution and Passivation of Iron and Zinc in Concentrated Potassium Hydroxide Solutions*, Final report to DOE, Contract 450561 (1981).
388. H.C. Brookes, F.J. Graham, *J. Chem. Soc., Faraday Trans.*, **89**, 547 (1993).
389. J. Howard, D. Pletcher, *J. Electroanal. Chem.*, **18**, 644 (1988).

- 390. T. Vålund, P. Sjöwall, *Electrochim. Acta*, **34**, 273 (1989).
- 391. M. Figuerola, R. Salvarezza, A. Arvia, *Electrochim. Acta*, **31**, 665 (1986).
- 392. J. Gomez Becerra, R.C. Salvarezza, A.J. Arvia, *Electrochim. Acta*, **33**, 613 (1988).
- 393. R. Kurtz, V. Henrich, *Surface Science*, **129**, 345 (1983).
- 394. O. Johnson, *Chemica Scripta*, **8**, 162 (1975).
- 395. J. Coad, J. Cunningham, *J. Electron Spectrosc.*, **3**, 449 (1974).
- 396. F.J. Graham, H.C. Brookes, *in preparation*.
- 397. H.C. Brookes, F.J. Graham, *in preparation*.
- 398. F.J. Graham, H.C. Brookes, *in preparation*.
- 399. H.C. Brookes, F.J. Graham, *in preparation*.

APPENDIX A

APPENDIX AXPS BINDING ENERGIES

Summary of XPS Binding Energies (BE) of Fe, Cr and O Species Reported
in the Literature For the Analysis of Fe, Cr and FeCr Alloys.

Element	Species	line	BE/eV	Ref.
Fe	Fe(0)	$2p_{3/2}$	706.75	A1
			707.3	A2
			706.8	A3
			706	A4
			707	A5
			706.8	A6
			706.8	A7
			706.9	A8
			706.8	A9
			705.9	A10
			706.5	A11
			707.5	A12
			707.7	A13
			706.8	A14
			707.0	A15
			707.0	A16
	FeO	$2p_{3/2}$	709.5	A8
			709.6	A11
			709.0	A13
			709.0	A14
			710.2	A17
	Fe ₂ O ₃	$2p_{3/2}$	711.0	A2
			711.0	A5
			711.0 α -Fe ₂ O ₃	A7
			711.0 α -Fe ₂ O ₃	A8
			710.97	A9
			711.6	A11
			709.9	A13
			711.0	A14

Element	Species	line	BE/eV	Ref.
Fe	Fe ₂ O ₃	2p _{3/2}	711.2	A15
			711.0	A18
			711.4	A19
			710.5	A20
			711.4 α -Fe ₂ O ₃	A21
	FeOOH	2p _{3/2}	711.3 γ -FeOOH	A7
			711.3 satellite @ 719.85	A8
			711.9 α -FeOOH	A8
			711.5	A9
			711.6 γ -FeOOH	A14
			711.4 α -FeOOH	A14
			710.9	A17
			711.0 α -FeOOH	A21
	Fe ₃ O ₄	2p _{3/2}	710.8	A7
			708.3	A8
			708.9	A10
			710.8	A11
			711.4	A13
			711.0	A14
			711.2	A18
			710.6	A19
			710.2	A20
	FeCr ₂ O ₄	2p _{3/2}	710.8	A19
			710.8	A20
	Fe ²⁺	2p _{3/2}	709.3	A3
			708	A4
			709	A5
	Fe ³⁺	2p _{3/2}	711.3	A3
			710.5	A4
			711	A5
			710.6	A16
	Fe ⁶⁺	2p _{3/2}	714	A7
Cr	Cr(0)	2p _{3/2}	574.1	A1
			574.1	A3
			573.5	A5
			574.7	A12
			574.1	A14
			574.3	A16
			574.1	A22
			574.0	A23
			573.5	A24

Element	Species	line	BE/eV	Ref.
Cr	Cr(0)	$2p_{3/2}$	574.1	A25
			574.2	A26
			574.1	A27
	CrO ₂	$2p_{3/2}$	576.1	A28
	Cr ₂ O ₃	$2p_{3/2}$	576.9	A2
			576.3	A3
			576.7	A5
			576.5	A14
			576.6	A17
			576.6	A24
			576.3	A25
			576.8	A26
			576.3	A27
			576.6	A28
			576.3	A29
			576.7	A29
			576.3	A30
			582.3	A31
	Cr(OH) ₃	$2p_{3/2}$	577.0	A3
			577.0	A14
			577.1	A22
			577.0	A25
			577.9	A26
			577.0	A29
			576.8	A30
	Cr(OH) ₃ ·4H ₂ O	$2p_{3/2}$	577.03	A9
	CrO ₃	$2p_{3/2}$	578.0	A2
			578.1	A3
			579.1	A14
			577.1	A24
			578.1	A25
			578.1	A27
			578.1	A29

Element	Species	line	BE/eV	Ref.	
Cr	CrOOH	2p _{3/2}	577.0	A27	
			576.8	A28	
	Cr ³⁺	2p _{3/2}	576.5	A5	
			576.9	A16	
	CrO ₄ ⁼	2p _{3/2}	579.3	A3	
			579.3	A25	
			579.3	A27	
			579.3	A29	
	Na ₂ CrO ₄	2p _{3/2}	584.9	A31	
	O	OH ⁻	1s	531.4	A1
531.4				A3	
531.9				A4	
532.2				MOH or MOOH	A6
531.4				γ-FeOOH	A7
531.4				α-FeOOH	A7
531.4				α, γ-FeOOH	A9
532.3				Cr(OH) ₃ ·0.4H ₂ O	A9
531.4				Cr(OH) ₃	A22
531.4					A25
531.4					A27
531.5					A30
531.2					A32
530.2				FeOOH	A33
531.6				Fe(OH) ₂	A33
O ⁼		1s	529.9	A1	
			529.9	A3	
			530.2	A4	
			530.7	MO	A6
			530.1	FeOOH	A7
			530.1	Fe ₃ O ₄	A7
			529.9	Fe ₂ O ₃	A7
			530.3	α-FeOOH	A8
			530.0	FeO	A8

Element	Species	line	BE/eV	Ref.
O	O ⁼	1s	530.0	γ -Fe ₂ O ₃ A8
			529.8	α -Fe ₂ O ₃ A8
			530.2	Fe ₂ O ₃ A9
			530.0	Fe ₂ O ₃ A9
			530.17	γ -FeOOH A9
			529.9	α -Fe ₂ O ₃ A11
			530.0	Cr ₂ O ₃ A22
			529.9	A25
			529.9	A27
			530.0	A32
			530.2	FeOOH A33
			530.2	Fe-O bonds A34
			530.6	Cr-O bonds A34
	H ₂ O	1s	533.0	A3
			533.0	A27
			532.9	A25
			532.8	ads. H ₂ O A33

APPENDIX REFERENCES

- A1. J. Lumsden, P. Stoker, *Surfaces, Inhibition and Passivation*, ed. E. McCafferty, R.J. Brodd, **86-7**, Electrochem. Soc. Inc., New Jersey (1986), p. 305.
- A2. W. Cieslak, F. Delnick, D. Peebles, J. Rogers, *Surfaces, Inhibition and Passivation*, ed. E. McCafferty, R.J. Brodd, **86-7**, Electrochem. Soc. Inc., New Jersey (1986), p. 368.
- A3. C. Clayton, L. Rosenzweig, M. Oversluizen, Y. Lu, *Surfaces, Inhibition and Passivation*, ed. E. McCafferty, R.J. Brodd, **86-7**, Electrochem. Soc. Inc., New Jersey (1986), p. 323.
- A4. V. Jovancicevic, R. Kainthla, Z. Tang, B. Yang, J. O'M. Bockris, *Surfaces, Inhibition and Passivation*, ed. E. McCafferty, R.J. Brodd, **86-7**, Electrochem. Soc. Inc., New Jersey (1986), p. 192.
- A5. I. Olefjord, *Corros. Sci.*, **15**, 687 (1975).
- A6. G. Okamoto, T. Shibata, *Passivity of Metals*, ed. R.P. Frankenthal, J. Kruger, Electrochem. Soc. Inc., New Jersey (1980), p. 646.
- A7. H. Konno, M. Nagayama, *Passivity of Metals*, ed. R.P. Frankenthal, J. Kruger, Electrochem. Soc. Inc., New Jersey (1980), p. 585.
- A8. N. McIntyre, D. Zetaruk, *Anal. Chem.*, **49**, 1521 (1977)
- A9. K. Asami, K. Hashimoto, S. Shimodaira, *Corros. Sci.*, **17**, 713 (1977)
- A10. J. Coad, J. Cunningham, *J. Electron Spectrosc.*, **3**, 449 (1974).
- A11. P. Mills, J. Sullivan, *J. Phys. D: Appl. Phys.*, **216**, 723 (1983).
- A12. G. Conner, *J. Vac. Sci. Technol.*, **15**, 343 (1978).
- A13. R. Kurtz, V. Henrich, *Surface Science*, **129**, 345 (1983).
- A14. K. Asami, K. Hashimoto, *Corros. Sci.*, **17**, 559 (1977).
- A15. C. Brundle, T. Chuang, K. Wandelt, *Surf. Sci.*, **68**, 459 (1977).
- A16. P. Marcus, I. Olefjord, *Corros. Sci.*, **28**, 589 (1988).
- A17. G. Allen, A. Curtis, A. Hooper, P. Tucker, *J. Chem. Soc.*, 1675 (1973).
- A18. J. Contour, G. Mouvier, *J. Catal.*, **40**, 324 (1975).
- A19. M. Oku, K. Hirokawa, *J. Electron Spectrosc.*, **8**, 475 (1976).
- A20. K. Hirokawa, M. Oku, *Talanta*, **26**, 855 (1979).
- A21. G. Allen, M. Curtis, A. Hooper, P. Tucker, *J. Chem. Soc (Dalton)*, 1525 (1974).
- A22. I. Olefjord, B. Brox, U. Jelvestam, *Proc. Electrochem. Soc.*, **84-9**, The Electrochem. Soc. Inc., New Jersey, 1984. p. 388.
- A23. *Handbook of X-Ray Photoelectron Spectroscopy*, Perkin Elmer Corp. (1979).

- A24. O. Johnson, *Chemica Scripta*, **8**, 162 (1975).
- A25. Y. Lu, C. Clayton, A. Brooks, *Corros. Sci.*, **29**, 863 (1989)
- A26. P. Marcus, J.M. Grimal, *Corros. Sci.*, **31**, 377 (1990).
- A27. A. Brooks, C.R. Clayton, K. Doss, Y. Lu, *J. Electrochem. Soc.*, **133**, 2459 (1986).
- A28. I. Ilemoto, K. Ishii, S. Kinoshita, H. Kurado, M. Franco, J. Thomas, *J. Solid State Chem.*, **17**, 425 (1976).
- A29. Y. Lu, C. Clayton, *J. Electrochem. Soc.*, **123**, 2571 (1985).
- A30. I. Olefjord, *Passivity of Metals and Semiconductors*, ed. M. Froment, Elsevier, Amsterdam (1983), p. 561.
- A31. J. Augustynski, *Passivity of Metals*, ed. R.P. Frankenthal, J. Kruger, The Electrochem. Soc. Inc., New Jersey (1980), p. 989.
- A32. I. Olefjord, *Mat. Sci and Eng.*, **242**, 161 (1981).
- A33. T. von Moltke, R.F. Sandenburg, *Proceedings of the 5th International Conference on Applied Corrosion Technology* (1990).
- A34. K. Asami, K. Hashimoto, S. Shimodaira, *Corros. Sci.*, **18**, 151 (1978).

APPENDIX B

PUBLICATIONS

The following are some of the papers, based on work presented in this thesis, that have been published :

1. H. Brookes, F. Graham, *J. Chem. Soc., Faraday Trans.*, **89**, 547 (1993).
A study of the anodic oxidation of stainless steel alloys, and their constituent elements, in acidic electrolytes.
2. F. Graham, H. Brookes, *Progress in the Understanding and Prevention of Corrosion, Vol 2*, Eds. J. M. Costa and A. D. Mercer, The Institute of Materials, London, (1993) p. 1055.
Anodic film formation on iron in alkaline cyanide electrolytes.
3. F. Graham, H. Brookes, *Electrochim. Acta*, **33**, 1475 (1989).
Growth of anodic films on Fe18Cr alloys.
4. F. Graham, H. Brookes, *Comm. of the Electron Microscopy Society of Southern Africa*, **21**, 273 (1991).
Growth of anodic films on iron in NaOH/NaCN electrolytes.
5. H. Brookes, F. Graham, *Cost Effective Corrosion Control into the 21st Century*, S.A. Corr Inst., (1994) p.459.
Corrosion of iron and ferrous alloys in alkaline cyanide electrolytes.
6. H. Brookes, F. Graham, *South African Journal of Chemistry*, in press.
Anodic film formation on iron : A voltammetric and XPS study.

Please note, that despite the fact that the author of this thesis appears as second author on several of the above papers (supervisory privilege!) all of these papers were in fact written by F. Graham.